Dissertation

SUBMITTED TO THE

Combined Faculties of the Natural Sciences and Mathematics
of the Ruperto-Carola-University of Heidelberg, Germany

FOR THE DEGREE OF

Doctor of Natural Sciences

Put forward by

Kilian Peter Heeg

born in Ulm, Germany

Oral examination: December 9th, 2014

X-Ray Quantum Optics With Mössbauer Nuclei In Thin-Film Cavities

Referees:

Priv.-Doz. Dr. Jörg Evers
Prof. Dr. Jörg Jäckel

Röntgenquantenoptik mit Mößbauerkernen in Dünnschichtkavitäten — In dieser Arbeit werden Dünnschichtkavitäten mit eingebetteten Mößbauerkernen, die nahe ihrer Resonanz mit Röntgenlicht wechselwirken, aus quantenoptischer Perspektive untersucht. Eine umfassende theoretische Beschreibung wird entwickelt und im linearen Anregungsraum, der für heutige Experimente von Bedeutung ist, werden kompakte analytische Ausdrücke für die Observablen gewonnen. Auch komplexe Kavitäten können in sehr guter Übereinstimmung mit früheren Experimenten und semiklassischen Methoden modelliert werden. Es wird gezeigt, dass die spektrale Antwort des Systems ohne magnetischer Hyperfeinstrukturaufspaltung der Kerne aus durchstimmbaren Fano-Resonanzen besteht. Diese Linienformkontrolle wird experimentell realisiert und ermöglicht es in guter Übereinstimmung mit den Vorhersagen spektroskopische Eigenschaften mit hoher Präzision zu bestimmen und die Phase der Kernresonanz zu rekonstruieren. Durch die Ausrichtung der Magnetisierung sowie der Lichtpolarisation können fortgeschrittene quantenoptische Levelschemata realisiert werden. In diesen werden vakuuminduzierte Kohärenzeffekte vorhergesagt und erfolgreich im Experiment bestätigt. Weiterhin wird gezeigt, dass die Gruppengeschwindigkeit von Röntgenlichtpulsen in der Kavität gesteuert werden kann. Eine Beobachtungsmethode dafür wird eingeführt und verwendet, um verlangsamtes Licht experimentell zu demonstrieren. Zuletzt werden nichtlineare Effekte, die mit zukünftigen Lichtquellen beobachtbar werden könnten, untersucht und ein nichtlinearer Mechanismus zur Linienformkontrolle wird diskutiert.

X-Ray Quantum Optics With Mössbauer Nuclei In Thin-Film Cavities — In this thesis thin-film cavities with embedded Mössbauer nuclei probed by near-resonant x-ray light are studied from a quantum optical perspective. A theoretical framework is developed and compact expressions for the observables are derived for the linear excitation regime, which is encountered in current experiments. Even advanced cavity layouts can be modeled in excellent agreement with the results of previous experiments and semi-classical approaches. In the absence of magnetic hyperfine splitting, the spectral response of the system is found to be formed by tunable Fano profiles. An experimental implementation of this line shape control allows to extract spectroscopic signatures with high precision and to reconstruct the phase of the nuclear transition in good agreement with the theoretical predictions. The alignment of medium magnetization and polarization control of the x-rays enable to engineer advanced quantum optical level schemes, in which vacuum induced coherence effects are predicted and successfully demonstrated in an experiment. Furthermore, it is shown that group velocity control for x-ray pulses can be achieved in the cavity. A scheme for its observation is proposed and then employed to experimentally confirm sub-luminal x-ray propagation. Finally, non-linear effects, which could become accessible with future light sources, are explored and a non-linear line shape control mechanism is discussed.

Within the framework of this thesis, the following articles were published in refereed journals:

- ***Vacuum-assisted generation and control of atomic coherences at x-ray energies***
  K. P. Heeg, H.-C. Wille, K. Schlage, T. Guryeva, D. Schumacher, I. Uschmann, K. S. Schulze, B. Marx, T. Kämpfer, G. G. Paulus, R. Röhlsberger, and J. Evers
  Physical Review Letters **111**, 073601 (2013)
- ***X-ray quantum optics with Mössbauer nuclei embedded in thin-film cavities***
  K. P. Heeg and J. Evers
  Physical Review A **88**, 043828 (2013)

Articles submitted for publication in refereed journals:

- ***Interferometric phase detection at x-ray energies via Fano resonance control***
  K. P. Heeg, C. Ott, D. Schumacher, H.-C. Wille, R. Röhlsberger, T. Pfeifer, and J. Evers
  submitted (2014)
- ***Tunable sub-luminal propagation of narrowband x-ray pulses***
  K. P. Heeg, J. Haber, D. Schumacher, L. Bocklage, H.-C. Wille, K. S. Schulze, R. Loetzsch, I. Uschmann, G. G. Paulus, R. Rüffer, R. Röhlsberger, and J. Evers
  submitted (2014), arXiv:1409.0365 [quant-ph]

„Nukular. Das Wort heißt nukular.“

— Homer J. Simpson

Contents

Chapter 1

Introduction

Quantum mechanics is a seminal tool for various applications in our everyday life as well as for our fundamental understanding of the universe. At its boundary to the science of light, the realm of quantum optics has experienced a tremendous progress in the last decades. Counterintuitive concepts to control light with matter or matter with light and the investigation of fundamental issues in quantum mechanics are indicative of the vast range of aspects which can be realized in the lab by now [1–3]. To put it in the words of Serge Haroche and Jean-Michel Raimond: "The quantum has already delivered a lot." [2]

This development in quantum optics has been very successful for microwaves, infrared or visible light. However, until recently the study in higher frequency domains has been neglected, mostly due to the lack of proper radiation sources. The currently emerging field of x-ray quantum optics aims to establish the concepts of quantum optics in this new parameter regime [4], where we can again expect that "the quantum will deliver a lot".

Despite the fact that x-ray radiation is not conceptually different from visible light in terms of the theory of electromagnetism, it is attended by a number of assets and drawbacks, since the structures employed as target materials and the handling in experiments can strongly differ from the lower frequency regime. X-rays, for example, allow to excite not only the valence, but also the inner shell electrons in atomic media, and thus can be employed to study exotic systems under extreme conditions. Due to their shorter wavelength, x-rays can be focused to the nanometer range [5, 6] and explore physics at the nanoscale and applications therein [7], they provide high spectral resolution as the diffraction limit of visible light is circumvented [8, 9] and experiments can be operated with near 100% detection efficiency [4].

A distinct drawback, though, is the availability of coherent light sources in the x-ray domain as required for most applications in the quantum optical context. However, recent developments make this aim come into reach: 3rd generation synchrotron radiation sources offer unprecedented beam qualities, such as a high beam brilliance, huge photon numbers, pulses in the range of several ten picoseconds and a high beam collimation, which enables the study of previously inaccessible systems [10]. Additionally, free-electron lasers can provide x-rays with even more favorable characteristics [11–13]. Future facilities [14–18] and enhancement schemes such as self-seeding [19] or two-color x-ray lasers [20] are expected to further enrich the spectrum of light sources, which are suitable for quantum optical experiments in the x-ray regime.

Naturally, the advent of these high-performance x-ray radiation sources opened up a vast field of applications in different disciplines, such as material science, condensed matter physics, spectroscopy or imaging in structural biology. Celebrated examples include nanocrystallography [21, 22], lensless imaging of single molecules [23–25] or viruses [26], femtosecond electronic responses [27] and non-linear optical effects [28]. Quantum mechanical aspects have been touched in experiments on parametric down conversion [9, 29–31], x-ray wave mixing [32], stimulated emission [33], x-ray control with light [34] and atomic inner-shell lasing [35]. On the theory side, numerous schemes have been suggested, such as x-ray frequency comb generation [36–38] or implementation of electromagnetically induced transparency at x-ray frequencies [39].

In spite of this progress, it is important to realize that the novel x-ray light sources are in many aspects inferior to, e.g., lasers in the visible regime. Samples in the x-ray domain cannot be driven continuously, but only irradiated with short radiation pulses. At the same time, multiple

sources with different x-ray frequencies are usually not available in a single lab. Additionally, 3rd generation synchrotron sources provide a low resonant photon intensity [7], such that the light-matter interaction is mainly characterized by linear processes. But perhaps most importantly, current x-ray radiation suffers from low coherence properties compared to the light in the lower frequency domain [40].

Full exploitation of quantum optics, however, requires coherent control, quantum effects and non-linear light-matter interaction. Hence, the ideas, phenomena and applications known from the visible regime cannot be directly transfered into the realm of x-ray physics. Rather, it is required to developed new approaches and techniques both on the theoretical and the experimental side, in order to establish the field of x-ray quantum optics. In particular, a more sophisticated control exploiting the concepts of coherence and interference is desirable.

While x-rays can in principle interact with the transitions of atomic inner-shell electrons, driving nuclear resonances forms an interesting alternative [41–43]. In particular, *Mössbauer nuclei* offer some unique features. Due to their recoilless transitions, they offer extremely narrow resonance widths and a high quality factor, which is an important prerequisite for precision spectroscopy [44, 45], precision measurements [46, 47] and quantum-assisted metrology at x-ray energies [48]. Mössbauer transitions can be studied both in the time and frequency domain [49] and the nuclei can be easily embedded in solid state or nanostructured targets. This way, distortions like atomic movement or collisions like in atomic gases are avoided and systems can be operated essentially decoherence-free [50]. Furthermore, in many situations the light-matter interaction is boosted by cooperative effects between the nuclei [51, 52].

These distinct features render Mössbauer nuclei a perfect candidate for the purpose of x-ray quantum optics. Especially the archetype Mössbauer nucleus ^{57}Fe with its transition at 14.4 keV and a line width of only 4.7 neV is understood in detail, the required technology and instrumentation is well established and it constitutes a proven setup in traditional experiments. Hence, it is no surprise that this Mössbauer isotope facilitated a number of successful experiments with a quantum optical context. Examples are single photon storage [53], γ-ray photon echos [54, 55], single photon superradiance and the measurement of the cooperative Lamb shift in nuclei [52], realizing the phenomena of electromagnetically induced transparency [56] and spontaneously generated coherences [50], coherent control of photon waveforms [57], line shape control and interferometric phase measurements on ^{57}Fe nuclei [58] and group velocity control of x-ray pulses [59].

Also on the theoretical side, a number of proposals exploiting the distinct features of Mössbauer nuclei for quantum optical purposes were suggested, such as creation of entanglement for x-ray photons [60, 61] or between macroscopic solid objects [62], controlling nuclear decay channels [63], storage and phase modulation of x-ray photons [64], field control of x-ray photons [65] and analyses on nuclear lasing [66–68]. Other suggestions involving the interaction of x-rays with nuclear transitions include nuclear population transfer by quantum optical means [69, 70] and coherence-enhanced studies on novel clocks based on nuclear transitions [48].

These examples illustrate that Mössbauer and thus also x-ray science can profit from well-established quantum optical concepts developed in the visible frequency range. However, as already pointed out above, the experimental implementations do not rely on a simple transfer of the setups from the optical to the x-ray frequency regime. Rather, the new domain requires to develop fundamentally new ideas. This can be already seen from the fact that, unlike for the visible regime, typically only a single beam with a single frequency is available for experiments in the x-ray domain. This way, sophisticated schemes had to be developed, such as external field control [53] or engineering tailored environments for the nuclei [50, 52, 56]. These novel concepts can potentially be ported back to the optical frequency range and thus enrich the field of traditional quantum optics as well.

While nuclei can, in principle, be driven directly by x-ray light sources [41, 69–71], it is the tailored environment of the nuclei mentioned above, which facilitates the exploration of a comprehensive set of quantum optical effects. In particular, embedding the Mössbauer isotopes into nanostructured cavities has proven to form an eligible platform. Planar cavities consisting

of different layers of different materials with thicknesses in the nanometer range, known as *thin-film cavities*, are probed in grazing incidence and have by now been utilized in a number of experiments [50, 52, 56, 58, 59].

These thin-film cavities have the distinct advantage that they can "trap" the x-rays between their mirrors and thereby significantly enhance the light-matter interaction, which becomes particularly important for experiments performed at current synchrotron radiation sources, where the resonant intensity of the radiation is still weak. In this sense, the thin-film cavities can as well be interpreted as waveguide structures. Waveguides have been studied in the context of light propagation and focusing of x-rays [72, 73], and recently also x-ray waveguides based on photonic crystals have been suggested [74]. Hence, synergistic effects of these two research fields can be expected for the future.

Resonant Mössbauer nuclei embedded into thin-film cavities will constitute the basic platform studied in this work. So far, this setting has been only investigated theoretically by means of semi-classical theories [51, 52, 56, 75–77]. For the full exploitation of quantum optics, though, also a theoretical framework based on the concepts of quantum mechanics is required [78]. Such a quantum theory would provide an alternative point of view on the x-rays and resonant nuclei in thin-film cavities. In particular, a microscopic understanding of the occurring processes would be gained. At the same time, the established theories have the drawback that they are based on a linear description of the light-matter interaction. Hence, these approaches are expected to break down as soon as non-linear scenarios, encountered at novel free-electron laser sources, need to be considered. In contrast, a self-consistent quantum description would naturally incorporate this high intensity limit and support a potential transfer of the Mössbauer phenomenon into a new regime in physics.

This work is dedicated to the development of such a theory. Moreover, the new theoretical approach will be used to explore thin-film cavities with embedded resonant Mössbauer nuclei from a quantum optical perspective, with the aim to control x-rays with matter as well as matter with x-rays. To this end, a strong focus is put on a close relation to realistic implementations, such that various experimental settings can be handled accurately. Throughout this work, the developed quantum theory is successfully applied to previously conducted as well as to novel experiments, which highlight the significance of thin-film cavities for the purpose of x-ray quantum optics.

Outline of this work

This thesis is structured as follows: In chapter 2 the general setting considered in this work is introduced. The layout and the basic properties of thin-film cavities are discussed and it is shown how the cavities together with the inclusion of resonant Mössbauer nuclei constitute a platform for the study of light-matter interaction at x-ray energies. Further, a brief overview of radiation sources and experimental schemes employed in the context of the Mössbauer effect is given. Next, a special focus is put on two experiments which greatly inspired this work: Utilizing thin-film cavities and Mössbauer nuclei, they were able to demonstrate the relation to the field of quantum optics for the first time [52, 56]. Finally, this introductory chapter covers two frameworks, which have been used so far in the theoretical modeling. The underlying principles of these descriptions are given and their advantages as well as their drawbacks are highlighted.

Motivated by this discussion, a full quantum theory is developed in chapter 3. To this end, a Hamiltonian for the system is set up and the model is generalized in terms of the density matrix via the master equation approach, to also cover incoherent effects such as leaky cavity modes or spontaneous emission of the nuclei. Since the full model can hardly be solved due to the large dimensionality of the Hilbert space, two approximations well justified in current synchrotron-based experiments are performed. The effective model is then applied to the case of an unmagnetized ^{57}Fe layer and compact expressions for the reflectance are derived and discussed. In particular, a superradiant enhancement and a collective Lamb shift as observed in Ref. [52] are reobtained. Finally, the relation between the stationary observables and the

situation encountered in an realistic scenario is shown, which qualifies the theory to be applied in experimental settings.

In chapter 4 the connection to such an experiment is explicitly achieved. In contrast to previous studies, the incidence angle of the driving x-ray field onto the cavity surface is exploited as an additional degree of freedom and using our quantum optical theory developed in chapter 3, we predict the possibility to engineer the spectral response in terms of tunable Fano resonances. This line shape control was experimentally explored together with the group of Ralf Röhlsberger and Hans-Christian Wille at the PETRA-III synchrotron source (DESY, Hamburg). Here, the measured data is analyzed, shows very good agreement to the theoretical predictions and furthermore reveals the origin of the cooperative Lamb shift in more detail. In addition, we demonstrate that the measured Fano resonances allow for the reconstruction of the phase of the nuclear response to the x-ray beam.

The effect of the magnetic hyperfine structure of the ^{57}Fe nucleus on the reflectance is studied in chapter 5. A semi-classical approach as well as the quantum optical model is employed for the description. With the latter theory, we can identify several distinct features in the spectra to stem from effects induced by the quantum nature of the vacuum, such as spontaneous generation of coherences. These predictions were confirmed in an experiment at the PETRA-III synchrotron source together with the Hamburg group and the results explicitly demonstrate the quantum optical characteristics.

In chapter 6 the theoretical description is extended to cover the complete experimental stage including detection devices in the time domain. This way, we show that narrowband x-ray pulses can be delayed due to the light-matter interaction the thin-film cavity. A scheme to generate such spectrally narrow x-ray pulses from broadband synchrotron radiation with existing technology is proposed. We utilized this scheme in collaboration with the group of Ralf Röhlsberger in an experiment at the European Synchrotron Radiation Source (ESRF, Grenoble). The measured data demonstrates the sub-luminal light propagation in good agreement with the theoretical predictions and x-ray time delays up to 35 ns are observed. Furthermore, the extended formalism is employed to provide an alternative point of view of measured spectra in Fourier space.

Up to this point, the theoretical description was limited to a single layer of resonant nuclei and a single cavity mode. In chapter 7 we extend our quantum optical model to include both multiple layers and multiple modes. It is shown that these additions enable a quantum optical description of a setting in thin-film cavities, which was used to realize the phenomenon of electromagnetically induced transparency [56]. A very good agreement to the predictions of the semi-classical theories is found.

In chapter 8 a first insight into the physics of thin-film cavities beyond synchrotron-based experiments is provided. High x-ray field strengths achieved with intense radiation sources can give rise to non-linear effects and are studied theoretically in two different ways. First, the stationary observables of an idealized system are studied by solving a Dicke-type model analytically. In a second approach, a short excitation pulse is considered and emission spectra for several configurations are computed numerically. This way, a novel control mechanism for the line shape is discovered.

Finally, the findings of this thesis are summarized in chapter 9 and an outlook on possible future working directions is presented.

Chapter 2

Background

In this chapter the layout of x-ray thin-film cavities is presented and the general setting encountered in this thesis is described. Basic features of the cavities, such as its waveguide modes, as well as the role of Mössbauer nuclei in the system are discussed and the typical observables of interest are identified. After this, we give a short recap of the quantum optical phenomena which have been observed in the light-matter interaction between the x-rays and the resonant nuclei in the cavity in previous experiments. This way, the capability of the thin-film cavities to constitute a platform for quantum optics in the x-ray domain is highlighted. Furthermore, the x-ray sources which are typically employed are briefly discussed, together with their implications in the related experiments.

We then turn to two frequently used and well established theoretical descriptions of the light-matter interaction in the cavities: Parratt's recursive method [75] and the layerformalism [77], which is implemented in the software package CONUSS [79, 80]. We review these semi-classical models, discuss their capabilities, but also identify some of their limitations to highlight the requirement for a full quantum description.

2.1 Description of the system

2.1.1 Thin-film cavity layout & basic properties

A thin-film cavity is formed by a stack of stratified materials in planar geometry. Each of the layers consists of a particular material with a typical thickness on the order of a few nanometers. This layered structure can be chosen in such a way that a waveguide or cavity is formed. This is achieved by combining materials with low electron density (e.g. carbon) in the center of the structure, and materials with high electron density (e.g. platinum or palladium) at outer layers, which then act as mirrors. The electron density directly translates into the index of refraction experienced by the probing x-ray light [77]. The spatial modulation of the refractive index then leads to reflection of the light at the boundaries, resulting in a waveguide-like or cavity structure.

Due to the small index of refraction variations at x-ray energies, the cavity is typically probed in grazing incidence, with small incidence angle θ with respect to the cavity surface, as illustrated in Fig. 2.1. This setting leads to total external reflection of the impinging light, whereas for incidence angles larger than a few mrad the reflection entirely vanishes. This special grazing incidence geometry represents the (000) Bragg reflection [77], for which a high intensity of the reflected beam is generally expected. However, it is the stratified nature of the cavity which renders the angular behavior more comprehensive.

Let us briefly analyze the reflection curve of the thin-film cavity as a function of the incidence angle θ. For small angles θ, the reflectance is close to unity due to total reflection. This is visualized in Fig. 2.2(a), where the field intensity distribution of the x-rays was calculated numerically using Maxwell's equations in an operator-split code on a two-dimensional grid, originally written by Jörg Evers. The corresponding cavity is formed by a Pt(2.6 nm)/C(7.9 nm)/ Fe(1.5 nm)/C(9.3 nm)/Pt layer system, in which the Pt layers act as waveguide mirrors. Beyond several mrad, the reflected intensity severely diminishes. However, also for intermediate angles it is possible for the reflection to vanish, as shown in the field intensity distribution in Fig. 2.2(b).

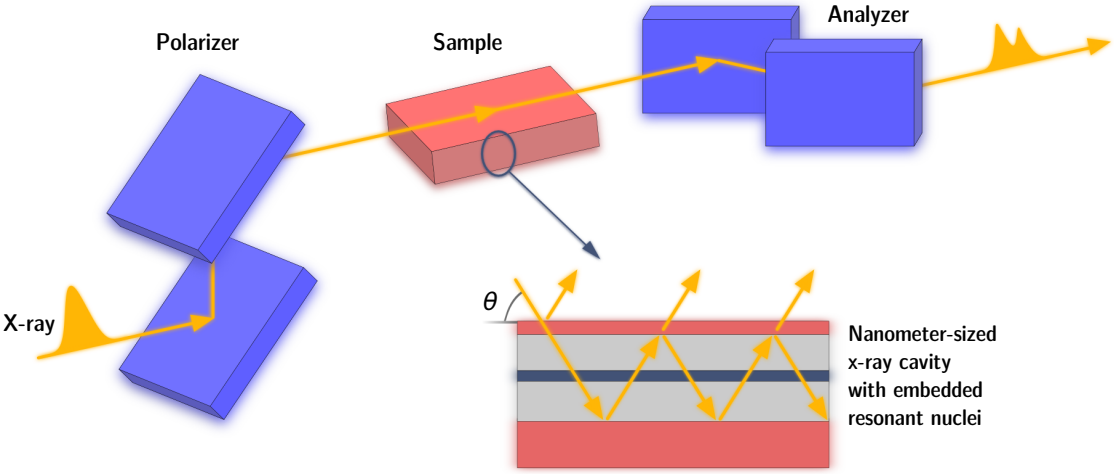

Figure 2.1: Schematic of the setup studied in this work: A thin-film cavity with embedded resonant Mössbauer nuclei is probed by hard x-rays, possibly under the influence of a magnetic field. The transmitted light contains signatures of the quantum mechanical interactions within the sample.

There, the cavity is probed at grazing incidence angle $\theta = 3$ mrad, far below the total reflection edge. The reduced reflection seen in Fig. 2.2(b) arises since the x-rays can evanescently couple into the cavity and can propagate in a guided mode until the light is finally fully transmitted or absorbed by the cavity materials. This resonant coupling into the modes is possible only for particular resonance angles. In Fig. 2.2(c) the complete reflection curve is shown for the range $0 \leq \theta \leq 10$ mrad and the features discussed above can be clearly observed. In the cavity analyzed here guided modes are resonantly driven, e.g, at the incidence angles $\theta \approx 3$ mrad, 4.2 mrad and 5.8 mrad. The field intensity distribution in the cavity for the first three guided modes is illustrated in the small panels of Fig. 2.2(c). Due to the multiple reflections at the cavity mirrors, it is substantially enhanced and visualizes the character of the modes.

Embedding a thin layer of resonant Mössbauer nuclei at the positions of the intensity amplifications has recently facilitated a platform for observing quantum optical phenomena in the x-ray regime [50, 52, 56, 58, 59]. But already before this route was developed, the system and related geometries have been studied in regard of purifying the nuclear reflection of γ-rays. By tuning to a guided mode resonance, the electronic reflection is suppressed by many orders of magnitude, and only the narrowband resonant amplitude originating from the resonant nuclei constitutes the signal. It is then monochromatized on the level of the natural line width of the nuclei and can be used in a subsequent experiment. In this context, the thin-film cavities were known as grazing incidence antireflection (GIAR) films [81–85].

2.1.2 Resonant Mössbauer nuclei

The recoilless emission or absorption of high energy photons in the x-ray or γ-ray regime from nuclei is known as the Mössbauer effect. It was discovered by Rudolf Mössbauer in 1958 [86] and was rewarded with the Nobel Prize in Physics three years after. Recoilless emission of γ quanta is possible, if the atomic nuclei are situated in a solid state target, such that the whole lattice absorbs the recoil, for which it is negligible due to its large mass [87]. The tiny line width of Mössbauer transitions has enabled the field of Mössbauer spectroscopy [88], which is utilized, e.g., in the analysis of mineralogical compounds and employed even in extraterrestrial environments [44]. A variant of this method has been used to measure the gravitational redshift predicted by the theory of general relativity [46, 47], highlighting the significance of the Mössbauer effect in the field of physics.

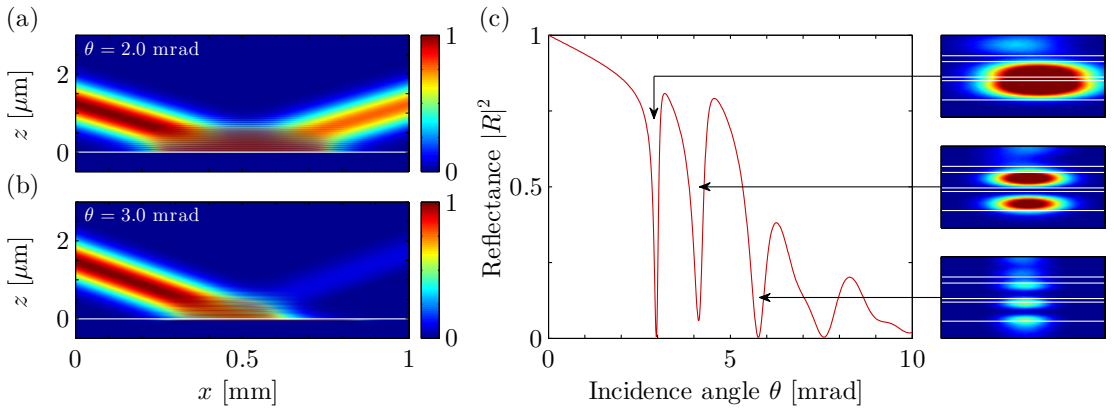

Figure 2.2: (a), (b) The field intensity distribution of x-rays impinging on the thin-film cavity in the absence of resonant nuclei is visualized. The reflection of the incident light is substantially suppressed at certain resonance angles, at which the light can resonantly couple into a guided mode in the cavity. Note that the scaling on the axes is different by several orders of magnitude. (c) The reflection curve is shown as a function of the x-ray incidence angle θ. Total reflection occurs for small angles. The dips in the reflection curve indicate resonant excitations of guided modes of the waveguide. The cavity field distribution of the first three guided modes, shown in the panels on the right, is strongly enhanced. In the three images of the intensity profiles only in the incidence angle differs. The panels cover a range of 0.6 mm in horizontal and of 40 nm in vertical direction. The white horizontal lines illustrate the boundaries of the cavity layers. Parameters are given in the main text.

So far, the waveguide introduced in the previous section has been discussed only in terms of electronic scattering of the x-rays from the materials of the layer system. For the purpose of x-ray quantum optics, layers of resonant Mössbauer nuclei can be embedded into the cavity in addition [50, 52, 56, 58, 59]. Such layers contain a large ensemble of nuclei, which can coherently interact with the probing x-ray light entering the waveguide. By carefully choosing the position of the nuclei inside the layer structure, as well as the resonantly driven mode of the waveguide (see Fig. 2.2(c)), the interaction between nuclei and the light inside the cavity can be controlled. In particular, different layers of nuclei can interact in a different way with the same cavity mode [56]. It is the inclusion of resonant nuclei which qualifies the considered system for applications in x-ray quantum optics. Close to nuclear resonances, the properties of the combined system of cavity and nuclei lead to a strong polarization and energy dependence of the scattered light.

The archetype Mössbauer transition is found in the ^{57}Fe isotope with a natural abundance of $\approx 2\%$. It features a recoilless transition at $\omega_0 = 14.4125$ keV ($\hbar = 1$ used here and in the following) with a line width of only $\gamma = 4.66$ neV [77]. In this work, we will primarily focus on this Mössbauer isotope, however, the theory developed here is as well applicable for other resonances.

2.1.3 X-ray sources

In order to perform experiments with Mössbauer nuclei, appropriate light sources in the x- or γ-ray regime are required. Historically, the required radiation was obtained from the radioactive decay of related elements. In his original experiment, Rudolf Mössbauer used the radioactive element ^{191}Os, which decayed into an excited state of the Mössbauer isotope ^{191}Ir via β decay. The subsequently emitted γ-ray photon then matched the Mössbauer transition frequency exactly and could be used to probe the ^{191}Ir nuclei in a second sample [86]. Also for the Mössbauer transition in ^{57}Fe, the decay of a ^{57}Co sample can serve as a proper radiation source.

These Mössbauer radioactive sources were recently employed in a number of experiments on quantum optical phenomena [54, 55, 57, 66, 89, 90], since they provide an unprecedented

narrowband spectral resolution. Mounting the source on a moving Doppler drive further allows to tune the frequency of the light. However, drawbacks are the non-deterministic emission of the photons, their random polarization, a reduced signal rate and poor collimation due to the emission into all directions ($\Omega = 4\pi$). Additionally, radioactive sources do not exist for all Mössbauer isotopes.

For this reason, it was suggested in 1974 to instead employ pulsed synchrotron radiation as a tunable source to probe Mössbauer transitions, which can overcome many of the obstacles mentioned above [91]. While photon science at synchrotron facilities was first performed parasitic to applications in particle physics, today's 3rd generation synchrotrons, in which undulators serve as high brilliance radiation sources, exist especially for this purpose. Dedicated nuclear resonance beamlines have been constructed at the large synchrotron facilities, the APS [92], the ESRF [93], SPring-8 [94] and PETRA-III [95], and provide x-ray pulses with a brilliance orders of magnitude higher than radioactive sources and pulse lengths on the order of several 10 ps. Typical synchrotron radiation is spectrally broad and exceeds the tiny line width of Mössbauer transitions by many order of magnitudes. Hence, in order to obtain spectrally narrow pulses, sophisticated monochromatization schemes are required. Synchrotron Mössbauer sources with resolutions in the range of the natural line width have been implemented, e.g., in Refs. [96–101].

But also the broadband synchrotron radiation can be used to probe Mössbauer resonances: Resonant nuclear scattering in forward direction constitutes the time-domain counterpart to the traditional Mössbauer spectroscopy [49, 102]. Due to the tiny line width of Mössbauer transitions, their characteristic emission time is very long compared to the time range in which the electronic dynamics takes place. For the Mössbauer isotope ^{57}Fe, e.g., the life time is $1/\gamma = 141$ ns. Thus, the prompt electronic response after an excitation with a short synchrotron pulse can be well separated from the nuclear signal, which then contains the desired information on the sample in its time spectra. A variant of this technique is known as the nuclear lighthouse effect, in which a rotating sample is used to map the time signal to an angular scale [103–105].

In the future novel light sources based on the concept of free-electron lasers [11] are expected to further enrich the variety of Mössbauer science and could in particular enable the step to nonlinear interactions [7]. In this work, however, we will primarily focus on scenarios performed at synchrotron radiation sources, only in Chap. 8 the influence of much higher intensities is studied. In synchrotron experiments, the photon occupation of the modes resonant with the narrow line width of ^{57}Fe is usually low, such that each synchrotron pulse typically provides less than one resonant photon on average. Hence, postselection via the detector counts effectively corresponds to single photon realizations [7, 52, 106, 107].

2.1.4 Experiments with relation to quantum optics

During the excitation of a homogeneous target of resonant nuclei with a synchrotron pulse with wave vector $\boldsymbol{k}$, not a single nucleus will be excited, but rather the spatially coherent superposition

$$|\psi\rangle = \frac{1}{\sqrt{N}} \sum_{n=1}^{N} e^{i\,\boldsymbol{k}\cdot\boldsymbol{R}^{(n)}} |g_1 g_2 \dots e_n \dots g_N\rangle \,, \tag{2.1}$$

in which the excitation is shared amongst the nuclei [51, 108]. The state $|\psi\rangle$ is known as nuclear exciton [51, 109], whereas in the quantum optical context it is known as the timed Dicke state [110]. This state has the property that it emits a photon in forward direction upon deexcitation, and hence this constitutes the nuclear forward scattering (NFS) setting. The decay, however, contains a complicated time behavior and does not follow a simple exponential decay. The reason for this is that the superposition given above is not a radiative eigenstate of the system [51, 111–113] and the emission characteristics of different coupled eigenstates are superimposed.

However, probing the resonant nuclei in the cavity setting introduced above, the excited state is also an radiative eigenstate, which then features an exponential decay. This was observed

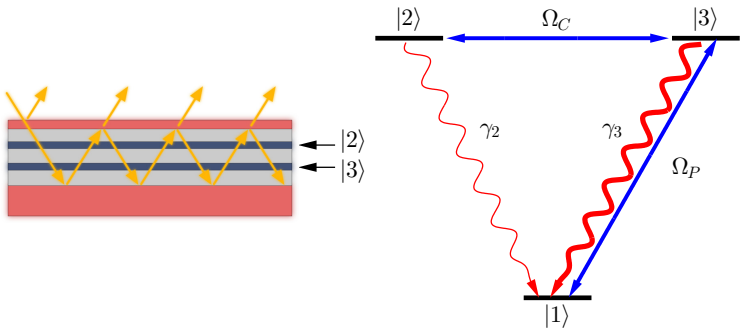

Figure 2.3: In the EIT scenario from Ref. [56] one resonant layer ("$|2\rangle$") is located at the field node of the driven mode, a second layer ("$|3\rangle$") is placed at the anti-node. Only the nuclei in the second layer are directly probed by an external field and are subjected to superradiance. An effective level scheme illustrating the interpretation of Ref. [56] is shown at the right hand side. The thicknesses of the lines denote the relative strength of the couplings. The formed system is equivalent to an EIT setting [116]. Notation adapted from Ref. [56].

by the group of Ralf Röhlsberger in the pioneering experiment described in Ref. [52], where a single layer of ^{57}Fe nuclei was embedded in a thin-film cavity. Interestingly, the decay rate did not match the natural line width of a single nucleus, but was substantially increased due to superradiance. Next to this cooperative phenomenon, the Purcell effect [114], which is the modification of the emission rate of nuclei due to the cavity environment, could further increase the line broadening observed in the experiment.

The decay rate of the timed Dicke state is predicted to be complex-valued and its imaginary part corresponds to a shift of the resonance energy. This is known as the collective Lamb shift [110], since it stems from the emission and absorption of virtual photons in the atomic ensemble. The cooperative shift for the ^{57}Fe nuclei was measured in the same experiment (Ref. [52]) by considering the spectral instead of the time resolved properties. Only after this observation of the collective Lamb shift, the effect could also be observed in the visible regime [115]. In the x-ray cavity setting the superradiant amplification and the magnitude of the Lamb shift sensitively depends on the cavity field intensities at the position of the resonant nuclei. By placing the material at the anti-node of the field intensity, a pronounced superradiance and Lamb shift is observed. The reason for this is that, figuratively spoken, the virtual photons emitted and reabsorbed by the nuclear ensemble can well transmitted via the cavity mode.

In a further experiment performed by the group of Ralf Röhlsberger, this targeted placement of resonant layers in the cavity was explicitly exploited [56]. Instead of a single thin resonant layer, two particularly placed layers of ^{57}Fe nuclei were embedded in the cavity. With the upper layer located at a field node and the lower one at an anti-node, it was possible to observe a distinct minimum in the center of the spectrum. This could be explained in terms of the phenomenon of electromagnetically induced transparency (EIT) [116, 117]. The interpretation given in Ref. [56] is depicted in Fig. 2.3 and explained in the following: Since one of the layers is placed in the field anti-node, the collective excited state of nuclei in this layer ("$|3\rangle$") is subjected to a high intensity of the cavity mode field and thus is strongly coupled to the ground state ("$|1\rangle$") via the x-ray pulse with strength Ω_P. The nuclei located in the second layer, placed at the cavity field node, are not driven directly. However, due to radiative couplings in the cavity, the two collective excited states of the two respective layers are mutually coupled via the rate Ω_C. At the same time, the excited state in the node layer decays only with its natural line width $\gamma_2 = \gamma$, while the nuclei in the anti-node are subjected to superradiant enhancement, such that $\gamma_3 \gg \gamma$. This way, a system equivalent to a standard EIT setting is realized, for which the central minimum in the spectrum is a key observable [116].

This experiment formed the first realization of EIT in the hard x-ray regime. Remarkably,

the experiment could be conducted with only a single driving field, which was provided by the synchrotron beam, whereas in standard EIT settings two coherent light sources are required. In the cavity setting, though, this second field is intrinsically provided via an intra-cavity coupling between the states in the two ^{57}Fe layers. Since EIT is related to lots of important phenomena such as creating slow light pulses [118], rendering a medium transparent on demand [119], and is assisted by huge optical non-linearities [120–122], the single photon realization of EIT might be a powerful tool to transfer the applications known from quantum optics in the visible regime to the x-ray domain. At the same time, this technique could of course be ported back to the visible regime in order to realize EIT related phenomena in an even broader class of systems.

The two experiments employing ^{57}Fe in thin-film cavities discussed above highlight that these cavities can form a platform for quantum optics in the x-ray domain. However, a complete theoretical description of the processes in the language of quantum optics is still lacking. Instead, semi-classical methods have been employed so far to model the experiments. In the next section, an introduction to two of these models will be given.

2.2 Existing semi-classical theories

2.2.1 Parratt's formalism

A well-established theoretical method to describe the reflection of x-rays from solid state targets was developed by Lyman G. Parratt [75]. While it was first employed in the study of surfaces, it was later also recognized that layered materials such as thin-film cavities can be described with this technique [81, 82, 123]. The method is based on the basic Fresnel reflection and transmission coefficients at the boundaries of the different materials occurring in the layer stack, which are self-consistently employed such that the reflection is described in all orders. The Fresnel coefficients are obtained from solving Maxwell's equations and for their calculation only the complex refractive indices as well as the x-ray frequency and the incidence angle are required.

With Parratt's formalism it is possible to calculate reflection curves as a function of the incidence angle. As we have seen before, this type of curve reveals the position of the guided modes in the waveguide via deep reflection minima. Also, it is possible to use the formalism to compute the field distribution inside the waveguide or cavity system [123]. However, it is not restricted to these cases. In this work we are primary interested in the case where resonant nuclei, i.e. ^{57}Fe atoms, are embedded in the layer system and modify the reflection as a function of the x-ray frequency. In fact, also this situation can be studied with Parratt's formalism. The transitions in the near-resonantly probed nuclei can be characterized via frequency dependent scattering amplitudes. Since the scattering amplitude is directly connected to the refractive index [77], the effect of the nuclei can straightforwardly be included in Parratt's formalism.

The predictions obtained from this formalism can be expected to serve as a benchmark for other theories, since it has proven to agree extremely well with experiments. Nevertheless, we want to emphasize that this method can be considered to be only a semi-classical one. The description of scattering amplitudes dates back to the origin of the development of quantum mechanics. The so-called Kramers-Heisenberg formula for the scattering of light at atomic resonances was published already in 1925 [124] and later extended to also include the finite lifetime of the atomic states [125]. However, in all cases the radiation field was solely treated classically and therefore, using Parratt's formalism, the processes in our considered cavity cannot fully be interpreted in the language of modern quantum mechanics.

Derivation of the cavity reflectance

In the following the essential expressions of Parratt's method will be derived.

Let us start by considering a stack of three materials with refractive indices n_1, n_2 and n_3 as sketched in Fig. 2.4. The bottom layer is considered to be infinitively thick, such that it

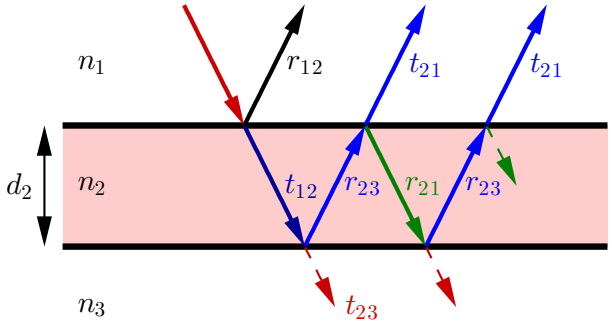

Figure 2.4: Reflection and transmission at a layer boundary. The Fresnel coefficients for reflection and transmission are denoted by r and t, respectively. The materials have the refractive indices n_1, n_2 and n_3. The thickness of centered layer is d_2.

only absorbs radiation and no intensity enters from below. We assume that x-rays impinge from material 1 onto the surface of the second layer and want to calculate the total reflection rate. This can be done by noting that the total rate can be written as a sum over infinitely many paths. The simplest one is a direct reflection on the surface, parametrized with the Fresnel reflection coefficient r_{12}. In the second possible path the light is transmitted into material 2 ("t_{12}"), reflected at the boundary to layer 3 ("r_{23}") and finally transmitted into the topmost material ("t_{21}"). But additionally, during the propagation of the light in layer 2, it accumulates a phase ϕ_2 twice and hence the path amplitude is modified by $\exp(2i\phi_2)$. High order reflections can be defined analogously.

Summing up all contributions, one obtains for the reflection coefficient including multiple reflections

$$\begin{aligned} r'_{12} &= r_{12} + t_{12}r_{23}t_{21}e^{2i\phi_2} + t_{12}r_{23}r_{21}r_{23}t_{21}e^{4i\phi_2} + \dots \\ &= r_{12} + t_{12}r_{23}t_{21}e^{2i\phi_2}\sum_{k=0}^{\infty}(r_{21}r_{23}e^{2i\phi_2})^k = r_{12} + \frac{t_{12}r_{23}t_{21}e^{2i\phi_2}}{1 - r_{21}r_{23}e^{2i\phi_2}} \,. \end{aligned} \tag{2.2}$$

Applying the relations $r_{12}^2 + t_{12}t_{21} = 1$ and $r_{21} = -r_{12}$ valid for the Fresnel coefficients, we find

$$r'_{12} = \frac{r_{12} + r_{23}e^{2i\phi_2}}{1 + r_{12}r_{23}e^{2i\phi_2}} \,. \tag{2.3}$$

This reflection coefficient is only valid at the bottom of the cavity, since for other layers the possible multiple reflections are not taken into account yet. However, Eq. (2.3) can easily be utilized for generalization in a recursive fashion, as we will show in the following. Let us assume that our cavity consists of M layers, where the layer M is infinitely thick. Then from Eq. (2.3) we know the full reflection coefficient at the boundary between layers $M-2$ and $M-1$

$$r'_{M-2,M-1} = \frac{r_{M-2,M-1} + r_{M-1,M}e^{2i\phi_{M-1}}}{1 + r_{M-2,M-1}r_{M-1,M}e^{2i\phi_{M-1}}} \,. \tag{2.4}$$

If we now want to calculate the full reflection amplitude between the next upper set of layers, $M-3$ and $M-2$, we can employ the same formula, but with the plain reflection coefficient $r_{M-2,M-1}$ replaced with that including multiple reflections, $r'_{M-2,M-1}$. This procedure can be applied recursively, until the topmost layer is reached. The recursion relation, which is the key of Parratt's formalism, reads [75, 82]

$$r'_{m-1,m} = \frac{r_{m-1,m} + r'_{m,m+1}e^{2i\phi_m}}{1 + r_{m-1,m}r'_{m,m+1}e^{2i\phi_m}} \,. \tag{2.5}$$

In addition to the cavity layers 1 to M, we artificially include a "vacuum layer" with refractive index $n = 1$ and with layer index $m = 0$ in the scheme. Then, the reflection coefficient of the whole cavity is given by

$$R = r'_{0,1} \, . \tag{2.6}$$

Next, we want to give the explicit formulas for the accumulated phases ϕ_m and the Fresnel coefficients. For this we note that in the hard x-ray regime, the refractive index is typically written as [77]

$$n = 1 - \delta + i\beta \, , \tag{2.7}$$

where δ and β are small real numbers. The reason behind this is that the frequencies of hard x-rays are typically well beyond any resonances, and electrons or dipoles in the material cannot follow the fast oscillations of the radiation field [126]. Therefore, the dielectric susceptibility is close to zero and determined by the off-resonant tails of the resonances at lower frequencies. The refractive index of a material can be computed, e.g., with the XRAYLIB-library [127].

With the refractive index at hand, we can now express the wave vector $\boldsymbol{k}$ inside the different materials. We define our coordinate system such that the surface normal of the cavity is aligned along z-direction. Maxwell's equations imply continuity of the wave vector along x- and y-component, hence we find for the transverse component in material m

$$k_z^{(m)} = \sqrt{(n_m k)^2 - (k^2 - k_z^2)} \, , \tag{2.8}$$

where k is the wave vector of the incident radiation in vacuum, $k_z = k \sin(\theta)$ is its z-component, θ the incidence angle and n_m is the refractive index of the material. From this, the Fresnel coefficient for the reflection can be obtained as

$$r_{m_1,m_2} = \frac{k_z^{(m_1)} - k_z^{(m_2)}}{k_z^{(m_1)} + k_z^{(m_2)}} \, . \tag{2.9}$$

Finally, the extra phase accumulated during propagation through material m is given by

$$\phi_m = k_z^{(m)} d_m \, , \tag{2.10}$$

where d_m is the thickness of the layer.

Inclusion of the resonant nuclei

With the formulas presented so far it is possible to calculate the angular dependent reflection curves for arbitrary cavity geometries. However, we are not yet able to also include the effect of the resonant nuclei. For this, we have to modify the refractive index and include the nuclear scattering amplitude [77]. Neglecting magnetic splitting and polarization dependence, the refractive index with the nuclear scattering amplitude of ^{57}Fe can be written as [52, 56, 77]

$$n_{^{57}\mathrm{Fe}} = 1 - \delta + i\beta - 2\pi \, \frac{\rho_N}{k_0^3} \, \frac{f_{\mathrm{LM}}}{2(1+\alpha)} \, \frac{2I_e + 1}{2I_g + 1} \, \frac{1}{2\Delta/\gamma + i} \, , \tag{2.11}$$

where $\rho_N = 83.18$ nm^{-3} is the nuclear density in α-iron, $k_0 = 73.039$ nm^{-1} the wave vector of the transition in ^{57}Fe, $f_{\mathrm{LM}} \approx 0.8$ the Lamb-Mössbauer factor, $\alpha = 8.56$ the factor of internal conversion, $I_e = 3/2$ [$I_g = 1/2$] the spins of the nuclear excited [ground] state, $\gamma = 4.66$ neV is the transition width of the resonance and $\Delta = \omega - \omega_0$ is the photon detuning from the transition energy $\omega_0 = 14.4125$ keV [49, 77]. Note that in Eq. (2.11) we adjusted the sign of the nuclear contribution for consistent notation. With our choice, the imaginary part is, like the electronic contribution in β, positive. Also, in contrast to the grazing incidence theories in Refs. [52, 56, 77], the denominator in Eq. (2.11) contains k_0^3 instead of $k_0^3 \sin(\theta)$, since the effect of the small incidence angle is already covered within the Parratt formalism.

2.2.2 Layerformalism

While Parratt's formalism gives accurate results for the reflection curves or simple spectra of nuclei embedded in thin-film cavities, it is not possible to treat arbitrary polarization directions, magnetic hyperfine or quadrupole splittings in the iron layer with the formulas given above. For these situations a self-consistent theory including multiple scattering to all orders has been developed. Instead of using a single scalar field amplitude to describe the intensity profile in the cavity, it is based on multidimensional vectors, containing the amplitudes for different scattering channels or polarizations. Since so-called layer matrices connect amplitude vectors at the different layer boundaries, we will denote this theory "layerformalism" throughout this work.

Below a brief introduction to the formalism is given, a detailed description can be found elsewhere [77]. Since this theoretical method allows to include a multitude of possible distortions like material roughness at the layer boundaries, and a vast range of effects, such as magnetic field distributions, it could be successfully used to model several experimental settings, such as in studies on magnetism in nanoscale materials [128–130]. Important for this work is the study in grazing incidence. The theory for this setting was developed in Ref. [76] and a numerical variant has been implemented in the software package CONUSS [79, 80]. Since the theoretical predictions have proven to agree extremely well with several experiments [52, 56, 128–131], CONUSS can be considered as a benchmark for other theory descriptions of the reflection from thin-film cavities with resonant nuclei.

In the following we restrict to the frequent setting without any magnetic splitting, incidence angles where cavity modes are driven resonantly, i.e. no electronic reflection occurs, and to a thin resonant layer. It was shown in Refs. [52] and [56] that in this case an analytic treatment of the reflection amplitude is possible. Here we will review this calculation with the aim to introduce the basic ideas and the capabilities of the layerformalism.

Reflectance for one resonant layer

The cavity layout with the notation used in the following is sketched in Fig. 2.5. An x-ray beam with wave vector k_0 impinges on the cavity surface under an incidence angle θ. The cavity consists of multiple layers and has the total thickness D. A single resonant iron layer at depth z_{Fe} will be included later. We denote $\vec{A}(z) = (A_+(z), A_-(z))^T$ as the field amplitude at position z, where A_+ and A_- are the transmitted and reflected parts, respectively. Note that we do not include any polarization dependence here, since our sample is not magnetized and hence no polarization rotation will take place. Otherwise, the field amplitude vector $\vec{A}(z)$ would consist of twice as many components to take into account the 2-dimensional polarization basis for each scattering channel.

The reflection coefficient is given by the ratio of the incident and the reflected field strength at the cavity surface.

$$R = \frac{A_-(0)}{A_+(0)} \,. \tag{2.12}$$

Note that in an experiment the reflectance $|R|^2$ is usually measured. The amplitude in depth z is related to the surface amplitude $\vec{A}(0)$ via

$$\vec{A}(z) = \boldsymbol{L}(z)\vec{A}(0) = \begin{pmatrix} L_{++}(z) & L_{+-}(z) \\ L_{-+}(z) & L_{--}(z) \end{pmatrix} \begin{pmatrix} A_+(0) \\ A_-(0) \end{pmatrix} \,. \tag{2.13}$$

Here $\boldsymbol{L}(z)$ is a matrix product of contributions from the individual layers. For each layer i we can define the layer matrix $\boldsymbol{L}_i$, which connects the field amplitude vectors at its two layer boundaries. The quantities $L_{ab}(z)$ denote the scattering rates from channel b to a at position z in the respective layer. The layer matrix is calculated as $\boldsymbol{L}_i(z) = e^{i\boldsymbol{F}_i z}$, where $\boldsymbol{F}$ is the so-called propagation matrix and contains the scattering amplitudes and refractive indices of the material. Hence, the physics of the light-matter interaction is contained in the propagation matrices.

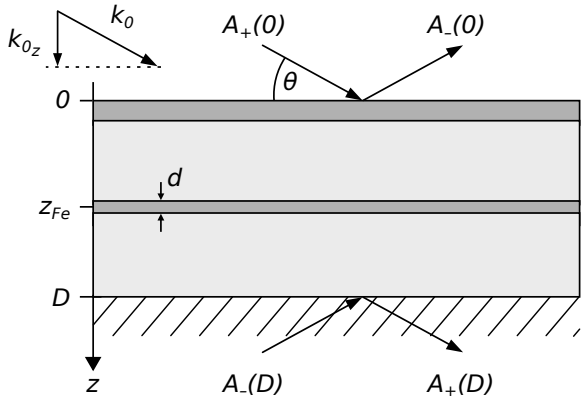

Figure 2.5: Schematic of a layer system with one resonant layer at depth z_{Fe}. $A_+(z)$ and $A_-(z)$ denote the transmitted and reflected field amplitudes at depth z, respectively.

For now we do not take into account the resonant nuclei in the thin ^{57}Fe layer, and only consider the electronic reflection R_0. From Eq. (2.13) we find

$$R_0 = \frac{A_-(0)}{A_+(0)} = -\frac{A_+(D)L_{-+}(D) - A_-(D)L_{++}(D)}{A_+(D)L_{--}(D) - A_-(D)L_{+-}(D)} \,. \tag{2.14}$$

With the constraint that no field enters from below, i.e. $A_-(D) = 0$, we thus obtain

$$R_0 = -\frac{L_{-+}(D)}{L_{--}(D)} \,. \tag{2.15}$$

Let us now include the ^{57}Fe nuclei in our analysis. We assume the iron layer has thickness d and is located around position z_{Fe} in the cavity. Since the layer is thin, we can expand its layer matrix

$$\boldsymbol{L}_{\mathrm{Fe}}(d) = \exp\left(i\boldsymbol{F}_{\mathrm{Fe}}d\right) \approx 1 + i\boldsymbol{F}_{\mathrm{Fe}}d \,. \tag{2.16}$$

While in the absence of resonant nuclei the field amplitudes at the surface and the bottom of the cavity were related by the product of layer matrices $\boldsymbol{L}(D)$, the relation is now augmented to

$$\begin{aligned}\vec{A}(D) &= \boldsymbol{L}(D)\big[\boldsymbol{L}^{-1}(z_{\mathrm{Fe}})\boldsymbol{L}_{\mathrm{Fe}}(d)\boldsymbol{L}(z_{\mathrm{Fe}})\big]\vec{A}(0) \\ &\approx \boldsymbol{L}(D)\big[1 + id\boldsymbol{L}^{-1}(z_{\mathrm{Fe}})\boldsymbol{F}_{\mathrm{Fe}}\boldsymbol{L}(z_{\mathrm{Fe}})\big]\vec{A}(0) \,.\end{aligned} \tag{2.17}$$

Now we will turn to the propagation matrix $\boldsymbol{F}_{\mathrm{Fe}}$ of the resonant layer. It can be written as

$$\boldsymbol{F}_{\mathrm{Fe}} = \begin{pmatrix} f_N & f_N \\ -f_N & -f_N \end{pmatrix} \,, \tag{2.18}$$

where f_N denotes the nuclear scattering amplitude, which is characterized by the nuclear resonances. Generally, the propagation matrix further contains electronic scattering contributions and the phase shift due to free propagation on the diagonals. For an ultrathin layer, however, these terms can be neglected due to the dominant effect of the nuclear scattering amplitudes. Since we do not consider a medium magnetization, ^{57}Fe features only a single transition and the scattering amplitude is given by the Lorentzian

$$f_N = \frac{f_0}{\Delta + i\frac{\gamma}{2}} \,, \tag{2.19}$$

where $\Delta = \omega - \omega_0$ is the detuning between the photon and the transition energy, γ is the transition width of the nuclear resonance and f_0 is an uninteresting prefactor.

With the nuclear scattering amplitude at hand, we can now evaluate the reflection coefficient. To this end, we again use that $A_-(D)$ vanishes, since no field enters from below the cavity. Additionally, we now employ that we operate the cavity at an incidence angle where a guided mode is driven and no electronic reflection occurs. This can be expressed by setting R_0, which was found in Eq. (2.15) to zero. In turn, this implies $L_{-+}(D) = 0$. Finally, we use that $L_{++}(z_{\mathrm{Fe}})L_{--}(z_{\mathrm{Fe}}) - L_{+-}(z_{\mathrm{Fe}})L_{-+}(z_{\mathrm{Fe}}) = \det(\boldsymbol{L}(z_{\mathrm{Fe}})) = 1$. This can be seen by noting that $\det(\exp(\boldsymbol{F})) = \exp(\mathrm{tr}(\boldsymbol{F}))$ and that the trace of the propagation matrices vanishes, c.f. Eq. (2.18). In the notation of Ref. [52], this gives rise to the reflection coefficient

$$R = \frac{idp^2}{\frac{1}{f_N} - idpq} \,, \tag{2.20}$$

with the field amplitude constants at depth z_{Fe}

$$p = L_{++}(z_{\mathrm{Fe}}) + L_{-+}(z_{\mathrm{Fe}}) \,, \tag{2.21}$$

$$q = L_{+-}(z_{\mathrm{Fe}}) + L_{--}(z_{\mathrm{Fe}}) \,. \tag{2.22}$$

Inserting the nuclear scattering amplitude from Eq. (2.19), we can rewrite the expression as

$$R = \frac{idf_0p^2}{\Delta + i\frac{\gamma}{2} - idf_0pq} \,. \tag{2.23}$$

From this form it can be seen that the shape of the reflectance is Lorentz-like. Compared to the single-nucleus resonance, the line profile is broadened ("Re(pq)") and shifted in frequency ("Im(pq)"). These are exactly the effects which have been observed in Ref. [52], where a superradiant broadening and a cooperative Lamb shift was measured for the spectrum, as discussed in Sec. 2.1.4.

From the analysis above it becomes visible that analytical expressions for the reflectance can be obtained from the layerformalism. This provides the basis to describe the form of the spectra and allows for a certain interpretation. However, the expression calculated in Eq. (2.23) lacks some information. For example, it is unclear what the relation between superradiance and collective Lamb shift is. They are both related to the field amplitude product pq, but Eq. (2.23) does not provide insights which could be used to specifically engineer a cavity in which one or the other effect dominates. Instead, this question can only be tackled with plain numerical simulations. Also, it would be desirable if some more microscopic insight could be gained from a theoretical description, i.e. in which way do the nuclei talk to each other in the sense that they exhibit collective behavior. Hence, an additional model based on quantum mechanical principles is well worth to be developed, such that the nuclear scattering in thin-film cavities can be understood from a more fundamental point of view. As a matter of course, even more questions will come up if more involved situations are considered. This covers the magnetization of the resonant layers such that different Zeeman sublevels are driven [50], incidence angles not being restricted to guided mode positions where the electronic reflection vanishes [58], or cavity layouts with multiple resonant layers [56].

Reflectance for two resonant layers

In the case of two resonant layers, the cavity is known to exhibit EIT-like spectra in the reflectance as discussed in Sec. 2.1.4. This was shown experimentally and confirmed theoretically by employing the layerformalism [56]. Similar to Eq. (2.17), the situation with two thin resonant layers at positions z_1 and z_2 with respective thicknesses d_1 and d_2, can be described with the layerformalism by relating the field amplitude vectors at different positions as

$$\vec{A}(D) \approx \boldsymbol{L}(D)\big[\boldsymbol{L}^{-1}(z_2)\,(1 + id_1\boldsymbol{F}_{\mathrm{Fe}})\,\boldsymbol{L}(z_2)\big]\big[\boldsymbol{L}^{-1}(z_1)\,(1 + id_1\boldsymbol{F}_{\mathrm{Fe}})\,\boldsymbol{L}(z_1)\big]\vec{A}(0) \,. \tag{2.24}$$

Let us now restrict to the EIT-case discussed in Ref. [56]. There, the positions of the layers are chosen such that the one closer to the surface is placed in a node of the cavity field, whereas the second layer is located at an anti-node. Assuming that the field intensity at the first resonant layer vanishes, one arrives at [56]

$$R = \frac{-id_2 f_N E_{2-+}}{1 + id_2 f_N E_{2--} - d_1 d_2 f_N^2 E_{1+-} E_{2-+}} \tag{2.25}$$

$$= \frac{-id_2 f_0 E_{2-+} \left(\Delta + i\frac{\gamma}{2}\right)}{\left(\Delta + i\frac{\gamma}{2}\right)\left(\Delta + i\frac{\gamma}{2} + id_2 f_0 E_{2--}\right) - d_1 d_2 f_0^2 E_{1+-} E_{2-+}} , \tag{2.26}$$

where $E_{a\cdot\cdot}$ are expressions involving field amplitudes at layer a. This result for the reflectance resembles an EIT-like spectrum [116], and the setup thus forms a system equivalent to the EIT case well known from the visible frequency regime.

Again, this analysis reveals that the layerformalism is capable of describing scenarios analytically. But the same restrictions as mentioned above hold and a complete microscopic insight to the processes in the cavity cannot be obtained from this theoretical model.

Finally, we want to stress that both the Parratt formalism and simulations performed with CONUSS, based on the layerformalism, yield identical results for reflection curves and spectra in the respective limits, and reproduce experimentally obtained data extremely well. Both formalism therefore ought to be considered as benchmarks for new theories. Apart from effects formed by a distorted electromagnetically environment or advanced material properties such as isomer shifts, the theories do not contain any adjustable parameters. On the other hand, the quantum description, which we will develop in the next chapter, will contain several coupling parameters. Generally, these coefficients need to be determined for each cavity geometry and cannot be calculated from scratch. Rather, the parameters need to be obtained by fitting the expressions of the quantum theory to the data obtained from the established self-consistent theories discussed above. In this sense, both types of theories are crucial for the accurate modeling and the full understanding of nuclear reflection from thin-film cavities.

Chapter 3

Quantum Optical Description

In this chapter, we *ab initio* develop a quantum optical framework for the modeling of large ensembles of nuclei embedded in thin-film cavities and probed in grazing incidence by hard x-rays. We start with the derivation of a master equation for the ensemble of nuclei coupled to the quantized cavity modes and include all magnetic sublevels, such that arbitrary alignments of the magnetization as well as the input- and output polarization can be analyzed. This way, a description for general purposes is obtained. In contrast to the existing approaches introduced in Sec. 2.2, the model encompasses non-linear and quantum effects, which could become accessible in future experiments.

Motivated by the present experimental state-of-the-art, we specialize to the case of lossy cavities and linear response. This allows us to derive analytic solutions by adiabatically eliminating the cavity modes and by characterizing the large ensemble of nuclei using just a few many-body quantum states. The corresponding master equation allows to fully identify and interpret all physical mechanisms contributing to the obtained results. We illustrate our framework by analyzing the archetype scenario of current experimental interest, which is the setting of a single unmagnetized layer of ^{57}Fe nuclei placed in the center of an x-ray cavity. Consistent with recent experimental results, our analysis predicts cooperative Lamb shifts and superradiance.

We find that our approach yields analytically equivalent results to established models in the respective limits. But it goes beyond the existing approaches by opening perspectives for the engineering of advanced quantum optical schemes in the hard x-ray regime. It enables the generalization to cases in which the quantum nature of the x-ray light is of relevance as, e.g., in quantum information theory. Moreover, it can cover situations in which the light source delivers many resonant photons per shot, such that non-linear effects become crucial, and offers full interpretation in terms of the involved physical processes.

3.1 Theoretical model

3.1.1 Cavity

The system we investigate is a thin-film cavity probed by hard x-rays as introduced in Sec. 2.1. On one hand, the probing incident light indicated by the field a_{in} in Fig. 3.1 can be reflected from the layer structure, with outgoing light indicated by photon operator a_{out}. On the other hand, the layer structure can be chosen in such a way that a cavity or waveguide is formed for the probing light. In this case, the probing light in addition can evanescently couple into waveguide modes, and eventually exit the layer structure to the side, as indicated by the photon operator b_{out} in Fig. 3.1. As already pointed out in Sec. 2.1, the incident x-ray beam can resonantly couple to waveguide modes inside the cavity at particular values for the angle of incidence θ.

It is instructive to characterize these modes in terms of the resonant cavity wave vector $\boldsymbol{k}_C$. First, we note that the external x-ray field with frequency ω and wave vector $\boldsymbol{k}$ can be divided into components $k_z = |\boldsymbol{k}| \sin(\theta)$ perpendicular and $k_x = |\boldsymbol{k}| \cos(\theta)$ parallel to the surface. In order to satisfy the continuity relations of Maxwell's equations at boundaries, the parallel components k_{Cx} inside and k_x outside the cavity must be identical. In contrast, the perpendicular component k_{Cz} of the mode is determined by parameters of the cavity such as the thickness of the layers and

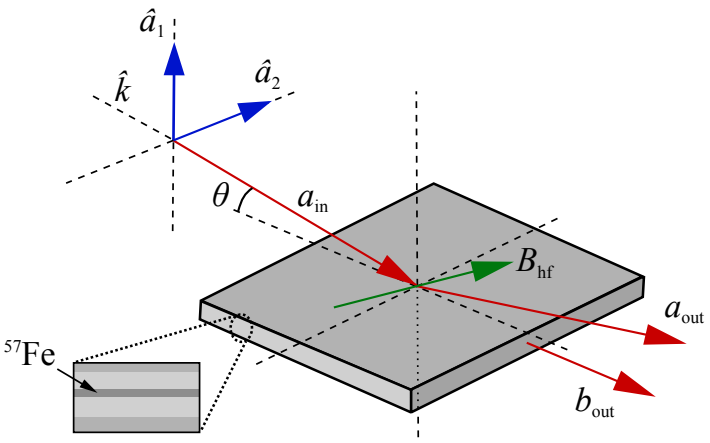

Figure 3.1: Schematic of the considered setup. The cavity contains a layer of resonant nuclei as indicated in the inset. It is probed by hard x-rays (red lines, a_{in}) with propagation direction $\hat{\boldsymbol{k}}$. The angle of incidence θ is of the order of a few mrad. The incident polarization in the $(\hat{\boldsymbol{a}}_1, \hat{\boldsymbol{a}}_2)$ plane (blue) together with the alignment of the magnetization $\boldsymbol{B}_{\mathbf{hf}}$ of the nuclei (green) sensitively determine the properties of the scattered light. Both, light reflected from the cavity (a_{out}) at output angle θ and light exiting the cavity on the front side (b_{out}) are considered.

the refractive indices and the order of the guided mode [132, 133]. This means the cavity exhibits resonances only in the direction perpendicular to the surface, while the parallel components of total resonance wave vector can be chosen freely.

In this chapter we will restrict the discussion to only one guided mode and assume, without loss of generality, that its resonance condition for k_{Cz} is fulfilled if an x-ray beam with the resonance frequency of the ^{57}Fe transition $\omega_0 = c \cdot k_0$ impinges on the layer surface under an angle of incidence θ_0. In this case $k_{Cz} = k_{0z} = k_0 \sin(\theta_0)$ and $k_{Cx} = k_{0x}$, and we find that the cavity mode is resonantly driven. If the angle of incidence is varied from θ_0 to a general angle θ, the perpendicular mode component k_{Cz} is still fixed by the same resonance condition $k_{Cz} = k_0 \sin(\theta_0)$ of the waveguide mode, while $k_{Cx} = |\boldsymbol{k}| \cos(\theta)$ can freely vary with θ. In other words, the mode of interest is not only characterized by cavity parameters, but also by the incident beam. For the total wave vector of the resonant cavity mode, this yields

$$|\boldsymbol{k}_C| = \sqrt{|\boldsymbol{k}|^2 \cos(\theta)^2 + k_0^2 \sin(\theta_0)^2}\,. \tag{3.1}$$

We now continue with the derivation of the Hamiltonian for this mode in the cavity and its driving due to the external field. In a first step, we do not yet take into account any polarization dependence. In the Schrödinger picture the Hamiltonian reads [1, 134–138]

$$H_M^{(S)} = \omega_C a^\dagger a + i\sqrt{2\kappa_R}\left(a_{\text{in}} e^{-i\omega t} a^\dagger - a_{\text{in}}^* e^{i\omega t} a\right)\,. \tag{3.2}$$

Here a [$a^\dagger$] is the photon annihilation [creation] operator for the field in the cavity, a_{in} characterizes the driving of the cavity mode by the external classical x-ray field with frequency ω, the coupling strength into the cavity mode is denoted by κ_R and $\omega_C = c \cdot |\boldsymbol{k}_C|$ is the mode resonance frequency. In a next step we transform the system into an interaction picture to eliminate the explicit time dependence in the Hamiltonian. We apply the unitary transformation

$$|\Psi^{(I)}\rangle = U^\dagger |\Psi^{(S)}\rangle \tag{3.3}$$

given by

$$U = \exp(-iH_T t)\,, \tag{3.4}$$

$$H_T = \omega\, a^\dagger a\,, \tag{3.5}$$

and obtain the perturbation Hamiltonian in the interaction picture

$$\begin{aligned} H_M^{(I)} &= U^\dagger H_M^{(S)} U - H_T \\ &= \Delta_C a^\dagger a + i\sqrt{2\kappa_R}\left(a_{\text{in}} a^\dagger - a_{\text{in}}^* a\right) . \end{aligned} \tag{3.6}$$

Here we introduced the cavity detuning $\Delta_C = \omega_C - \omega$. For a small angular deviation $\Delta\theta = \theta - \theta_0 \ll 1$ from the resonant incident angle θ_0 and $\omega \approx \omega_0$ we find from Eq. (3.1)

$$\begin{aligned} \Delta_C &= \sqrt{\omega^2 \cos\left(\theta_0 + \Delta\theta\right)^2 + \omega_0^2 \sin\left(\theta_0\right)^2} - \omega \\ &\approx -\omega\theta_0 \Delta\theta , \end{aligned} \tag{3.7}$$

such that the detuning is proportional to the incidence angle and the frequency of the incident light.

Now we generalize this Hamiltonian to the case including polarization. We denote the beam propagation direction as $\hat{\boldsymbol{k}}$, where the "hat" indicates a normalized unit vector. Since $\theta_0 \ll 1$, the direction of the incident, reflected and transmitted beam can be considered as equal, parallel to $\hat{\boldsymbol{k}}$. As a consequence, their respective polarizations $\hat{\boldsymbol{a}}_{\text{in}}$, $\hat{\boldsymbol{a}}_{\text{out}}$ and $\hat{\boldsymbol{b}}_{\text{out}}$ are located in the plane defined by the layer surface normal $\hat{\boldsymbol{a}}_1$ and $\hat{\boldsymbol{a}}_2 = \hat{\boldsymbol{a}}_1 \times \hat{\boldsymbol{k}}$. Including both these polarizations as different modes a_1 and a_2 in our calculation, the Hamiltonian in the interaction picture becomes

$$\begin{aligned} H_M = {} & \Delta_C {a_1}^\dagger a_1 + \Delta_C {a_2}^\dagger a_2 \\ & + i\sqrt{2\kappa_R}\left[\left(\hat{\boldsymbol{a}}_1^* \cdot \hat{\boldsymbol{a}}_{\text{in}}\right) a_{\text{in}} a_1^\dagger - \left(\hat{\boldsymbol{a}}_{\text{in}}^* \cdot \hat{\boldsymbol{a}}_1\right) a_{\text{in}}^* a_1\right] \\ & + i\sqrt{2\kappa_R}\left[\left(\hat{\boldsymbol{a}}_2^* \cdot \hat{\boldsymbol{a}}_{\text{in}}\right) a_{\text{in}} a_2^\dagger - \left(\hat{\boldsymbol{a}}_{\text{in}}^* \cdot \hat{\boldsymbol{a}}_2\right) a_{\text{in}}^* a_2\right] . \end{aligned} \tag{3.8}$$

Here, $(\hat{\boldsymbol{a}}_i^* \cdot \hat{\boldsymbol{a}}_j)$ are scalar products between two different polarization unit vectors.

Next to the coherent dynamics described by Eq. (3.8), also incoherent processes need to be considered. This is particular important as in typical experiments, the cavity has a relatively low Q factor [52]. It is important to note that incoherent processes such as spontaneous emission evolve a pure quantum mechanical state into an incoherent mixture of states, which cannot be described using a wave function. Therefore, we include incoherent processes using the master equation approach [1, 139, 140] for the system's density matrix ρ. In this framework, the governing equation replacing the usual Schrödinger equation is

$$\frac{d}{dt}\rho = -i[H, \rho] + \mathcal{L}[\rho] , \tag{3.9}$$

where the commutator part $[\cdot, \cdot]$ characterizes the coherent evolution by the Hamiltonian H, and the Lindblad operator $\mathcal{L}[\rho]$ models incoherent processes. For arbitrary operators $\mathcal{O}^+$ and $\mathcal{O}^-$, a contribution to the latter can be defined as

$$\mathcal{L}[\rho, \mathcal{O}^+, \mathcal{O}^-] = \left(\mathcal{O}^+\mathcal{O}^-\rho + \rho\mathcal{O}^+\mathcal{O}^- - 2\mathcal{O}^-\rho\mathcal{O}^+\right) . \tag{3.10}$$

With this definition, the photon loss out of modes a_1 and a_2 can be written as [134–136, 139, 141]

$$\mathcal{L}_M[\rho] = -\,\kappa\,\mathcal{L}[\rho, a_1^\dagger, a_1] - \kappa\,\mathcal{L}[\rho, a_2^\dagger, a_2] . \tag{3.11}$$

Note that cavity loss in the present framework not only arises due to incoherent scattering or absorption in the layer structure, but also by outcoupling of the cavity field into the modes characterizing reflectance and transmittance. The total rate κ contains all of these loss processes. In the absence of nuclei, $\mathcal{L}[\rho] = \mathcal{L}_M[\rho]$. With nuclei embedded in the cavity, further incoherent processes associated with the nuclei arise, which we discuss in Sec. 3.1.4.

3.1.2 Input-output relations

In an experiment not the internal modes in the cavity, but the reflected (a_{out}) or transmitted beams (b_{out}) are observed. These output field operators can be calculated using the input-output formalism [142, 143]. Assuming polarization-sensitive detection with detector polarization $\hat{\boldsymbol{a}}_{\mathrm{out}}$ they read

$$\begin{aligned} a_{\mathrm{out}} &= -a_{\mathrm{in}}\,(\hat{\boldsymbol{a}}^*_{\mathrm{out}}\cdot\hat{\boldsymbol{a}}_{\mathrm{in}}) \\ &\quad + \sqrt{2\kappa_R}\,[(\hat{\boldsymbol{a}}^*_{\mathrm{out}}\cdot\hat{\boldsymbol{a}}_1)\,a_1 + (\hat{\boldsymbol{a}}^*_{\mathrm{out}}\cdot\hat{\boldsymbol{a}}_2)\,a_2]\;, \qquad (3.12) \\ b_{\mathrm{out}} &= \sqrt{2\kappa_T}\,[(\hat{\boldsymbol{a}}^*_{\mathrm{out}}\cdot\hat{\boldsymbol{a}}_1)\,a_1 + (\hat{\boldsymbol{a}}^*_{\mathrm{out}}\cdot\hat{\boldsymbol{a}}_2)\,a_2]\;. \qquad (3.13) \end{aligned}$$

Note that the transmission b_{out} only receives contributions originating from the modes a_1 and a_2 inside the cavity, while a_{out} also contains the part of the incident light a_{in} directly reflected from the cavity. The coupling constant κ_R in Eqs. (3.12) and (3.13) is equal to the corresponding one in Eq. (3.8), as both describe the coupling between the same internal and external modes. This parameter can be controlled by changing, e.g. the thickness of the topmost layer, see Sec. 3.3.1. Further, we note that $\kappa \geq \kappa_R + \kappa_T$, because the cavity is not only damped by coupling into the outgoing modes, but also by internal loss, as discussed below Eq. (3.11). This condition is crucial for fulfilling the energy conservation.

3.1.3 Observables

To guide the further analysis, it is useful to consider possible observables accessible in a typical experiment. These are primarily the reflectance (scattering into a_{out} in Fig. 3.1) and the transmittance (scattering into b_{out} in Fig. 3.1). With the output field operators introduced in Sec. 3.1.2 at hand, one can readily calculate the reflection and transmission coefficient as [137]

$$R = \frac{\langle a_{\mathrm{out}}\rangle}{a_{\mathrm{in}}}\,, \qquad (3.14)$$

$$T = \frac{\langle b_{\mathrm{out}}\rangle}{a_{\mathrm{in}}}\,. \qquad (3.15)$$

Note that in current experiments, the reflected (transmitted) intensity $|R|^2$ ($|T|^2$) is measured, since phase information is often not accessible. By making use of an interferometric setup, also phase information could be retrieved. We emphasize that the definitions for the observables presented above are only valid in the linear regime, realized in current experiments with synchrotron radiation. A generalized discussion of the reflectance beyond the linear regime will be given in Chap. 8.

Another observable of interest which can easily be accessed with the formalism developed here is the photon correlation function [144–146]

$$g^{(2)}(\tau) = \frac{\langle a^\dagger_{\mathrm{out}}(0)a^\dagger_{\mathrm{out}}(\tau)a_{\mathrm{out}}(\tau)a_{\mathrm{out}}(0)\rangle}{\langle a^\dagger_{\mathrm{out}}a_{\mathrm{out}}\rangle^2}\,. \qquad (3.16)$$

It can be used to determine the photon statistics (at $\tau = 0$) as a function of any parameter or, if the operators are evaluated at different times ($\tau \neq 0$), photon (anti-)bunching [145, 146]. This way, quantum properties of the scattered light can be accessed. It should be noted that Eq. (3.16) characterizes temporal correlations between individual photons along the propagation direction of the scattered light, rather than spatial correlations in a transverse cross section through the propagating beam.

In this work we will focus on the reflectance $|R|^2$ calculated with Eq. (3.14) since it is of interest in current experiments.

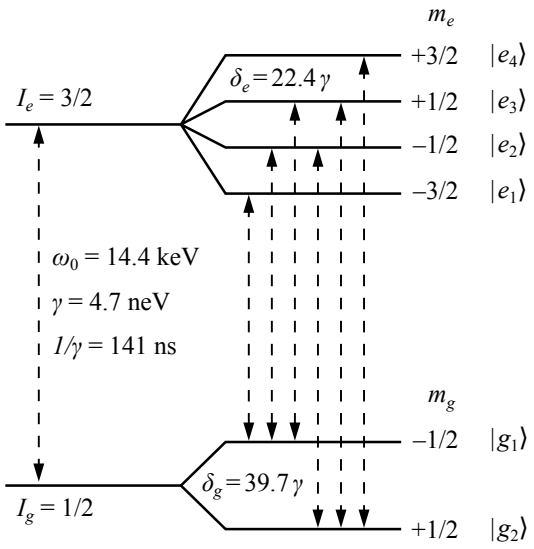

Figure 3.2: The Mössbauer transition in ^{57}Fe. In the presence of a magnetic hyperfine field the two levels split up and six M1 transitions can be driven.

3.1.4 Inclusion of the resonant nuclei

So far, we formulated the equations for an empty cavity. Next, we include the resonant nuclei and focus on the most frequently used archetype Mössbauer isotope ^{57}Fe, for which the level scheme is illustrated in Fig. 3.2. This isotope features a transition from the ground state to the first excited state at $\omega_0 = 14.4$ keV with single-nucleus line width $\gamma = 4.7$ neV. In the absence of magnetic fields, it acts as a two-level system. In the presence of magnetic fields, the ground and excited states with $I_g = 1/2$ and $I_e = 3/2$ split into multiplets shown in Fig. 3.2. In general, six different transitions between ground and excited states are possible. Note that the considered transition is a magnetic dipole (M1) transition. Since the polarization vectors of the radiation are typically given in terms of the electric field component, we also chose this notation for consistency. However, at the same time this means that the transition axes in the nuclei should be redefined accordingly. An alternate way would be to identify the polarization vectors with the magnetic component of the radiation. We furthermore specialize to the case of a single layer of nuclei, which we place at a maximum of the field intensity distribution of the cavity, in order to maximize the nucleus-field interaction. For the first guided mode, this maximum is approximately located in the center of the cavity, as seen from Fig. 2.2(c).

But before we consider the general case with a magnetic hyperfine splitting, let us first consider the simplest case of a single two-level nucleus with ground state $|g\rangle$, excited state $|e\rangle$ and transition energy $\omega_0 = \omega_e - \omega_g$ and only one cavity mode a. This amounts to omitting the polarization dependence in this first step. In the Schrödinger picture the free time evolution of the nucleus and its coupling to the cavity mode in rotating wave approximation can be written as [1]

$$H_N^{(S)} = \omega_g |g\rangle\langle g| + \omega_e |e\rangle\langle e| + g S_+ a + g^* a^\dagger S_- \,. \tag{3.17}$$

Here $S_+ = |e\rangle\langle g|$ and $S_- = |g\rangle\langle e|$ denote the nuclear raising and lowering operators, respectively, and g is the coupling constant between the mode a and the nucleus. Note that effects beyond the rotating-wave-approximation could be included in Eq. (3.17) by means of a unitary transformation as discussed in Refs. [111, 112], which would lead to corrections to the coupling constant g and to the transition energy $\omega_e - \omega_g$. Since these parameters are typically obtained by fitting the quantum optical model to experimental or numerical data, these corrections are assumed

Table 3.1: Overview of the M1 allowed transitions in the ^{57}Fe nucleus with transition index μ. Shown are the involved states, the transition energy ΔE relative to the energy at vanishing magnetization ω_0, the Clebsch-Gordan coefficient c_μ and the polarization type. Linear polarization is denoted by π^0, right (left) circular polarization as σ^+ (σ^-).

μ	Transition	ΔE	c_μ	Polarization
1	$\|g_1\rangle \leftrightarrow \|e_1\rangle$	$-\delta_g/2 - 3/2\delta_e$	1	σ^-
2	$\|g_1\rangle \leftrightarrow \|e_2\rangle$	$-\delta_g/2 - 1/2\delta_e$	$\sqrt{2/3}$	π^0
3	$\|g_1\rangle \leftrightarrow \|e_3\rangle$	$-\delta_g/2 + 1/2\delta_e$	$\sqrt{1/3}$	σ^+
4	$\|g_2\rangle \leftrightarrow \|e_2\rangle$	$\delta_g/2 - 1/2\delta_e$	$\sqrt{1/3}$	σ^-
5	$\|g_2\rangle \leftrightarrow \|e_3\rangle$	$\delta_g/2 + 1/2\delta_e$	$\sqrt{2/3}$	π^0
6	$\|g_2\rangle \leftrightarrow \|e_4\rangle$	$\delta_g/2 + 3/2\delta_e$	1	σ^+

to be already included in the respective quantities. In order to transform the Hamiltonian for both the nuclei and the cavity modes into an time-independent interaction picture we alter the transformation from Eq. (3.5) to

$$H_T = \omega\, a^\dagger a + \omega_g\, |g\rangle\langle g| + (\omega_g + \omega)|e\rangle\langle e| \,. \tag{3.18}$$

This yields

$$H_N^{(I)} = -\Delta|e\rangle\langle e| + gS_+ a + g^* a^\dagger S_- \,. \tag{3.19}$$

Here, we defined the detuning $\Delta = \omega - \omega_0$ as the energy difference between the external x-ray field and the bare transition energy of the nucleus.

Now we will continue with the general case including a possible magnetic hyperfine splitting caused by a field $\boldsymbol{B}_{\mathrm{hf}}$. When a ferromagnetically ordered layer of α-iron is placed in the cavity, already a relatively weak external field can align a strong internal magnetization of ≈ 33 T, resulting in a level splitting of several line widths γ. The energy difference between two adjacent ground (excited) sub-states is denoted by δ_g (δ_e) in the following. For $B \approx 33$ T the values of δ_g and δ_e are 39.7γ and 22.4γ, respectively [51].

Using a similar transformation as above, the free evolution of N nuclei and their coupling to the cavity modes a_1 and a_2 is given by the Hamiltonian

$$H_N = \sum_{n=1}^{N} H_0^{(n)} + H_{C_1}^{(n)} + H_{C_2}^{(n)} \tag{3.20}$$

with the diagonal part

$$H_0^{(n)} = \sum_{j=1}^{2} \delta_g(j - \tfrac{3}{2})\; |g_j^{(n)}\rangle\langle g_j^{(n)}| + \sum_{j=1}^{4} \left(\delta_e(j - \tfrac{5}{2}) - \Delta\right)\; |e_j^{(n)}\rangle\langle e_j^{(n)}| \,. \tag{3.21}$$

The coupling between the nth atom and the mode a_j reads

$$H_{C_j}^{(n)} = \sum_{\mu=1}^{6} \left[(\hat{\boldsymbol{d}}_\mu^* \cdot \hat{\mathbf{a}}_j)\, g_\mu^{(n)} S_{\mu+}^{(n)} a_j + (\hat{\mathbf{a}}_j^* \cdot \hat{\boldsymbol{d}}_\mu)\, {g_\mu^{(n)}}^* a_j^\dagger S_{\mu-}^{(n)} \right] \,, \tag{3.22}$$

where the sums run over the six possible transitions (see Tab. 3.1). The operator $S_{\mu+}^{(n)}$ [$S_{\mu-}^{(n)}$] acts only on atom n and is the raising [lowering] operator on transition μ. The normalized dipole moment $\hat{\boldsymbol{d}}_\mu$ of transition μ is defined with respect to the quantization axis of the nuclei. As mentioned before, we want to denote the electric field components of the fields by the polarization

vectors $\hat{\boldsymbol{a}}_{\text{in}}$ and $\hat{\boldsymbol{a}}_{\text{out}}$. Since ^{57}Fe features a M1 transition, the quantization axis $\hat{\boldsymbol{\pi}}^0$ of the linearly polarized transitions is not equal to the magnetic field axis $\hat{\boldsymbol{B}}_{\text{hf}}$. Rather, to determine $\hat{\boldsymbol{\pi}}^0$, the vector $\hat{\boldsymbol{B}}_{\text{hf}}$ has to be rotated by 90° in the $(\hat{\boldsymbol{a}}_1, \hat{\boldsymbol{a}}_2)$ plane perpendicular to the beam propagation axis.

The coupling constant

$$g_\mu^{(n)} = g\, c_\mu\, e^{i\,\phi^{(n)}} \tag{3.23}$$

consists of the coupling constant g, the Clebsch-Gordan coefficient c_μ of the transition and a phase factor that accounts for the position $\boldsymbol{R}^{(n)}$ of the nucleus.

Another contribution which has to be included in the description of the nuclei is spontaneous emission. It can take place on each of the six transitions μ, weighted with their respective Clebsch-Gordan coefficients c_μ^2. The effect of spontaneous emission is described with the Lindblad operator [1, 140]

$$\mathcal{L}_{\text{SE}}[\rho] = \sum_{n=1}^{N} \mathcal{L}_{\text{SE}}^{(n)}[\rho] \tag{3.24}$$

$$\mathcal{L}_{\text{SE}}^{(n)}[\rho] = -\frac{\gamma}{2} \sum_{\mu=1}^{6} c_\mu^2\, \mathcal{L}[\rho, S_{\mu+}^{(n)}, S_{\mu-}^{(n)}] \tag{3.25}$$

where $\mathcal{L}[\rho, \cdot, \cdot]$ is defined in Eq. (3.10). Note that the expressions in Eq. (3.25) characterize the total line width of single nuclei. Therefore, the rate of spontaneous emission γ is taken as the natural line width of the ^{57}Fe nucleus, even though part of this line width arises from internal conversion rather than from radiative decay.

3.1.5 The full model

The full master equation including the equations of motion of the nuclei as well as for the photonic modes is

$$\frac{d}{dt}\rho = -i[H_M + H_N, \rho] + \mathcal{L}_M[\rho] + \mathcal{L}_{\text{SE}}[\rho]\ . \tag{3.26}$$

With this equation it is in principle possible to perform calculations for arbitrary settings. However, the size of the system's Hilbert space a priori is infinite, because in general arbitrary occupation numbers of the photon modes are possible. Restricting the maximum number of photons per mode considered in the calculation to n_{ph}, the Hilbert space still scales as $6^N(n_{ph}+1)^2$ with N being the number of nuclei in the cavity, which is impractically large to be solved efficiently even for relatively small n_{ph}. Next, we will therefore use a different ansatz to overcome the obstacle of the fast growing Hilbert space, which in addition provides more insight in the underlying physics as even analytic predictions can be made.

3.2 Effective master equation

In the last part we formulated the fundamental equations for our setup, which have the disadvantage that they cannot be directly solved analytically due to the large dimensionality of the Hilbert space. In this section, we apply two physically motivated approximations. First, we make use of the fact that for typical parameters, the dissipative dynamics dominates the cavity evolution, such that the occupation number of the photon modes in the cavity remains small. Then, these photonic modes can be adiabatically eliminated to obtain effective equations of motion for the nuclei only, as explained in detail in Sec. 3.2.1. Second, in the case of a weak probe field, i.e. in linear response, the system of N nuclei can be transformed into a new basis where only few

excited states are coupled to the ground state. As shown in section 3.3 and chapters 4 and 5, relatively simple and compact analytic expressions can be found for the reflection coefficient in this case.

3.2.1 Adiabatic elimination of the cavity modes

The thin-film cavities which are used in typical experiments have a low quality factor Q [52], which corresponds to a large decay constant κ in our model, see Eq. (3.11). As κ is much larger than the atom-field coupling strength g, the dynamics of the modes a_1 and a_2 is mainly governed by fast dissipation, which is known as the bad-cavity regime [135, 136, 146]. This allows us to adiabatically eliminate the modes [134, 135]. For this, we approximate $\frac{d}{dt}a_j = 0$. Starting with the Heisenberg equation of motion for the operator a_j

$$\frac{d}{dt}a_j = i[H_M + H_N, a_j] - \kappa a_j \tag{3.27}$$

we arrive at

$$a_j = \frac{\sqrt{2\kappa_R}a_{\mathrm{in}}(\hat{\boldsymbol{a}}_j^*\cdot\hat{\boldsymbol{a}}_{\mathrm{in}}) - i\sum_{n,\mu}(\hat{\boldsymbol{a}}_j^*\cdot\hat{\boldsymbol{d}}_\mu)g_\mu^{(n)^*}S_{\mu-}^{(n)}}{\kappa + i\Delta_C}\,. \tag{3.28}$$

Before we continue with the effective equations for the nuclei let us consider the reflection coefficient as defined in Eq. (3.14). Inserting the expressions Eq. (3.28) for a_j yields

$$\begin{aligned} R = \frac{\langle a_{\mathrm{out}}\rangle}{a_{\mathrm{in}}} = &\left(\frac{2\kappa_R}{\kappa + i\Delta_C} - 1\right)\hat{\boldsymbol{a}}_{\mathrm{out}}^*\cdot\hat{\boldsymbol{a}}_{\mathrm{in}} \\ &- \frac{i}{a_{\mathrm{in}}}\frac{\sqrt{2\kappa_R}}{\kappa + i\Delta_C}\sum_{n,\mu}\left(\hat{\boldsymbol{a}}_{\mathrm{out}}^*\cdot\mathbb{1}_\perp\cdot\hat{\boldsymbol{d}}_\mu\right)g_\mu^{(n)^*}\langle S_{\mu-}^{(n)}\rangle\,. \end{aligned} \tag{3.29}$$

Here, we defined $\mathbb{1}_\perp = \hat{\boldsymbol{a}}_1\hat{\boldsymbol{a}}_1^* + \hat{\boldsymbol{a}}_2\hat{\boldsymbol{a}}_2^* = \mathbb{1} - \hat{\boldsymbol{k}}\hat{\boldsymbol{k}}^*$. Note that this expression contains outer products rather than inner (scalar) products. We see that the reflection coefficient consists of two contributions. Consistent with the layerformalism [77] we can identify the first term in Eq. (3.29) with the electronic scattering contribution, which is isotropic. A particularly interesting case arises if the cavity is operated exactly in resonance with the guided mode, i.e., $\Delta_C = 0$. If in addition $\kappa = 2\kappa_R$ is fulfilled, then the reflection originating from the cavity vanishes completely. The latter condition is known as *critical coupling* condition [141]. If the total cavity decay rate is not matched to the in- and out-coupling of light from the cavity, then the *over- or undercritically coupled* regime is realized, in which the reflected light is not completely canceled on resonance. The coupling regimes will be discussed in more detail in Sec. 3.3.1. The second term in Eq. (3.29) describes the contribution to the reflection which is due to the nuclei. This contribution is not isotropic or polarization-preserving in general, and can contribute even if the polarizations of the incident beam and the detected radiation are orthogonal to each other.

We now continue with the adiabatic elimination of the cavity modes. Having established expressions for the field operators a_j and $a_j^\dagger$, they can be inserted into the master equation (3.26) to obtain the effective equations of motion for the nuclei. For the coherent dynamics, we obtain the Hamiltonian

$$H_{\mathrm{eff}} = \sum_{n=1}^{N}\left(H_0^{(n)} + H_\Omega^{(n)}\right) + \sum_{n,m=1}^{N} H_{\mathrm{LS}}^{(n,m)} \tag{3.30}$$

with free evolution $H_0^{(n)}$ as defined in Eq. (3.21) and the new terms

$$H_\Omega^{(n)} = \Omega\sum_\mu\left(\hat{\boldsymbol{d}}_\mu^*\cdot\mathbb{1}_\perp\cdot\hat{\boldsymbol{a}}_{\mathrm{in}}\right)g_\mu^{(n)}S_{\mu+}^{(n)} + \Omega^*\sum_\mu\left(\hat{\boldsymbol{a}}_{\mathrm{in}}^*\cdot\mathbb{1}_\perp\cdot\hat{\boldsymbol{d}}_\mu\right)g_\mu^{(n)^*}S_{\mu-}^{(n)}\,, \tag{3.31}$$

$$H_{\mathrm{LS}}^{(n,m)} = \delta_{\mathrm{LS}}\sum_{\mu,\nu}\left(\hat{\boldsymbol{d}}_\mu^*\cdot\mathbb{1}_\perp\cdot\hat{\boldsymbol{d}}_\nu\right)g_\mu^{(n)}g_\nu^{(m)^*}S_{\mu+}^{(n)}S_{\nu-}^{(m)} \tag{3.32}$$

arising from the adiabatic elimination procedure with parameters

$$\Omega = \frac{\sqrt{2\kappa_R} a_{\mathrm{in}}}{\kappa + i\Delta_C} , \tag{3.33}$$

$$\delta_{\mathrm{LS}} = -\frac{\Delta_C}{\kappa^2 + \Delta_C^2} . \tag{3.34}$$

The Hamiltonian $H_\Omega^{(n)}$ describes an effective coupling between ground and excited states for each atom n. As expected, the transition dipole moments are not coupled to the polarization of the external beam by a direct product, but the direction vectors are mediated via the tensor $\mathbb{1}_\perp$ which reflects the intermediate light propagation in the two eliminated modes. To analyze the effect of $H_{\mathrm{LS}}^{(n,m)}$ we first consider the special case $n = m$ and $\mu = \nu$, i.e., operators for the same transition in the same atom. It can be seen that in this case, the product $S_{\mu+}^{(n)} S_{\nu-}^{(m)}$ reduces to an operator of the form $|e\rangle\langle e|$ for atom $n = m$. Therefore, this term in the Hamiltonian is an energy shift, which can be interpreted as an additional AC-Stark or Lamb shift emerging from the coupling of the atom to the two modes in the cavity. The terms with $n \neq m$ involving the same transition in different atoms are known as dipole-dipole interactions [140, 147] and lead to a collective Lamb shift [110]. In the cases $\mu \neq \nu$, a coherent coupling between two different transitions emerge [140, 147, 148].

Apart from these Hamiltonian contributions, the adiabatic elimination also gives rise to incoherent dynamics beyond spontaneous emission as characterized by Eq. (3.25). The total Lindblad operator is found as

$$\mathcal{L}_{\mathrm{eff}}[\rho] = \mathcal{L}_{\mathrm{SE}}[\rho] + \mathcal{L}_{\mathrm{cav}}[\rho] \tag{3.35}$$

with the new term

$$\mathcal{L}_{\mathrm{cav}}[\rho] = -\zeta_S \sum_{n,m=1}^{N} \sum_{\mu,\nu=1}^{6} \left(\hat{\boldsymbol{d}}_\mu^* \cdot \mathbb{1}_\perp \cdot \hat{\boldsymbol{d}}_\nu\right) g_\mu^{(n)} g_\nu^{(m)*} \, \mathcal{L}[\rho, S_{\mu+}^{(n)}, S_{\nu-}^{(m)}] , \tag{3.36}$$

and

$$\zeta_S = \frac{\kappa}{\kappa^2 + \Delta_C^2} . \tag{3.37}$$

The contributions with $n = m$ and $\mu = \nu$ in Eq. (3.36) have the same form as those characterizing spontaneous emission. As we will find in Sec. 3.3, they lead to superradiance, i.e., an acceleration of the incoherent decay [52]. The terms with $n = m$ and $\mu \neq \nu$ are the so-called cross-decay terms [140, 147] and give rise to an incoherent coupling between different transitions. Interestingly, these terms can lead to coherences [140]. This will be discussed in more detail in Chap. 5.

In both the coherent and the incoherent additions arising from the adiabatic elimination, the dipole moments are not coupled via the usual free space scalar product $\hat{\boldsymbol{d}}_\mu^* \cdot \hat{\boldsymbol{d}}_\nu$, but by the form $\hat{\boldsymbol{d}}_\mu^* \cdot \mathbb{1}_\perp \cdot \hat{\boldsymbol{d}}_\nu$. We emphasize that this generally permits non-vanishing couplings between *orthogonal* states, which is fundamentally different from the situation in free space [149, 150]. This fact can be exploited to engineer a variety of different quantum optical level schemes as will be shown in Chap. 5.

Effect of quantum noise

In the derivation of the effective master equation above, we adiabatically eliminated the cavity modes. To this end, the equation of motion for annihilation operators a were written as

$$\frac{d}{dt} a = i[H, a] - \kappa a . \tag{3.38}$$

The commutator part denotes the coherent evolution of the operator, i.e. the Heisenberg equation of motion [151]. The second term accounts for the incoherent dynamics, i.e. the cavity decay. Strictly speaking, however, the latter part is incomplete, because the quantum noise operators have been dropped. In the following we will shortly discuss their meaning and discuss why they can be neglected in the first place.

Let us start by recalling that the cavity decay is a consequence of the coupling of the modes to an environment, which in our case is a reservoir of harmonic oscillators. Using the density matrix approach to describe the systems' dynamics alone by tracing out the environment gives rise to the incoherent part of the master equation. However, if one is not interested in working with the density matrix but rather with quantum operators, the problem of the coupling to the reservoir must be formulated differently. This is known as the Heisenberg-Langevin approach [1].

The result of the Heisenberg-Langevin approach for the case of damping via a reservoir of closely spaced oscillators, forming the electromagnetic quantum vacuum, is required here. In this situation, the equation of motion for the annihilation operator a is [1]

$$\frac{d}{dt}a = -\kappa a + F_a(t) \;, \tag{3.39}$$

where F_a is a noise operator and accounts for the reservoir. The noise operator satisfies the relations

$$\langle F_a \rangle = \langle F_a^\dagger \rangle = \langle F_a F_a \rangle = \langle F_a^\dagger F_a^\dagger \rangle = 0 \;, \tag{3.40}$$

$$\langle F_a^\dagger(t) F_a(t') \rangle = 2\kappa n_{\mathrm{th}} \delta(t-t') \;, \tag{3.41}$$

$$\langle F_a(t) F_a^\dagger(t') \rangle = 2\kappa (n_{\mathrm{th}}+1) \delta(t-t') \;, \tag{3.42}$$

$$\langle F_a^\dagger a \rangle = \langle a^\dagger F_a \rangle = \kappa n_{\mathrm{th}} \;. \tag{3.43}$$

Here n_{th} is the usual thermal bosonic occupation number. This yields

$$\frac{d}{dt}\langle a \rangle = -\kappa \langle a \rangle + \langle F_a \rangle = -\kappa \langle a \rangle \;, \tag{3.44}$$

$$\frac{d}{dt}\langle a^\dagger a \rangle = -2\kappa \langle a^\dagger a \rangle + \langle a^\dagger F_a \rangle + \langle F_a^\dagger a \rangle = -2\kappa \langle a^\dagger a \rangle + 2\kappa n_{\mathrm{th}} \;. \tag{3.45}$$

Since the thermal energy kT for room temperature is much smaller than the x-ray transition energies, the thermal occupation number n_{th} is negligible. Thus, we recover the same equations of motion as if we had dropped the noise operator in the beginning and the use of Eq. (3.38) is justified.

3.2.2 Linear response

Current experiments employing the 14.4 keV resonance line in ^{57}Fe in thin-film cavities are mostly performed at modern synchrotron light sources. As discussed in Sec. 2.1.3, typically less than one resonant photon is provided in the narrow line width of ^{57}Fe [7, 52, 106, 107]. Thus, the driving field a_{in} can be considered weak, which together with the moderate nucleus-cavity coupling justifies a calculation of the reflectance in linear response. Of course, this ansatz has to be revisited if future experiments are performed at an seeded x-ray free-electron laser [11] or x-ray free-electron laser oscillator [15–18] with thousands of resonant photons per pulse, or if better cavities could be designed.

Let us assume that the nuclei are initially in the collective ground state

$$|G\rangle = \underbrace{|g_1^{(1)}\rangle \ldots |g_1^{(N_1)}\rangle}_{N_1} \underbrace{|g_2^{(N_1+1)}\rangle \ldots |g_2^{(N)}\rangle}_{N_2} \tag{3.46}$$

where $|g_1\rangle$ and $|g_2\rangle$ denote the two magnetic sublevels of the ground state, and N_i is the number of nuclei in ground state $|g_i\rangle$ ($i \in \{1,2\}$). Note that $N_1 + N_2 = N$, and at room temperature and in

thermal equilibrium also $N_1 = N_2$, since the Boltzmann factor $\exp(-\delta_g/k_BT)$ is approximately one. Nevertheless, for now we consider the general case and keep N_1 and N_2 variable. Further, we assume that due to the weak probe beam only one atom can be excited at a time and omit higher excited states. In addition, we neglect other collective ground states as the nuclei will not be redistributed due to the application of a weak probe field. We define the singly excited states

$$|E_{\mu_e}^{(n)}\rangle = S_{\mu+}^{(n)}|G\rangle = |g_1^{(1)}\rangle \dots |e_{\mu_e}^{(n)}\rangle \dots |g_2^{(N)}\rangle\,, \tag{3.47}$$

in which the nth atom has been excited on transition μ. Further we define a collective state, closely related to the timed Dicke state [51, 110, 152],

$$|E_{\mu}^{(+)}\rangle = \frac{1}{\sqrt{N_{\mu_g}}} \sum_{n}^{N_{\mu_g}} e^{i\,\phi^{(n)}} |E_{\mu_e}^{(n)}\rangle\,, \tag{3.48}$$

which characterizes the coherent superposition of all possible excitations of the nuclei after absorption of a photon on transition μ where μ_g [μ_e] denote the state index of the ground [excited] state of the transition. Note that atoms in ground state $|g_n\rangle$ can only be excited along the transition μ if their initial ground state match, i.e. $|g_n\rangle = |g_{\mu_g}\rangle$, otherwise $S_{\mu+}^{(n)}|G\rangle = 0$. With these definitions the equations (3.31), (3.32) and (3.36) in the subspace of at most one excitation simplify to

$$H_\Omega = \Omega g \sum_\mu \big(\hat{\boldsymbol{d}}_\mu^* \cdot \mathbb{1}_\perp \cdot \hat{\boldsymbol{a}}_{\rm in}\big) c_\mu \sqrt{N_{\mu_g}} |E_\mu^{(+)}\rangle\langle G| + \text{H.c.}\,, \tag{3.49}$$

$$H_{\rm LS} = \delta_{\rm LS}|g|^2 \sum_{\mu,\nu} \big(\hat{\boldsymbol{d}}_\mu^* \cdot \mathbb{1}_\perp \cdot \hat{\boldsymbol{d}}_\nu\big)\, c_\mu c_\nu \sqrt{N_{\mu_g} N_{\nu_g}} |E_\mu^{(+)}\rangle\langle E_\nu^{(+)}| \tag{3.50}$$

$$\mathcal{L}_{\rm cav}[\rho] = -\zeta_S |g|^2 \sum_{\mu,\nu} \big(\hat{\boldsymbol{d}}_\mu^* \cdot \mathbb{1}_\perp \cdot \hat{\boldsymbol{d}}_\nu\big) c_\mu c_\nu \sqrt{N_{\mu_g} N_{\nu_g}}\, \mathcal{L}\Big[\rho, |E_\mu^{(+)}\rangle\langle G|, |G\rangle\langle E_\nu^{(+)}|\Big]\,. \tag{3.51}$$

In this basis only one ground and a maximum of six (collective) excited state are present. This reduced basis allows for a considerable simplification of the analytical calculations since also the reflection coefficient from Eq. (3.29) can be written in the reduced basis as

$$\begin{aligned} R = &\left(\frac{2\kappa_R}{\kappa + i\Delta_C} - 1\right) \hat{\boldsymbol{a}}_{\rm out}^* \cdot \hat{\boldsymbol{a}}_{\rm in} \\ &- \frac{i}{a_{\rm in}} \frac{\sqrt{2\kappa_R}}{\kappa + i\Delta_C} g^* \sum_\mu \left(\hat{\boldsymbol{a}}_{\rm out}^* \cdot \mathbb{1}_\perp \cdot \hat{\boldsymbol{d}}_\mu\right) c_\mu \sqrt{N_{\mu_g}}\, \langle E_\mu^{(+)}|\rho|G\rangle\,. \end{aligned} \tag{3.52}$$

This is a remarkable result, since the complicated system of N interacting nuclei and 2 cavity modes is now reduced to an effective single-particle problem without loss of generality within the applied approximations well justified at current experimental conditions.

To calculate the reflection coefficient in linear response we employ the following method. We set $\langle G|\rho|G\rangle = 1$, as population redistributions only occur in second order of the probe field. Next, we consider the coherences $\langle E_\mu^{(+)}|\rho|G\rangle$ which are directly coupled to the ground state via H_Ω. These off-diagonal density matrix elements are the only ones which are non-vanishing in first order in the probing x-ray field Ω. Their steady state is obtained from the equations of motion by the condition $\langle E_\mu^{(+)}|\frac{d}{dt}\rho|G\rangle = 0$. The corresponding set of linear equations can be solved easily. Finally, the obtained steady state is inserted into Eq. (3.52) to obtain the desired reflectance in linear response.

3.3 Application to an unmagnetized ^{57}Fe layer

In a first step, we apply the general formalism to a particular experimental setup, in order to demonstrate its capabilities and consistency with previous formalisms.

We consider the simplest case without hyperfine splitting, i.e. $\boldsymbol{B}_{\mathrm{hf}} = 0$ and therefore $\delta_g = \delta_e = 0$. In this case the result will be independent of the choice of the quantization axis. For simplicity we set $\hat{\boldsymbol{\pi}}^0 \parallel \hat{\boldsymbol{a}}_{\mathrm{in}}$ such that only the linear polarized transitions $\mu = 2$ ($|g_1\rangle \leftrightarrow |e_2\rangle$) and $\mu = 5$ ($|g_2\rangle \leftrightarrow |e_3\rangle$) are driven, see Tab. 3.1. We introduce the state

$$|+\rangle = \sqrt{\frac{N_1}{N}}|E_2^{(+)}\rangle + \sqrt{\frac{N_2}{N}}|E_5^{(+)}\rangle\,, \tag{3.53}$$

and obtain

$$H_\Omega = \sqrt{\tfrac{2}{3}N}\Omega g|+\rangle\langle G| + \mathrm{H.c.} \tag{3.54}$$

$$H_{\mathrm{LS}} = \tfrac{2}{3}N\delta_{\mathrm{LS}}|g|^2|+\rangle\langle+| \tag{3.55}$$

$$\mathcal{L}_{\mathrm{cav}}[\rho] = -\tfrac{2}{3}N\zeta_S|g|^2\,\mathcal{L}\Big[\rho, |+\rangle\langle G|, |G\rangle\langle+|\Big]\,. \tag{3.56}$$

Thus, we have transformed our system to an effective two-level system which consists only of one ground state $|G\rangle$ and one excited state $|+\rangle$. In the same way, the sum in Eq. (3.52) reduces to $(\hat{\boldsymbol{a}}^*_{\mathrm{out}}\cdot\hat{\boldsymbol{a}}_{\mathrm{in}})\sqrt{\frac{2}{3}N}\langle+|\rho|G\rangle$. Consequently, only the coherence $\langle+|\rho|G\rangle$ has to be calculated in order to obtain the reflectance. The equation of motion is

$$\langle+|\dot{\rho}|G\rangle = -i\sqrt{\tfrac{2}{3}N}\Omega g + i\left(\Delta + i\tfrac{\gamma}{2} + \tfrac{2}{3}N|g|^2(i\zeta_S - \delta_{\mathrm{LS}})\right)\langle+|\rho|G\rangle\,, \tag{3.57}$$

where we used the populations in linear response $\langle G|\rho|G\rangle = 1$ and $\langle+|\rho|+\rangle = 0$. Since $\langle+|\rho|G\rangle$ is not coupled to any other density matrix elements in Eq. (3.57), its steady state can be readily obtained from solving the single equation $\langle+|\dot{\rho}|G\rangle = 0$ for the coherence $\langle+|\rho|G\rangle$. The reflection coefficient given by Eq. (3.52) evaluates to

$$\begin{aligned} R &= \left(\frac{2\kappa_R}{\kappa + i\Delta_C} - 1\right)\hat{\boldsymbol{a}}^*_{\mathrm{out}}\cdot\hat{\boldsymbol{a}}_{\mathrm{in}} - \frac{i}{a_{\mathrm{in}}}\frac{\sqrt{2\kappa_R}}{\kappa + i\Delta_C}\frac{\left(\hat{\boldsymbol{a}}^*_{\mathrm{out}}\cdot\hat{\boldsymbol{a}}_{\mathrm{in}}\right)\frac{2}{3}|g|^2N\Omega}{\Delta + i\frac{\gamma}{2} + \frac{2}{3}|g|^2N(i\zeta_S - \delta_{\mathrm{LS}})} \\ &= \left[\left(\frac{2\kappa_R}{\kappa + i\Delta_C} - 1\right) - i\,\frac{2\kappa_R}{(\kappa + i\Delta_C)^2}\,\frac{\frac{2}{3}|g|^2N}{\Delta + i\frac{\gamma}{2} + \frac{2}{3}\frac{|g|^2N}{\Delta_C - i\kappa}}\right]\left(\hat{\boldsymbol{a}}^*_{\mathrm{out}}\cdot\hat{\boldsymbol{a}}_{\mathrm{in}}\right)\,. \end{aligned} \tag{3.58}$$

As a cross check we verified that this result is also obtained when choosing a different quantization axis, such that other transitions couple to the incident light. The result, however, in general does depend on the condition $N_1 = N_2$ of equal ground state population, as otherwise the different transitions have different probabilities according to the ratio of N_1 and N_2. The polarization dependence $\hat{\boldsymbol{a}}^*_{\mathrm{out}}\cdot\hat{\boldsymbol{a}}_{\mathrm{in}}$ is independent of the layer system, and solely determined by the incident and the detection polarization. This is the expected result, as no direction in space is distinguished in the layer system without magnetic quantization axis.

3.3.1 Reflection from the empty cavity

In order to interpret the spectrum of the reflectance, we first recall that the first addend obtained in Eq. (3.58) represents the electronic scattering contribution from the waveguide. Considering the expression in more detail, we note that its first contribution ("$2\kappa_R/(\kappa+i\Delta_C)$") stems from the light which entered the cavity mode and is subsequently emitted again, the second part ("-1") is due to the direct reflection on the cavity surface. As mentioned above, in the case $2\kappa_R = \kappa$, the so-called critical coupling condition is realized [141], in which the electronic reflection completely vanishes on resonance, i.e. $\Delta_C = 0$. For $2\kappa_R > \kappa$ [$2\kappa_R < \kappa$], the overcritical [undercritical] coupling is realized.

Let us analyze these coupling conditions in more detail by considering the angular dependency of the cavity reflection in the absence of resonant nuclei. As already shown in Sec. 2.1.1, the

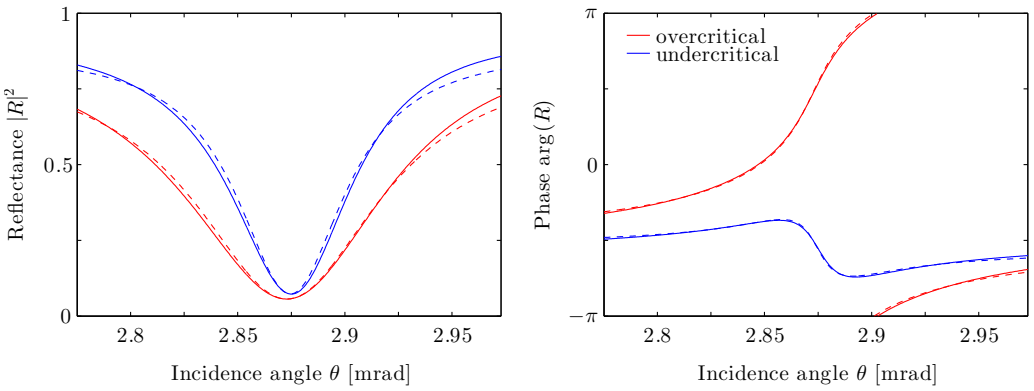

Figure 3.3: The reflectance around an over- ($2\kappa_R > \kappa$, red) and undercritically ($2\kappa_R < \kappa$, blue) coupled cavity mode is shown. The solid curves are calculated with Parratt's formalism, the dashed lines are fits of the quantum optical theory. The two coupling conditions can be distinguished from the phase behavior around the mode resonance. Parameters are given in the main text.

guided modes give rise to distinct minima in the reflection curve. Here, we consider two cavities formed by the layer stack Pd/C (10 nm)/Fe (3 nm)/C (10 nm)/Pd and specify to the first guided mode only. The thickness of the topmost Pd layer is 3.5 nm and 5.5 nm for the two cavities, respectively. The reflection curve of the cavities was calculated using Parratt's formalism, and the quantum optical expression

$$R = A\left(-1 + \frac{2\kappa_R}{\kappa + i\Delta_C}\right) \tag{3.59}$$

with $A \in \mathbb{C}$ and $\Delta_C \sim (\theta - \theta_0)$ as suggested by Eq. (3.7) was fitted to the numerical data. In this procedure, the complex values of the reflection coefficient were used. This way, also the phase behavior around the resonance of the guided mode is properly captured. The resulting curves are shown in Fig. 3.3.

Interestingly, the fits to the numerical data revealed that two different regimes are realized with the two cavities. In the case where the thickness of the upper Pd layer is 3.5 nm, we found that $2\kappa_R > \kappa$ and thus the cavity mode is overcritically coupled. In contrast, the first guided mode of the cavity with thickness 5.5 nm of the Pd layer is undercritically coupled.

Looking solely at the reflectance $|R|^2$, the two cavities exhibit a similar shape and the two coupling regimes cannot be distinguished. However, if the phase behavior around the guided modes is considered, the regimes can be properly identified, as visualized in the right panel of Fig. 3.3. The phase in the overcritical case changes more rapidly and asymptotically ends up in different branches.

Thus, we see that the coupling regime can be controlled by choosing a suitable thickness of the topmost layer in the cavity. This is also in accordance with an intuitive picture: The thinner the topmost layer, the more light can couple from the external field to the cavity mode. Mathematically, this corresponds to a large coupling constant κ_R, for which the overcritically regime is realized in turn.

3.3.2 Nuclear reflection

We now continue with the reflection coefficient calculated in Eq. (3.58). Its second addend arises from the resonant nuclei in the cavity. Defining the parameters

$$\Delta_{\mathrm{LS}} = \frac{2}{3}\,\delta_{\mathrm{LS}}\,|g|^2 N = -\frac{2}{3}\,|g|^2 N\,\frac{\Delta_C}{\kappa^2 + \Delta_C^2}\,, \tag{3.60}$$

$$\gamma_S = \frac{4}{3}\,\zeta_S \;\; |g|^2 N = \quad \frac{4}{3}\,|g|^2 N\,\frac{\kappa}{\kappa^2 + \Delta_C^2}\;, \tag{3.61}$$

the nuclear part of the reflection coefficient can be rewritten as

$$R_N \sim \frac{1}{\Delta - \Delta_{\mathrm{LS}} + \frac{i}{2}(\gamma + \gamma_S)}\;. \tag{3.62}$$

This shape is a Lorentzian which describes the response of an effective two-level system with transition frequency shifted by Δ_{LS} and spontaneous emission enhanced by γ_S. Consistent with our theoretical modeling, the two levels correspond to the collective ground and the collective excited state of the nuclear ensemble. Note that even though g is very small, the parameters Δ_{LS} and γ_S will generally be of importance due to the large number of nuclei $N \gg 1$.

The adiabatic elimination of the cavity modes revealed couplings between the nuclei mediated by the cavity, such that collective effects emerge. The spontaneous emission enhancement γ_S is the well-known superradiance, and the energy shift Δ_{LS} is a collective Lamb shift, both experimentally observed in Ref. [52]. We see that both quantities contain contributions depending on cavity parameters (δ_{LS}, ζ_S). These can be related to the Purcell effect [114], which is the enhancement of spontaneous emission due to the cavity environment. The other contributions describes the cooperative behavior, as evidenced by the scaling with N.

3.3.3 Numerical results

At this point it is instructive to discuss the actual values of the cavity parameters κ, κ_R, Δ_C and the coupling coefficient g. From the structure of Eq. (3.58) for the reflection coefficient, we note that the final result will be invariant under a rescaling ξ of the parameters κ, κ_R, Δ_C and $N|g|^2$. Using numerical data calculated by CONUSS [79, 80] for the cavity considered in Fig. 2.2 as a reference, we find that, consistent with our expectations from Eq. (3.7), Δ_C depends on the actual angle of incidence θ in the vicinity of the first order guided mode fulfilling the relation $\Delta_C = \delta_C \cdot \Delta\theta$, while all other parameters remain constant. In particular, we find the values (in units of γ) $\kappa = 45\xi$, $\kappa_R = 25\xi$, $\delta_C = -0.5\xi/\mu\mathrm{rad}$ and $\sqrt{N}|g| = \sqrt{1400\xi}$. By comparison of $\Delta_C = \delta_C \cdot \Delta\theta$ with Eq. (3.7), the actual value for the scaling factor can be determined as $\xi \approx 18000$. Note that this also justifies the adiabatic elimination performed in Sec. 3.2.1 since using the obtained parameters, we explicitly find $\kappa \gg \sqrt{N}|g|$.

A sustained motivation in cavity electrodynamics is the realization of the strong coupling regime, in which distinct quantum features such as vacuum Rabi splitting can be observed [2, 3, 146, 153]. It is encountered if the coupling strength g between an atom and a cavity mode exceeds the decay rates κ and γ of the system. In our cavity, though, this is not the case. Nevertheless, the so-called collective strong coupling regime is realized [154, 155], in which

$$\frac{|g|^2 N}{\kappa\,\gamma} \gg 1\;. \tag{3.63}$$

Hence, the phenomena observed in the cavity can thus be expected to be governed by cooperative effects.

The reflectance $|R|^2$ calculated from Eq. (3.58) is shown in Fig. 3.4. Note that the data shown in Fig. 3.4 does not contain any free scaling parameter, as the reflectance calculated from Eq. (3.58) automatically yields the experimentally accessible values in the range between 0 and 1. In the upper panel we qualitatively recover the shape of a typical electronic reflectivity curve across a single cavity resonance. To this end, we chose $\theta_0 = 2.96$ mrad which is also the angle of the first guided mode in Fig. 2.2. In addition, we set the detuning $\Delta = 10^3\gamma$ such that the nuclear part of the reflection is strongly suppressed and only the electronic part contributes. As a reference, we also show corresponding numerical results obtained with CONUSS. It is clearly visible that in the vicinity of the first guided mode our theory matches the numerical data

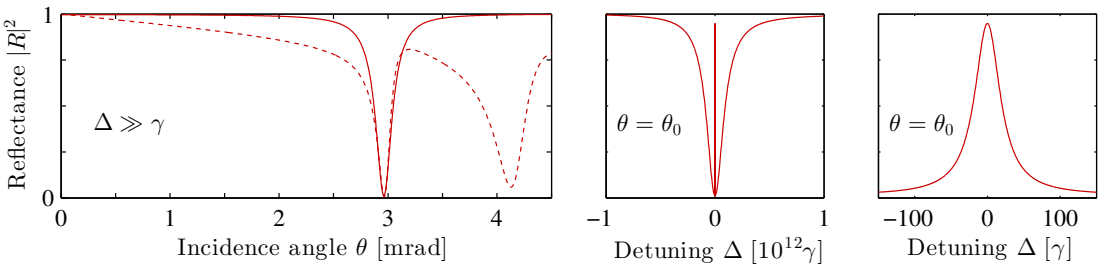

Figure 3.4: Reflectance of the cavity containing an unmagnetized ^{57}Fe layer. The first panel shows $|R|^2$ as a function of the grazing incidence angle θ. The nuclear part is strongly detuned such that only the electronic reflectivity curve is visible. Parameters as in the main text and $\theta_0 = 2.96$ mrad. The dashed line corresponds to the reflectivity curve from Fig. 2.2 calculated by CONUSS. The central panel shows the reflectance for fixed $\theta = \theta_0$. The narrow nuclear resonance is located in the center of the broad cavity resonance, where it appears as a sharp spike. The right panel shows a magnification of the central panel around the nuclear resonance. The nuclear spectrum is a Lorentzian which is significantly broadened due to superradiance.

calculated with CONUSS very well. Since we included only one guided mode in our calculation, only one minimum in the reflectivity curve is obtained instead of multiple dips in the CONUSS data. Also, an overall envelope of the reflection, which in reality drops to smaller values for angles larger than the critical angle of total reflection, is not included in the theory, but visible in the CONUSS data. We emphasize that in our theory the width of the guided mode depends on the order of the scaling parameter ξ. But since ξ was derived independently using Eq. (3.7), the proper width and the agreement with the numerical data serves also as a consistency check for our theory.

We now turn to the spectrum $|R(\Delta)|^2$ at the cavity resonance, i.e. $\theta = \theta_0$. We find that a variation of the detuning $\Delta = \omega - \omega_0$ also affects the cavity detuning Δ_C, since it depends on both ω and ω_0 explicitly, see Eq. (3.7). Therefore we rewrite Δ_C as a function of Δ and other constant parameters and show the results in the bottom panel of Fig. 3.4. In the bottom left panel we observe that the guided mode formed by the cavity affects the spectrum over a very large detuning range. Only in the center we observe the effect of the embedded nuclei, where the typical Lorentzian line shape of the nuclear resonance is found. A magnification of this nuclear response is shown in the bottom right panel. As expected from the theoretical predictions and in contrast to the resonance curve of a single ^{57}Fe nucleus in free space, it is significantly broadened due to superradiance and the Purcell effect captured in γ_S.

We conclude from our analysis that if one is only interested in spectral ranges several 10γ around the nuclear resonance, it is safe to assume that Δ_C is independent of Δ. The reason is that for any given angle θ, the cavity forms a nearly perfect flat background over the range of the nuclear response, as seen from Fig. 3.4. In the following work, the cavity detuning Δ_C will thus be treated as a constant parameter.

Finally, we note that Eq. (3.60) implies that the Lamb shift Δ_{LS} is zero for vanishing cavity detuning, which is also visible from the right panel in Fig. 3.4. This is in contrast to the experiment reported in Ref. [52], where a non-vanishing value was measured in an analogous setting. This puzzle of the Lamb shift will be solved in Chap. 4.

3.3.4 Conservation of probability

With the linear result for the reflectance at hand, we can now also turn to the transmission T in the waveguide. This observable was defined in Eq. (3.15) and from Eqs. (3.12) and (3.13) it can be seen that it is closely related to the reflection coefficient R. The differences are the absence of the reflection amplitude directly at the cavity surface and an overall scaling factor. In particular,

we find

$$R = \left(\frac{2\kappa_R}{\kappa + i\Delta_C} - 1\right) - i\,\frac{2\kappa_R}{(\kappa + i\Delta_C)^2}\,\frac{\frac{2}{3}|g|^2 N}{\Delta + i\frac{\gamma}{2} + \frac{2}{3}\frac{|g|^2 N}{\Delta_C - i\kappa}}\,, \tag{3.64}$$

$$T = \left(\frac{2\sqrt{\kappa_R \kappa_T}}{\kappa + i\Delta_C}\right) \quad - i\,\frac{2\sqrt{\kappa_R \kappa_T}}{(\kappa + i\Delta_C)^2}\,\frac{\frac{2}{3}|g|^2 N}{\Delta + i\frac{\gamma}{2} + \frac{2}{3}\frac{|g|^2 N}{\Delta_C - i\kappa}}\,. \tag{3.65}$$

At this point it should be verified, if the probability is conserved, i.e. the sum of the reflectance and the transmittance must not exceed unity. Computing the modulus squared of the expressions above, we indeed find

$$|R|^2 + |T|^2 = 1 - \frac{12\kappa_R\left[4|g|^2 N\gamma + 3(\gamma^2 + 4\Delta^2)(\kappa - \kappa_R - \kappa_T)\right]}{\left|6(\kappa + i\Delta_C)(\Delta + i\frac{\gamma}{2}) + 4i|g|^2 N\right|^2}\,. \tag{3.66}$$

Since $\kappa - \kappa_R - \kappa_T \geq 0$ as explained in Sec. 3.1.2, this implies

$$0 \leq |R|^2 + |T|^2 \leq 1\,. \tag{3.67}$$

The remaining fraction to unity corresponds to the light which is absorbed in the cavity material or emitted into other modes which were not considered here.

3.4 Emission spectrum after a δ-pulse excitation

In the sections above we derived the equations of motion which can be used to describe the cavity system in the linear regime for arbitrary magnetization of the ^{57}Fe layer. Using them, we are able to calculate the frequency dependence of the reflection spectrum. However, so far it is yet unclear if the results we derived above will directly compare to an realistic experimental setting and the calculated reflectance is accessible in an experiment. The crucial point is the following: Strictly speaking, we calculated the steady state, i.e. the system response at the time $t \to \infty$ and the cavity was assumed to be continuously driven under the influence of a monochromatic field with frequency ω.

This has to be compared to the situation encountered at current x-ray sources. They, in contrast, deliver only extremely short pulses in the ranges of a few 10 ps, even shorter pulse durations are achieved with free-electron lasers [15, 17]. At the same time, already the Fourier limit implies that these δ-like pulses do not consist of a single frequency, but provide very broad, nearly flat spectra over the energy range of the nuclear resonances. Therefore the steady state case with a monochromatic driving field is clearly not met in current experimental settings.

However, the steady state solutions directly compare to the emission spectrum $S(\omega)$ after an excitation with a δ-like pulse in the linear regime, as we will show in the following. Hence, they directly correspond to the situation which is accessible in current synchrotron experiments. The reason for this equivalence of the two types of spectra can be understood with the argument given below.

The incident δ-like pulse can be written as a superposition of plain waves of all frequencies ω, where we neglect prefactors for now. Operated in the linear regime, each of these plain waves will interact with the cavity separately. Since the individual plain waves monochromatic and correspond to a continuous wave, their reflection is given by the single frequency steady state solution calculated in the previous sections. Combining all the frequency components again, the steady state solution function $R_{\mathrm{SS}}(\omega)$ is obtained. On the other hand, the δ-pulse excitation of the cavity system causes the emission spectrum $S(\omega)$. Hence, the two quantities directly compare

to each other in the linear regime. This is also illustrated in the following visualization.

$$\begin{aligned}
&\overbrace{\delta(t)}^{\text{pulse}} && \rightarrow && \overbrace{R(\delta(t))}^{\text{interaction with cavity}} && \rightarrow && \overbrace{S(\omega)}^{\text{emission spectrum}} \\
&\propto \sum_\omega e^{i\omega t} && \rightarrow R\left(\sum_\omega e^{i\omega t}\right) \\
& && = \underbrace{\sum_\omega R\left(e^{i\omega t}\right)}_{\text{linearity}} && \rightarrow && \underbrace{R_{\mathrm{SS}}(\omega)}_{\text{steady state reflectance}}
\end{aligned}$$

Next to this intuitive picture on the agreement of the two spectra, it can be shown analytically that the general emission spectrum $S(\omega)$ reduces to the reflection spectra calculated via the steady state technique. This will be presented in the following.

Definition of the emission spectrum

Let us begin to define the emission spectrum properly. An exact definition often depends on the type of the conducted experiment and has been discussed in the literature quite extensively [156]. In the following we will shortly motivate the definition chosen here. The general definition of the time resolved reflection rate including non-linear effects (c.f. Sec. 8.1) is given by

$$\langle a_{\mathrm{out}}(t)^\dagger a_{\mathrm{out}}(t)\rangle \ , \tag{3.68}$$

and corresponds to the number of photons detected at time t. In order to obtain any information on the frequency behavior, it is necessary to transform the operators such as $a_{\mathrm{out}}(t)$ into Fourier space

$$a_{\mathrm{out}}(\omega) = \frac{1}{\sqrt{2\pi}} \int e^{i\omega t} a_{\mathrm{out}}(t)\, dt \ . \tag{3.69}$$

From this we can define

$$\langle a_{\mathrm{out}}(\omega)^\dagger a_{\mathrm{out}}(\omega)\rangle = \frac{1}{2\pi} \int e^{-i\omega(t_1-t_2)} \langle a_{\mathrm{out}}(t_1)^\dagger a_{\mathrm{out}}(t_2)\rangle\, dt_1 dt_2 \ . \tag{3.70}$$

In the spirit of Eq. (3.68), this expression corresponds to the number of photons with frequency ω and thus is a meaningful quantity for the emission spectrum. Note that $a_{\mathrm{out}}(\omega)^\dagger a_{\mathrm{out}}(\omega)$ is hermitian and hence the expectation value is a real number. Taking the Fourier transform of $\langle a_{\mathrm{out}}(t)^\dagger a_{\mathrm{out}}(t)\rangle$ directly will generally not result in a real value and therefore cannot be considered as an observable. This is connected to the fact, that also for the classical radiation field the amplitudes and not the intensities are required to transform between time and frequency domain. Hence, we use for the emission spectrum

$$S(\omega) = \langle a_{\mathrm{out}}(\omega)^\dagger a_{\mathrm{out}}(\omega)\rangle \ . \tag{3.71}$$

This choice is not restricted to continuous driving with monochromatic fields, but also holds for arbitrary incident pulse shapes. As mentioned before, the definition of the spectrum of a quantized field has been under debate, but Eq. (3.71) is considered appropriate for most situations [157]. The emission spectrum contains two-time expectation values, which need to be computed using more sophisticated techniques such as the quantum regression theorem [158]. Note that in the stationary case, the two-time expectation value depends only on the time difference $t_1 - t_2$. Then, the well known Wiener-Khintchine theorem for the power spectrum is obtained from Eq. (3.71) [157]. Note that the same definitions connected with input-output operators have been used also in previous studies [159].

Calculation of the emission spectrum in the linear regime

Let us now turn to an explicit analysis of the emission spectrum defined above. In the case of weak driving, i.e. the linear regime, the two-time average in Eq. (3.70) separates as

$$\langle a_{\mathrm{out}}(t_1)^\dagger a_{\mathrm{out}}(t_2)\rangle \approx \langle a_{\mathrm{out}}(t_1)^\dagger\rangle\langle a_{\mathrm{out}}(t_2)\rangle \ . \tag{3.72}$$

This well be discussed in more detail in Sec. 8.1 when we analyze the non-linear features in our model. With this approximation at hand, we obtain for the emission spectrum

$$S(\omega) = |\langle a_{\mathrm{out}}(\omega)\rangle|^2 \ . \tag{3.73}$$

However, we are more interested in the spectrum as a function in the detuning $\Delta = \omega - \omega_0$. Therefore we have to calculate

$$a_{\mathrm{out}}(\Delta) = \frac{1}{\sqrt{2\pi}} \int e^{i\Delta t} \tilde{a}_{\mathrm{out}}(t) dt \ , \tag{3.74}$$

with

$$\tilde{a}_{\mathrm{out}}(t) = a_{\mathrm{out}}(t) e^{i\omega_0 t} = -a_{\mathrm{in}}(t) e^{i\omega_0 t} + \sqrt{2\kappa_R} a(t) e^{i\omega_0 t} \ , \tag{3.75}$$

according to Eq. (3.12) and neglecting polarization dependence for the moment.

Next, we restrict our analysis to the case of a δ-like incident pulse

$$a_{\mathrm{in}}(t) = \tilde{a}_{\mathrm{in}} \delta(t) \ . \tag{3.76}$$

Since this pulse does not have a well-defined cw-frequency ω, we need to alter the transformation Hamiltonian for the interaction picture in Eq. (3.18) from our model by replacing ω by ω_0. As a consequence, $\Delta = 0$ and $\Delta_C = \omega_C - \omega_0$ now holds. In this interaction picture we now obtain for the input-output relation

$$\tilde{a}_{\mathrm{out}}(t) = -\tilde{a}_{\mathrm{in}} \delta(t) + \sqrt{2\kappa_R} a(t) \ , \tag{3.77}$$

where we have used that $\delta(t) = \delta(t) e^{i\omega_0 t}$.

Assuming that the cavity equilibrates much faster than the nuclear dynamics changes, we can again eliminate the cavity modes adiabatically and obtain (c.f. Eq. (3.52))

$$\begin{aligned} \langle \tilde{a}_{\mathrm{out}}(t)\rangle &= -\tilde{a}_{\mathrm{in}} \delta(t) + \sqrt{2\kappa_R} \langle a(t)\rangle \\ &= \left(\frac{2\kappa_R}{\kappa + i\Delta_C} - 1 \right) (\hat{\boldsymbol{a}}^*_{\mathrm{out}} \cdot \hat{\boldsymbol{a}}_{\mathrm{in}}) \tilde{a}_{\mathrm{in}} \delta(t) \\ &\quad - i \frac{\sqrt{2\kappa_R}}{\kappa + i\Delta_C} g^* \sum_\mu \left(\hat{\boldsymbol{a}}^*_{\mathrm{out}} \cdot \mathbb{1}_\perp \cdot \hat{\boldsymbol{d}}_\mu \right) c_\mu \sqrt{N_{\mu_g}} \langle E^{(+)}_\mu | \rho(t) | G \rangle \ . \end{aligned} \tag{3.78}$$

For simplicity, we rewrite this equation in vector representation

$$\langle \tilde{a}_{\mathrm{out}}(t)\rangle = A \, \tilde{a}_{\mathrm{in}} \delta(t) + \vec{B} \cdot \vec{\rho}(t) \ , \tag{3.79}$$

where $\vec{\rho}(t)$ consists of six, i.e. the number of transitions, elements

$$[\vec{\rho}(t)]_\mu = \langle E^{(+)}_\mu | \rho(t) | G \rangle \ . \tag{3.80}$$

Now we need to solve for $\vec{\rho}(t)$. As this vector contains only coherences, its initial value vanishes, $\vec{\rho}(0) = 0$. Using the effective Hamiltonian and the effective Lindblad operators obtained from the adiabatic elimination, we can set up the equations of motion for the coherences. These equations of motion are identical to those in the steady state scenario, however, with the following

differences. First, the driving field a_{in} is to be replaced by $\tilde{a}_{\text{in}}\delta(t)$ and as we discussed before, it is $\Delta = 0$ and $\Delta_C = \omega_C - \omega_0$. The equations in vector representation take the form

$$\frac{d}{dt}\vec{\rho}(t) = M \cdot \vec{\rho}(t) + \vec{K}\,\tilde{a}_{\text{in}}\delta(t)\;, \tag{3.81}$$

where M is a matrix of size 6×6. We see that all time dependence is only contained in the inhomogeneous part of the equation in terms of a δ-function. This makes it possible to solve for the spectrum analytically. We recall that we are interested in the expression $\langle a_{\text{out}}(\Delta)\rangle$ defined in Eq. (3.74). We find

$$\begin{aligned}\langle a_{\text{out}}(\Delta)\rangle &= \frac{1}{\sqrt{2\pi}}\int e^{i\Delta t}\langle\tilde{a}_{\text{out}}(t)\rangle dt \\ &= \frac{1}{\sqrt{2\pi}}\int e^{i\Delta t}\left(A\,\tilde{a}_{\text{in}}\delta(t) + \vec{B}\cdot\vec{\rho}(t)\right)dt \\ &= \frac{A\tilde{a}_{\text{in}}}{\sqrt{2\pi}} + \frac{1}{\sqrt{2\pi}}\,\vec{B}\cdot\int e^{i\Delta t}\vec{\rho}(t)dt\;.\end{aligned} \tag{3.82}$$

To evaluate the integral we utilize the Laplace transform

$$\mathcal{L}\{f(t)\}(s) = \int_0^\infty f(t)e^{-st}dt\;, \tag{3.83}$$

which has the property

$$\mathcal{L}\{\tfrac{d}{dt}f(t)\}(s) = s\mathcal{L}\{f(t)\}(s) - f(0)\;. \tag{3.84}$$

Together with Eq. (3.81), we obtain

$$\mathcal{L}\{\tfrac{d}{dt}\vec{\rho}(t)\}(s) = s\mathcal{L}\{\vec{\rho}(t)\}(s) = M\cdot\mathcal{L}\{\vec{\rho}(t)\}(s) + \vec{K}\tilde{a}_{\text{in}}\;, \tag{3.85}$$

such that

$$\mathcal{L}\{\vec{\rho}(t)\}(s) = (s\mathbb{1} - M)^{-1}\cdot\vec{K}\tilde{a}_{\text{in}}\;. \tag{3.86}$$

Noting that $\vec{\rho}(t) = 0$ for $t \le 0$, we can identify the integral in Eq. (3.82) with $\mathcal{L}\{\vec{\rho}(t)\}(-i\Delta)$ and we obtain

$$\langle a_{\text{out}}(\Delta)\rangle = \frac{A\tilde{a}_{\text{in}}}{\sqrt{2\pi}} + \frac{\tilde{a}_{\text{in}}}{\sqrt{2\pi}}\,\vec{B}\cdot\left[-(i\Delta\mathbb{1} + M)^{-1}\cdot\vec{K}\right]\;. \tag{3.87}$$

Normalizing this spectral expression accordingly with

$$a_{\text{in}}(\Delta) = \frac{1}{\sqrt{2\pi}}\int e^{i\Delta t}a_{\text{in}}(t)dt = \frac{\tilde{a}_{\text{in}}}{\sqrt{2\pi}} \tag{3.88}$$

yields the reflectance after an δ-pulse excitation

$$R_\delta(\Delta) = \frac{\langle a_{\text{out}}(\Delta)\rangle}{a_{\text{in}}(\Delta)} = A + \vec{B}\cdot\left[-(i\Delta\mathbb{1} + M)^{-1}\cdot\vec{K}\right]\;. \tag{3.89}$$

In particular, we see that the driving field strength $\tilde{a}_{\text{in}}$ cancels, which is expected for the linear regime we are considering.

Comparison with the steady state reflectance

Let us now compare this result with the steady state solutions we calculated before. For this, let us write the reflectance in a similar form as we did for the δ-pulse case (c.f. Eq. (3.79))

$$R_{\mathrm{SS}}(\Delta) = \frac{\langle a_{\mathrm{out}} \rangle}{a_{\mathrm{in}}} = A + \frac{\vec{B} \cdot \vec{\rho}_{\mathrm{SS}}(\Delta)}{a_{\mathrm{in}}} \ . \tag{3.90}$$

At the same time, we can formally write the equations of motion in vector representation as well. However, in contrast to Eq. (3.81), we need to take into account the detuning Δ which does not vanish in the steady state analysis. Since the detuning acts only on the elements itself and does not couple different coherences, it can be included as an additional diagonal term

$$\frac{d}{dt}\vec{\rho}_{\mathrm{SS}} = (M + i\Delta\mathbb{1}) \cdot \vec{\rho}_{\mathrm{SS}} + \vec{K}\, a_{\mathrm{in}} \ . \tag{3.91}$$

Note that in the equations above, A, $\vec{B}$, M and $\vec{K}$ are identical to the variables defined in the analysis for the δ-pulse spectrum. The steady state of the coherences can now readily be solved as

$$\vec{\rho}_{\mathrm{SS}}(\Delta) = -\left(M + i\Delta\mathbb{1}\right)^{-1} \cdot \vec{K}\, a_{\mathrm{in}} \ , \tag{3.92}$$

which finally yields

$$R_{\mathrm{SS}}(\Delta) = \frac{\langle a_{\mathrm{out}} \rangle}{a_{\mathrm{in}}} = A + \vec{B} \cdot \left[-\left(M + i\Delta\mathbb{1}\right)^{-1} \cdot \vec{K} \right] \ . \tag{3.93}$$

Comparing Eq. (3.89) and Eq. (3.93), it can be seen that the same result is obtained in both cases and therefore

$$R_{\mathrm{SS}}(\Delta) = R_{\delta}(\Delta) \tag{3.94}$$

in the linear regime. This shows that a simple steady state analysis can be performed instead of a more complicated time integration of the equations of motion and justifies the calculation technique performed in many parts of this work.

Chapter 4

Fano Line Shape Control & Interferometric Phase Detection

The deterministic control of light-matter interactions is a longstanding vision with key challenges and applications across all natural sciences. Close to resonances in matter, characteristic spectroscopic signatures are imprinted onto the radiation field. For an isolated system with a single line resonance, this is the well-known Lorentzian profile given by the formula

$$\sigma_{\mathrm{Lorentz}} \propto \frac{1}{1+\epsilon^2} \,, \tag{4.1}$$

where ϵ denotes the energy detuning from the resonance in units of its transition width. In high-energy physics the same shape is known as Breit-Wigner distribution. But as soon as the probed system evolves on different indistinguishable quantum pathways, the line shape is modified by interference. In particular, asymmetric Fano resonances [160] arise if a spectrally broad continuum quantum-mechanically interferes with a spectrally narrow bound state, which is provided by a matter resonance. Fano profiles are parameterized by the simple expression

$$\sigma_{\mathrm{Fano}} \propto \frac{(q+\epsilon)^2}{1+\epsilon^2} \,. \tag{4.2}$$

Determined by the parameter q, both symmetric and antisymmetric line shapes can be engineered, possibly with very narrow characteristics.

Fano resonances have been predicted already in 1935 [161] and by now are recognized as important tool across many disciplines such as atomic physics [162–165], solid-state physics [166–170], and nuclear physics [171]. Recently, it was demonstrated that Fano interferences can be interpreted in the time domain, which paves a way for the active and dynamical control of spectroscopic line shapes [172].

A notable platform to study Fano resonances in the optical regime is the setting of waveguide and cavity systems [169, 170, 173], where the continuum channel necessary for the interference is straightforwardly provided. This suggests, that Fano interference might arise as well in the x-ray domain using thin-film cavities.

Asymmetric line shapes for nuclear resonances at x-ray energies have previously been predicted or observed [83, 85, 174–179]. However, they were neither analyzed or interpreted in the context of Fano line shapes, nor was it clear whether the line shapes are Fano profiles at all.

In this chapter, we show that they are and demonstrate Fano line-shape control in the interaction of Mössbauer nuclei in thin-film cavities. For this, we apply the quantum optical formalism developed in Chap. 3 and theoretically show how Fano profiles can arise and how they can be controlled dynamically. We then discuss the implementation, which we used to experimentally explore the Fano line shapes together with the group of Ralf Röhlsberger, Hans-Christian Wille (both from DESY, Hamburg), Thomas Pfeifer and Christian Ott (MPIK, Heidelberg).

In a first application, we extract spectroscopic signatures such as the cooperative Lamb shift from the data, highlighting their dynamical aspects. Based on these signatures, we are able to understand the thin-film cavities in greater detail and find how they can be modeled with even higher accuracy. In this course, the Lamb shift observed in the spectra is understood in more

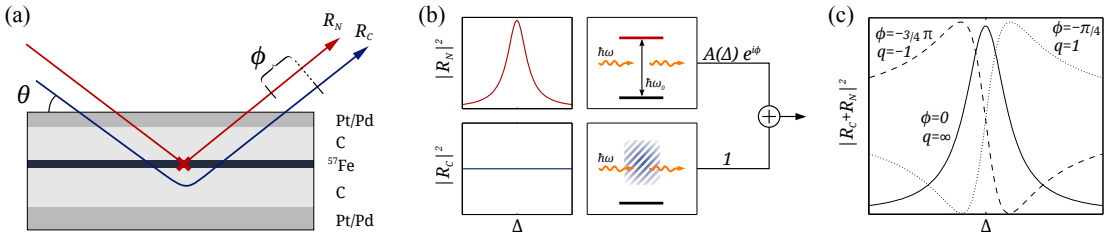

Figure 4.1: Schematic setup and origin of the Fano interference. (a) X-ray light is reflected by a thin-film cavity under a grazing angle θ. The Pt/Pd layers act as cavity mirrors and C as the guiding layer. The reflection by the empty cavity (R_C, blue) and from the embedded ^{57}Fe nuclei in the center (R_N, red) have a phase difference ϕ which can be controlled via the incidence angle θ. (b) The empty-cavity reflection forms a broad spectral continuum ("1", bottom), whereas the isolated "bound state" nuclear response $A(\Delta)$ (top) is of Lorentzian shape. (c) The interference of these two paths leads to Fano line shapes, with asymmetry controlled by the phase ϕ.

detail. In a second application we demonstrate how the measured Fano spectra can be employed to perform phase sensitive measurements of the nuclear resonances, which constitutes a first step towards state tomography in the x-ray energy domain.

4.1 Fano line shape control

The general scheme which we discuss in the following is illustrated in Fig. 4.1. Resonant ^{57}Fe nuclei are placed in the x-ray cavity and the spectral response of the nuclei in the light reflected in grazing incidence off the cavity is observed. To motivate this setup, we start with an intuitive picture.

We interpret our cavity as an interferometer, since the x-ray reflectance can be divided into two pathways as depicted in Fig. 4.1. In the first path, the light is reflected by the cavity alone. This path acts as the continuum channel independent of the frequency on the scale of the spectrally narrow Mössbauer absorption. In the second path, the x-rays interact with the resonant nuclei. This leads to a Lorentzian reflection amplitude and acts as the bound state channel. Under these conditions, the total reflectance can be written as

$$|R|^2 \propto \left|1 + e^{i\phi} A(\Delta)\right|^2 , \tag{4.3}$$

where $A(\Delta)$ is a complex Lorentzian amplitude and $\Delta = \omega - \omega_0$ is the frequency detuning between x-ray frequency ω and nuclear resonance frequency ω_0. Generally, these two channels have a phase difference, which we will denote as ϕ in the following. Such a relative phase can directly be mapped to the Fano q asymmetry parameter, which in turn determines the shape of the resonance [172]. Thus, if the continuum contribution, formed by electronic scattering of the cavity, interferes with the Lorentzian nuclear bound state contribution, we can expect to observe Fano line shapes. Controlling the relative phase ϕ in an experiment would further allow dynamical control of the line profile.

4.1.1 Theoretical description

Let us now continue with a more elaborated theoretical analysis. The distribution into the two pathways introduced above can also be motivated theoretically. In Chap. 3 the reflection amplitude for a single layer of unmagnetized ^{57}Fe nuclei in the cavity has already been calculated.

There, we found for the complex reflection coefficient $R = R_C + R_N$ with (c.f. Eq. (3.58))

$$R_C = \frac{2\kappa_R}{\kappa + i\Delta_C} - 1 \,, \tag{4.4}$$

$$R_N = -i\,\frac{2\kappa_R}{(\kappa + i\Delta_C)^2}\,\frac{\frac{2}{3}|g|^2 N}{\Delta + i\frac{\gamma}{2} + \frac{2}{3}\frac{|g|^2 N}{\Delta_C - i\kappa}} \,. \tag{4.5}$$

Here, the first term R_C characterizes the scattering from the cavity in the absence of nuclei, the second term R_N accounts for the nuclear part of the reflection. This shows that the reflection spectrum indeed consists of the interference signal between a continuum channel and a bound state contribution as required for Fano interference. However, at this stage it is not yet clear if the line shape also resembles the formula from Eq. (4.2), which is the signature for the Fano profile.

To address this question, we rewrite the reflectance in terms of the dimensionless energy ϵ in a first step. In our case, though, the nuclear response is modified by cooperative phenomena. The bound state Lorentzian is not centered on the nuclear resonance, but shifted by the collective Lamb shift. Moreover, its width is superradiantly broadened from the natural line width. Hence, we correct for the collective Lamb shift and the enhanced decay rate in the definition of the scaled energy ϵ. Furthermore, we specialize to the critical coupling condition ($2\kappa_R = \kappa$, see Sec. 3.3.1), which can be implemented experimentally, e.g., by adjusting the thickness of the topmost layer of the cavity. Doing so, we obtain the reflectance

$$|R|^2 = \frac{|\epsilon + q|^2}{1 + \epsilon^2}\,\sigma_0 \tag{4.6}$$

with

$$\epsilon = \frac{\Delta - \Delta_{\mathrm{LS}}}{\Gamma/2} \,, \tag{4.7}$$

$$q = \frac{\Gamma - \gamma}{\Gamma}\,\frac{\kappa}{\Delta_C} + i\,\frac{\gamma}{\Gamma} \,, \tag{4.8}$$

$$\sigma_0 = (1 + \kappa^2/\Delta_C^2)^{-1} \,, \tag{4.9}$$

$$\Delta_{\mathrm{LS}} = -\frac{2}{3}\,\frac{|g|^2 N\,\Delta_C}{\kappa^2 + \Delta_C^2} \,, \tag{4.10}$$

$$\Gamma = \gamma + \frac{4}{3}\,\frac{|g|^2 N\,\kappa}{\kappa^2 + \Delta_C^2} \,. \tag{4.11}$$

This resembles exactly the anticipated expression for a Fano resonance. Note that q has an imaginary component, which corresponds to an incoherent loss channel [180, 181]. We emphasize that in the strongly superradiant case $\Gamma \gg \gamma$ the loss channels can be neglected, such that an ideal implementation of the Fano model is achieved. In contrast, in the opposite limit $\Gamma \approx \gamma$, without enhancement of the spectral line width, $|R|^2 \approx \sigma_0$ without any spectral signatures. It is therefore the collectively enhanced decay rate which enables the Fano implementation with full visibility of the reflectance modulation.

In the intuitive interferometric picture developed above, we used that the continuum and the bound state reflection channel have a phase difference ϕ which determines the asymmetry of the spectral profile. Relating the Fano q parameter and the relative phase as $\phi = \arg(q - i)$, we can rewrite the reflectance to

$$|R|^2 = \left|1 + \, e^{i\phi}\,\frac{|q - i|}{\epsilon + i}\right|^2 \sigma_0 \,. \tag{4.12}$$

This form resembles the interferometric model anticipated above and illustrated in Fig. 4.1, in which a broad continuum channel ("1") interferes with a Lorentzian bound state amplitude formed by the ensemble of nuclei, controlled via the phase ϕ.

Table 4.1: Equivalent notations for the cavity reflection coefficient in the absence of a magnetic field, the reflectance and their respective interpretation. The coefficients are given in Tabs. 4.2 and 4.3.

Interpretation	R	$\lvert R\rvert^2$
Quantum optical theory	$R_C - i\frac{2\kappa_R}{(\kappa+i\Delta_C)^2}\frac{\frac{2}{3}\lvert g\rvert^2 N}{\Delta + i\frac{\gamma}{2} + \frac{2}{3}\frac{\lvert g\rvert^2 N}{\Delta_C - i\kappa}}$ $R_C - ia_0 e^{i\phi_0}\frac{1}{\epsilon+i}$	
Fano spectrum	$-ia_0 e^{i\phi_0}\left(\frac{1}{q-i}+\frac{1}{\epsilon+i}\right)$ $-i\frac{a_0}{a_1}e^{i\phi_0}\left(e^{-i\phi}+\frac{a_1}{\epsilon+i}\right)$	$\frac{a_0^2}{a_1^2}\frac{\lvert q+\epsilon\rvert^2}{1+\epsilon^2}$
Interferometer	$-ia_0 e^{i\phi_0}\left(\frac{1}{a_1}e^{-i\phi} + a_N e^{i\phi_N}\right)$	$a_0^2\left(a_1^{-2} + a_N^2 + 2\frac{a_N}{a_1}\cos(\phi+\phi_N)\right)$

Table 4.2: Coefficients in Tab. 4.1 for different parameter regimes.

Model assumptions	R_C	q
no dispersion[1], critical coupling[2], no incoherent loss[3]	$-1+\frac{\kappa}{\kappa+i\Delta_C}$	$\frac{\kappa}{\Delta_C}$
no dispersion[1], critical coupling[2]	$-1+\frac{\kappa}{\kappa+i\Delta_C}$	$\frac{\Gamma-\gamma}{\Gamma}\frac{\kappa}{\Delta_C}+i\frac{\gamma}{\Gamma}$
no dispersion[1]	$-1+\frac{2\kappa_R}{\kappa+i\Delta_C}$	$i+ia_0\frac{\kappa-i\Delta_C}{\kappa-2\kappa_R+i\Delta_C}$
with dispersion, $R_C(\theta_{\min})=0$	$-\frac{2\kappa_R}{\kappa+i\Delta_{C,\min}}+\frac{2\kappa_R}{\kappa+i\Delta_C}$	$\frac{\Gamma-\gamma}{\Gamma}\frac{\kappa^2+\Delta_C\Delta_{C,\min}}{\kappa(\Delta_C-\Delta_{C,\min})}+i\frac{\gamma}{\Gamma}$

Table 4.3: Global variables in Tabs. 4.1 and 4.2.

$a_0 = \frac{2\kappa_R}{\kappa}\frac{\Gamma-\gamma}{\Gamma}$	$a_1 = \lvert q-i\rvert$	$a_N = \frac{1}{\sqrt{1+\epsilon^2}}$
$\phi_0 = 2\arg\left(\frac{\kappa}{\Delta_C}-i\right)$	$\phi = \arg(q-i)$	$\phi_N = \arg(\epsilon-i)$
$\epsilon = \frac{\Delta-\Delta_{\mathrm{LS}}}{\Gamma/2}$	$\Delta_{\mathrm{LS}} = -\frac{2}{3}\frac{\lvert g\rvert^2 N\,\Delta_C}{\kappa^2+\Delta_C^2}$	$\Gamma = \gamma + \frac{4}{3}\frac{\lvert g\rvert^2 N\,\kappa}{\kappa^2+\Delta_C^2}$
$\Delta_C = \delta_C(\theta-\theta_0)$	$\Delta_{C,\min} = \delta_C(\theta_{\min}-\theta_0)$	

[1] $\theta_0 = \theta_{\min}, \Delta_{C,\min} = 0$
[2] $2\kappa_R = \kappa$
[3] $\Gamma \gg \gamma$

A broader overview of the different forms for the reflection coefficient with their respective interpretation is given in Tab. 4.1.

A similar phase mapping between the Fano q parameter and the phase ϕ was found in Ref. [172], where absorption lines of auto-ionizing helium have been studied. However, it is different by a factor 2 from the relation found here. The reason for this is that, in contrast to Ref. [172], our continuum is not the free space vacuum, but situated in a cavity environment. The cavity vacuum contribution to the reflectance also undergoes a phase shift upon a change of the incidence angle, and thus the relative phase is reduced, as we will briefly show in the following. For simplicity, we restrict to the superradiant limit $\Gamma \gg \gamma$, such that $q = \kappa/\Delta_C$ and $\phi = \arg(\frac{\kappa}{\Delta_C} - i)$. Starting from Eqs. (4.4) and (4.5), we find for the cavity continuum channel R_C and the nuclear bound state contribution R_N

$$R_C = -i\frac{1}{q+i} \qquad = -i\, e^{i\phi}\, \frac{1}{\sqrt{1+q^2}}\,, \tag{4.13}$$

$$R_N = -i\, \frac{q-i}{q+i}\, \frac{1}{\epsilon+i} = -i\, e^{2i\phi}\, \frac{1}{\epsilon+i}\,. \tag{4.14}$$

From this we observe that the phase of the continuum path is shifted by ϕ, whereas the nuclear contribution experiences a phase shift which is twice as large. Therefore, in our setup the relative phase between the two channels is ϕ.

This Fano phase and, equivalently, the q parameter defined in Eq. (4.8) depends on the cavity detuning Δ_C. Close to the cavity eigenmode resonance at $\Delta_C = 0$, one can linearize $\Delta_C \approx \delta_C \cdot \Delta\theta_0$, where $\Delta\theta_0 = \theta - \theta_0$ is the deviation of the incidence angle θ from the angle θ_0 at which the cavity mode is driven resonantly. According to our theoretical model developed in Chap. 3, θ_0 is also the angle $\theta_{\min}$ at which the cavity reflectance would vanish in the absence of any resonant nuclei. We will see later that this is not always the case and requires an extended description of the cavity reflection amplitude. In any case, the fact that the incidence angle θ enters the Fano q parameter, remains. Hence, it can be used to control the Fano line shape. We note that a change in the incidence angle also modifies the cooperative Lamb shift Δ_{LS} and the superradiant transition width Γ, since a variation of the incidence angle θ leads to a different initial excitation imprinted on the nuclei by the probing x-ray field [51, 112, 179].

4.1.2 Experimental realization

Guided by the group of Ralf Röhlsberger and Hans-Christian Wille (DESY, Hamburg) and together with Thomas Pfeifer and Christian Ott (MPIK, Heidelberg), we have experimentally explored the nuclear Fano line shape control at the Dynamics Beamline P01 of the PETRA III synchrotron radiation source (DESY, Hamburg) [95]. Since the interferometric nature suggests a dependence of the line profile on the optical material constants, the group of Ralf Röhlsberger prepared two cavities with Pt and Pd as mirror materials, respectively (see Fig. 4.1).

We employed nuclear resonant scattering, where a short broadband incident pulse excites the nuclei, and subsequently the delayed scattered photons are detected in a time window $40-190$ ns after excitation. Far-off-resonant background photons are suppressed using a high-resolution monochromator for the incident light. To record the spectrum of the scattered light, a spectrally narrow resonant absorber foil (consisting of a 6 μm thick stainless steel foil enriched to 95% in ^{57}Fe) was used, which was scanned in energy across the nuclear resonance with the help of a Doppler drive as described in more detail in Sec. 6.1.

Cavity 1 is formed by a Pt(2.1 nm)/C(32 nm)/Pt(12 nm) (top to bottom) layer system with the Pt layers acting as the mirrors and the C as guiding layer. A 1.2 nm thick active layer of ^{57}Fe was placed in the center of the carbon layer. Cavity 2 is a Pd(4 nm)/C(36 nm)/Pd(14 nm) layer system, with a 1.2 nm thick ^{57}Fe layer in the center.

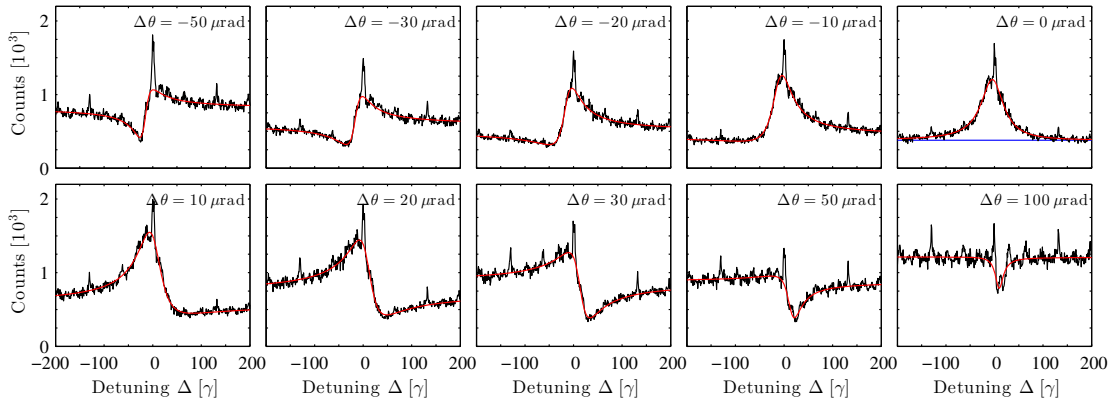

(a) Spectra for cavity 1

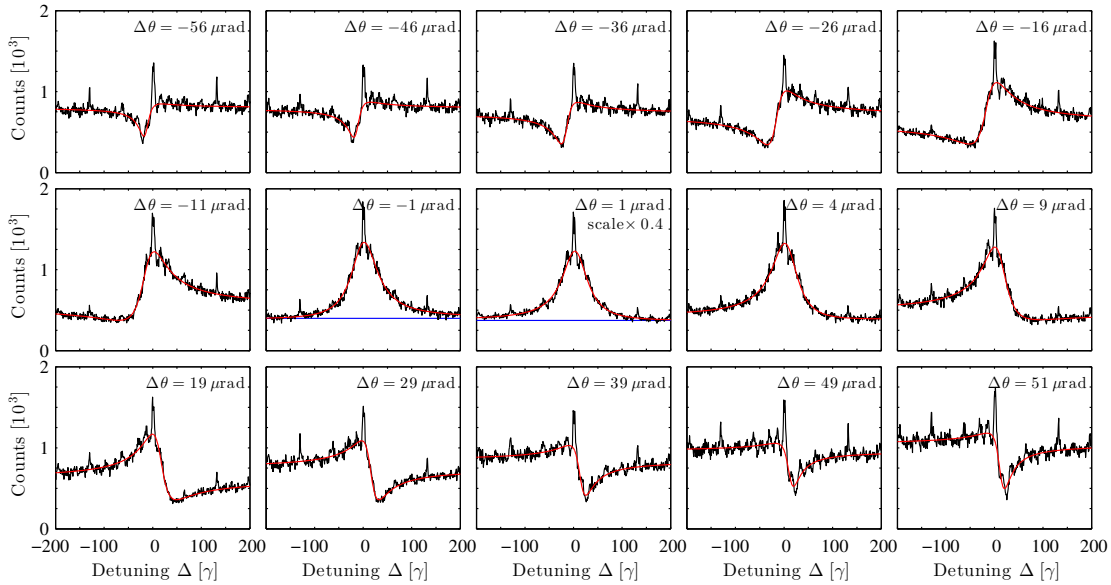

(b) Spectra for cavity 2

Figure 4.2: Fano line shape control with nuclei. The different panels show the reflected intensity at different relative incidence angles $\Delta\theta = \theta - \theta_{\min}$ of the probing x-ray field. A Lorentzian shape is obtained for $\Delta\theta \approx 0$ μrad. Asymmetric Fano line shapes are observed away from $\theta_{\min}$. The narrow spikes at $\Delta \approx 0$ and $\pm 130\gamma$ visible in all panels are artifacts of the measurement procedure. Note that unnormalized experimental raw data is shown without baseline subtraction. Therefore the intensities in the different panels cannot directly be compared. Black lines show experimental data, overlayed red curves are theory fits. The blue horizontal lines at $\Delta\theta \approx 0$ μrad serve as a guide to the eye and indicate the slight asymmetry of the line shapes.

Results

Experimentally recorded spectra for cavity 1 and 2 are shown in Figs. 4.2(a) and 4.2(b), respectively. In both cases, the reflection spectra were measured for several incidence angles θ around $\theta = \theta_{\min}$, where the cavity reflectance assumes a deep minimum at frequencies far off the nuclear resonance.

Clearly, the incidence angle acts as a knob to control the spectral response from a Lorentzian shape for $\theta = \theta_{\min}$ to strongly asymmetric line shapes. Already at $\Delta\theta \approx 50$ μrad, almost inverted line shapes are observed.

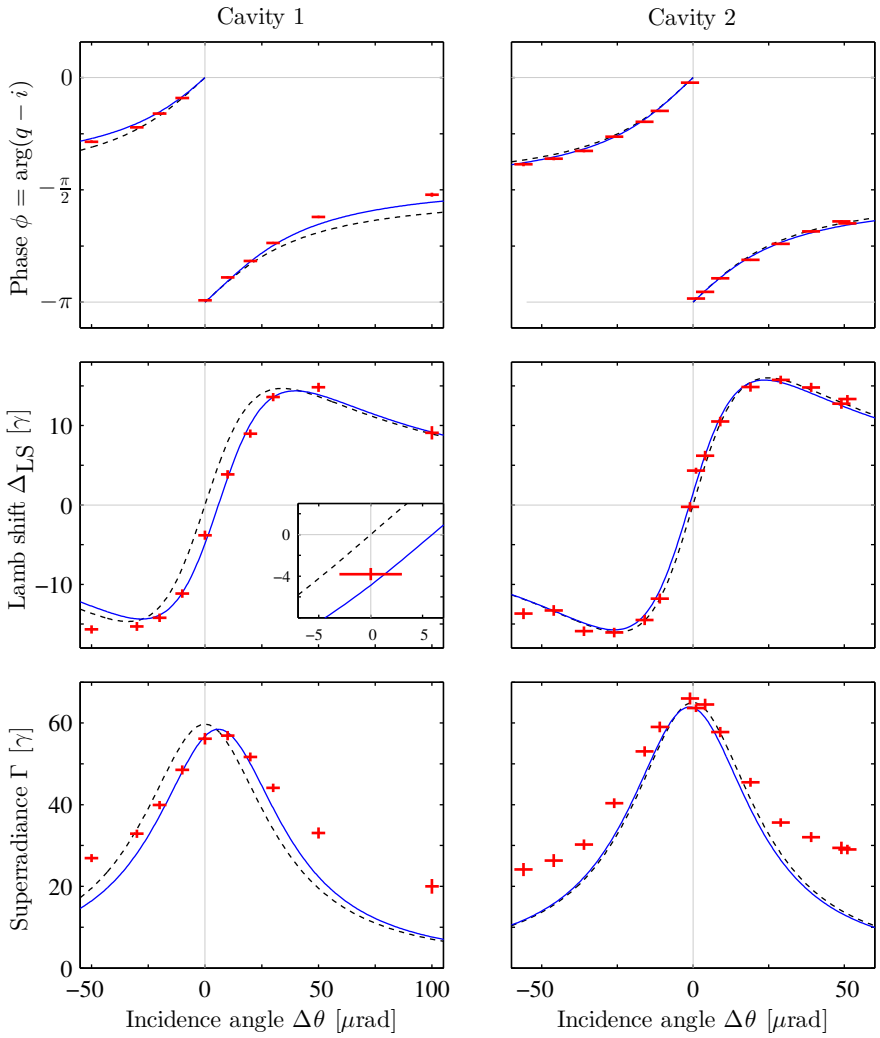

Figure 4.3: Fano q parameter characterizing the line shape, cooperative Lamb shift Δ_{LS}, and superradiant line broadening Γ as a function of the relative incidence angle $\Delta\theta = \theta - \theta_{\mathrm{min}}$. Left [right] panel shows results for cavity 1 [cavity 2]. Red dots are experimental data, extracted by fitting the generic Fano line shape Eq. (4.15). Dashed black lines show theoretical predictions from Eqs. (4.8), (4.10) and (4.11) assuming $\theta_{\mathrm{min}} = \theta_0$. Solid blue lines show the predictions of the theory including a cavity dispersion phase. The inset shows the non-vanishing Lamb shift at θ_{min} for cavity 1 in more detail.

For a quantitative analysis of the experimental data, we fitted a generic Fano profile

$$|R|^2 = a + b\,\frac{(q+\epsilon)^2}{1+\epsilon^2}\,, \quad \epsilon = \frac{\Delta - \Delta_{\mathrm{LS}}}{\Gamma/2} \tag{4.15}$$

with free parameters $\{a, b, q, \Delta_{\mathrm{LS}}, \Gamma\}$ to each experimentally recorded spectrum. This form is independent of our theoretical model and only assumes a generic Fano profile. Each fit was repeated multiple times with randomly modified initial parameters to avoid bias, and the respective results are indistinguishable within their error bars.

Clearly, these fits match the measured spectra very well, as seen from the red theory curves in Figs. 4.2(a) and 4.2(b). But beyond the agreement of the fits with the overall spectral shape, we can employ the fits to determine the superradiant decay width Γ, the cooperative Lamb shift

Δ_{LS}, as well as the Fano q parameter as a function of the incidence angle θ independent of our theoretical model.

In Fig. 4.3, we compare these experimental results (red) with the theoretical predictions from Eqs. (4.8), (4.10) and (4.11) (gray dashed lines). The error bars along ordinates are 95% CL fit errors, along abscissae an angular uncertainty of ± 3 μrad accommodates for systematic uncertainties in the experimental setting. Generally, the measured parameters have the same angular dependency as the quantum optical theory predicts. For cavity 2, the agreement is very good, whereas for cavity 1, the predictions for the superradiance and the cooperative Lamb shift appear to have a systematic shift compared to the measured data. In particular, as shown in the inset, cavity 1 has a non-vanishing Lamb shift at $\Delta\theta = 0$, whereas the theory from Eq. (4.10) predicts $\Delta_{\mathrm{LS}} = 0$. This is also related to the puzzle why a non-zero value for the Lamb shift was measured for the Lorentz spectrum in Ref. [52]. As we will show in the next sections, this effect is caused by the material dispersion and strongly depends on the choice of the mirror material of the cavity.

But before we turn to this problem, we first comment on the deviations for the superradiant decay width Γ at large incidence angles in Fig. 4.3. Here, the experimental data apparently show a tendency to much broader resonance lines. However, these values were obtained form the fits and as one can see from Figs. 4.2(a) and 4.2(b), for large $\Delta\theta$ the recorded spectra are superimposed with an oscillatory structure. The reason for this is that in order to measure the cavity spectra, a stainless steel foil is required as detection device (c.f. Sec. 6.1). Especially for large $\Delta\theta$ interferences between the scattering paths of this device and the cavity become prominent. As soon as their oscillation period is comparable with the tiny spectroscopic signature of the Fano line shape, these two structures overlap and the Fano resonance cannot unambiguously be identified anymore. Hence, the discrepancy is largely caused by the detection method. In Sec. 6.4.2 we will provide an alternative approach for obtaining spectral properties from the data in these cases.

4.1.3 Influence of additional cavity dispersion phases

In the last section we have seen that the experimentally determined values for the Lamb shift and the superradiant enhancement are systematically shifted from the theory predictions in the case of cavity 1, whereas for cavity 2 no shift is visible. Since the main difference of the two cavities employed in the experiment is the choice of the mirror materials, platinum and palladium, respectively, this suggests that their material properties are crucial for the observed effect. In the following, we will show that the shift can be explained in terms of an additional material depended phase in one of the reflection channels.

Asymmetric empty-cavity line shapes

We begin with the analysis be considering the reflection curves in more detail. In Fig. 4.4 the cavity reflection in the absence of resonant nuclei is shown as a function of the incidence angle θ.

It is readily seen that the response of cavity 1 is asymmetric around the reflection minimum, whereas that of cavity 2 is almost symmetric. This was observed in the experiment and also confirmed by numerical calculations using CONUSS [79, 80]. On the other hand, however, the quantum optical theory we used so far, always predicts a symmetric behavior, since from Eq. (4.4) and $\Delta_C = \delta_C(\theta - \theta_0)$ (c.f. Eq. (3.7)) we find

$$|R_C(\theta)|^2 = 1 - \frac{4\kappa_R(\kappa - \kappa_R)}{\kappa^2 + \delta_C^2(\theta - \theta_0)^2} \,. \tag{4.16}$$

Clearly, this does not match the asymmetric reflection curve for cavity 1, as indicated in Fig. 4.4. Hence, we need to extend our quantum optical theory to properly cover this aspect.

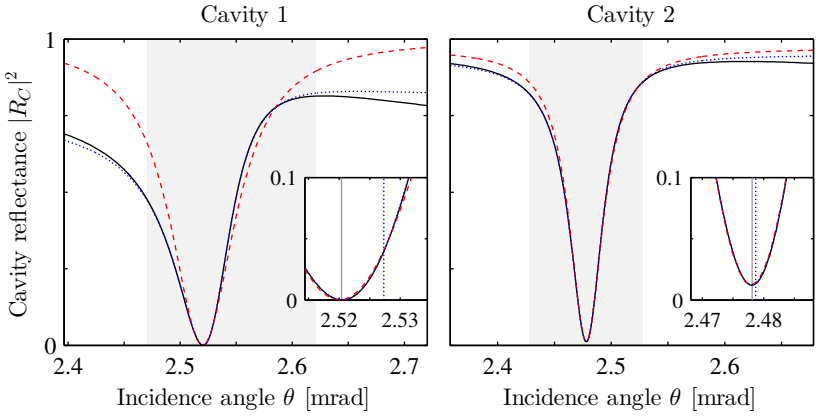

Figure 4.4: Empty-cavity response $|R_C|^2$ around the first guided mode. Shaded areas depict the range of experimentally accessed θ. Numerical data calculated with CONUSS is shown as solid black line. The quantum optical models are fitted around the reflectance minimum. In contrast to $|R_C|^2$ (red dashed curve), the models $|R'_C|^2$ including a material dispersion phase (blue dotted curve) can reproduce the asymmetry around θ_{min}. The insets show the minima in more detail. For cavity 1 the true guided mode resonance angle θ_0 (vertical blue dotted line) determined with the extended model clearly differs from the experimentally accessible θ_{min} (vertical gray line), while for cavity 2 the angles θ_0 and θ_{min} almost coincide.

In order to include the asymmetry in our theory, we consider the cavity reflection R_C from Eq. (4.4) in more detail. First, we rewrite $R_C = R_D + R_M$ with

$$R_D = -1 \,, \tag{4.17}$$

$$R_M = \frac{2\kappa_R}{\kappa + i\,\delta_C(\theta - \theta_0)} \,, \tag{4.18}$$

and note that the amplitude R_D describes the amplitude of light directly reflected from the cavity surface, while R_M corresponds to the light which enters the cavity mode and subsequently leaves it again in reflection direction. Both amplitudes together form the broad continuum in our setup relative to the narrow nuclear response. But since the two different paths are affected in different ways by the cavity material dispersion, it is reasonable to include a relative phase between these amplitudes. Possible origins include dispersion in the cavity or Goos-Hänchen phase shifts [182] of the directly reflected amplitude.

In the following we denote this relative phase between the two cavity reflection channels by ϕ_C. In our equations for the reflection coefficient, we augment $R_D = -1$ to $R'_D = -\exp(i\phi_C)$, which yields the modified continuum response

$$R'_C = -e^{i\phi_C} + \frac{2\kappa_R}{\kappa + i\,\delta_C(\theta - \theta_0)} \,. \tag{4.19}$$

Here, we assigned the relative phase ϕ_C to the amplitude of the direct reflection on the cavity surface for simplicity. An analytically equivalent result would be obtained if the phase was attributed to κ_R in the second term. Note, however, that then for consistency also the κ_R in the nuclear amplitude R_N from Eq. (4.5) needed to be changed accordingly.

Indeed, we found that with a suitably chosen phase ϕ_C in Eq. (4.19) the reflectance curve agrees very well with excellent agreement to the one predicted by CONUSS over the relevant range of incidence angles, see Fig. 4.4. We found that the asymmetry is more pronounced for a larger phase ϕ_C.

Consistent with the interpretation that the relative phase arises from material dispersion, we found that ϕ_C depends strongly on the thickness and the complex refractive index of the mirror

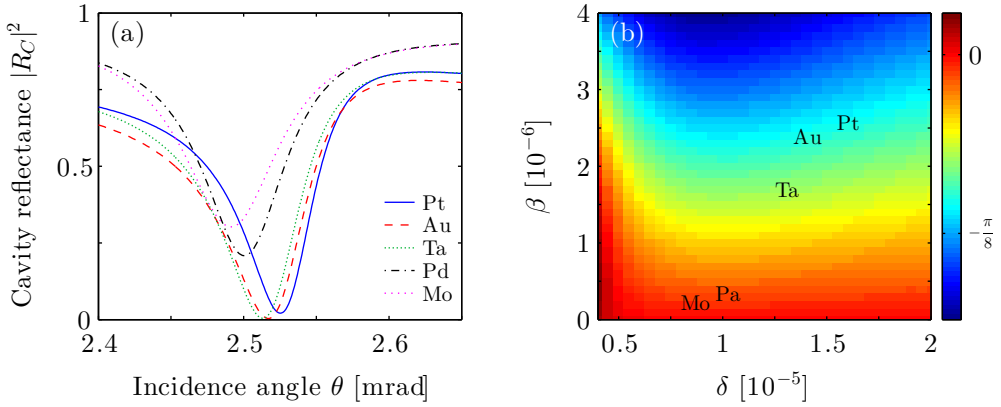

Figure 4.5: Influence of the mirror layer material on the asymmetry in the reflectance curve. (a) Reflectance curves for different materials. The top layer thickness set to 2.5 nm in all cases. The dimensions of the remaining layers are as in cavity 1 described in the main text. (b) Dependence of the asymmetry quantified by the phase ϕ_C on the refractive index $n = 1 - \delta + i\beta$ of the mirror layers. The values have been obtained by a fit of the numerical data to the extended model $|R'_C|^2$. Phase shifts for mirror layer materials Pt, Au, Ta, Pa, and Mo are indicated in the figure.

layers. This is illustrated in Fig. 4.5(a), where different mirror materials have been chosen in an otherwise identical cavity. The asymmetry of the reflection curve is strongly influenced by the choice of the material. In Fig. 4.5(b), we analyzed the dependence of the phase ϕ_C on the cavity mirror material in more detail.

To this end we varied the complex refractive index $n = 1 - \delta + i\beta$ of the mirror material and computed the respective reflection curves using Parratt's formalism (see Sec. 2.2.1). For each refractive index, the phase ϕ_C was obtained from a fit of Eq. (4.19) to the numerical data. From Fig. 4.5(b) it can be seen that especially the imaginary part of the refractive index, which is responsible for absorption in the material, influences the asymmetry, as revealed by stronger variation of ϕ_C along this axis. In our experiment, we have used cavities with platinum and palladium as mirror materials. Therefore, two different regimes of the phase ϕ_C could be explored: The nearly symmetrical and the strongly asymmetrical case, realized by the Pd and the Pt cavity, respectively.

Effect of asymmetric empty-cavity lines on the spectroscopy results

Apart from the asymmetry in the reflectance curve, the newly introduced phase ϕ_C also has an influence on the line shape of the full cavity reflectance including the nuclear amplitude. To illustrate this effect, let us first interpret Eq. (4.19) in a different context. Since the first part in Eq. (4.19) is in general complex for $\phi_C \neq 0$, and the second term is real for $\theta = \theta_0$ at the guided mode resonance angle, the cavity reflectance $R'_C(\theta = \theta_0)$ cannot be zero any more. Rather, it is minimized at a different angle θ_{min}. Generally, the two angles θ_0 and θ_{min} do not coincide, which is in contrast to the original theory developed in Chap. 3. Defining the cavity reflectance to vanish at θ_{min}, i.e. $R'_C(\theta_{\mathrm{min}}) = 0$, we can write

$$e^{i\phi_C} = \frac{2\kappa_R}{\kappa + i\delta_C\,(\theta_{\mathrm{min}} - \theta_0)} = \frac{2\kappa_R}{\kappa + i\Delta_{C,\mathrm{min}}}\,. \tag{4.20}$$

Here, we introduced

$$\Delta_{C,\mathrm{min}} = \delta_C\,(\theta_{\mathrm{min}} - \theta_0)\,. \tag{4.21}$$

Adding the nuclear contribution R_N to obtain the full reflectance, we find

$$|R'|^2 = |R'_C + R_N|^2 = \frac{|\epsilon + q'|^2}{1+\epsilon^2}\,\sigma'_0\,, \tag{4.22}$$

$$\epsilon = \frac{\Delta - \Delta_{\mathrm{LS}}}{\Gamma/2}\,, \tag{4.23}$$

$$q' = \frac{\Gamma-\gamma}{\Gamma}\frac{\kappa^2 + \Delta_C\Delta_{C,\mathrm{min}}}{\kappa\,(\Delta_C - \Delta_{C,\mathrm{min}})} + i\,\frac{\gamma}{\Gamma}\,, \tag{4.24}$$

$$\sigma'_0 = \frac{\left(2\kappa_R\,(\Delta_C - \Delta_{C,\mathrm{min}})\right)^2}{(\kappa^2+\Delta_C^2)(\kappa^2+\Delta_{C,\mathrm{min}}^2)}\,. \tag{4.25}$$

Again, a Fano line shape is obtained, but with modified σ_0 and q as compared to the symmetric case where $\phi_C = 0$ and $\Delta_{C,\mathrm{min}} = 0$.

Now, the Lorentzian spectrum ($q' \to \pm\infty$) is not realized at $\Delta_C = 0 \Leftrightarrow \theta = \theta_0$ anymore (c.f. Eq. (4.8)), but at $\Delta_C - \Delta_{C,\mathrm{min}} = 0 \Leftrightarrow \theta = \theta_{\mathrm{min}}$, which can be seen from Eq. (4.24). This is expected, since the symmetric Lorentzian line profile, as also understood from traditional Fano theory [160, 161], arises in the absence of the continuum contribution. In contrast, the bound state nuclear contribution is unaffected by the modification of the empty-cavity response. Therefore, the Lamb shift Δ_{LS} and the superradiant line width Γ are still centered around the true cavity eigenmode resonance at the angle θ_0.

Consequently, if θ_0 deviates from θ_{min}, the corresponding spectra are shifted, as observed for cavity 1 in Fig. 4.3, for which our extended theory predicts a difference of ≈ 5 μrad between θ_0 and θ_{min}. In contrast, cavity 2 made out of a different material has a negligible dispersion phase, such that $R_C \approx R'_C$ and only an insignificant angular shift arises. Theory curves taking into account a potential dispersion phase are shown in Fig. 4.3 as solid blue lines and match the experimental results very well.

The deviation of θ_{min} from θ_0 also explains why a recent experiment observed a non-zero collective Lamb shift at resonance [52], even though theoretically a vanishing Lamb shift is predicted by our initial theory developed in Chap. 3. The experiment measured at θ_{min}, which did not coincide with the angle θ_0 for resonant excitation of the cavity mode, for which the vanishing shift would be theoretically predicted.

4.1.4 Concluding remarks

Summarizing the previous sections, we have demonstrated both theoretically and experimentally, that the x-ray reflection spectra of thin-film cavities with embedded resonant nuclei exhibit Fano interference. We exploited the full agreement between theory and experiment to access spectroscopic signatures such as line broadenings or shifts. In this process, we could unravel the origin of the Lamb shift on resonance. Hence, the setup might also provides an avenue towards precision metrology at neV energy and Å distance scales.

Furthermore, we found that our cavity represents a versatile and robust x-ray interferometer, with external phase control. This phase control concept provides access to a large application potential of Fano processes in the x-ray region [169, 170]. In the next section we will exploit the interferometric nature of the cavity and show that even phase sensitive measurements of the nuclear resonances can be performed.

4.2 Interferometric phase detection

The full characterization of the light–matter interaction depends both on the intensity and the phase of the light. Detectors in the x-ray domain, however, are only sensitive to the intensity [183]. This lack of the phase knowledge is an omnipresent problem for many applications

in the x-ray domain, such as in crystallography [21, 184–186] or lensless imaging [24]. Here, we demonstrate phase-sensitive measurements on a quantum system in the x-ray regime.

As we have seen in the previous section, the Fano profiles in the thin-film cavity can be understood from the theoretical expression which contains two different amplitudes for the reflected light. The first channel is the reflection from the empty cavity, the second contribution is due to the resonant ^{57}Fe nuclei in the cavity. The setting with these two paths can therefore be interpreted in terms of an interferometer with two arms. The technique of interferometry is an important method with applications across all the natural sciences [187]. In our case, one arm contains the resonant nuclei, which, in the absence of a magnetic field, act as a collective two-level system as shown in Sec. 3.3. This realizes an archetype nuclear two-level quantum system (TLS). Via the second interferometer path, the empty-cavity reflection, the phase of the TLS can be determined as we will show in the following.

Regarding the interferometric nature of the cavities, the recorded spectra correspond to the signal at one of the output ports of the interferometer. As the non-TLS arm is tuned, the relative phase between the two channels is changed. This enables us to determine the amplitude and the phase of the optical response of the TLS. In order to apply this ansatz, the non-TLS path needs to be controllable by means of an external parameter, while at the same time the TLS-arm should be unaffected by it. In our cavity, it is possible to use the incidence angle θ to control both the amplitude and the phase of the non-TLS path as we have seen in the discussion of the Fano line shapes above. However, also the nuclear response is modified upon a change of θ, since the Lamb shift and the superradiant broadening depend on the incident angle (c.f. Fig. 4.3). Hence, phase determination from the raw experimental data is not possible, rather, we first need to rescale the measured spectra to the dimensionless energy $\epsilon = (\Delta - \Delta_{\mathrm{LS}})/(\Gamma/2)$. Then, without any approximations, the reflection coefficient can be written as

$$R \propto \frac{1}{q-i} + \frac{1}{\epsilon+i} \,. \tag{4.26}$$

Here, the first summand corresponds to the non-TLS arm and depends on the incidence angle θ. The second part describes the TLS arm of the interferometer, which now only depends on the rescaled energy ϵ. In this formulation, it is now possible to determine the amplitude and phase of the TLS by appropriately tuning the non-TLS arm of the interferometer, i.e. the empty-cavity response.

In order to implement this phase retrieval with our experimental data, the measured spectra need to be rescaled to the dimensionless energy ϵ. To this end, we use the generic Fano fits obtained in the previous section. For the further analysis we make no assumptions that the spectra are Fano profiles, as it would obviously spoil an unbiased determination of the phase. Instead, we employed a general ansatz for the reflectance

$$|R(\Delta\theta,\epsilon)|^2 \sim \left| r_C(\Delta\theta) e^{-i\phi(\Delta\theta)} + r_N(\epsilon) e^{i\phi_N(\epsilon)} \right|^2 \,, \tag{4.27}$$

where r_C and r_N are real functions. Furthermore, we assume that $r_N(\epsilon \to \pm\infty) = 0$ vanishes at large detunings, which holds for any off-resonantly driven resonance. From this, we define

$$\begin{aligned} \xi(\Delta\theta,\epsilon) &= \frac{|R(\Delta\theta,\epsilon)|^2 - |R(0,\epsilon)|^2 - |R(\Delta\theta,\pm\infty)|^2}{2|R(0,\epsilon)||R(\Delta\theta,\pm\infty)|} \\ &= \cos\left(\phi + \phi_N\right). \end{aligned} \tag{4.28}$$

Having ξ at hand for several values of $\Delta\theta$ and for a fixed energy ϵ, the nuclear phase $\phi_N(\epsilon)$ can now be determined. To this end, the relation between $\Delta\theta$ and the cavity phase $\phi(\Delta\theta) = \arg\left(q(\Delta\theta) - i\right)$, which is known from the quantum optical description, is employed. Inserting the relation in Eq. (4.28), the nuclear phase is obtained by fitting the cosine to the measured ξ for all available $\Delta\theta$ values. Repeating this procedure for multiple ϵ yields the function $\phi_N(\epsilon)$.

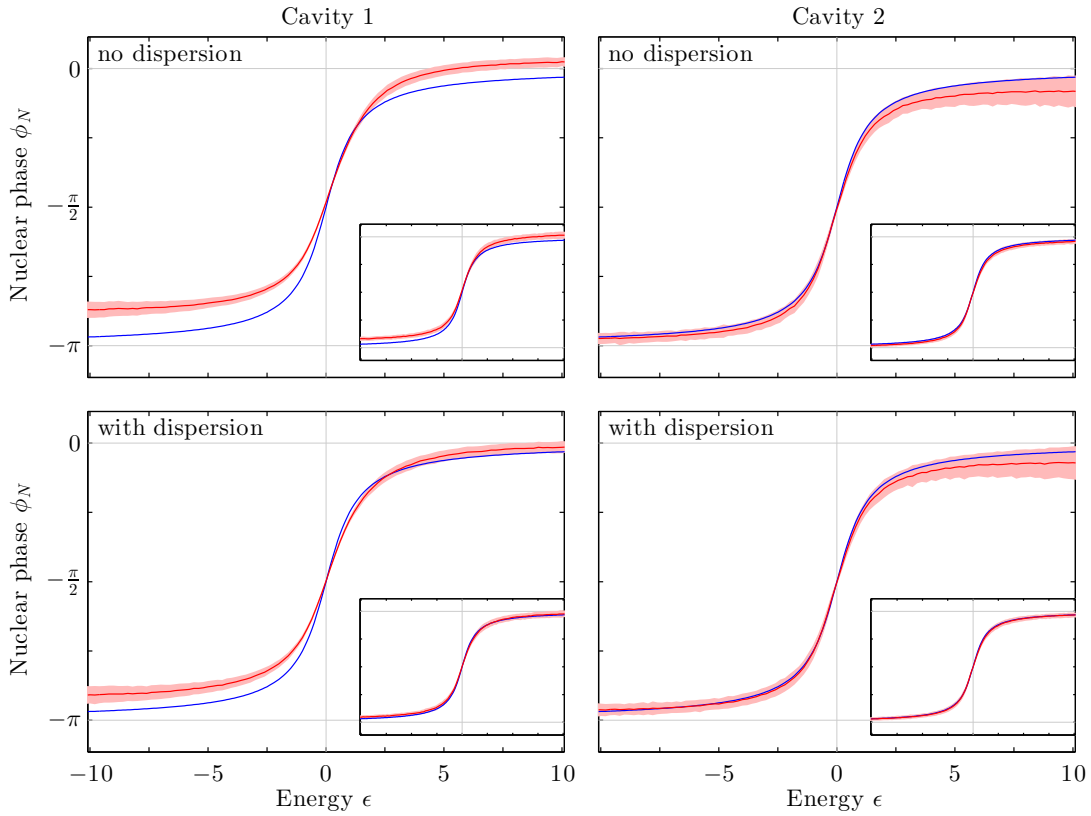

Figure 4.6: Reconstructed nuclear phase (red) as a function of the scaled energy ϵ of the TLS formed by the resonant nuclei in the two cavities. The shaded areas denote the error ranges of the retrieved TLS phases. In the top panels the dispersion phase was not taken into account, in the lower panels it was included to the phase model for the cavity. The theoretically expected phase of the Lorentzian typical for a TLS is shown in blue. The insets show reconstructed phases where a model function for the nuclear amplitude was used (see main text).

To evaluate $\xi(\Delta\theta, \epsilon)$ from the experimental data without making assumptions about to the line shape to be reconstructed, we fitted a general rational function $R_{\mathrm{rat}} = (a_0 + a_1\epsilon + a_2\epsilon^2)/(b_0 + b_1\epsilon + b_2\epsilon^2)$ to the data, normalized it to $0 \leq R_{\mathrm{rat}} \leq 1$, and evaluated it at the according values for $\Delta\theta$ and ϵ. Since the angle $\Delta\theta = 0$ was not measured for the second cavity, we obtained $|R(0, \epsilon)|$ from the mean of the results for $\Delta\theta = \pm 1$ μrad. To take into account the errors of the determined $\xi(\Delta\theta, \epsilon)$, 1000 fits with data values sampled from the individual error ranges of the variables in R_{rat} and of $\Delta\theta$ were performed for each given ϵ. Each of the fits results in a value $\phi_N^{(i)} \pm \Delta\phi_N^{(i)}$ for the nuclear phase. We weighted each $\phi_N^{(i)}$ with $(\Delta\phi_N^{(i)})^{-2}$ and for the subsequent work the mean and standard error of this set were used.

Clearly, the phase retrieval depends on the model employed for the empty-cavity response, i.e. the non-TLS arm of the interferometer which is used to scan the TLS. As we have seen before, the Fano line shape results indicate the presence of a dispersion phase in the cavity path. Hence, the model function of the non-TLS arm and also the nuclear phase, which is to be reconstructed, depends on the choice if we include this dispersion phase or not.

In the top panels of Fig. 4.6, the nuclear phases retrieved without including the dispersion phase are shown for both cavities. Clearly, their shape is similar to the expected Lorentzian phase profile $\arg\left((\epsilon + i)^{-1}\right)$ typical for a TLS. However, a constant offset in the phase for cavity 1 is observed. The reason for this is that cavity 1 exhibits a large dispersion phase in the

non-TLS path and the Fano q parameter is modified to q' given in Eq. (4.24). Including the dispersion phases to the model function by using the relation $\phi = \arg(q'(\Delta\theta) - i)$, a much better agreement with the theoretical prediction of a Lorentz profile is found, as shown in the lower panels of Fig. 4.6. The phase of the TLS in cavity 2 is largely unaffected by this, since its dispersion phase is insignificant. However, for both cavities we observe deviations form the expected Lorentzian shape for large values of ϵ. We found that the discrepancy is mainly caused by a numerical artifact. For large ϵ, the reflectance $|R(0,\epsilon)|$ becomes very small. As this value appears in the denominator of Eq. (4.28), already a small absolute error in the reflectance can result in a large error in ξ. Consequently, the TLS phase obtained from these ξ deviates from the expected result. This is exemplified in the following. Replacing the critical reflectance $|R(0,\epsilon)|$ in the denominator of Eq. (4.28) with the theoretically expected value $(1+\epsilon^2)^{-1/2}$, the phase reconstruction scheme is repeated and the results are shown in the insets of Fig. 4.6. It can be seen that this procedure, in combination with including the dispersion phase, yields perfect agreement with the expected TLS phase. Additionally, the error bars are significantly reduced. This highlights that the small value in the denominator is indeed the main cause for the observed discrepancy.

We emphasize that the method demonstrated here does not depend on the Lorentzian line profile, but can be used to reconstruct the phase of arbitrary nuclear line shapes. For example, it can be employed for advanced x-ray quantum optical level schemes involving multiple magnetic hyperfine states with selectively coupled resonances [50, 56]. To do so, as demonstrated above, the measured spectra have to be normalized to the dimensionless energy ϵ. This can be achieved by first characterizing the cavity by measuring the Fano line shapes with the known relations for the cooperative Lamb shift and the superradiant enhancement. Once the cavity properties, in particular the relation between the incidence angle θ and the cavity phase ϕ, are known, a magnetic splitting could be induced and the phase of the potentially non-trivial nuclear response could be reconstructed employing the same ansatz as used above.

4.2.1 State tomography at x-ray energies

To fully exploit quantum effects, an essential requirement is the capability to determine the quantum state of a given system. The techniques of phase-sensitive measurements are a prerequisite for the development of quantum state tomography, i.e. the reconstruction of quantum states [188, 189]. This quantum state tomography has been successfully demonstrated at optical frequencies [190], but remains an open challenge in the x-ray regime.

In our setup the quantum state of interest is the TLS formed by the collective behavior of he ^{57}Fe nuclei in the cavity. Further, the incident x-ray pulse has a duration in the 10-100 ps range, whereas the natural life time of the single nuclei is 141 ns. Hence, the preparation of the TLS state in the low-excitation regime is near-instantaneous and the measurement of the subsequently emitted light, which we can use for its characterization, is independent.

A full state tomography would comprise a measurement of the TLS density matrix [189]. Due to the time gating used in the present experiment, the absolute values of the density matrix elements are not directly accessible from our data. However, we can characterize the vital properties of the off-diagonal density matrix elements. The x-ray photons are coherently scattered, preserving their energy. Selecting all detection events of a particular photon energy ϵ therefore provides access to a large number of identically prepared TLS states. Repeated measurements on the light emitted by identically prepared TLS states then enables us to determine the characteristics of the off-diagonal density matrix element $\rho_{eg} = \langle e|\rho|g\rangle$, where $|g\rangle$ [$|e\rangle$] denotes the ground [excited] state of the TLS. Up to an unknown scaling factor, it can be decomposed into

$$\rho_{eg}(\Delta) \sim \sigma_{eg}(\Delta) \cdot e^{i\phi_\rho(\Delta)} \,, \tag{4.29}$$

where $\sigma_{eg}(\Delta)$ contains the spectral form and ϕ_ρ is the phase of the density matrix element. The spectral shape is trivially obtained from the pure nuclear spectrum shown in Figs. 4.2(a)

and 4.2(b). In addition, our phase-sensitive measurements provides a handle to determine the desired phase of the off-diagonal density matrix elements, since ρ_{eg} is directly proportional to the light amplitude emitted by the TLS. This can already be seen by noting that the nuclear contribution to the reflected field amplitude $R_N \propto r_N \exp(i\phi_N)$ is directly proportional to the off-diagonal density matrix element ρ_{eg}, see Chap. 3. In a more general way, this relation is also obtained by considering the radiation emitted from a dipole transition as [148]

$$\boldsymbol{E}^{(+)}_{\text{scat}} = \frac{k^2}{4\pi\epsilon_0 r} e^{i(\boldsymbol{k}\boldsymbol{r}-\omega t)} \, (\hat{\boldsymbol{r}} \times \boldsymbol{d}) \times \boldsymbol{r} \cdot S_- \, , \tag{4.30}$$

where $\boldsymbol{d}$ is the TLS dipole moment assumed parallel to the polarization, and S_- the transition operator from the upper to the lower state. Since $\langle S_- \rangle = \rho_{eg}$, the measured nuclear phase ϕ_N can be identified with the phase ϕ_ρ of the off-diagonal density matrix elements.

The phase-sensitive interferometric measurement of the optical response of a TLS demonstrated here opens a number of promising research directions. Combinations of the techniques developed here with measurements of the magnitude of the density matrix elements, either via detecting light intensity or conversion electrons [191], could lead to the development of complete quantum state tomography at x-ray energies.

Chapter 5

Vacuum Induced Coherences In ^{57}Fe

In the previous chapters we have discussed properties and effects of the thin-film cavity with an embedded ^{57}Fe layer. However, so far a possible magnetization in the layer of resonant nuclei and its influence on the reflection spectrum was not considered. Since a magnetic field induces a hyperfine splitting of the nuclear resonances, different transitions can be driven in principle and the interpretation of the system clearly goes beyond the physics of two-level systems. At the same time, a magnetization in the layer will define a quantization axis, such that the polarization invariance is broken. Thus, the polarization of the incident radiation and at the detector have to be treated explicitly in the theoretical descriptions. These new aspects offer a great potential, since the systems under investigation posses additional degrees of freedom, which can be controlled externally. Hence, it can be expected that flexible schemes can be engineered, and additionally new physical phenomena will be observed if a magnetic control of the setup is exploited.

On the theory side, the layerformalism we introduced in Sec. 2.2.2 is capable of covering the magnetization and polarization dependence [77] and hence the software package CONUSS [79, 80] can again serve as a benchmark for other theories. In this chapter we will show that even compact analytical expressions for the cavity reflectance can often be found employing the layerformalism. But as emphasized before, a quantum description is highly desirable in order to understand the microscopic effects in the cavity and to provide a proper interpretation. The quantum optical description we developed in Chap. 3 has been designed to also allow for magnetic hyperfine splittings and covers the full polarization dependency. Therefore, it is well suited to be applied in this advanced scenario as well.

As a main result we will see that, surprisingly, the vacuum itself spontaneously induces coherences in the ^{57}Fe nuclei [140, 147, 148], which manifests itself in characteristic spectral line shapes. Finally, we will present experimental results for the spectra, which were obtained in collaboration with the group of Ralf Röhlsberger, Hans-Christian Wille (both at DESY, Hamburg), the Institute for Optics and Quantum Electronics in Jena and the Helmholtz Institute Jena.

5.1 Geometrical settings

As mentioned in the introduction, the focus of this chapter is a cavity in which the magnetic hyperfine splitting of the nuclei is explicitly considered. An iron layer in the cavity will spontaneously build up ferromagnetic order, if its thickness exceeds a few nanometers. In turn, the internal magnetization can be aligned already by applying relatively weak external magnetic field. The internal field strength in α-iron is typically around 33 T [51], which results in a Zeeman splitting of the ground and excited states of the nuclear transition as illustrated in Fig. 3.2.

In addition to the magnetically induced splitting of the nuclear resonances, the polarization of the incoming x-ray beam as well as of the detected radiation plays a crucial role. The relative orientation of the incident polarization with respect to the quantization axis in the cavity determines which transitions in the Zeeman-splitted ^{57}Fe nuclei are driven. Also, the relative strength of the different excitations channels can be controlled this way. The same holds for the reflected radiation. Since each transition in the nucleus emits radiation only along its polarization axis, a suitable choice of the detector's polarization orientation allows to selectively read out

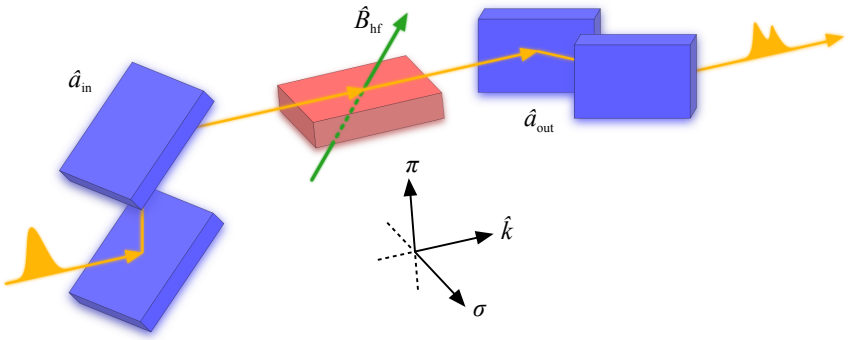

Figure 5.1: The setup discussed in this chapter is sketched. The thin-film cavity with the embedded ^{57}Fe nuclei marked in red is subjected to a magnetic field, such that different transitions in the nuclei can be driven. In addition, the polarization dependence is taken into account. Experimentally, it can be controlled, e.g., with a polarimeter as shown in blue color above.

different combinations of the transitions. Experimentally, dedicated x-ray polarization optics as illustrated in Fig. 5.1 can be employed to exploit this degree of control. The polarization plane of the incident and the detected x-rays can be defined by linear x-ray polarizer crystals before and behind the sample [192–194].

In this chapter we will consider different geometrical configurations of the magnetization direction and polarization choices. The orientations are defined with respect to the beam propagation axis $\hat{\boldsymbol{k}}$, the layer surface normal $\boldsymbol{\pi}$ and $\boldsymbol{\sigma} = (\hat{\boldsymbol{k}} \times \boldsymbol{\pi})$. The vectors $\boldsymbol{\pi}$ and $\boldsymbol{\sigma}$ correspond to the directions $\hat{\boldsymbol{a}}_1$ and $\hat{\boldsymbol{a}}_2$ defined Fig. 3.1 and used in the derivation of the quantum optical description in Chap. 3. However, for consistency with the notation of the layerformalism [77], we will use the axes $\boldsymbol{\pi}$ and $\boldsymbol{\sigma}$ in the following. Denoting the polarization of the incident [outgoing] x-ray beam by $\hat{\boldsymbol{a}}_{\mathrm{in}}$ [$\hat{\boldsymbol{a}}_{\mathrm{out}}$] and the magnetization, and thus quantization axis by $\hat{\boldsymbol{B}}_{\mathrm{hf}}$, we consider the following configurations:

$\boldsymbol{\pi}$ geometry: $\hat{\boldsymbol{a}}_{\mathrm{in}} \parallel \hat{\boldsymbol{a}}_{\mathrm{out}} \parallel \boldsymbol{\pi}$, $\hat{\boldsymbol{B}}_{\mathrm{hf}} \parallel \boldsymbol{\sigma}$
In this simple geometry, the magnetic component of the incident light is parallel to the magnetization axis of the nuclei. Therefore, only linearly polarized $\Delta m = 0$ transitions are driven.

$\boldsymbol{\sigma}$ geometry: $\hat{\boldsymbol{a}}_{\mathrm{in}} \parallel \hat{\boldsymbol{a}}_{\mathrm{out}} \parallel \hat{\boldsymbol{B}}_{\mathrm{hf}} \parallel \boldsymbol{\sigma}$
Here, the magnetic component is perpendicular to the quantization axis and hence only circular polarized $\sigma^{\pm}$ transitions are driven.

Faraday geometry: $\hat{\boldsymbol{a}}_{\mathrm{in}} \parallel \boldsymbol{\sigma}$, $\hat{\boldsymbol{a}}_{\mathrm{out}} \parallel \boldsymbol{\pi}$, $\hat{\boldsymbol{B}}_{\mathrm{hf}} \parallel \hat{\boldsymbol{k}}$
In this configuration, the polarizer and analyzer setting suppresses any background signal, consisting of photons whose polarization has not been rotated upon an interaction with the nuclei in the cavity. Since the magnetization is perpendicular to the magnetic field component of the incident pulse, again only $\Delta M = \pm 1$ transitions are driven. However, due to the different polarization choice compared to the σ *geometry*, a differing optical response is expected.

Half-Faraday geometry: $\hat{\boldsymbol{a}}_{\mathrm{in}} \parallel \boldsymbol{\sigma}$, $\hat{\boldsymbol{a}}_{\mathrm{out}} \parallel \boldsymbol{\pi}$, $\hat{\boldsymbol{B}}_{\mathrm{hf}} \parallel \boldsymbol{\sigma} + \hat{\boldsymbol{k}}$
Also here, only photons resonantly scattered at the ^{57}Fe layer will arrive at the detector. All six transitions in the ^{57}Fe nucleus will be driven by the x-ray beam.

45°-Voigt geometry: $\hat{\boldsymbol{a}}_{\mathrm{in}} \parallel \boldsymbol{\pi} + \boldsymbol{\sigma}$, $\hat{\boldsymbol{a}}_{\mathrm{out}} \parallel \boldsymbol{\pi} - \boldsymbol{\sigma}$, $\hat{\boldsymbol{B}}_{\mathrm{hf}} \parallel \boldsymbol{\sigma}$
The properties of this configuration are similar to those of the *Half-Faraday geometry*. Due to different polarizations of the incident and outgoing beam, the interaction in the cavity and the observed spectra are expected to be different.

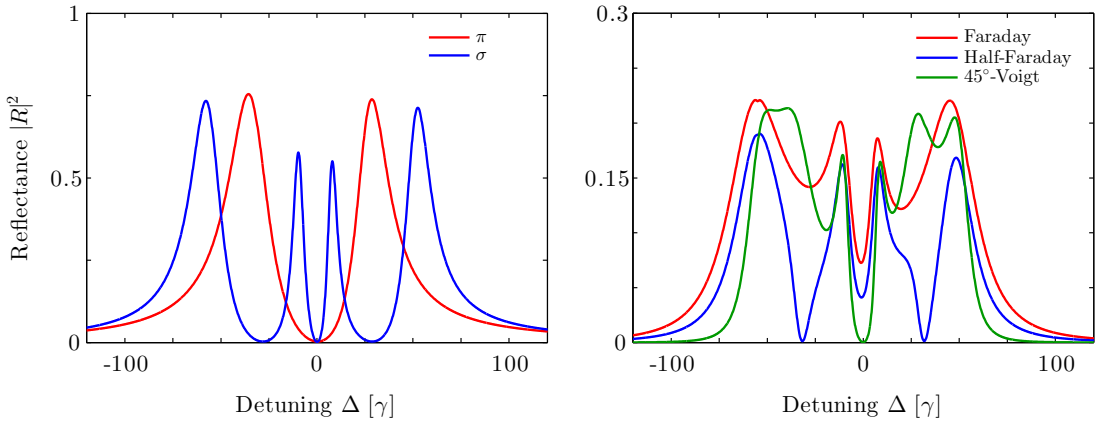

Figure 5.2: Spectra of the cavity with a magnetized ^{57}Fe layer calculated with CONUSS are shown for the different geometrical configurations introduced in the main text.

Note that in a realistic experimental situation, the magnetic field can only be aligned in the $(\boldsymbol{\sigma}, \hat{\boldsymbol{k}})$ plane of the layer as the layer thickness along $\boldsymbol{\pi}$ is too small for an unspoiled spin alignment. However, nearly arbitrary choices for the magnetization direction can be mimicked by rotating the polarizer and analyzer instead.

In order to get a first impression on the spectra of the configurations defined above, we perform numerical simulations with the software package CONUSS for the layer system defined in Tab. 5.1. The computations are performed at $\theta = 3.35$ mrad, where the first guided mode of the cavity is excited. The results are shown in Fig. 5.2. Clearly, the spectra go beyond the Lorentzian response of a two-level system and indicate, that multiple transitions in the ^{57}Fe nuclei contribute to the observed reflectance.

A prominent feature of the spectra in Fig. 5.2 are repeatedly occurring maxima and minima, found in all spectra. At some of the minima, the reflected signal even drops to the baseline. This observation is an explicit sign of interference effects, which occur between the involved transitions in the cavity. However, at this point it is unclear which kind of physical phenomenon gives rise to those interferences and how the presence of the deep minima can be interpreted. Answering this question is the central subject of this chapter.

5.2 Semi-classical derivation of the reflectance

We have seen above that the reflectance spectra in the presence of a magnetic splitting of the ^{57}Fe nuclei can become rather complex. Accordingly, also the theoretical treatment of these cases is slightly more involved. In this section, we will derive expressions for the reflection coefficient using the layerformalism (see Sec. 2.2.2), which is also the basis for CONUSS. To this end, the

Table 5.1: Toy level system used to analyze the influence of magnetization.

Material	Thickness [nm]
Pt	2.5
C	6
^{57}Fe	2
C	6
Pt	∞

perturbative ansatz of Refs. [52, 56], where the reflection coefficient was calculated in the absence of a magnetization, is generalized here.

We start by recapitulating the basic elements of this analytic approach, which was introduced in Sec. 2.2.2. The field amplitudes of the transmitted and reflected light at depth z of the layer system are combined in the two-dimensional vector $\vec{A}(z)$. Products of so-called layer matrices $\boldsymbol{L}$ connect the field amplitudes at different positions. Each layer contributes to this product with its layer matrix $\boldsymbol{L}_i$, which depends on its material composition. In particular, for the resonant layer, the matrix can be written as $\boldsymbol{L}_{\mathrm{Fe}}(z) = \exp(i\boldsymbol{F}_{\mathrm{Fe}}z)$, where $\boldsymbol{F}_{\mathrm{Fe}}$ is the propagation matrix and contains the nuclear scattering amplitude f_N. The reflection coefficient is obtained from the ratio of the reflected and incident field amplitude at the surface of the cavity.

Let us briefly sketch how the polarization and magnetization can be included in this treatment. Since any polarization can be written as a linear combination of components along the two axes $\boldsymbol{\pi}$ and $\boldsymbol{\sigma}$ perpendicular to the beam propagation direction $\hat{\boldsymbol{k}}$, the field amplitude vector $\vec{A}(z)$ can simply be extended to four components. Then, it contains the field amplitudes for the transmitted and reflected light for two polarization directions each. Consequently, the layer- and propagation matrices are to be extended to the size 4×4. Instead of a scattering amplitude f_N, we use a 2×2 scattering matrix $\boldsymbol{f}_N$ to properly take the polarization dependence into account. The form of the scattering matrix is determined by the magnetization of the ^{57}Fe layer. Generally, the propagation and layer matrices couple all individual amplitudes in $\vec{A}$ with each other, such that a straightforward computation as performed in Sec. 2.2.2 is not possible. However, in the special case in which $\boldsymbol{f}_N$ can be diagonalized, so-called eigenpolarizations can be defined. In a physical picture, their property is that they do not mix with the respective second eigenpolarization upon scattering in the cavity. For the case of eigenpolarizations, the situation reduces to the case without magnetization in the analysis: The reflection coefficient of each eigenpolarization can be calculated separately and by projecting the incident light polarization, as well as the detector axis onto the eigenpolarizations, the coefficients for the respective reflectivities are found.

5.2.1 Decomposition into two eigenpolarizations

Next, the fact that the diagonalized scattering matrix $\boldsymbol{f}_N$ allows for the calculation of amplitudes for two independent eigenpolarizations, will be discussed in more detail. For the field amplitude vector we write $\vec{A} = (A_{+\boldsymbol{\sigma}}, A_{+\boldsymbol{\pi}}, A_{-\boldsymbol{\sigma}}, A_{-\boldsymbol{\pi}})^T$, where $A_{\pm}$ denotes the transmitted and reflected field amplitudes in the canonical polarization basis $(\boldsymbol{\sigma}, \boldsymbol{\pi})$. Let us assume that the scattering matrix $\boldsymbol{f}_N$ can indeed be diagonalized and write for the scattering matrix in the canonical basis

$$\boldsymbol{f}_N = \boldsymbol{U}\tilde{\boldsymbol{f}}_N\boldsymbol{U}^\dagger \,, \tag{5.1}$$

with the diagonal scattering matrix

$$\tilde{\boldsymbol{f}}_N = \begin{pmatrix} f_{N\boldsymbol{\eta}} & 0 \\ 0 & f_{N\boldsymbol{\zeta}} \end{pmatrix} . \tag{5.2}$$

The unitary matrix $\boldsymbol{U}$ transforms between the canonical polarization basis and the eigenpolarizations $(\boldsymbol{\eta}, \boldsymbol{\zeta})$, in which the scattering matrix is diagonal. Including polarization, the propagation matrix $\boldsymbol{F}_{\mathrm{Fe}}$ from Eq. (2.18) becomes

$$\boldsymbol{F}_{\mathrm{Fe}} = \begin{pmatrix} \boldsymbol{f}_N & \boldsymbol{f}_N \\ -\boldsymbol{f}_N & -\boldsymbol{f}_N \end{pmatrix} = \begin{pmatrix} \boldsymbol{U} & 0 \\ 0 & \boldsymbol{U} \end{pmatrix} \begin{pmatrix} \tilde{\boldsymbol{f}}_N & \tilde{\boldsymbol{f}}_N \\ -\tilde{\boldsymbol{f}}_N & -\tilde{\boldsymbol{f}}_N \end{pmatrix} \begin{pmatrix} \boldsymbol{U}^\dagger & 0 \\ 0 & \boldsymbol{U}^\dagger \end{pmatrix} , \tag{5.3}$$

and for the layer matrix we find

$$\boldsymbol{L}_{\mathrm{Fe}}(z) = \exp(i\,\boldsymbol{F}_{\mathrm{Fe}}\,z) = \begin{pmatrix} \boldsymbol{U} & 0 \\ 0 & \boldsymbol{U} \end{pmatrix} \tilde{\boldsymbol{L}}_{\mathrm{Fe}}(z) \begin{pmatrix} \boldsymbol{U}^\dagger & 0 \\ 0 & \boldsymbol{U}^\dagger \end{pmatrix} , \tag{5.4}$$

with

$$\tilde{\boldsymbol{L}}_{\mathrm{Fe}}(z) = \exp\left(i \begin{pmatrix} \tilde{\boldsymbol{f}}_N & \tilde{\boldsymbol{f}}_N \\ -\tilde{\boldsymbol{f}}_N & -\tilde{\boldsymbol{f}}_N \end{pmatrix} z \right) = \begin{pmatrix} 1+if_{N\boldsymbol{\eta}}z & 0 & if_{N\boldsymbol{\eta}}z & 0 \\ 0 & 1+if_{N\boldsymbol{\zeta}}z & 0 & if_{N\boldsymbol{\zeta}}z \\ -if_{N\boldsymbol{\eta}}z & 0 & 1-if_{N\boldsymbol{\eta}}z & 0 \\ 0 & -if_{N\boldsymbol{\zeta}}z & 0 & 1-if_{N\boldsymbol{\zeta}}z \end{pmatrix} . \tag{5.5}$$

Finally, let us now transform the field amplitude vector $\vec{A}$ into the diagonal basis via

$$\vec{\tilde{A}} = (A_{+\boldsymbol{\eta}}, A_{+\boldsymbol{\zeta}}, A_{-\boldsymbol{\eta}}, A_{-\boldsymbol{\zeta}})^T = \begin{pmatrix} \boldsymbol{U}^\dagger & 0 \\ 0 & \boldsymbol{U}^\dagger \end{pmatrix} \vec{A} \tag{5.6}$$

We find that in the new basis the field amplitudes at different positions are related by (see Eq. (2.13))

$$\vec{\tilde{A}}(z) = \tilde{\boldsymbol{L}}_{\mathrm{Fe}}(z)\vec{\tilde{A}}(0) . \tag{5.7}$$

From the form of the matrix $\tilde{\boldsymbol{L}}_{\mathrm{Fe}}$ in Eq. (5.5), we immediately notice that only the transmitted and reflected field amplitudes of the same eigenpolarization are mutually coupled. Hence, the equation for a single eigenpolarization $\boldsymbol{\rho} = \boldsymbol{\eta}, \boldsymbol{\zeta}$ can be written in the reduced form

$$\begin{aligned} \begin{pmatrix} A_{+\boldsymbol{\rho}}(z) \\ A_{-\boldsymbol{\rho}}(z) \end{pmatrix} &= \begin{pmatrix} 1+if_{N\boldsymbol{\rho}}z & if_{N\boldsymbol{\rho}}z \\ -if_{N\boldsymbol{\rho}}z & 1-if_{N\boldsymbol{\rho}}z \end{pmatrix} \begin{pmatrix} A_{+\boldsymbol{\rho}}(0) \\ A_{-\boldsymbol{\rho}}(0) \end{pmatrix} \\ &= \exp\left(i \begin{pmatrix} f_{N\boldsymbol{\rho}} & f_{N\boldsymbol{\rho}} \\ -f_{N\boldsymbol{\rho}} & -f_{N\boldsymbol{\rho}} \end{pmatrix} z \right) \begin{pmatrix} A_{+\boldsymbol{\rho}}(0) \\ A_{-\boldsymbol{\rho}}(0) \end{pmatrix} . \end{aligned} \tag{5.8}$$

This is exactly the same form as we found in the discussion without polarization dependence in Sec. 2.2.2. Therefore, the solution of the reflection coefficient for a single eigenpolarization can be reused in this analysis. In particular, in the case where the electronic reflection vanishes since the cavity is driven at a guided mode, the reflection coefficient is given in Eq. (2.20). In this expression, f_N has now to be replaced with the eigenvalues $f_{N\boldsymbol{\rho}}$ of the scattering matrix. Thus, the remaining task is the diagonalization of the nuclear scattering matrix and the according projection of the driving and detector polarization onto the axes of the eigenpolarizations.

Above, we neglected terms stemming from the electronic contribution of non-resonant layers for clarity. Their scattering matrices are always diagonal and have identical eigenvalues, though, and do not rotate the polarization of the x-rays. Therefore their responses to the light field seen at different polarization directions is always identical. Naturally, also no polarization mixing occurs in the basis of the eigenpolarizations. Hence, the layer matrices with the electronic contributions can simply be multiplied to Eq. (5.8) at the according positions.

5.2.2 The nuclear scattering matrix

The nuclear scattering in the canonical polarization basis is characterized by the scattering matrix $\boldsymbol{f}_N$. As we have seen above, the reflection coefficient can be expressed analytically if it can be diagonalized. Here we consider the pure nuclear contribution to the scattering matrix and neglect the non-resonant electronic part. Following Ref. [77], it can then be written as

$$\boldsymbol{f}_N \propto \begin{pmatrix} N_{\boldsymbol{\sigma\sigma}} & N_{\boldsymbol{\sigma\pi}} \\ N_{\boldsymbol{\pi\sigma}} & N_{\boldsymbol{\pi\pi}} \end{pmatrix} , \tag{5.9}$$

where $N_{\boldsymbol{\rho\xi}}$ denotes the scattering from channel $\boldsymbol{\xi}$ into channel $\boldsymbol{\rho}$. The coefficients read (see Eq. (4.15) in Ref. [77])

$$\begin{aligned}
N_{\boldsymbol{\sigma\sigma}} &= F_{+1} + F_{-1} + (\boldsymbol{\pi}\cdot\hat{\boldsymbol{B}})^2(2F_0 - F_{+1} - F_{-1}) \\
N_{\boldsymbol{\sigma\pi}} &= -i(\hat{\boldsymbol{k}}\cdot\hat{\boldsymbol{B}})(F_{+1} - F_{-1}) - (\boldsymbol{\sigma}\cdot\hat{\boldsymbol{B}})(\boldsymbol{\pi}\cdot\hat{\boldsymbol{B}})(2F_0 - F_{+1} - F_{-1}) \\
N_{\boldsymbol{\pi\sigma}} &= i(\hat{\boldsymbol{k}}\cdot\hat{\boldsymbol{B}})(F_{+1} - F_{-1}) - (\boldsymbol{\sigma}\cdot\hat{\boldsymbol{B}})(\boldsymbol{\pi}\cdot\hat{\boldsymbol{B}})(2F_0 - F_{+1} - F_{-1}) \\
N_{\boldsymbol{\pi\pi}} &= F_{+1} + F_{-1} + (\boldsymbol{\sigma}\cdot\hat{\boldsymbol{B}})^2(2F_0 - F_{+1} - F_{-1})\ .
\end{aligned} \tag{5.10}$$

From the matrix above, it can be seen that for general choices of the magnetization axis $\hat{\boldsymbol{B}}$ a strong polarization mixing occurs. The scattering functions F_M contain the scattering amplitudes of the corresponding $\Delta m = M$ transitions, e.g. F_{-1} describes the scattering of the x-rays at σ^- transitions in the nucleus. Following Eq. (4.78) in Ref. [77], they consist of the sum over the two ground states g in the ^{57}Fe resonance, i.e. the sum over the two transitions with $\Delta m = M$. The resonance frequencies of the transitions are defined with respect to the transition energy at vanishing magnetization ω_0. Their energy shifts were already given in Tab. 3.1. In the same notation we can write for the scattering functions ($m_e = m_g + M$)

$$F_M \propto \sum_g \frac{\langle \frac{1}{2}, m_g; 1, M | \frac{3}{2}, m_e\rangle^2}{\Delta - (m_e\delta_e + m_g\delta_g) + i\gamma/2}\ , \tag{5.11}$$

where $\langle \frac{1}{2}, m_g; 1, M | \frac{3}{2}, m_e\rangle$ denotes the Clebsch-Gordan coefficient of the respective transition. In particular, neglecting the global scaling factor, they read

$$\begin{aligned}
F_{-1} &= \frac{1/3}{\Delta + i\frac{\gamma}{2} + \frac{1}{2}\delta_g - \frac{1}{2}\delta_e} + \frac{1}{\Delta + i\frac{\gamma}{2} - \frac{1}{2}\delta_g - \frac{3}{2}\delta_e}\ , \\
F_0 &= \frac{2/3}{\Delta + i\frac{\gamma}{2} + \frac{1}{2}\delta_g + \frac{1}{2}\delta_e} + \frac{2/3}{\Delta + i\frac{\gamma}{2} - \frac{1}{2}\delta_g - \frac{1}{2}\delta_e}\ , \\
F_{+1} &= \frac{1}{\Delta + i\frac{\gamma}{2} + \frac{1}{2}\delta_g + \frac{3}{2}\delta_e} + \frac{1/3}{\Delta + i\frac{\gamma}{2} - \frac{1}{2}\delta_g + \frac{1}{2}\delta_e}\ .
\end{aligned} \tag{5.12}$$

From Eqs. (5.10) and (5.12), we can immediately see that for vanishing magnetization, i.e. where no Zeeman splitting occurs and $\delta_e = \delta_g = 0$, all scattering functions $F_{\pm1}, F_0$ coincide and therefore the scattering matrix in Eq. (5.9) is diagonal with identical eigenvalues. Hence, the polarization-insensitivity of the scenario without a magnetic splitting is recovered.

Let us now calculate the eigenvalues $f_{N\boldsymbol{\eta}}$ and $f_{N\boldsymbol{\zeta}}$ of the scattering matrix $\boldsymbol{f}_N$ for the cases $\hat{\boldsymbol{B}} \perp \hat{\boldsymbol{k}}$ and $\hat{\boldsymbol{B}} \parallel \hat{\boldsymbol{k}}$. This corresponds to most geometries we defined in Sec. 5.1. We find

$$\begin{aligned}
f_{N\boldsymbol{\eta}}^{\hat{\boldsymbol{B}}\perp\hat{\boldsymbol{k}}} &\propto F_{-1} + F_{+1}\ , \\
f_{N\boldsymbol{\zeta}}^{\hat{\boldsymbol{B}}\perp\hat{\boldsymbol{k}}} &\propto 2F_0\ , \\
f_{N\boldsymbol{\eta}}^{\hat{\boldsymbol{B}}\parallel\hat{\boldsymbol{k}}} &\propto 2F_{-1}\ , \\
f_{N\boldsymbol{\zeta}}^{\hat{\boldsymbol{B}}\parallel\hat{\boldsymbol{k}}} &\propto 2F_{+1}\ .
\end{aligned} \tag{5.13}$$

The proper normalized eigenvectors are denoted by $\hat{\boldsymbol{f}}_{N\boldsymbol{\eta}}$ and $\hat{\boldsymbol{f}}_{N\boldsymbol{\zeta}}$. These are required in the following, since the projection of the incident and outgoing polarization onto the eigenpolarization axes also plays a crucial role for the full reflectance.

With the knowledge of the scattering matrix eigenvalues and the reflection coefficient for a single eigenpolarization (see Eq. (2.20)), it is now possible to construct the total response as

$$\begin{aligned}
R = {} & R_{\text{Eigenpol}}\left(f_{N\boldsymbol{\eta}}\right)\ \left(\hat{\boldsymbol{a}}_{\text{out}}^*\cdot\hat{\boldsymbol{f}}_{N\boldsymbol{\eta}}\right)\left(\hat{\boldsymbol{f}}_{N\boldsymbol{\eta}}^*\cdot\hat{\boldsymbol{a}}_{\text{in}}\right) \\
& + R_{\text{Eigenpol}}\left(f_{N\boldsymbol{\zeta}}\right)\ \left(\hat{\boldsymbol{a}}_{\text{out}}^*\cdot\hat{\boldsymbol{f}}_{N\boldsymbol{\zeta}}\right)\left(\hat{\boldsymbol{f}}_{N\boldsymbol{\zeta}}^*\cdot\hat{\boldsymbol{a}}_{\text{in}}\right)\ ,
\end{aligned} \tag{5.14}$$

with

$$R_{\text{Eigenpol}}(T) = \frac{idp^2}{\frac{1}{T} - idpq} \,. \tag{5.15}$$

Note that, in contrast to Sec. 2.2.2, the coefficients p and q are now rescaled parameters to compensate for the factors of proportionality in the nuclear scattering amplitude. Moreover, these constants are independent of the chosen eigenvalue and depend only on the cavity geometry.

Finally, we consider the case where the incident or the detected beam are not fully polarized. For example, this is of interest if no analyzer is used in the optical path, but all photons independent on their polarization arrive at the detector. We construct the reflection tensor

$$\boldsymbol{R} = R_{\text{Eigenpol}}\left(f_{N\boldsymbol{\eta}}\right) \left(\hat{\boldsymbol{f}}_{N\boldsymbol{\eta}} \hat{\boldsymbol{f}}^*_{N\boldsymbol{\eta}}\right) \tag{5.16}$$

$$+ R_{\text{Eigenpol}}\left(f_{N\boldsymbol{\zeta}}\right) \left(\hat{\boldsymbol{f}}_{N\boldsymbol{\zeta}} \hat{\boldsymbol{f}}^*_{N\boldsymbol{\zeta}}\right) \,, \tag{5.17}$$

where the vector products denote outer products. In the case of a linear polarized beam and a polarization sensitive detector we can calculate the reflection as the scalar quantity

$$R = \hat{\boldsymbol{a}}^*_{\text{out}} \cdot \boldsymbol{R} \cdot \hat{\boldsymbol{a}}_{\text{in}} \tag{5.18}$$

in agreement with Eq. (5.14). For a general incoming and outgoing polarization the reflection can be calculated with Eq. (4.73) in Ref. [77] as

$$|R|^2 = \text{Tr}\left(\boldsymbol{\rho}_{\text{out}} \boldsymbol{R} \boldsymbol{\rho}_{\text{in}} \boldsymbol{R}^\dagger\right) \,. \tag{5.19}$$

Here $\boldsymbol{\rho}_{\text{in}}$ and $\boldsymbol{\rho}_{\text{out}}$ denote the density matrix of the initial and final polarization state, respectively.

5.2.3 Analytical solutions for the reflection coefficients

We are now able to compute the reflection coefficients for the geometries defined in Sec. 5.1. Using the decomposition into eigenpolarizations, we find

$$\begin{aligned}
R_\pi &= R_{\text{Eigenpol}}(2F_0) \,, \\
R_\sigma &= R_{\text{Eigenpol}}(F_{-1} + F_{+1}) \,, \\
R_{\text{Faraday}} &= \tfrac{i}{2} R_{\text{Eigenpol}}(2F_{+1}) - \tfrac{i}{2} R_{\text{Eigenpol}}(2F_{-1}) \,, \\
R_{\text{Voigt}} &= \tfrac{1}{2} R_{\text{Eigenpol}}(2F_0) - \tfrac{1}{2} R_{\text{Eigenpol}}(F_{-1} + F_{+1}) \,.
\end{aligned} \tag{5.20}$$

Since for the *Half-Faraday geometry* the scattering matrix does not decompose into two eigenpolarizations, its reflection coefficient cannot be written in this simple form with the methods presented here, but only computed numerically.

The expressions for the reflectance we derived in Eq. (5.20) are shown in Fig. 5.3. All curves have been created with the same set of parameters and agree to the predictions calculated by CONUSS very well, indicating the consistency of our derivation above. Since in the *Faraday* and the *45°-Voigt geometry* the incident polarization is chosen perpendicular to the detected polarization, all electronic scattering signal is suppressed. Only the nuclear scattering signal arrives at the detector. In the other two geometrical settings shown in Fig. 5.3, though, the electronic signal is only minimized since the cavity is operated in the first guided mode minimum. Any residual electronic effect contributes to the reflection coefficient beyond the one given in Eq. (5.20). Allowing for a complex offset for the reflectivity, this can be compensated.

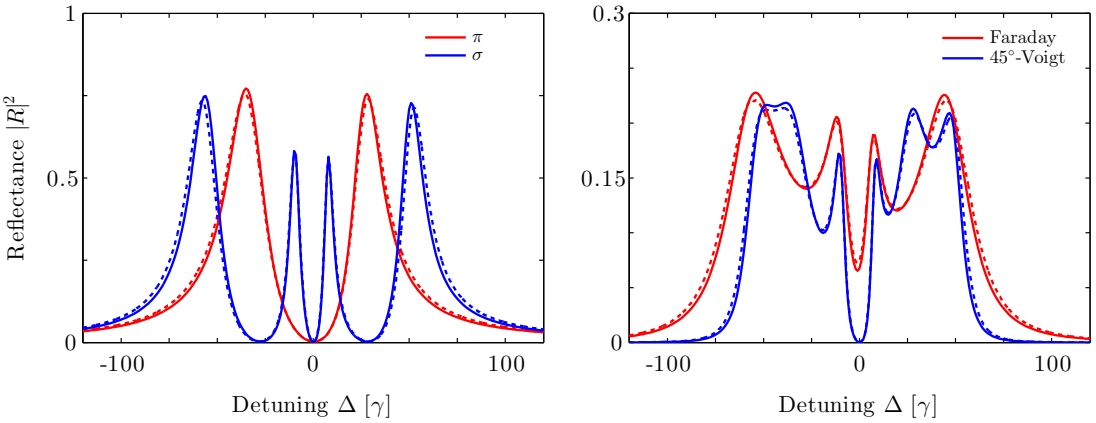

Figure 5.3: Spectra of the cavity with a magnetized ^{57}Fe layer calculated from Eq. (5.20) (solid lines) and simulations by CONUSS (dashed lines) are shown for different geometrical configurations. For all curves the parameters $dpq = (-7.8 + i2.7)\gamma$ and $|dp^2| = 7.7\gamma$ were used. Additionally, for the π and the σ *geometry*, an offset $r = 0.006 + i0.065$ in the reflection coefficient accounts for the residual response of the electronic scattering, which is blocked by polarization filtering in the geometries depicted in the right panel.

5.3 Quantum optical approach

Even though we found analytical expressions for most of the geometrical configurations defined in Sec. 5.1, it is yet unclear which is the underlying mechanism that causes the sharp minima observed in the reflection spectra. This question will be resolved in the next sections. In contrast to the previous analysis which was based on the semi-classical layerformalism, we will apply our quantum optical model to the scenario with a magnetized ^{57}Fe layer, in which then multiple Zeeman-splitted transitions can be driven. It will be shown that the occurrence of the interference minima are caused by vacuum induced coherences. But before we turn to this effect in detail, we first apply the quantum description to our setting.

5.3.1 Quantum model for a magnetized ^{57}Fe layer

In this section we include the magnetic hyperfine splitting to the quantum optical model developed in Chap. 3. There, we formulated the equations of motion for the general case including a possible magnetization. However, so far, only for $\boldsymbol{B}_{\mathrm{hf}} = 0$ explicit expressions for the reflection coefficient were calculated. Since in the absence of a Zeeman splitting only one ground and one excited state has to be taken into account, for these calculation essentially only the solution of a two-level system was required. Here, the degeneracy of the ground and excited states in the ^{57}Fe nucleus is lifted and thus multiple resonances in the spectrum of the reflectance are expected. Since the magnetization tags one direction in space, the rotational invariance observed in the results for the unmagnetized layer will break down. In Secs. 3.2.1 and 3.2.2 we found that an analytic treatment is still feasible in the linear regime as only one collective ground state $|G\rangle$ is coupled to up to six collective excited states $|E_\mu^{(+)}\rangle$, each one resembling one transition μ. According to Eq. (3.52), the steady state values of the coherences $\langle E_\mu^{(+)}|\rho|G\rangle$ need to be calculated to obtain the reflection coefficient, which corresponds to the task of solving a linear system of equations with up to six unknown variables.

If the six collective transitions were independent of each other, the nuclear part of the reflection coefficient would be the sum of the respective Lorentz curves. However, this is not the case here as the transitions are mutually coupled via the Hamiltonian H_{LS} and via the Lindblad operator $\mathcal{L}_{\mathrm{cav}}[\rho]$ in Eqs. (3.50) and (3.51). These couplings depend on the orientation of $\hat{\boldsymbol{B}}_{\mathrm{hf}}$. Moreover,

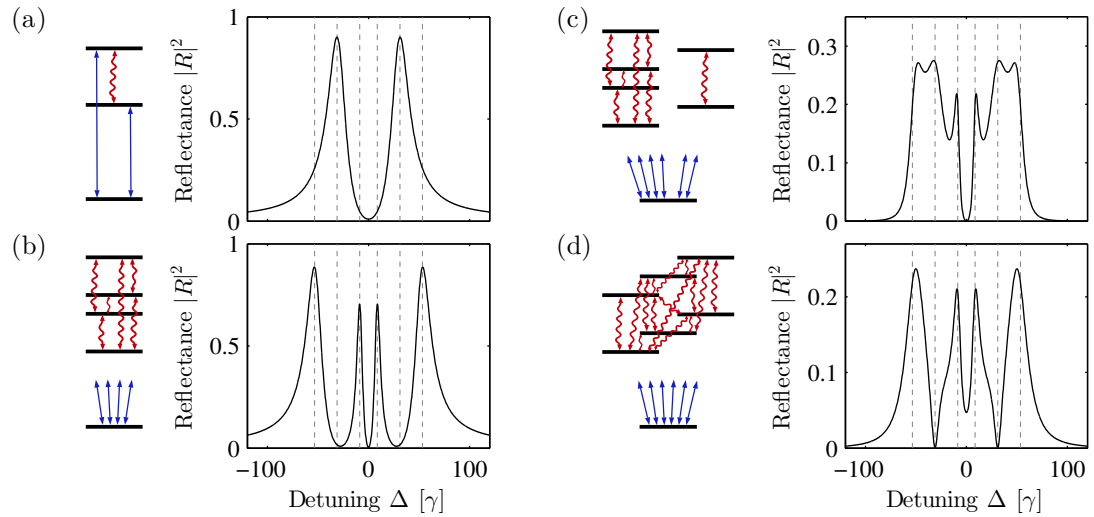

Figure 5.4: Engineering of nuclear level schemes. Depending on the choice of the input polarization and the nuclear magnetization axes, different level schemes are obtained. The configurations (a) π *geometry*, (b) σ *geometry*, (c) *45°-Voigt geometry* and (d) *Half-Faraday geometry* are shown. The obtained level scheme are shown on the left, and the right column shows the corresponding reflectance. The excited states $|E_\mu^{(+)}\rangle$ are mutually coupled due to H_{LS} and $\mathcal{L}_{\mathrm{cav}}$ (red curly arrows) and coherently probed by H_Ω (blue). Spontaneous decay channels and Lamb shifts are not shown in the level diagram for clarity. The vertical lines in the reflectance plots indicate the resonance frequencies of the six transitions. Other parameters are as in Fig. 3.4.

the incidence and detection polarizations $\hat{\boldsymbol{a}}_{\mathrm{in}}$ and $\hat{\boldsymbol{a}}_{\mathrm{out}}$ influence the obtained spectra in a non-trivial way. Therefore, we expect significant deviations in the spectra from a naive sum of Lorentzians and a strong dependence on the relative orientation of the axes $\hat{\boldsymbol{B}}_{\mathrm{hf}}$, $\hat{\boldsymbol{a}}_{\mathrm{in}}$ and $\hat{\boldsymbol{a}}_{\mathrm{out}}$.

Effective level schemes for different choices of the polarization and magnetization alignment are shown in Fig. 5.4. The number of excited states and, equally important, their respective couplings induced by the cavity modes are modified considerably. This indicates that a vast range of different quantum optical level schemes can be engineered in a single sample, only by suitably choosing the different polarization and magnetization axes. Accordingly, also the reflectances differ from each other as can be seen in the right panel of Fig. 5.4. Comparing the spectra with those calculated numerically with CONUSS in Fig. 5.2 or with the layerformalism in Fig. 5.3, the agreement is excellent.

This is a first indication that our quantum optical model is applicable also in the case of magnetized ^{57}Fe layers. But the consistency between the models goes beyond the similarities observed in the figures above. We calculate the analytical expressions for the reflection coefficient using the equations of motion for the coherences defined in Eqs. (3.49)–(3.51) for the different geometrical settings. Note that in our notation introduced in Chap. 3, the equations are given for the coupling of the electrical polarization vectors $\hat{\boldsymbol{a}}_{\mathrm{in}}$ and $\hat{\boldsymbol{a}}_{\mathrm{out}}$ to the electric components of the transition axes $\hat{\boldsymbol{\pi}}^0$ and $\hat{\boldsymbol{\sigma}}^\pm$. Since ^{57}Fe features a M1 transition, the quantization axis $\hat{\boldsymbol{\pi}}^0$ is therefore not identical to the magnetization direction $\hat{\boldsymbol{B}}_{\mathrm{hf}}$, but rotated by 90° in the ($\boldsymbol{\pi}$, $\boldsymbol{\sigma}$) plane.

Solving for the steady state coherences $\langle E_\mu^{(+)}|\rho|G\rangle$, we find for the reflection coefficients (c.f. Eq. (3.52))

$$\begin{aligned} R_\pi &= R_C + R_T(2F_0)\,, \\ R_\sigma &= R_C + R_T(F_{-1} + F_{+1})\,, \\ R_{\mathrm{Faraday}} &= \tfrac{i}{2}R_T(2F_{+1}) - \tfrac{i}{2}R_T(2F_{-1})\,, \end{aligned}$$

$$R_{\mathrm{Voigt}} = \tfrac{1}{2} R_T(2F_0) - \tfrac{1}{2} R_T(F_{-1} + F_{+1}) \,, \tag{5.21}$$

with

$$R_C = \frac{2\kappa_R}{\kappa + i\Delta_C} - 1 \,, \tag{5.22}$$

$$R_T(T) = \frac{\kappa_R \, |g|^2 N}{2i \, (\kappa + i\Delta_C)^2} \; \frac{1}{\frac{1}{T} + \frac{|g|^2 N}{4(\Delta_C - i\kappa)}} \,, \tag{5.23}$$

and $F_0, F_{\pm 1}$ as in Eq. (5.12). Comparing these results with the reflection coefficient in Eq. (5.20) which we obtained previously with the layerformalism, we find perfect agreement even on the analytical level. The quantum optical approach naturally includes the electronic scattering response R_C for the π and σ *geometry*, which in case of the layerformalism had to be added manually in the curves shown in Fig. 5.3. For the nuclear response, a direct mapping of the functions $R_T(T)$ and $R_{\mathrm{Eigenpol}}(T)$ in Eq. (5.15) can be found for the two respective results by identifying

$$\begin{aligned} \sqrt{d}\, p \;&\sim\; \frac{|g|\sqrt{N}\sqrt{2\kappa_R}}{2(\Delta_C - i\kappa)} \,, \\ \sqrt{d}\, q \;&\sim\; \frac{i|g|\sqrt{N}}{2\sqrt{2\kappa_R}} \,. \end{aligned} \tag{5.24}$$

In particular, from these relations it can be seen that the atom number scaling of both theories is in accordance as $d \propto N$.

Our analysis reveals that the two methods yield identical results for the reflectance in the linear regime even on the analytical level, despite their completely independent approaches. It is instructive to compare the central elements in the two descriptions. In the layerformalism, the scattering amplitudes for two transitions coupling to linearly and four transitions coupling to circularly polarized light enter. Also within the quantum optical framework, we naturally obtain these six transitions. This analogy is expected, since both the approaches are linear in the probing field. Another analogy exists in the couplings between the different transitions. As in the quantum optical description they are mediated via the tensor $\mathbb{1}_\perp$ (c.f. Eqs. (3.50) and (3.51)), it is easy to see that for (anti-) parallel or orthogonal orientation of $\boldsymbol{B}_{\mathrm{hf}}$ with respect to $\hat{\boldsymbol{k}}$, the excited states split into distinct subsets which are not mutually coupled. This is visualized in the effective level diagrams shown in Fig. 5.4, where in particular the scheme of the *45°-Voigt geometry* consists of two groups of excited states. This corresponds to the situation in which the scattering matrix in the layerformalism decomposes as it can be written as a combination of two eigenpolarizations (see Sec. 5.2.1).

Interestingly, the quantum optical calculation presented here does not rely on this decomposition into subsets of excited states. Even for the most general case a linear system of six coupled equation has to be solved, still allowing for analytic expressions for the reflectance. This includes the setting of the *Half-Faraday geometry*, where, using the layerformalism, it was not possible to find an expression with the ansatz employed in this work. In contrast, the quantum optical approach enables analytic calculations for general choices of the axes and agrees with the previous numerical results. Note, however, that the obtained analytical results are too bulky to be presented here.

Detailed discussion of the $\boldsymbol{\pi}$ *geometry*

In the section above we found analytic solutions of our quantum optical model for different geometrical settings. Here, we will theoretically discuss an exemplary case in more detail with the aim to understand the origin of the spectral features in more detail. To this end, we consider the π *geometry* shown in Fig. 5.4(a), where $\hat{\boldsymbol{a}}_{\mathrm{in}} \parallel \hat{\boldsymbol{a}}_{\mathrm{out}} \parallel \boldsymbol{\pi}$, $\hat{\boldsymbol{B}}_{\mathrm{hf}} \parallel \boldsymbol{\sigma}$. Here, only the linearly polarized transitions ($\mu = 2, 5$, c.f. Tab. 3.1) are driven. For simplicity we set $N_1 = N_2 = N/2$

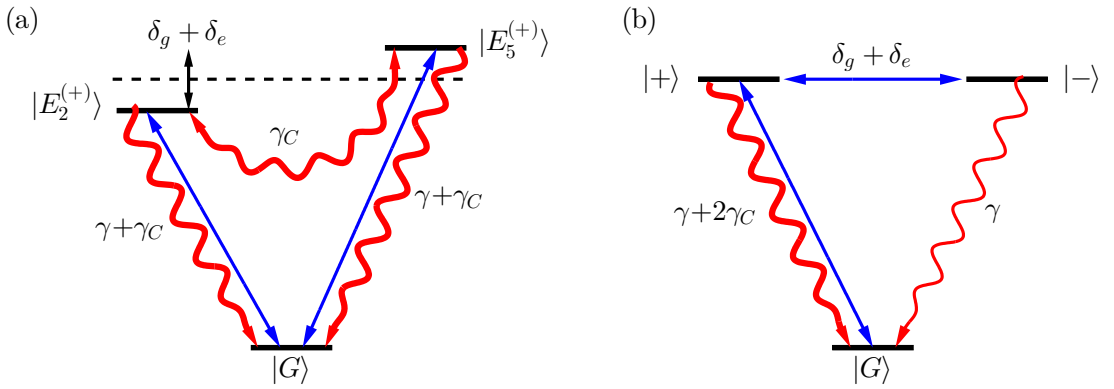

Figure 5.5: The effective level system obtained if the linearly polarized transitions are driven by the probing field in the presence of a magnetic splitting. Collective Lamb shifts are not considered in the figure for clarity. (a) The collective ground state $|G\rangle$ is coherently coupled to the two possible excited states (solid blue arrows). Both states decay superradiantly (singly-headed red curly arrows) and are coupled via cross-decay terms (double-headed curly arrow). (b) After a basis transition, only the symmetric state $|+\rangle$ is probed by the incident field. It is coupled to the antisymmetric state $|-\rangle$, which is metastable on the superradiantly accelerated decay time scale of $|+\rangle$ since it decays only at the single-nucleus incoherent decay rate.

for the distribution of the nuclear ground states in the following. Similar to the analysis without magnetization discussed in Sec. 3.3, we introduce the states

$$|+\rangle = \frac{1}{\sqrt{2}}\left(|E_5^{(+)}\rangle + |E_2^{(+)}\rangle\right) , \tag{5.25}$$

$$|-\rangle = \frac{1}{\sqrt{2}}\left(|E_5^{(+)}\rangle - |E_2^{(+)}\rangle\right) . \tag{5.26}$$

The full Hamiltonian written in this basis is found from our general theory as

$$\begin{aligned} H = &-\Delta\big(|+\rangle\langle+| + |-\rangle\langle-|\big) + \tfrac{1}{2}(\delta_g+\delta_e)\big(|+\rangle\langle-| + |-\rangle\langle+|\big) \\ &+ \left(\sqrt{\tfrac{2}{3}N}\Omega g|+\rangle\langle G| + \text{H.c.}\right) + \tfrac{2}{3}N\delta_{\text{LS}}|g|^2|+\rangle\langle+| . \end{aligned} \tag{5.27}$$

This form reveals that only the fully symmetric state $|+\rangle$ of all allowed singly excited states is driven by the applied probe field. But in contrast to the case without magnetic field, the symmetric state $|+\rangle$ is coupled to a different state $|-\rangle$ in the presence of the magnetic field splitting, such that now a system of two linear equations needs to be solved. For the full treatment one has to consider the decay of the two involved excited states in addition. It turns out that the density matrix element $\langle+|\rho|G\rangle$ decays exponentially due to spontaneous emission and enhanced by superradiance with rate $\frac{1}{2}\gamma + \frac{2}{3}N\zeta_S|g|^2$, while $\langle-|\rho|G\rangle$ decays only with rate $\gamma/2$. Since the superradiant decay is much faster than intrinsic spontaneous emission, $|-\rangle$ is metastable on the evolution timescale of $|+\rangle$. The origin of the suppression of the decay lies in the special form of the incoherent dynamics in Eq. (3.51). Due to the presence of the cross-decay terms (the parts with $\mu \neq \nu$), not the bare excited states $|E_2^{(+)}\rangle$ and $|E_5^{(+)}\rangle$, but the (anti-)symmetrized states $|+\rangle$ and $|-\rangle$ are the radiative eigenstates with respect to the total decay. Hence, the cross-decay terms naturally induce a coherence between the excited states which is known as spontaneously generated coherence (SGC). These SGC will be discussed in detail in the next section.

The full level scheme for this particular orientation of polarizations and magnetization is shown in more detail in Fig. 5.5. The complexity of the large ensemble of nuclei readily visible in the single-nucleus basis $|E_\mu^{(+)}\rangle$ is entirely hidden in the description with $|+\rangle$ and $|-\rangle$. In the latter

basis, the nuclear ensemble can be identified with a typical V or Λ level scheme, as required for electromagnetically induced transparency (EIT) [116]. Therefore, it is clear that we rediscover the well known transparency dip known from EIT also in the reflectance of our system. The deep interference minima in other geometric realizations can be understood in a similar way.

5.3.2 Spontaneously generated coherences

Before we continue with our analysis of the x-ray cavity, we will give a brief excursus on spontaneously generated coherences (SGC) in this section and illustrate their role in quantum optical systems and their influence on related phenomena.

A short review of SGC

The seemingly simple process of spontaneous emission (SE) is surprisingly complex [148]. It is not an inevitable intrinsic immutable property of a given quantum system, but can be tailored to one's advantage. Already the golden rule expression $\gamma \sim |\boldsymbol{d}|^2 D(\omega)$, where $\boldsymbol{d}$ is the dipole moment, and $D(\omega)$ the bath mode density, points to two fundamentally different approaches. On the one hand, the environment or bath can be modified. For example, increasing the mode density via a cavity leads to enhanced emission (Purcell effect [114]), whereas band gaps in photonic crystals can suppress SE. On the other hand, the dipole moment $\boldsymbol{d}$ by which the system couples to the bath provides another handle to manipulate spontaneous emission. Decoherence-free subspaces are a prominent example for this approach [195, 196]. However, somewhat surprisingly, the vacuum itself can induce cancellation of SE in this spirit. Ironically, the interaction with the vacuum which is the origin of spontaneous emission trips itself up by inducing a dynamics which eventually leads to a cancellation of the emission.

In a multi-level quantum system virtual photons can in principle be emitted on one transition, and re-absorbed on another transition. This leads to an atomic coherence between the upper states involved, which is known as a spontaneously generated coherence (SGC) [140, 147, 148]. This coherence in turn leads to destructive interference between the emission channels from the upper to the common lower state, effectively modifying or even canceling SE – a key challenge in quantum engineering. A multitude of fascinating applications have been suggested in this context, such as lasing without inversion [197–199], modifying the resonance fluorescence [200, 201], enhancing non-linear responses [202], quantum control of light propagation [203, 204], quantum coherence in semiconductor-based devices [205, 206], creation of entanglement [207], stabilization of coherence in quantum computation schemes [208, 209] or increasing the efficiency of solar cells [210] or quantum heat engines [211].

The archetype model system for SGC is a three-level system with two upper and one common lower state (V-configuration) [140, 147, 148]. If SGC between upper states is established, the system can be trapped in the excited states despite its coupling to the environment.

However, so far, stringent conditions on the appearance of SGC have hindered an experimental realization, even though a number of setups have been suggested to circumvent these conditions [140, 147], however, at the cost of requiring complex geometries [150, 212], or extended level schemes and external driving fields [213–215]. One experiment aimed at observing SGC in a V-type level structure [216], but its results could not be reproduced [217]. Previously, it has been shown that observations in artificial quantum systems [205] can be interpreted in terms of SGC [199].

The reason for this lack of experimental evidence are two major requirements on the structure of the quantum system, which are hardly ever fulfilled simultaneously, hindering an experimental implementation. First, the dipole moments of the transitions absorbing and emitting the virtual photon must be nonorthogonal. Second, the involved transition energies have to be near-degenerate on the level of the respective transition widths. Otherwise, the virtual photon emitted by the first transitions cannot be absorbed on the second. More fundamentally, the conditions

are related to the fact that it must not be possible to know in principle which of the different decay pathways was taken [218].

An alternative route to observing vacuum-induced coherences is to switch to Λ-type atoms in which a common excited state decays to multiple lower states. In Λ-type atoms, the requirement of non-orthogonal dipole moments can be alleviated, if an extra interaction is used to erase the knowledge to which of the different lower states the atom has decayed. Only then, interference can occur. For example, detection of a spontaneously emitted photon in a particular direction with particular polarization can project the atom into a superposition of two ground states [219, 220], as the photon does not allow to extract the information of the emission pathway. Also quantum eraser like setups can remove the which-way information in the atomic state after SE, such that the transient vacuum-induced coherence does affect the dynamics [221–223]. Alternatively, the stringent conditions of near-degenerate transitions with non-orthogonal quantum systems have recently been realized in an artificial three-level quantum system in Λ-configuration [224]. But all of these approaches have the drawback that the SE of the excited state cannot be suppressed in Λ-type setups, prohibiting most desirable applications.

SGC in a toy model

In order to show some properties of a system exhibiting the SGC phenomenon, we consider an archetype level scheme in V-configuration in the following. It consists of a ground state $|g\rangle$ and two excited states $|1\rangle$ and $|2\rangle$. This is very similar to the setting resembling the π *geometry*, which we discussed in the previous section. A general master equation is then used to describe the time evolution of the density matrix ρ for this multi-level system. Following the discussion and notation in Ref. [140], it reads

$$\frac{d}{dt}\rho = -\frac{i}{\hbar}[H,\rho] - \frac{1}{2}\sum_{i,j=1}^{2}\gamma_{ij}\mathcal{L}\left[\rho, S_{i+}, S_{j-}\right] \ . \tag{5.28}$$

The first part constitutes the von-Neuman equation [151], responsible for the coherent evolution of the density matrix. The Lindblad-type operators

$$\mathcal{L}\left[\rho, S_{i+}, S_{j-}\right] = S_{i+}S_{j-}\rho + \rho S_{i+}S_{j-} - 2S_{j-}\rho S_{i+} \tag{5.29}$$

in the second term cover the incoherent process such as spontaneous emission. Here, $S_{i+} = |i\rangle\langle g|$ $[S_{i-} = |g\rangle\langle i|]$ denotes the raising [lowering] operator on transition i. Let us first take a look at the Lindblad terms in Eq. (5.28) with $i = j$. These parts yield the well-known process of spontaneous emission from the upper levels $|i\rangle$ to the ground state $|g\rangle$. Setting up the equations of motion for the populations, we obtain

$$\frac{d}{dt}\langle i|\rho|i\rangle = -\gamma_{ii}\langle i|\rho|i\rangle \qquad \forall i \in \{1,2\} \ , \tag{5.30}$$

$$\frac{d}{dt}\langle g|\rho|g\rangle = \gamma_{11}\langle 1|\rho|1\rangle + \gamma_{22}\langle 2|\rho|2\rangle \ , \tag{5.31}$$

which correspond to the exponential decays of the two excited states to the ground state, as one would expect.

Next, we include the terms from Eq. (5.28) with $i \neq j$, which are known as cross-damping or cross-decay terms [140, 147]. In free space, the decay rates γ_{ij} are found as

$$\gamma_{ij} = \sqrt{\gamma_{ii}\gamma_{jj}}\,\frac{\boldsymbol{d}_i \cdot \boldsymbol{d}_j^*}{|\boldsymbol{d}_i||\boldsymbol{d}_j^*|}. \tag{5.32}$$

Here $\boldsymbol{d}_i$ is the dipole moment of the transition $|g\rangle \leftrightarrow |i\rangle$. It can be immediately recognized that the cross-damping terms only contribute if the dipole moments are nonorthogonal, as states

above. For simplicity, we set $\gamma_{11} = \gamma_{22} = \gamma$ and denote the cosine between the transition dipole moments by p, such that $\gamma_{12} = \gamma_{21} = p\gamma$. This results in the master equation

$$\begin{aligned}\frac{d}{dt}\rho = &-\frac{\gamma}{2}\ (|1\rangle\langle 1|\rho + \rho|1\rangle\langle 1| - 2|g\rangle\langle 1|\rho|1\rangle\langle g|)\\ &-\frac{\gamma}{2}\ (|2\rangle\langle 2|\rho + \rho|2\rangle\langle 2| - 2|g\rangle\langle 2|\rho|2\rangle\langle g|)\\ &-\frac{p\gamma}{2}\,(|1\rangle\langle 2|\rho + \rho|1\rangle\langle 2| - 2|g\rangle\langle 2|\rho|1\rangle\langle g|)\\ &-\frac{p\gamma}{2}\,(|2\rangle\langle 1|\rho + \rho|2\rangle\langle 1| - 2|g\rangle\langle 1|\rho|2\rangle\langle g|)\ .\end{aligned} \tag{5.33}$$

A straightforward interpretation of this equation cannot be gained, hence, we transform the system into a symmetrized basis. We introduce the states

$$|\pm\rangle = \frac{1}{\sqrt{2}}\,(|1\rangle \pm |2\rangle) \tag{5.34}$$

and obtain for the master equation [140, 147]

$$\begin{aligned}\frac{d}{dt}\rho = &-\frac{\gamma}{2}(1+p)\,(|+\rangle\langle +|\rho + \rho|+\rangle\langle +| - 2|g\rangle\langle +|\rho|+\rangle\langle g|)\\ &-\frac{\gamma}{2}(1-p)\,(|-\rangle\langle -|\rho + \rho|-\rangle\langle -| - 2|g\rangle\langle -|\rho|-\rangle\langle g|)\ .\end{aligned} \tag{5.35}$$

In this form it is easily recognized that the decay rate of the symmetric state is enhanced, while for the antisymmetric state it is suppressed. In the limit of parallel transition dipole moments, i.e. $p = 1$, the state $|-\rangle$ is even immune to spontaneous emission.

The effect, that coherences are spontaneously generated can be best seen from the long time behavior of this system. If the atom is initially prepared in the bare excited states, this can be rewritten in the symmetrized basis

$$|\psi_i\rangle = |1\rangle = \frac{1}{\sqrt{2}}\,(|+\rangle + |-\rangle)\ . \tag{5.36}$$

Consequently, upon free propagation of this system, the population in state $|+\rangle$ will decay, but a fraction of the atom will always reside in the excited states due to the non-zero initial overlap with the stable state $|-\rangle$. Hence, for long times the system the system will be in the state

$$\begin{aligned}\rho_f &= \frac{1}{2}|g\rangle\langle g| + \frac{1}{2}|-\rangle\langle -|\\ &= \frac{1}{2}|g\rangle\langle g| + \frac{1}{4}|1\rangle\langle 1| + \frac{1}{4}|2\rangle\langle 2| - \frac{1}{4}|1\rangle\langle 2| - \frac{1}{4}|2\rangle\langle 1|\ .\end{aligned} \tag{5.37}$$

This way, population has been transfered to the second excited state $|2\rangle$ [201] and a coherence between the two upper states is spontaneously built up, which is commonly denoted as spontaneously generated coherence. This is a remarkable result, since the cross-damping terms does not obey a unitary time evolution and thus can be seen as an incoherent process.

Finally, we extend our discussion to the non-degenerate case of the excited states and shift the resonance energies by $\pm\delta$. Further, we apply a weak coherent driving field Ω in the Hamiltonian and calculate the susceptibility, i.e. the response of the system to the radiation field, given by $\chi \propto -\langle 1|\rho|g\rangle - \langle 2|\rho|g\rangle$. Results with included and omitted cross-damping terms are shown in Fig. 5.6. Without the effect of SGC, the result is a plain superposition of two Lorentzians, each one resembling one of the resonances, without any interference phenomena. The outcome drastically changes if the cross-damping terms are included in the calculation. In the center of the two resonances the imaginary part of the susceptibility completely vanishes, indicating the absence of absorption. As we have already shown in the last section, this is reminiscent of

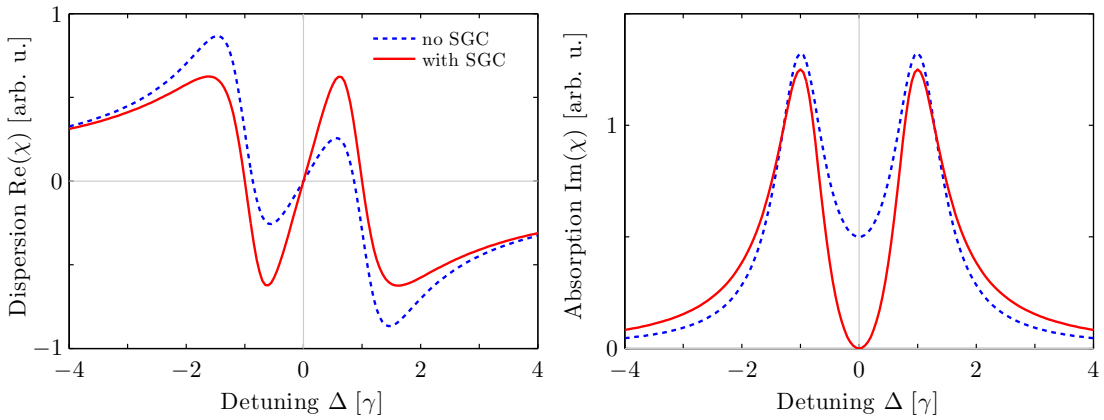

Figure 5.6: The susceptibility of an archetype 3-level SGC scheme in V-configuration is shown. Dashed curves indicate the relations for a system with SGC turned of. In the SGC case, the absorption vanishes one resonance. Parameters used: $\Omega = 0.1\gamma$, $\delta = \gamma$.

electromagnetically induced transparency (EIT). In EIT, interference occurs due to the coherent couplings in the Hamiltonian. Here, despite the analytical equivalence to the EIT case, the underlying effect differs. The cross-damping terms induce SGC between the excited states which in turn is reflected in interference appearances.

5.3.3 SGC in the x-ray cavity setting

On the basis of the discussion on the π *geometry*, we have exemplarily seen that cross-damping terms spontaneously generate coherences in the ^{57}Fe nuclei. In addition, it was shown that these SGC cause deep interference minima in the medium response. Therefore, it is expected that SGC are the reason for the prominent minima observed in the reflectance of our cavity in the different geometrical settings as well.

Employing the layerformalism, which is based on the semi-classical description of the light-matter interaction in the cavity, the different physical processes contributing to the spectrum can not be distinguished in detail. Furthermore, the model does not provide a handle to interpret the signatures in the reflectance. The quantum optical description, however, allows us to clearly identify, separate and characterize all physically relevant processes contributing to the result.

Effect of SGC on the reflectance

In the general master equation characterizing the dynamics of the cavity and the embedded nuclei, it is possible to artificially switch off the effect of SGC by omitting the cross-damping terms in Eq. (3.51). Note that an according procedure cannot be applied for the semi-classical methods. We performed calculations with and without SGC and the results are summarized in Fig. 5.7. The blue curves in the upper panels correspond to the reflectance spectra calculated for the *Faraday geometry*, the *Half-Faraday geometry* and the *45°-Voigt geometry*, showing the same structure as already observed in the simulations by CONUSS (Fig. 5.2) and by the layerformalism (Fig. 5.3). The red curves correspond to the spectra where the effect of SGC was artificially turned off. Clearly, the results are different. In particular, the two deep minima in the *Half-Faraday geometry* and, interestingly, the disappearance of the central dip in the *Faraday geometry* are clear indications of SGC.

For the *45°-Voigt geometry*, however, the spectra including and omitting SGC agree up to a scaling factor and the deep interference minimum in the center occurs for both cases. The reason for this is connected with the polarization for the reflected x-rays, which is chosen by an

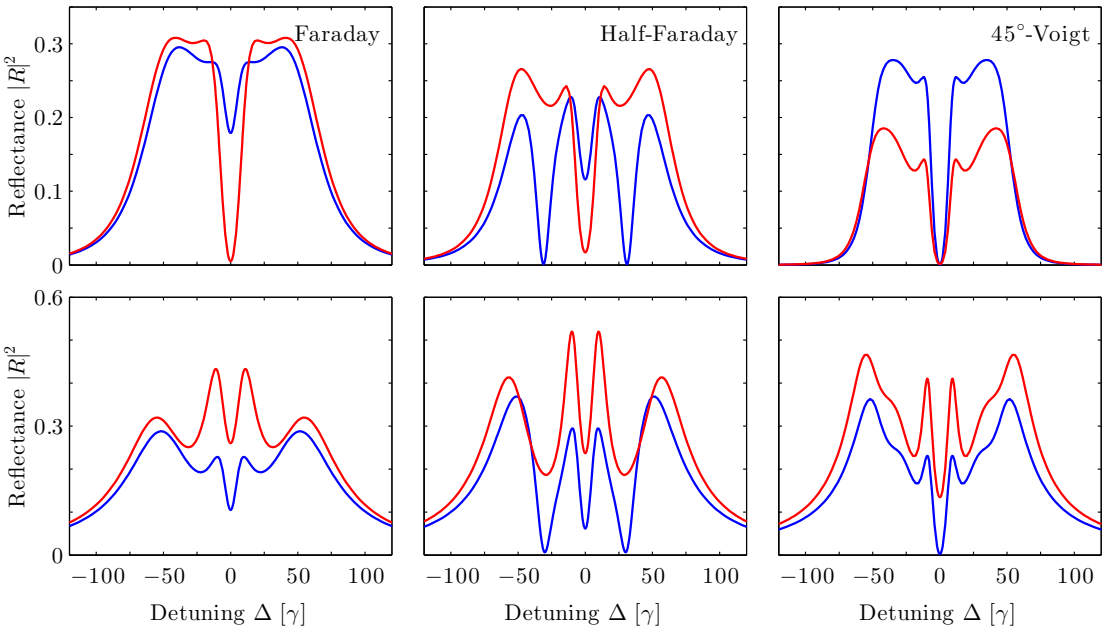

Figure 5.7: Calculated reflection spectra for the *Faraday geometry*, the *Half-Faraday geometry* and the *45°-Voigt geometry*. The blue curves represent the full reflectance obtained by the quantum optical model, red curves show simulations where the SGC couplings were omitted. In the top row the polarization of the reflected x-rays was included, in the lower row it was not taken into account, mimicking a polarization-insensitive detection. Scaled parameters are $\kappa = 45\gamma, \kappa_R = 25\gamma, |g|^2 N = 2500\gamma^2, \Delta_C = 0$.

analyzer crystal. This polarization-sensitive measurement can act as an interferometer, which effectively induces interferences between different scattering paths in the polarimeter. This can lead to spectral signatures which can overlap with the desired SGC structures. Note that the first polarizer in the setup alone cannot induce such spectral signatures, as it merely prepares a well-defined polarization state. Only the second analyzer crystal can erase the which way information and therefore give rise to interference structures.

To disentangle this interference effect from the influence of SGC on the reflection spectra, we performed further simulations, in which a polarization-insensitive detector is assumed. This can be achieved in the same way as presented in Eq. (5.19) for the layerformalism. The results are shown in the lower panels in Fig. 5.7. The effect of the analyzer crystal is particularly well visible in the case of the *45°-Voigt geometry*. Comparing the two curves with and without analyzer crystal for the case without SGC, one finds that the analyzer crystal alone can already induce a deep interference minimum at zero detuning. Only by removing the analyzer in the optical path, the central dip in the spectrum can be fully attributed to the presence of SGC.

Origin of SGC

Having identified the process leading to the prominent structures in the reflectance, this raises the question, why the SGC contributions are crucial in our setting, whereas they do not contribute, e.g., for atoms in free space. Interestingly, in our setup, SGC emerge due to two fundamentally different mechanisms.

The first contribution visualized in Fig. 5.8(a) occurs on the basis of single nuclei, and arises from the fact that for certain parameter choices, the nuclei experience a spatially anisotropic photonic density of states in the cavity. To illustrate this, suppose a quantization axis parallel to $\boldsymbol{\pi}$, induced by a perpendicular magnetization direction $\hat{\boldsymbol{B}}_{\mathrm{hf}}$. The two-dimensional polarization space in the cavity transverse to the propagation direction $\hat{\boldsymbol{k}}$ can be described by the orthonormal

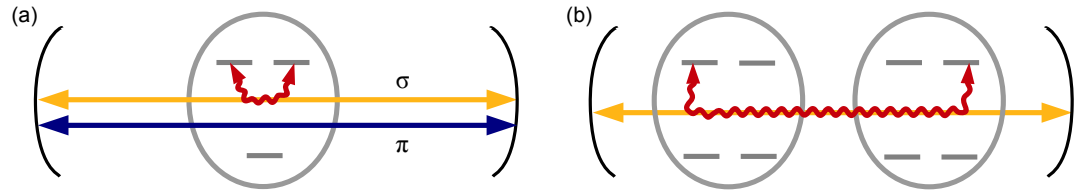

Figure 5.8: Origin of the spontaneously generated coherences. (a) For certain orientations of $\hat{\boldsymbol{B}}_{\mathrm{hf}}$ relative to $\hat{\boldsymbol{k}}$, the relevant nuclear transitions couple only to a single cavity polarization, giving rise to an anisotropic cavity vacuum and SGC between orthogonal transition dipoles. (b) In a collective effect photons are exchanged between different transitions in different nuclei. Probing the cavity as a whole results in effective SGC.

basis vectors $\boldsymbol{\pi}$ and $\boldsymbol{\sigma}$. In this configuration, the $\Delta m = 0$ transitions have dipole moments parallel to $\boldsymbol{\pi}$, whereas the $\Delta m = \pm 1$ transitions have dipole moments proportional to $\boldsymbol{\sigma} \pm i\hat{\boldsymbol{k}}$. Thus, the circularly polarized photons can only interact with the cavity mode polarized along $\boldsymbol{\sigma}$, but not with that along $\boldsymbol{\pi}$. As a result, the cavity appears as having only one polarization, and thus a spatially anisotropic density of states. As predicted theoretically in Refs. [150, 212], an anisotropy of this type leads to SGC. In contrast, in free space, two polarization modes would contribute, and the two (non-zero) SGC contributions of the two polarizations cancel each other. This mechanism can also be interpreted in terms of a "hidden metastable state" [225]. In our case, the anisotropic vacuum leads to the formation of a nuclear state which is metastable with respect to the cavity mode. Note, however, that this state is not metastable with respect to the remaining free space vacuum modes, and, therefore, does not exist in free space. Finally, we note that even though being a single-nucleus effect, it is assisted by cooperativity, since superradiant line broadening larger than the energetic splitting of the two transitions renders them indistinguishable.

The second mechanism giving rise to SGC is a collective effect involving multiple nuclei [226], see Fig. 5.8(b). Suppose, a photon is emitted by one nucleus with linear polarization on a $m_e = 1/2 \rightarrow m_g = 1/2$ transition. It can be re-absorbed in a different nucleus on the $m_g = -1/2 \rightarrow m_e = -1/2$ transition with dipole moment (anti-)parallel to the emitting dipole moment. On this microscopic level, this constitutes an interaction between two different nuclei. The probe beam, however, does not resolve the dynamics of the individual nuclei, but probes the ensemble-cavity system as a whole. As a consequence, this exchange process inside the cavity appears as an effective coupling between different excited states within the level scheme of the single effective nucleus. In this sense, the complicated many-body dynamics of the ensemble of nuclei mediated by the cavity acts as a "quantum simulator" [227], which mimics a single effective quantum system with properties which go beyond those of each of the individual nuclei. Here, we specifically exploit this simulation technique to induce SGC in the effective level scheme observed by the x-ray beam probing the total ensemble-cavity system.

5.4 Experimental realization and results

To verify the SGC experimentally, a planar x-ray cavity consisting of a Pd(5 nm)/C(40 nm)/ Pd(20 nm) layer system with a 2.5 nm thick ^{57}Fe layer placed in the center of the carbon layer was prepared by the group of Ralf Röhlsberger. In order to avoid perturbing nuclear hyperfine interactions at the ^{57}Fe/C interface, the ^{57}Fe was sandwiched between two 0.6 nm layers of ^{56}Fe, which in the present context has identical properties except for the resonance that we probe. At the total thickness of 3.7 nm the Fe layer orders ferromagnetically with the magnetization confined to the plane of the film due to the magnetic shape anisotropy. In this environment the magnetic hyperfine field at the ^{57}Fe nucleus amounts to ≈ 33 T that lifts the degeneracy of

the magnetic sublevels, resulting in up to six dipole-allows transitions with specific polarization properties. The spectral response of the system is probed via the reflectance of the cavity for near-resonant x-rays impinging on the cavity in grazing incidence.

Managed by the group of Ralf Röhlsberger, Hans-Christian Wille, and with support from the Institute for Optics and Quantum Electronics in Jena and the Helmholtz Institute Jena, we performed the experiments at the PETRA III synchrotron radiation source (DESY, Hamburg) [95] employing the method of nuclear resonant scattering. This technique relies on the pulsed broadband excitation of nuclear levels followed by the time-resolved detection of the delayed photons that are emitted on a timescale $\tau = 1/\gamma$ after resonant excitation. To determine the energy spectrum of the cavity reflection signal from the time-resolved data, we used a resonant analyzer foil (1 μm stainless steel, enriched to 95% in ^{57}Fe, providing a single line transmission with a spectral width of $\approx$ 10 neV) that was mounted on a Doppler drive. Single photons were counted as function of energy detuning Δ within a time window from 50 - 190 ns after excitation. Under these conditions one obtains a very close correspondence of the measured data with the energy spectra of the cavity reflectivity, similar to the method reported in Ref. [52]. This approach will be discussed in more detail in Sec. 6.1.4. For the detection we employ two different approaches. First, a polarimetry setup provided by the Institute for Optics and Quantum Electronics in Jena and the Helmholtz Institute Jena was integrated into the experiment [194] in order to fully take advantage of the six possible polarization-sensitive transitions resulting from the magnetic hyperfine splitting. The polarimeter consists of two Si(840) polarizer crystals in crossed setting with the sample in-between, so that it ideally only transmits photons whose polarization has been rotated ($\boldsymbol{\sigma} \rightarrow \boldsymbol{\pi}$) upon the interaction with the nuclei. This way, the polarization state of the scattered photons can be selected while off-resonant background photons are suppressed by almost 10 orders of magnitude. Experimentally, we explore the *Faraday geometry*, the *Half-Faraday geometry* and the *45°-Voigt geometry*. In all three configurations strong orthogonal scattering $\boldsymbol{\sigma} \rightarrow \boldsymbol{\pi}$ takes place.

However, for certain geometries, the polarimeter setup can act as an interferometer, thereby hindering the unambiguous detection of SGC as shown in the previous section. In particular, the central dip predicted for the *45°-Voigt geometry* caused by SGC is superimposed with an interference structure induced by the detection setup if the analyzer is used. To clearly separate the effect of SGC, the analyzer was omitted in a second detection approach and the spectrum for the *45°-Voigt geometry* was recorded using a high resolution monochromator for the incident light to suppress the non-resonant background. This way, all interference structures can directly be attributed to SGC.

The experimental data was evaluated by Ralf Röhlsberger, and the measured spectra are shown in Fig. 5.9 in combination with calculated spectra obtained by CONUSS. Taking into account the detection technique, the numerical simulations reproduce the data very well. In particular, the deep interference minima due to SGC are clearly visible. In the case of the *Faraday geometry* it turned out that the spectrum can be explained only if, quite conceivable, a slight misalignment of the internal magnetic field is assumed. As calculations indicate, this causes further minima already for small angles, as shown in the red curve in the upper left panel in Fig. 5.9. Interestingly, we found that these minima also arise due to the presence of SGC. The remaining difference between the simulation and the data is mainly due to time-gating effects during the measurement process. Note that since the data for the *45°-Voigt geometry* was recorded without the analyzer crystal to suppress non-interacting photons, the background rate is significantly higher despite the time gating.

The reduction of the reflected intensity at certain detunings can directly be traced back to the presence of non-decaying metastable excited states, formed due to the presence of SGC [201]. Our measurements therefore amount to a direct observation of SGC between excited states, inducing a modified spontaneous decay. It should be noted that we observe near-perfect interference minima in the *Half-Faraday* and *45°-Voigt geometry* in the sense that the reflected intensities drop down to the baseline. In the language of quantum optics, this indicates that the system is essentially

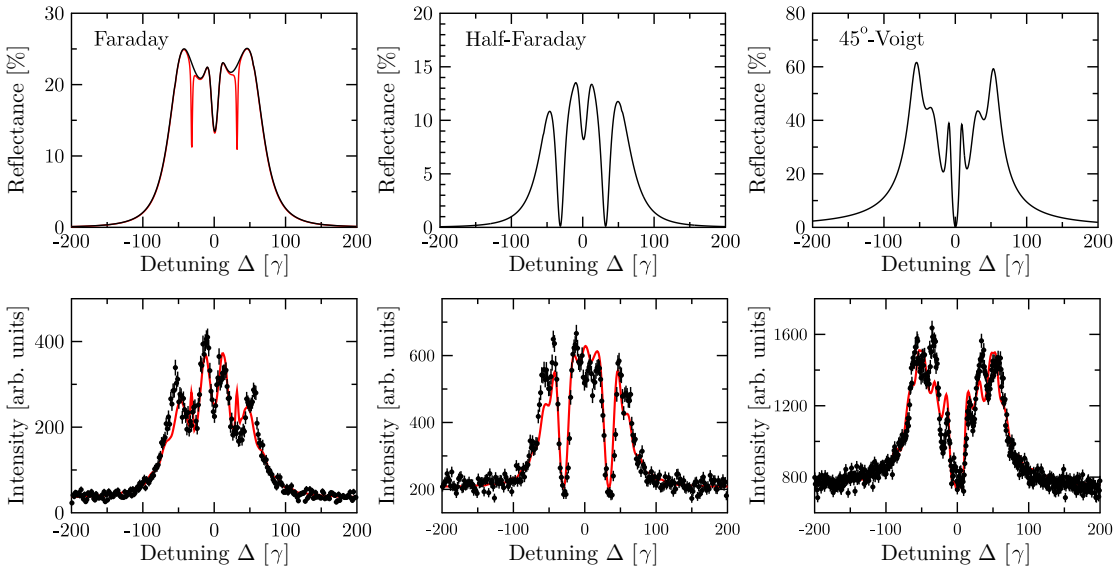

Figure 5.9: Theoretical predictions and experimental results. The three columns show data for three magnetization geometries. Theoretical predictions obtained with CONUSS are presented in the upper row. In the lower row the experimental data and simulations taking into account the scattering geometry, the measurement process and the sample parameters are shown. The additional red curve in the top left panel shows the result predicted with a small angular deviation used to model the experimental data in the bottom right panel. The dips in the reflected intensity down to the background baseline for the *Half-Faraday* and the *45°-Voigt geometry* clearly indicate the presence of SGC in an essentially decoherence-free system. Image adapted from Ref. [50].

decoherence-free over the experimental time scales, as any perturbation would inevitably lead to loss of coherence, and therefore, of a reduction of the interference leading to the SGC minimum in the spectra.

Our results not only provide an avenue to the exploitation of SGC, but also demonstrate that genuinely new systems like high-grade noise free quantum optical level schemes can be engineered in the nuclear regime. The capitalization of the hyperfine splitting together with a suitable choice of the polarization and the magnetization in particular enables us to realize continuously tunable and dynamically reconfigurable quantum optical level schemes in the hard x-ray regime. A single simple solid state target system thus can be manipulated dynamically and on demand to perform different tasks. The range of accessible level schemes becomes even richer if the hyperfine splitting is combined with cavities involving multiple ensembles of resonant atoms [56], possibly subject to individually differing magnetizations. Future setups could also involve dynamical control of the physical target structure [55]. Finally, it should be noted that our approach to realize SGC is not restricted to nuclear resonances, but can also be applied with atoms, ions, or artificial quantum systems properly placed in cavities.

Chapter 6

Time Domain Control Of X-Ray Pulses

Manipulation of light propagation is a well-recognized technique with applications in different branches in optics. In particular, sub-luminal light pulses are known to undergo enhanced nonlinearities [121], enable quantum entanglement schemes [122] and allow for optical switching or light storage [228]. First demonstrated in the visible frequency regime [229–231], slow light has by now been implemented in a number of platforms [232, 233], particularly also in cavity settings [234, 235]. Slowing down light pulses, or more precisely, reducing their group velocity, is possible if the refractive index changes rapidly as a function of the wavelength in a suitable dielectric material. Ideally, the absorption of the light should be small at the same time. Such a dispersion relation can be found, e.g., in systems featuring electromagnetically induced transparency (EIT) [116, 118].

Manipulation of light propagation has also been reported in the x-ray regime. In Ref. [90], a delayed peak in the transmitted x-ray light intensity has been observed. In this case, however, the pulse delay is induced by the propagation of the light through a doublet absorber structure rather than electromagnetically induced transparency or related effects, and can be interpreted as arising from transitions between super- and subradiant states. Also coherent storage of light via rapid control of the applied quantization field has been reported [53]. Other experiments with nuclei observed electromagnetically induced transparency [56], related spontaneously generated coherences with equivalent susceptibilities [50], or other transparency mechanisms [66, 89]. However, these experiments concentrated on spectral properties and did not study the delay or the actual pulse propagation.

Here, we investigate the reflection of spectrally narrow x-ray pulses from a thin-film cavity in the time domain. We find that by engineering a suitable nuclear level scheme in the cavity, the time-resolved response of the x-ray pulse can be manipulated, such that sub-luminal light propagation is realized. Furthermore, we introduce a scheme in which this time delay can be observed using broadband synchrotron light instead of spectrally narrow x-rays and, hence, is easily accessible with existing equipment. Our implementation includes a conventional Mössbauer drive, which is typically placed in the optical path to measure the reflectance spectrum. We show that this additional element can as well be exploited for the desired time-domain study.

In this chapter we will first perform a theoretical analysis of a full experimental stage including the Mössbauer drive and show how it can be used to access the spectral properties of the cavity in an experimental setting. Next, we discuss the basic concepts of sub-luminal light propagation and show its relation to the x-ray pulse reflection from our cavity. This allows us to tailor cavity designs in which the time-domain related effects are maximized. In a next step, we present the experimental implementation, in which we observed x-ray time delays up to 35 ns. This experiment was carried out together with the group of Ralf Röhlsberger (DESY, Hamburg), Rudolf Rüffer (ESRF, Grenoble) and with support from the Institute for Optics and Quantum Electronics in Jena and the Helmholtz Institute Jena. In the last section, our theoretical analysis is extended to describe the measured time-resolved signal in Fourier space. Distinct features of this representation are discussed and an alternate method to extract spectroscopic signatures is introduced. Finally, this novel method is applied to experimental data.

6.1 Analysis of the complete experimental stage

With the theory developed in the previous chapters, we are able to calculate the response of the cavity with embedded resonant nuclei for a vast range of settings, including arbitrary magnetization of the sample and adjustable polarization of the incident and reflected light. The focus of this part will be the question which properties of this response can actually be observed experimentally. In chapters 4 and 5 we already showed measurement results for the reflection spectra, however, a detailed description how they could be obtained is still lacking. In order to address this problem we will review the typical scheme employed in experimental settings.

An incident x-ray pulse formed by synchrotron radiation closely resembles a δ-like pulse in the time domain. Current synchrotron sources produce pulse lengths of several 10-100 ps. On the timescale of the lifetime of the nuclear transition which is several orders of magnitudes larger, the δ-like pulse description can be considered valid. Already from its Fourier limit it is clear that the x-ray pulse contains many frequencies. As calculated in Sec. 3.4, the spectrum of the reflected light is given by the reflectance $|R_{\mathrm{Cavity}}(\Delta)|^2$. Naively, the spectral components could be analyzed in a spectrometer or separated by a grating, such that different positions on the detector screen correspond to different frequencies. However, this is essentially an impossible task due to the lack of suitable optical elements in the x-ray regime and also since the characteristic line width $\gamma = 4.66$ neV is much too small to be resolved in this fashion.

Alternatively, the time response can be measured in an experiment relatively simple. The narrow properties in the frequency domain translate directly in long time scales. The time response $R_{\mathrm{Cavity}}(t)$ is given by the Fourier transform of $R_{\mathrm{Cavity}}(\Delta)$ and detectors with time resolution of some ns are well suited to record such time spectra. A time spectrum was measured, for example, in Ref. [52] in order to prove the existence of a superradiant state in the cavity. The time response of a Lorentz-like spectrum as we found for the reflectance in Sec. 3.3 in the case of an unmagnetized layer would be given by an exponential decay. The time spectrum for the case of magnetized layers is slightly more advanced, since we found that SGC features appear in the reflectance, see Chap. 5. However, only the absolute value $|R_{\mathrm{Cavity}}(t)|$ and not the phase information is experimentally accessible in this way. This prohibits to obtain the full spectral information. For example, the collective Lamb shift measured in Ref. [52] would only manifest in an inaccessible global phase in the time domain response.

Hence, in order to measure spectral properties of the light reflected from the cavity, other techniques have to be applied. One method would be not to probe the cavity with broadband synchrotron radiation, but with spectrally narrow x-ray pulses. Such pulses are provided in the radioactive emission from ^{57}Co sources like in traditional Mössbauer spectroscopy. Alternatively, various schemes exist in which a narrowband pulse is created from synchrotron radiation, see Sec. 2.1.3. But both approaches typically suffer from a low signal rate. In order to measure the cavity spectrum, another method is often employed: An additional frequency-selective element is placed in the optical path of the experiment, which allows to determine spectral properties of the cavity.

The device which we discuss here is a stainless steel foil enriched in ^{57}Fe which is operated in nuclear forward scattering (NFS) geometry. In this setting, the x-ray impinges parallel to the foil's surface normal and excites a collective nuclear state in the sample, which is known as nuclear exciton [51, 109]. This state relaxes by emitting radiation primarily in forward direction. Similar as the cavity, a frequency dependent response function is mapped to the light field by the NFS foil and we denote this response by $T_{\mathrm{NFS}}(\Delta)$. In order for the foil to be operated as a frequency-selective device, it is mounted on a Doppler- or Mössbauer drive. In this case, if the foil is moving with velocity v, the frequency seen by the sample is shifted by the Doppler detuning Δ_D as

$$\omega' = \omega \left(1 + \frac{v}{c}\right) = \omega + \Delta_D \, . \tag{6.1}$$

Due to the large magnitude of the radiation frequency ω, only velocities in the range of some

mm/s are required to scan the interesting ranges of the spectra several line widths around the resonance frequency. In the laboratory frame the response function of the foil can be written as $T_{\mathrm{NFS}}(\Delta - \Delta_D)$ and the combined response of the cavity and the ^{57}Fe foil is simply the product of the two response functions in frequency domain

$$R_{\mathrm{total}}(\Delta, \Delta_D) = \underbrace{R_{\mathrm{Cavity}}(\Delta)}_{\text{Cavity reflection}} \cdot \underbrace{T_{\mathrm{NFS}}(\Delta - \Delta_D)}_{^{57}\text{Fe foil transmission}} . \tag{6.2}$$

If a time sensitive avalanche photo detector is used in the experiment, the measured signal is the absolute value of the Fourier transform of the full response

$$I(t, \Delta_D) = \left| \frac{1}{\sqrt{2\pi}} \int e^{-i\Delta t}\, R_{\mathrm{Cavity}}(\Delta) \cdot T_{\mathrm{NFS}}(\Delta - \Delta_D)\, d\Delta \right|^2 . \tag{6.3}$$

In contrast to the time spectrum of a cavity alone, the intensity measured with the ^{57}Fe foil in the optical path depends on the externally controllable parameter Δ_D. As we will show in Sec. 6.1.4, for large times $I(t, \Delta_D) \sim |R_{\mathrm{Cavity}}(\Delta_D)|^2$ and hence the spectrum of the cavity can be retrieved.

6.1.1 Time-domain interpretation

In the discussion above we used that the combined response of the cavity and the ^{57}Fe foil is the product of the individual response functions in frequency domain. This shall be motivated in the following. To this end, the time-resolved signal at the detector is calculated in the time domain picture. We will assume that the driving field strength is weak and the light-matter interaction can be treated linearly.

Let us assume an arbitrary input pulse shape in time domain defined by the complex field $E(t)$. If the pulse is reflected at the cavity, the process of reflection can be considered independently at each point of time due to linearity. Combining the individual responses of the field at different times, we can write the full amplitude via a convolution of the input pulse and the time domain response of the cavity $E(t) * R_{\mathrm{Cavity}}(t)$. At the next stage, the pulse interacts with the Mössbauer drive. Denoting its time domain response by $T_{\mathrm{NFS}}(t, \Delta_D)$, the signal behind the drive is given by

$$I(t, \Delta_D) \propto |E(t) * R_{\mathrm{Cavity}}(t) * T_{\mathrm{NFS}}(t, \Delta_D)|^2 . \tag{6.4}$$

At this point we can apply the convolution theorem reversely, which states that the Fourier transform of a convolution in time domain is equivalent to a multiplication of the corresponding functions in frequency domain. Thus, we obtain from Eq. (6.4)

$$I(t, \Delta_D) \propto \left| \int e^{-i\Delta t}\, E(\Delta) \cdot R_{\mathrm{Cavity}}(\Delta) \cdot T_{\mathrm{NFS}}(\Delta, \Delta_D)\, d\Delta \right|^2 . \tag{6.5}$$

If the incident x-ray pulse is δ-like, i.e. $E(t) \propto \delta(t)$, the pulse described in frequency domain is a constant and the expression above reduces to Eq. (6.3) from the last section.

The time-domain formulation of the interaction sequence might give a more intuitive picture why the frequency domain responses can simply be multiplied. Though, we emphasize that this holds only in the linear regime. As soon as the radiation field reflected from the cavity, i.e. a_{out}, exhibits non-linear or quantum mechanical features such as photon (anti-)bunching, the two devices in the optical path cannot be considered independently. Rather, the Mössbauer drive then needs to be "driven" with the operator $a_{\mathrm{out}}(t)$ instead of the classical field $\langle a_{\mathrm{out}} \rangle(t)$, such that the quantum properties are correctly transfered between the two devices. Then, in addition, a full quantum theory for the NFS setting of the ^{57}Fe foil which includes non-linear effects would be required to adequately model the Mössbauer drive.

6.1.2 Theoretical description

Now we consider a realistic experimental setup, in which the thin-film cavity is placed in the optical path together with a thin stainless steel foil, mounted on a Doppler drive. The foil contains resonant ^{57}Fe nuclei and constitutes an additional frequency-selective element. In this setting, the incident light is reflected from the cavity and is sent through the stainless steel foil in forward scattering geometry. Subsequently, the x-rays are detected. The theoretical description of this setting is discussed in the following.

Cavity reflection coefficient

With the quantum optical theory presented in Chap. 3, the spectral properties of the x-rays reflected from the cavity can be calculated. In Chap. 5, it was shown how the theory can also be applied in the case of a magnetic hyperfine splitting of the resonant ^{57}Fe nuclei and arbitrary polarization settings. The complex reflection coefficient of the cavity is denoted by $R_{\mathrm{Cavity}}(\Delta)$. Accordingly, we write for the response in the time domain, i.e. its Fourier transform, $R_{\mathrm{Cavity}}(t)$.

For a plain cavity without magnetization, the reflectance consists of an energy-independent part given by the cavity background as well as the nuclear response, yielding a Lorentzian line shape modified by cooperative phenomena, see Eq. (3.58). The spectral expression can be transformed into time domain as

$$\begin{aligned} R_{\mathrm{Cavity}}(t) &= \frac{1}{\sqrt{2\pi}} \int R_{\mathrm{Cavity}}(\Delta)\, e^{-i\Delta t} d\Delta \\ &= \left(-1 + \frac{2\kappa_R}{\kappa + i\Delta_C}\right) \sqrt{2\pi}\, \delta(t) - \frac{\frac{4}{3}\kappa_R |g|^2 N}{(\kappa + i\Delta_C)^2} \sqrt{2\pi}\, \theta(t)\, \exp\left(-\left(\tfrac{\gamma}{2} + \tfrac{2}{3}\, \tfrac{|g|^2 N}{\kappa + i\Delta_C}\right) t\right) , \end{aligned} \tag{6.6}$$

where the second term constitutes an exponentially decaying function characteristic of a Lorentz spectrum. Note that the Fourier transform is sometimes defined with a different sign convention in the exponent. However, since the nuclear resonances have the form $(\Delta + i\gamma/2)^{-1}$, our choice is required in order to imply causality, as indicated in the Heaviside step function $\theta(t)$.

Another important cavity setting is a configuration featuring spontaneously generated coherences (SGC), see Chap. 5. In the simplest scenario, a magnetic field causes a splitting in the ^{57}Fe nuclei and with suitable polarization choice, only the linearly polarized transitions are driven. This is denoted as the π *geometry* (c.f. Sec. 5.1). The corresponding reflection coefficient is given in Eq. (5.21). In order to calculate its Fourier transform, we consider the spectral expression

$$\tilde{R}(\Delta) = \left[2\left(\frac{c_1}{\Delta + \delta_1 + i\frac{\gamma}{2}} + \frac{c_2}{\Delta + \delta_2 + i\frac{\gamma}{2}}\right)^{-1} + c_0\right]^{-1} \tag{6.7}$$

which has an equivalent structure as the cavity reflection coefficient. Its Fourier transform is found as

$$\begin{aligned} \tilde{R}(t) &= \frac{1}{\sqrt{2\pi}} \int_{-\infty}^{\infty} \tilde{R}(\Delta)\, e^{-i\Delta t} d\Delta \\ &= \sqrt{\tfrac{\pi}{2}}\, e^{-\frac{\tilde{\Gamma}}{2} t}\, \Theta(t) \left[2\tfrac{\partial\tilde{\Omega}}{\partial c_0} \sin\left(\tfrac{\tilde{\Omega} t}{2}\right) - i(c_1 + c_2) \cos\left(\tfrac{\tilde{\Omega} t}{2}\right)\right] \end{aligned} \tag{6.8}$$

with the constants

$$\tilde{\Gamma} = \gamma - \tfrac{i}{2} c_0 (c_1 + c_2) - i(\delta_1 + \delta_2)\,, \tag{6.9}$$

$$\tilde{\Omega} = \left[(\delta_1 - \delta_2)^2 + (\tfrac{c_0}{2})^2 (c_1 + c_2)^2 + c_0 (\delta_1 - \delta_2)(c_1 - c_2)\right]^{\frac{1}{2}} . \tag{6.10}$$

Eq. (6.8) can easily be verified by transforming this expression back into the frequency domain. Note that the time domain response of the *Faraday geometry* can be calculate using this result as well, as its spectral reflection coefficient consists of two summands of the form of $\tilde{R}$.

Transmission function of the ^{57}Fe foil

In frequency domain, the influence of the stainless steel foil enriched in ^{57}Fe, i.e. the Mössbauer drive, can be described with the single-line transmission function [236–241]

$$T_{\mathrm{NFS}}(\Delta) = \exp\left(-\frac{iL\gamma/4}{\Delta - \Delta_D + \frac{i}{2}\gamma}\right), \tag{6.11}$$

where $\Delta = \omega - \omega_0$ is the detuning from the nuclear resonance, Δ_D accounts for an additional detuning due to the Doppler shift of the moving drive, $L = \sigma_0 f_{\mathrm{LM}} n d$ denotes an effective thickness consisting of cross section $\sigma_0 = 2464$ kbarn, Lamb-Mössbauer factor $f_{\mathrm{LM}} \approx 0.8$, number density of resonant nuclei $n = 75$ nm^{-3} and foil thickness d. In the time domain, the response of the stainless steel foil is given by the Fourier transform of Eq. (6.11) and reads

$$T_{\mathrm{NFS}}(t) = \sqrt{2\pi}\delta(t) - \theta(t) e^{-\frac{\gamma}{2}t - i\Delta_D t}\sqrt{\frac{\pi L\gamma}{2t}} J_1\left(\sqrt{L\gamma t}\right) . \tag{6.12}$$

Here $\delta(t)$ denotes the Dirac delta function, $\theta(t)$ the Heaviside step function and J_1 the Bessel function of first order.

6.1.3 Time-resolved intensity at the detector

As explained above, the frequency domain signal arriving at the detector can be described via the product of the cavity reflection coefficient and the transmission function of the Mössbauer drive

$$I(\Delta, \Delta_D) \propto |R_{\mathrm{Cavity}}(\Delta) \cdot T_{\mathrm{NFS}}(\Delta, \Delta_D)|^2 . \tag{6.13}$$

Transforming the amplitude into the time domain yields the time-resolved signal at the detector

$$R(t, \Delta_D) = \frac{1}{\sqrt{2\pi}} \int_{-\infty}^{\infty} R_{\mathrm{Cavity}}(\Delta)\, T_{\mathrm{NFS}}(\Delta, \Delta_D)\, e^{-i\Delta t} d\Delta , \tag{6.14}$$

$$I(t, \Delta_D) \propto |R(t, \Delta_D)|^2 . \tag{6.15}$$

This expression was already given in Eq. (6.3) and corresponds to the quantity which is accessible in experiments. While the Fourier integral can be straightforwardly computed numerically for general choices of the cavity reflection coefficient, it is instructive to perform an analytical study. To this end, we use the series representation of the transmission function

$$T_{\mathrm{NFS}}(\Delta, \Delta_D) = \exp\left(-\frac{iL\gamma/4}{\Delta - \Delta_D + \frac{i}{2}\gamma}\right) = \sum_{n=0}^{\infty} \frac{(-iL\gamma/4)^n}{n!} (\Delta - \Delta_D + i\gamma/2)^{-n} . \tag{6.16}$$

Next, we split the sum in two parts, where the first summand covers $n = 0$ and the second the rest. For the full temporal response, we obtain

$$R(t, \Delta_D) = R_\delta(t) + R_{\mathrm{SNXP}}(t, \Delta_D) , \tag{6.17}$$

with

$$R_\delta(t) = (2\pi)^{-\frac{1}{2}} \int R_{\mathrm{Cavity}}(\Delta)\, e^{-i\Delta t} d\Delta , \tag{6.18}$$

$$R_{\mathrm{SNXP}}(t, \Delta_D) = \sum_{n=1}^{\infty} \frac{(-iL\gamma/4)^n}{n!} (2\pi)^{-\frac{1}{2}} \int R_{\mathrm{Cavity}}(\Delta)(\Delta - \Delta_D + i\gamma/2)^{-n}\, e^{-i\Delta t} d\Delta . \tag{6.19}$$

The abbreviations chosen for the indices denote that the respective quantities form the responses of δ-like and spectrally narrow x-ray pulses (SNXP) interacting with the cavity. This will become apparent in Sec. 6.3.1. The contribution $R_\delta(t)$ corresponds to the temporal responses of photons which did not interact with the Mössbauer drive, while $R_{\mathrm{SNXP}}(t, \Delta_D)$ is the amplitude of those photons which did interact. From Eq. (6.18) it can be seen that $R_\delta(t)$ is the Fourier transform of the cavity response only. Hence, often, it can be easily calculated with the expressions given above.

Let us now turn to the second part $R_{\mathrm{SNXP}}(t, \Delta_D)$. Since the integral in each summand of R_{SNXP} contributes mainly in the small range around $\Delta \approx \Delta_D$ we expand the cavity reflection coefficient $R_{\mathrm{Cavity}}(\Delta)$ around Δ_D. Since the cavity spectrum is typically broadened due to superradiance, it can be assumed that the amplitude in this range is constant. However, the phase of the reflection coefficient demands for a more thorough treatment, since first, it can change rapidly, and second, the phase in the Fourier transform is known to typically carry more information [242]. Hence, we expand the phase up to first order and our approximation reads

$$R_{\mathrm{Cavity}}(\Delta) \approx R_{\mathrm{Cavity}}(\Delta_D)\, e^{i(\Delta-\Delta_D)\tau}\ , \tag{6.20}$$

where we have defined

$$\tau = \frac{\partial \arg[R_{\mathrm{Cavity}}]}{\partial \Delta}\Big|_{\Delta_D}\ . \tag{6.21}$$

We will see in Sec. 6.2.2 that this quantity is also the delay, which a pulse experiences during the propagation through the cavity [243]. Inserting the approximation from above into Eq. (6.19), we obtain

$$\begin{aligned}
&R_{\mathrm{SNXP}}(t, \Delta_D) \\
&\quad\approx \sum_{n=1}^{\infty} \frac{(-iL\gamma/4)^n}{n!}(2\pi)^{-\frac{1}{2}} \int R_{\mathrm{Cavity}}(\Delta_D)(\Delta - \Delta_D + i\gamma/2)^{-n}\, e^{i(\Delta-\Delta_D)\tau}\, e^{-i\Delta t} d\Delta \\
&\quad= \sum_{n=1}^{\infty} \frac{(-iL\gamma/4)^n}{n!}(2\pi)^{-\frac{1}{2}} \int (\Delta + i\gamma/2)^{-n}\, R_{\mathrm{Cavity}}(\Delta_D)\, e^{-i\Delta_D t}\, e^{-i\Delta(t-\tau)} d\Delta \\
&\quad= \sum_{n=1}^{\infty} \frac{(-iL\gamma/4)^n}{n!} R_{\mathrm{Cavity}}(\Delta_D) e^{-i\Delta_D t}(2\pi)^{-\frac{1}{2}} \int (\Delta + i\gamma/2)^{-n}\, e^{-i\Delta(t-\tau)} d\Delta \\
&\quad= \sum_{n=1}^{\infty} \frac{(-iL\gamma/4)^n}{n!} R_{\mathrm{Cavity}}(\Delta_D) e^{-i\Delta_D t}(2\pi)^{-\frac{1}{2}} \left(2\pi(-i)^n e^{-\frac{\gamma}{2}(t-\tau)}\Theta(t-\tau)\frac{(t-\tau)^{n-1}}{(n-1)!}\right) \\
&\quad= -\, e^{-\frac{\gamma}{2}(t-\tau)}\Theta(t-\tau) R_{\mathrm{Cavity}}(\Delta_D) e^{-i\Delta_D t} \sqrt{\frac{\pi L\gamma}{2(t-\tau)}} J_1\left(\sqrt{L\gamma(t-\tau)}\right)\ .
\end{aligned} \tag{6.22}$$

The exponential envelope and the Bessel function shape could already be seen in Eq. (6.12) and represent the well-known structure from the time response in nuclear forward scattering. Apart from the prompt part contained in $R_\delta(t)$, Eq. (6.12) would be reobtained in the absence of the cavity, i.e. $R_{\mathrm{Cavity}} = 1$ and thus $\tau = 0$.

6.1.4 Measuring the cavity spectrum

The total field signal detected in an experimental setting is given by Eq. (6.17) and contains the significant information related to the cavity. In general, both summands R_δ and R_{SNXP} contribute to the observed intensity. However, for large times t, the second term outlives the first contribution. The reason for this is that its response decays exponentially with the rate of the natural line width γ which can be seen from Eq. (6.22), whereas R_δ decays much faster due to the superradiant enhancement, c.f. Eq. (6.6).

Therefore, the summand R_{SNXP} determines the observed signal at large times. Since it is proportional to the cavity reflection coefficient, the cavity spectrum can be measured by recording the signal in a suitable time gating window $[t_1, t_2]$ as

$$|R_{\mathrm{Cavity}}(\Delta_D)|^2 \propto \int_{t_1}^{t_2} I(t, \Delta_D) dt \; . \tag{6.23}$$

This procedure to measure the cavity spectrum was successfully employed in Secs. 4.1.2 and 5.4 as well as in Refs. [50, 52]. From Eq. (6.17) it becomes clear that a late starting point t_1 for the time gating is desirable, since for times shortly after the initial excitation R_δ will also contribute to the recorded signal and interference terms appear. On the other hand, a late starting point is at the cost of counting statistics. Hence, it is advisable to record the data in the complete time range and select an optimized time gating window in the subsequent data analysis. Further, this would allow to employ alternative schemes to measure the energy-resolved spectra, such as the one described in Ref. [240].

Going beyond integrating over the available time range to determine the reflectance spectrum, let us take a closer look at the time dependence of the recorded intensity. As already noted before, the long-time signal R_{SNXP} shows the characteristics of the NFS time signal. In particular, the Bessel function in Eq. (6.22) causes a beating pattern due to its roots where $J_1 = 0$. In contrast to the typical NFS spectrum, however, the signal is shifted by the time τ. Obviously, this shift is induced by the cavity. As we will show in the next sections, this reveals sub-luminal propagation of x-ray pulses in the cavity.

6.2 Slow light and delayed x-ray pulses

Since the result in the previous section suggests a possible time delay, we will review the basic theory describing the propagation of light pulses and the related group velocity control. Additionally, we study the reflection of x-ray pulses in the time domain and show the relation between those two effects.

6.2.1 Propagation of light pulses in dispersive media

Let us assume a spectrally narrow pulse $E(\omega)$, centered around the frequency ω_0, which propagates through a dispersive medium of length L and with refractive index $n(\omega) = \sqrt{1+\chi(\omega)} \approx 1 + \chi(\omega)/2$. Behind the medium, the pulse can be described in time domain by

$$E(L,t) = \frac{1}{\sqrt{2\pi}} \int E(\omega) e^{i(kL-\omega t)} d\omega \; , \tag{6.24}$$

with complex wave vector $k = n(\omega)\omega/c = k_R + ik_I$. Close to the resonance in an atomic EIT-like medium, the susceptibility χ allows for the expansion

$$k_R(\omega) \approx k_R(\omega_0) + \frac{\partial k_R}{\partial \omega}\Big|_{\omega_0} (\omega - \omega_0) \; , \tag{6.25}$$

$$k_I(\omega) \approx k_I(\omega_0) \; , \tag{6.26}$$

in which the linear order of k_I vanishes. Then, the field becomes

$$E(L,t) = \frac{1}{\sqrt{2\pi}} e^{-k_I(\omega_0)L} \; e^{-i(\omega_0 t - k_R(\omega_0)L)} \int E(\omega) e^{i(\omega-\omega_0)\left(\frac{\partial k_R}{\partial \omega}\big|_{\omega_0} L - t\right)} d\omega \; , \tag{6.27}$$

where the first exponential accounts for absorption, the second for a global phase velocity and the integral covers the pulse envelope propagating with the group velocity v_{gr}. According to

Eq. (6.27), it reads [116]

$$v_{\mathrm{gr}} = \left(\frac{\partial k_R}{\partial \omega}\Big|_{\omega_0} \right)^{-1} = \left(\frac{\partial}{\partial \omega} \frac{\omega\, n_R}{c} \right)^{-1} \Big|_{\omega=\omega_0} = \frac{c}{n_R + \omega \frac{\partial n_R}{\partial \omega}}\Big|_{\omega=\omega_0} . \tag{6.28}$$

From this expression it can be seen that a suitable tailored refractive index allows for the control of the pulse propagation velocity v_{gr}. A dispersion relation in which $\omega \frac{\partial n_R}{\partial \omega} \gg 1$ can give rise to extremely reduced group velocities.

6.2.2 Time delay in pulse reflection

Now let us turn to a related setting, in which we assume the reflection of light pulses from complex structures, such as a cavity. This covers the setting in this work, however the following discussion is not restricted to the x-ray regime.

Again, we assume a spectrally narrow pulse $E(\omega)$ with central frequency ω_0. It is reflected by a cavity with complex reflection coefficient $R_{\mathrm{Cavity}}(\omega)$. For an analogy with the pulse propagation discussed in the previous section, we also describe it in time domain as

$$E(t) = \frac{1}{\sqrt{2\pi}} \int E(\omega) R_{\mathrm{Cavity}}(\omega) e^{-i\omega t} d\omega \, , \tag{6.29}$$

where we omitted the phase $k \cdot L$ of free propagation for simplicity. If the incident pulse $E(\omega)$ is spectrally narrow on the scale of the reflection coefficient, the latter can be approximated by (c.f. Eq. (6.20))

$$R_{\mathrm{Cavity}}(\omega) \approx R_{\mathrm{Cavity}}(\omega_0)\; e^{i(\Delta - \Delta_D)\tau} \, , \tag{6.30}$$

$$\tau = \frac{\partial \arg[R_{\mathrm{Cavity}}]}{\partial \omega}\Big|_{\omega_0} . \tag{6.31}$$

With this approximation, we obtain for the reflected pulse

$$E(t) = \frac{1}{\sqrt{2\pi}} R_{\mathrm{Cavity}}(\omega_0) e^{-i\omega_0 t} \int E(\omega) e^{i(\omega-\omega_0)(\tau - t)} d\omega \, . \tag{6.32}$$

Similar as in the last section, the first parts describe a global phase change and account for absorption, while the integral covers the propagation of the pulse envelope. From the equation above it can immediately be recognized that the envelope propagation is influenced by the cavity, as it is shifted in time. This means, the pulse is delayed by the time τ compared to the case where a reflection structure is absent.

We thus find that the pulse is delayed by the time τ, defined in Eq. (6.31), due to the cavity dispersion without distortion of the pulse shape, as it is well known from cavities and waveguides in the visible regime [244, 245]. Depending on the exact phase relation in R, light pulses slower ($\tau > 0$) and also faster ($\tau < 0$) than the speed of light can be obtained in general.

Comparing results of the envelope propagation for the reflected pulse in Eq. (6.32) and for the slow light in dispersive media in Eq. (6.32), we can identify

$$\frac{\partial \,\mathrm{Re}(\chi)}{\partial \omega}\Big|_{\omega_0} \sim \frac{2c}{\omega_0 L} \frac{\partial \arg(R)}{\partial \omega}\Big|_{\omega_0} . \tag{6.33}$$

Similar, from the comparison of the absorption factors we find

$$\mathrm{Im}\left(\chi(\omega_0)\right) \sim -\frac{2c}{\omega_0 L} \log\left(|R(\omega_0)|\right) \, . \tag{6.34}$$

From these relations we can directly see that the phase and the modulus of the complex reflection coefficient effectivly take the role of the real and imaginary part of the atomic susceptibility,

respectively [243]. Hence, a direct mapping between the theories for light propagation in atomic gases and for nuclear reflection is obtained. Finally, we note that relations (6.33) and (6.34) are directly found by comparing

$$\exp\left(i\,\frac{\omega_0 L}{2c}\,\chi\right) \sim R\,. \tag{6.35}$$

6.2.3 Calculation of the x-ray time delay in different cavity settings

In the section above we have seen that spectrally narrow pulses can experience a time delay upon the reflection from structures such as a thin-film cavity. In the following, we calculate the expected time delay of such x-ray pulses with the aim to find a setting in which this time domain effect is strongly pronounced and at the same time is suited for a realistic experimental setting.

In order to calculate the time delay, the complex reflection coefficient R has to be determined. However, so far, our quantum description of the light-matter interaction was only compared to the established methods in terms of the absolute value of the reflection, but not yet via its phase, which is required for the time delay calculation. Therefore, we performed benchmarking simulations with Parratt's formalism and the software package CONUSS.

Further, we solve for the reflection coefficient by explicitly solving for the stationary field distribution with Maxwell's equations on a 2-d grid. To this end, an operator-split method is applied and the paraxial approximation is employed. The effect of the nuclear resonances can be included in the refractive index, as we already did for the simulations with Parratt's formalism (see Sec. 2.2.1). An example of a calculation field intensity in the absence of resonant nuclei is shown in Fig. 2.2(a) and (b). Performing this simulation with different x-ray energies as initial conditions, the complex reflection coefficient is obtained by evaluating the field amplitude far behind the cavity.

With those four different approaches the phase characteristics of the reflection were calculated and, apart from an insignificant global phase factor, we found very good agreement amongst the methods, indicating the consistency of our analysis. For the description with the quantum optical model, we had to take into account the dispersion phase effect discovered in Chap. 4 as well. In the following discussion on different cavity settings, we restrict ourselves to only one theory curve in the figures. Exemplarily, we analyzed the cavity defined in Tab. 6.1 with platinum and palladium as mirror material. In a first setting, we omitted any magnetic splitting and probed the cavity in the first guided mode minimum, such that the system exhibits a Lorentzian line profile. The corresponding time delay is shown in Fig. 6.1 for different pulse frequencies. Clearly, sub-luminal light propagation is realized, since the time delay around the resonance is positive. Interestingly, the predictions for the Pt and Pd cavities strongly differ. To understand this disparity, we introduce

$$T = \int_{-\infty}^{\infty} \tau(\Delta) d\Delta \tag{6.36}$$

as a measure how well a time delay in the cavity is realized. By noting that the reflection coefficient of a plain cavity can be written in the form $R \propto (q-i)^{-1} + (\epsilon+i)^{-1}$ where q is the

Table 6.1: Cavity parameters used in the time delay analysis (top to bottom).

Material	Thickness [nm]
Pt/Pd	2.92
C	7.58
^{57}Fe	1.75
C	9.33
Pt/Pd	∞

complex Fano q parameter (c.f. Tab. 4.1), and

$$\frac{d}{d\Delta}\arg\big(R(\Delta)\big) = \frac{d}{d\Delta}\arctan\left(\frac{\mathrm{Im}(R(\Delta))}{\mathrm{Re}(R(\Delta))}\right), \tag{6.37}$$

we find

$$T = \int_{-\infty}^{\infty} \frac{1}{1+\epsilon^2}\, d\epsilon - \int_{-\infty}^{\infty} \frac{\mathrm{Im}(q)}{\mathrm{Im}(q)^2 + \big(\mathrm{Re}(q)+\epsilon\big)^2}\, d\epsilon\,. \tag{6.38}$$

The first integral evaluates to π, while the result of the second integral depends on the sign of $\mathrm{Im}(q)$. In total, we find

$$T = \begin{cases} 0\,, & \text{if } \mathrm{Im}(q) > 0 \\ \pi\,, & \text{if } \mathrm{Im}(q) = 0 \\ 2\pi\,, & \text{if } \mathrm{Im}(q) < 0 \end{cases}. \tag{6.39}$$

For the cavities considered above, the case $\mathrm{Im}(q) > 0$ is realized for Pt mirrors, while with Pd for the mirror materials, $\mathrm{Im}(q) < 0$ and consequently a much stronger pronounced time delay is observed on average. For typical cavity settings, the condition of a negative imaginary part of the Fano q parameter reduces to the requirement of an overcritically coupled cavity (see Sec. 3.3.1). Hence, engineering a cavity with a thin surface layer often results in a more distinct time delay which is desired for an unambiguous observation in an experiment.

Next, we apply a magnetic field to the ^{57}Fe nuclei in the cavity under discussion, such that the π *geometry* from Sec. 5.1 featuring the phenomenon of spontaneously generated coherences (SGC) is realized. In this setting, the two linearly polarized transitions are driven. The predicted time delays for narrowband pulses are shown in the right panel in Fig. 6.1. The features of the time domain effects are evidently more pronounced as in the analysis of the unmagnetized cavity. In addition to the time delay already observed before, the cavity with the Pt mirrors even has a broad range in which $\tau < 0$. This corresponds to x-ray pulses with group velocities faster than the speed of light. Note, however, that this does not violate the principles of special relativity as information cannot be transmitted this way [244, 246]. Also, the super-luminal light propagation is typically accompanied by a high absorption, rendering its detection complicated. For propagation in dispersive media, this can be seen from the susceptibility behavior shown in Fig. 5.6. A negative slope in the real part corresponding to fast light goes along with a high absorption, visible from the imaginary part of the susceptibility. Similar characteristics can be observed for the reflection of x-ray pulses from the cavity.

Also for the cavity layouts including magnetized ^{57}Fe nuclei, we can calculate the quantity T as a measure for the total time delay. For the cavity with Pt as mirrors, we obtain $T = 0$, while for the Pd cavity one finds $T = 4\pi$. This indicates, that suitably engineered cavities operated in SGC settings are a promising candidate for observing distinct values for the time delay τ.

We emphasize that a much broader range of cavities could be analyzed in terms of their time delay. For example, the time domain control can further be manipulated by changing the incidence angle θ, thereby causing strongly asymmetric line shape profiles, or by considering more complex magnetization and polarization directions. It is important to note that the time delay τ is only well defined if a definite polarization arrives at the detector, since for its calculation the phase of the reflection coefficient is required. For an incoherent mixture of the field polarization as described in Eq. (5.19), the phase $\arg(R)$ and hence the delay τ is not well defined. In addition to the cavity layouts mentioned above, also the EIT-cavity employed in Ref. [56] should be mentioned here. Since the smoking-gun-signature of EIT is sub-luminal light propagation, it should be expected that also in this setting a large time delay is observed. Indeed, we find very pronounced values close to the resonance. However, the frequency range of the extreme values is very narrow and overlaps with the EIT minimum in the reflection rate, such that the signal arriving at the detector is strongly suppressed. Therefore, in summary, a well-suited candidate for observing slow light in the x-ray domain is a cavity operated in a SGC setting.

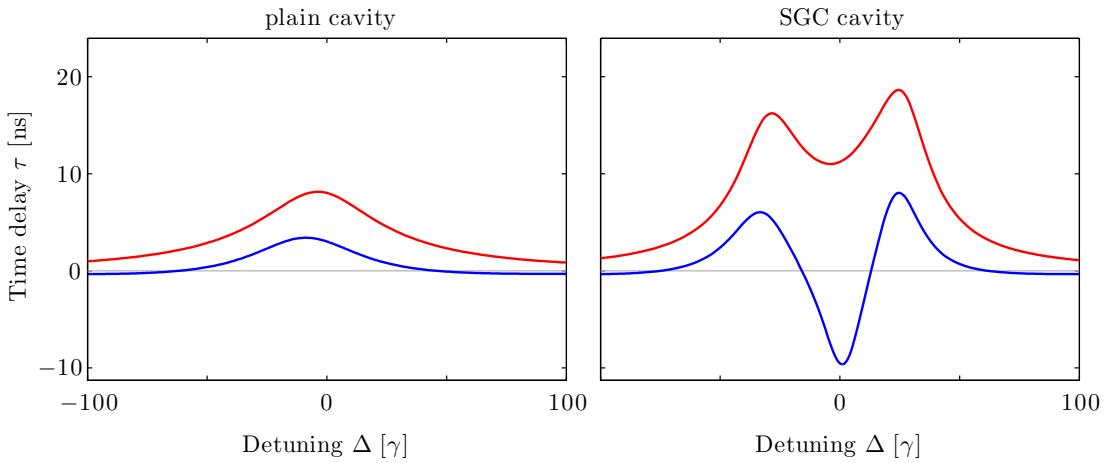

Figure 6.1: Time delay τ for pulses with central frequency Δ, reflected from the cavity defined in Tab. 6.1 for Pt (blue) and Pd (red) as mirror material. In the right panel a magnetization in the ^{57}Fe layer causes a Zeeman splitting and the π *geometry* (see Sec. 5.1) is realized. In this case even super-luminal light propagation can be realized.

6.3 Experimental implementation

6.3.1 Narrowband x-ray pulse generation schemes

We have seen in the previous section that our thin-film cavity can be employed to modify the time domain characteristics of reflected x-rays. However, the desired group velocity control with sub- or super-luminal light propagation and subsequent applications require a spectrally narrow x-ray pulse (SNXP) in the first place. Below, we will briefly review some existing schemes how such pulses can be created and introduce a novel method, in which an SNXP is effectively created from broadband synchrotron radiation (SR).

In the x-ray regime, narrow-band radiation is provided by Mössbauer radioactive sources. However, they are not pulsed, except for scenarios where special modulation schemes are applied [57]. Pulsed x-ray sources of choice are SR sources which provide high-brilliance beams and repetition rates in the order of some $10 - 100$ ns. Here, the technique of nuclear resonant spectroscopy is an established method [49]. It relies on broadband excitation of nuclear levels and subsequent detection of the delayed nuclear decay signal. However, narrowband filtering of a single line from SR with sufficient rejection ratio, which is required for group velocity control, is challenging since the beam has a bandwidth orders of magnitude larger than the nuclear resonance. One approach in this direction has been recently successfully demonstrated [97, 98, 101]. In this case, a narrowband, pure nuclear reflection from a $^{57}FeBO_3$ crystal is employed to suppress the enormous fraction of non-resonant photons in the incident beam. Other approaches for suppression of the off-resonant photons rely on polarization filtering [50, 192] or on a high-speed mechanical chopper [247]. In the latter method, an ^{57}Fe foil acts as a bandpass filter and adds a tail of delayed narrow-band light scattered by the nuclei to the x-ray pulse, as shown in in Fig. 6.2(a). The chopper is operated such that it blocks the temporally short broadband incident pulse, but lets the delayed signal pass. As a result, the absorption dip induced by the iron foil is converted into a SNXP, which can then be used in an subsequent experiment. We note that the characteristics of the generated SNXP spectrum are primarily determined by the thickness of the iron foil. A thin or less enriched foil results in a single peak structure, whereas for enriched thicker foils effectively a double-hump distribution well-known from nuclear resonance scattering is created [248, 249]. These two cases are illustrated as dashed and solid lines, respectively, in the insets of Fig. 6.2(a).

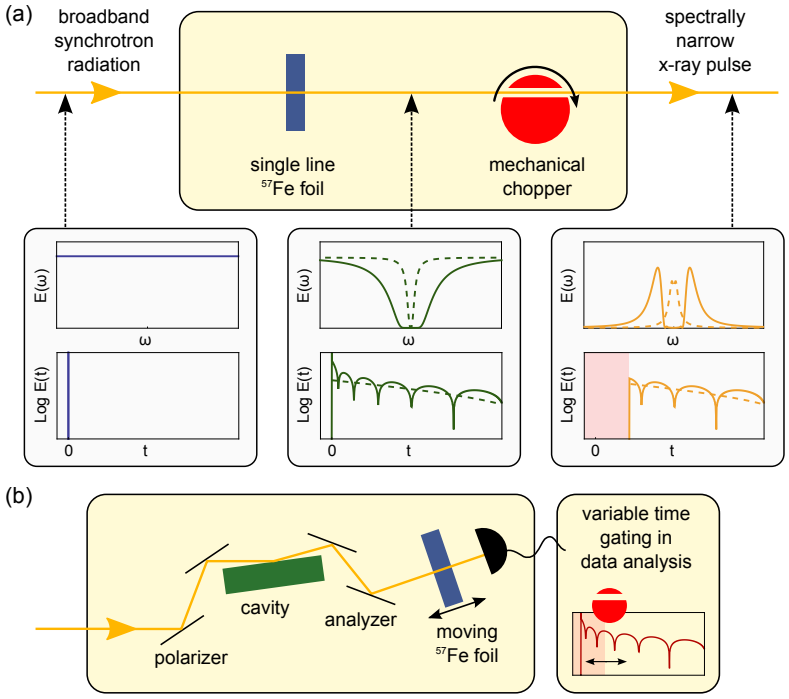

Figure 6.2: (a) Possible setup for the generation of SNXP from broadband synchrotron radiation. A single line ^{57}Fe foil imprints an absorption band on the initially flat spectrum. This absorption is converted into a SNXP by a mechanical chopper which suppresses the unscattered prompt response, but not the delayed nuclear response. The insertions depict the frequency- and time-resolved amplitude of the field at the corresponding stages of the scheme for a thick (solid lines) and thin (dashed lines) ^{57}Fe foil. (b) Actual implementation of the pulse generation scheme in our experiment. A polarimeter blocks the background photons such that neither a mechanical chopper nor a high-resolution monochromator for the SR is required. The variable a posteriori time gating facilitates the analysis of the delayed SNXP.

Actual implementation

The group velocity control could thus be explored using a combination of the SNXP generation in Fig. 6.2(a) with the actual nuclear delay line formed by the thin-film cavity. Moving the cavity allows to selectively tune the desired pulse delay. Instead, here, we employ a related approach which avoids the need for a mechanical chopper. In our scheme shown in Fig. 6.2(b), the initial broadband SR pulse is directed into a high purity x-ray polarimeter [194], which embeds the cavity containing the nuclei. After the polarimeter, the x-rays pass the ^{57}Fe foil, and subsequently are detected in the time domain by an avalanche photo diode.

Compared to the setup in Fig. 6.2(a), in our scheme, the order of the cavity and the ^{57}Fe foil are reversed. This is possible, since all responses are linear. Second, instead of moving the cavity to tune the group delay, the ^{57}Fe foil is moved, which is easier to realize and equivalent via a change of reference frame since both the source and the detection are spectrally broad. Most importantly, the mechanical chopper essential for the setup in Fig. 6.2(a) is not required in our scheme, since the polarimeter is operated in crossed setting. Thus, only those photons arrive at the detector, whose polarization has been rotated throughout the interaction with the nuclei. Thereby, the non-resonant background is removed, such that no high-resolution monochromator for the incident SR pulse is required, and the remaining signal can be detected without time gating. Apart from the simplification of the experimental setup, this also opens the possibility to a posteriori choose arbitrary time gatings in the data analysis. This is of interest, since after the ^{57}Fe foil, the resulting detection signal becomes $R(t) = R_\delta(t) + R_{\mathrm{SNXP}}(t)$ in the notation of the

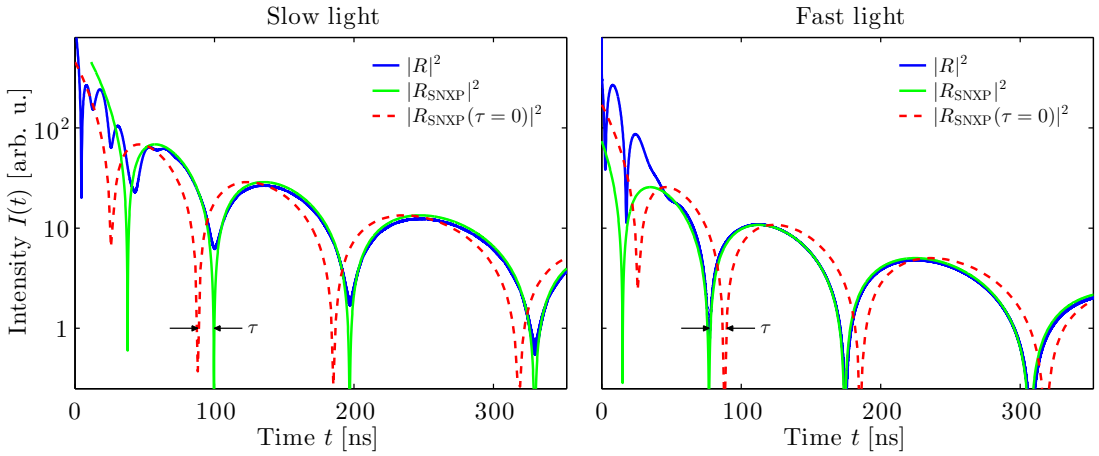

Figure 6.3: Slow and fast light can be observed using suitable cavities. At late times, the full signal is essentially given by the response of a spectrally narrow x-ray pulse. The time delay τ of such pulses is clearly observed in the shifted minima, which is a well-suited signature for an experimental realization. Parameters are explained in the main text.

theory description already established in Sec. 6.1.3. Here, $R_\delta(t)$ corresponds to the response of the photons which passed the ^{57}Fe foil without interacting. The photons, however, which interacted with the foil are distinguished and constitute the SNXP as illustrated in Fig. 6.2. Therefore, their response $R_{\mathrm{SNXP}}(t)$ forms the signal of a SNXP that has interacted with the cavity. In Sec. 6.1.4 we have already seen that the desired delayed part $R_{\mathrm{SNXP}}(t)$ can be separated from $R_\delta(t)$ by time gating, as the part $R_\delta(t)$ decays significantly faster for long times, and our approach allows to optimize this time gating throughout the data analysis.

An alternate point of view of the two schemes can be given by means of the theoretical description in the time domain. In the SNXP generation scheme from Ref. [247] visualized in Fig. 6.2(a), the sequence can be described by

$$R_{\mathrm{SNXP}}(t) = [T_{\mathrm{NFS}}(t) \cdot \theta(t - t_0)] * R_{\mathrm{Cavity}}(t) \; . \tag{6.40}$$

Here, the first part describes the SNXP generation using a chopper in time domain, where t_0 denotes the time from which the light can pass the chopper. Subsequently, the pulse interacts with the cavity, expressed via a convolution. In our implementation from Fig. 6.2(b), the full stage corresponds to the expression

$$R(t) = [R_{\mathrm{Cavity}}(t) * T_{\mathrm{NFS}}(t)] \cdot \theta(t - t_0) \; . \tag{6.41}$$

In this scheme, the signal is chopped in time domain only after the interaction with the two devices in the optical path. A thorough calculation of this signal was performed above, starting at Eq. (6.17). Here, we perform a simplified analysis.

Generally, the responses obtained in the two schemes characterized via Eq. (6.40) and Eq. (6.41) differ from each other. However, as mentioned before, they agree in certain limits. To illustrate this, we note that the time response of the cavity $R_{\mathrm{Cavity}}(t')$ mainly contributes at $t' = 0$ due to its superradiant decay. Then, $R_{\mathrm{Cavity}}(t')\,\theta(t - t_0 - t') \approx R_{\mathrm{Cavity}}(t')\,\theta(t - t_0)$ and we can rewrite the convolution integral in Eq. (6.40) to

$$\begin{aligned} R_{\mathrm{SNXP}}(t) &= \int T_{\mathrm{NFS}}(t - t')\theta(t - t' - t_0) R_{\mathrm{Cavity}}(t') dt' \\ &\approx \int T_{\mathrm{NFS}}(t - t')\theta(t - t_0) R_{\mathrm{Cavity}}(t') dt' \\ &= [T_{\mathrm{NFS}}(t) * R_{\mathrm{Cavity}}(t)] \cdot \theta(t - t_0) = R(t) \end{aligned} \tag{6.42}$$

Clearly, the approximation used here is very crude and should only be seen as an supportive argument to our statement: The true pulse generation scheme and our approach are closely related and our implementation can indeed be used to obtain the desired information on a SNXP reflected by the cavity.

To also deliver a more reliable argument, we turn to numerical calculations of the responses of the two schemes. To this end, we consider the cavity defined in Tab. 6.1, operated in π *geometry* SGC setting. The time resolved intensities are shown in Fig. 6.3. In the left [right] panel the cavity with Pd [Pt] as mirror material with Doppler detuning of the ^{57}Fe foil $\Delta_D = -40\gamma$ [0γ] was chosen. In both cases the thickness of the foil was taken as 5.6 μm.

The first important thing to note from Fig. 6.3 is that at late times, the full response $R(t)$ is indeed essentially given by the SNXP contribution only. This now gives a clear numerical argument that the two discussed schemes are equivalent on large time scales. Second, we notice that the SNXP response is indeed shifted in the time domain, indicating a delay which is induced by the nuclei in the cavity. This way, both a positive and a negative time delay can be engineered, which corresponds to slow and fast light in the cavity.

The dispersion of the nuclei in the cavity result in a delay of the pulse without distortion. This can be seen already from the structure of $R_{\mathrm{SNXP}}(t)$ calculated in Eq. (6.22), where the delayed pulse is unaffected apart from a scaling factor and the time delay τ. The same behavior can be observed from the simulations shown in Fig. 6.3.

The time delay can be best seen from the shifted minima of the Bessel envelope in the response $R_{\mathrm{SNXP}}(t)$. In order to exploit this feature in an experiment, a relatively thick iron foil should be utilized, such that multiple beatings can be observed in the time spectrum. Additionally, the employed cavity should exhibit a large superradiant enhancement, because in this situation the unwanted response part $R_\delta(t)$ is diminished.

6.3.2 Measurements of the time delay

Guided by the group of Ralf Röhlsberger (DESY, Hamburg) and Rudolf Rüffer (ESRF, Grenoble), we performed the experiment at the ID18 nuclear resonance beam line at the European Synchrotron Radiation Source (ESRF, Grenoble) [93] using the setup sketched in Fig. 6.2(b). The x-ray cavity consists of a Pd(2 nm)/C(20 nm)/^{57}Fe(3 nm)/C(21 nm)/Pd(10 nm)/Si layer system which is probed in grazing incidence such that the fundamental guided cavity mode is resonantly excited. The high purity x-ray polarimeter provided by the Institute for Optics and Quantum Electronics in Jena and the Helmholtz Institute Jena is described in more detail in Ref. [194]. A magnetic field is applied along the beam propagation direction, defining the quantization axis for the magnetic hyperfine splitting in the ^{57}Fe layer. In this setting, the *Faraday geometry* as defined in Sec. 5.1 is realized and vacuum-mediated couplings between the different hyperfine levels arise, which lead to steep linear dispersions as in EIT systems such that large time delays τ are expected. Note that in contrast to previous experiments focusing on the measurement of the absorption spectra [50, 52, 56], here, a full transparency of the medium on resonance is not desirable, as it would correspond to zero intensity in reflection, prohibiting a detection of the propagated pulse. Therefore, the cavity system is chosen such that steep dispersion is obtained while maintaining sufficient intensity in reflection direction to enable the pulse detection. The additional stainless steel foil with ^{57}Fe for the SNXP generation with thickness 10 μm was mounted on a Doppler drive, such that pulses with different central frequencies $\omega_{\mathrm{SNXP}} = \omega_0 + \Delta_D$ could be generated (see Fig. 6.2(b)).

Due to the narrow nuclear linewidth, the SNXP consists, on average, of less than one photon. Triggering data acquisition on the detection of a photon at the detector thus essentially leads to post-selection of single photon SNXP. In the experiment, we registered the photon time of arrival together with the Doppler drive velocity for each signal photon separately. This enables us to analyze the intensity of the light registered by the detector as function of the pulse center frequency and time, as shown in Fig. 6.4. Clearly, the time spectra of near-resonant pulses

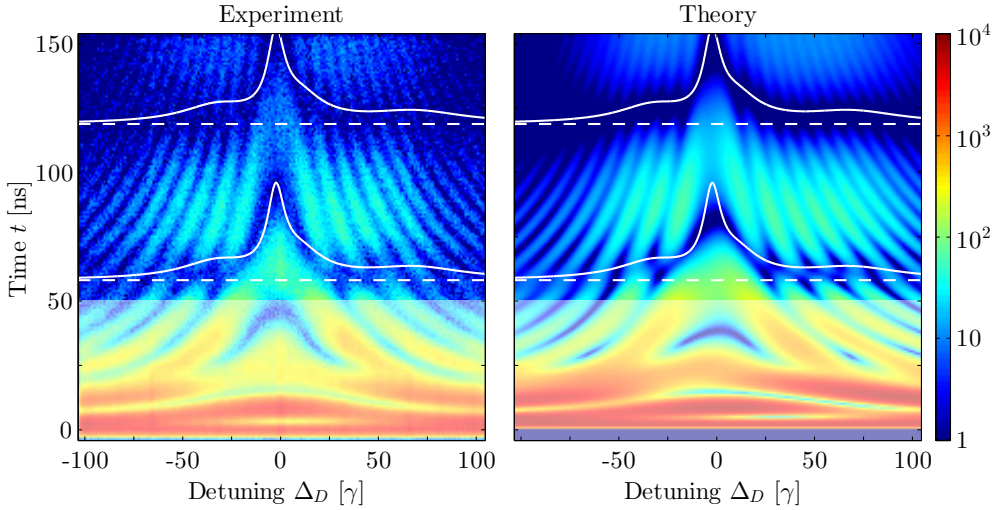

Figure 6.4: Photon counts registered by the detector as function of time and Doppler detuning of the ^{57}Fe foil. White dashed lines indicate theoretical predictions for beating minima positions without pulse delay. Solid white curves show corresponding predictions including the delay. Close to resonance $\Delta_D \approx 0$, the temporal response is clearly shifted compared to the off-resonant case. The additional oscillatory structure superimposing the data is due to the residual response R_δ of the incident synchrotron pulse. The bleached area covering times $t \leq 50$ ns contains mostly data from this initial δ-pulse excitation and is excluded from the data analysis.

($\Delta_D \approx 0$) are delayed compared to those of the off-resonant pulses, which can best be seen from the shifted beating minima at $t \approx 60$ ns and 120 ns. This is illustrated in more detail in Fig. 6.5(a), where time spectra at resonance and far off-resonance are shown. From the theoretical analysis, we could identify the additional oscillatory structures superimposing the simple temporal shift of the registered intensity by τ predicted in $R_{\mathrm{SNXP}}(t)$ as arising from residuals of $R_\delta(t)$ in the data.

To determine the free parameters of our theory from the experimental data shown in Fig. 6.4, we minimized the deviation from the recorded data and the theoretical values calculated numerically with Eq. (6.15). To account for the steep gradient along the time axis, the intensities were normalized along the detuning axis for each given time step. The best agreement was found for the scaled cavity parameters $\kappa = 45\gamma$, $|g|^2 N = 3285\gamma^2$, $\Delta_C = -28.1\gamma$ and the effective thickness $L = 126.3$ corresponding to a foil with thickness 10 μm enriched to $\approx 85\%$ in ^{57}Fe in the Mössbauer drive.

From the experimental data shown in Fig. 6.4, we extracted the time delay τ of the x-ray pulses by fitting the analytical response function with variable τ to the data. The result is shown in Fig. 6.5(b). As expected, around the cavity resonance where the nuclear susceptibility exhibits a steep positive linear dispersion, substantial pulse delays up to 35 ns are observed. Away from the nuclear resonance, the delay reduces until it becomes zero off-resonance.

The experimental time delay was determined by fitting the analytic expression for the time spectrum using Eqs. (6.17), (6.18) and (6.22) to the measured data for each Doppler detuning Δ_D. In Eq. (6.18) the Fourier transform of the reflection coefficient is calculated. This can be done analytically, since the in the *Faraday geometry* it can be expressed as a sum of two π *geometry*-like spectra, for which the Fourier transform was already calculated in Sec. 6.1.2. In our analysis, the cavity parameters determined above and a global scaling factor were kept constant, such that the only free parameter is the time delay τ entering Eq. (6.22). In order to extract the delay of the SNXP only, we suppress the contribution of the incident δ-like pulse by restricting the fit range to times $t \geq 50$ ns.

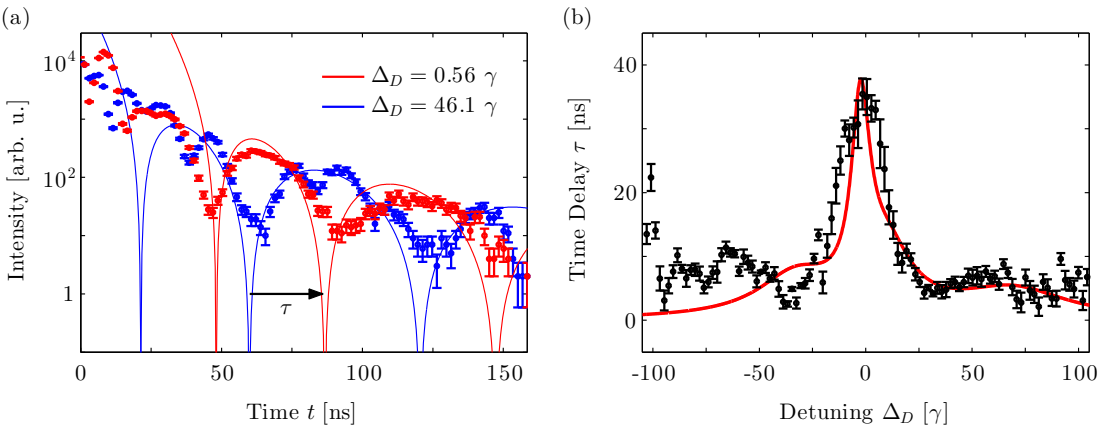

Figure 6.5: (a) Sections through Fig. 6.4 at constant energies Δ_D. Close to resonance, the time spectrum is clearly shifted compared to the off-resonant case. Solid lines are theoretical predictions for the pulse part R_{SNXP} only, which is expected to deviate from the experimental data at initial times due to the omission of $R_\delta(t)$. (b) Time delay for the SNXP as function of the detuning Δ_D between SNXP and the nuclear resonance. Black dots show the delay extracted from the experimental data. The red solid curve shows the corresponding theoretical prediction. Error bars are described in the main text.

We found that due to the oscillatory structure of the data, the fit result can be affected by the starting value chosen for τ. To extract unbiased values for τ from the data, we employed the following method: First, the best fit τ_0 over 50 equidistantly distributed initial values in the range from $\tau = -0.1/\gamma$ to $0.4/\gamma$ was determined. Second, we performed another 50 fits with initial values in the range $\pm\ 0.25/\gamma$ around the previously determined τ_0. Third, from these fits only the ones with $-0.1/\gamma \leq \tau \leq 0.4/\gamma$ were kept, since values outside this range clearly indicate an artifact caused by the oscillatory structure. Finally, we weight each τ with the inverse of its fit's variance to take into account the fit quality. From this final set of time delays τ the mean value and its standard error were determined.

Small distortions in the experiment, such as imperfect magnetization of the ^{57}Fe layer, can result in a difference of the actual and the theoretically predicted spectrum. Far off-resonance, where $R_{\mathrm{Cavity}}(\Delta_D) \ll 1$, this can lead to a large relative error. Since $R_{\mathrm{SNXP}}(t, \Delta_D)$ in the fit function also depends on the spectrum $R_{\mathrm{Cavity}}(\Delta_D)$, its amplitude is affected by the same error. Since the global scaling factor was kept constant, the time delay τ obtained from the fit might therefore be distorted. This explains the discrepancies to the theoretical predictions in Fig. 6.5(b) at large detunings.

In summary, we have demonstrated group velocity control for spectrally narrow hard x-ray pulses, yielding controllable pulse delays of up to 35 ns via sub-luminal light propagation. From simulations of the x-ray pulse dynamics, in which Maxwell's equations were solved numerically (c.f. Sec. 6.2), we determined an upper bound for the propagation length of the pulse inside the cavity of about 1 mm, which translates into an upper bound for the reduced group velocity of the SNXP of $v_{\mathrm{gr}} < 10^{-4}c$. The group velocity control was enabled by a powerful method to measure the response of an SNXP, which requires neither mechanical choppers nor a high-resolution monochromatization of the incident SR light, and thus provide a route towards nuclear quantum optics experiments beyond dedicated nuclear resonance beam lines. This way, slow light, EIT and related phenomena in the future could enable the coherence-based enhancement of non-linear interaction between x-rays and nuclei [116]. Next to this primary goal, our scheme presented here could also be used to measure the phase of the response of an unknown sample, since the observed time delay is directly related to the phase of the optical response of the cavity-nuclei system.

6.4 Time-resolved intensity in Fourier space

We have seen above, that in order to measure the spectrum which is reflected from a thin-film cavity, a Mössbauer drive, i.e. a vibrating foil with ^{57}Fe nuclei, is typically placed in the optical path. If the latter is moving with velocity v, its resonance frequency is Doppler shifted by $\Delta_D = \omega_0 v/c$ and thus the cavity spectrum is scanned by means of an externally controllable frequency Δ_D. In frequency domain this setup is fully characterized by the product of the complex reflection and transmission coefficients of the respective elements in the optical path. Since we are often interested in the spectral properties, such as Lamb shifts and superradiant decays, it would be desirable to directly have access to this frequency space product in an experiment. However, as discussed before, only the absolute value of its Fourier transform is measured, from which the properties of the system are to be reconstructed. Since the phase information of the time response is lost, it is not possible to obtain the original spectrum via the inverse transformation. A method of second choice, though, is to transform the *real-valued* data back into frequency domain, hoping that signatures of some spectral properties remain. The procedure is roughly illustrated below.

$$\underbrace{R_{\mathrm{Cavity}}(\Delta)\cdot T_{\mathrm{NFS}}(\Delta-\Delta_D)}_{\text{spectral information}} \xrightarrow{\mathrm{FT}^{-1}} R(t,\Delta_D) \xrightarrow{|\cdot|^2} \underbrace{I(t,\Delta_D)}_{\substack{\text{experimentally}\\ \text{available}}} \xrightarrow{\mathrm{FT}} \underbrace{I(\omega,\Delta_D)}_{\substack{\text{remaining}\\ \text{spectral}\\ \text{information?}}}$$

In the following, we will first perform a theoretical analysis and calculate the Fourier picture of the time-resolved intensity. Then, we will exemplarily identify a property in this domain which allows us to extract the Lamb shift in the cavity with an alternate method to the one used before in Sec. 4.1.2. Finally, we will apply our analysis to real experimental data.

6.4.1 Theoretical analysis

Let us begin with a short recap of the formal theoretical description. As discussed in Sec. 6.1.2, the response of the ^{57}Fe foil upon the transmitted x-rays can be described with the transmission function

$$T_{\mathrm{NFS}}(\Delta,\Delta_D) = \exp\left(-\frac{iL\gamma/4}{\Delta-\Delta_D+\frac{i}{2}\gamma}\right), \tag{6.43}$$

and the cavity reflection spectrum is generally taken as $R_{\mathrm{Cavity}}(\Delta)$. The time resolved intensity at the detector is given by (c.f. Eq. (6.3))

$$I(t,\Delta_D) = \frac{1}{2\pi}\left|\int_{-\infty}^{\infty} R_{\mathrm{Cavity}}(\Delta)\, T_{\mathrm{NFS}}(\Delta,\Delta_D)\, e^{-i\Delta t} d\Delta\right|^2 . \tag{6.44}$$

This is the quantity which is directly measurable in an experiment. Now, we aim to exploit the complementarity of time and frequency, and evaluate this function in Fourier space

$$I(\omega,\Delta_D) = \frac{1}{\sqrt{2\pi}}\int_{-\infty}^{\infty} I(t,\Delta_D) e^{i\omega t} dt\,. \tag{6.45}$$

In Sec. 6.1.3 it was shown that the time resolved intensity $I(t,\Delta_D)$ can be approximated as (c.f. Eq. (6.17))

$$I(t,\Delta_D) = \left|R_\delta(t) + R_{\mathrm{SNXP}}(t,\Delta_D)\right|^2 , \tag{6.46}$$

where $R_\delta(t)$ is the Fourier transform of the cavity spectrum $R_{\mathrm{Cavity}}(\Delta)$ and

$$R_{\mathrm{SNXP}}(t,\Delta_D) = -e^{-\frac{\gamma}{2}(t-\tau)}\theta(t-\tau) R_{\mathrm{Cavity}}(\Delta_D) e^{-i\Delta_D t}\sqrt{\frac{\pi L\gamma}{2(t-\tau)}} J_1\left(\sqrt{L\gamma(t-\tau)}\right) . \tag{6.47}$$

Next, let us look at the cavity reflection coefficient $R_{\mathrm{Cavity}}(\Delta)$ and its Fourier transform $R_\delta(t)$ in more detail. In the case without a magnetic splitting in the ^{57}Fe nuclei, the cavity spectrum has a general Fano profile (see Tab. 4.3). Hence, in frequency space, the cavity reflection amplitude consists of a constant continuum contribution and a Lorentz profile. In time domain, this translates into a $\delta(t)$-pulse and a part with an exponential decay. The $\delta(t)$-pulse, however, is usually not recorded in the experiment and suppressed by a time gating mechanism. Thus, we will neglect this contribution in the following analysis. Keeping the term would not affect our results, since the transformation of the time signal $\propto \delta(t)$ into Fourier space only results in a constant offset.

In the case where the magnetic splitting gives rise to SGC (see Chap. 5), the cavity spectrum and thus its time domain response is more complex. But as shown in Sec. 6.1.2, the simplest case with two interacting resonances featuring SGC can also be transformed into time domain analytically. The result can be written as a sum of multiple exponential decays and thus, the situation is comparable to the case without magnetic splitting. In the following we will, for simplicity, restrict our analysis to a cavity response of the form

$$R_\delta(t) = R_{\mathrm{Lorentz}}\theta(t)e^{-zt}\,, \qquad \mathrm{Re}\,(z) > 0\,. \tag{6.48}$$

This expression could easily be extended to SGC-type time spectra by adding additional terms $\propto \theta(t)e^{-z't}$ with different z'. For an unmagnetized cavity, which we consider here, the constants in Eq. (6.48) are given by

$$R_{\mathrm{Lorentz}} = \sqrt{2\pi}\frac{4\kappa_R|g|^2N}{3(\Delta_C - i\kappa)^2} \tag{6.49}$$

$$z = \frac{\gamma}{2} + \frac{2|g|^2N}{3(\kappa + i\Delta_C)} = \frac{\Gamma}{2} + i\Delta_{\mathrm{LS}}\,, \tag{6.50}$$

where Γ and Δ_{LS} correspond to the superradiantly enhanced decay rate and the collective Lamb shift.

Now let us transform the time resolved intensity into Fourier space. For this, we expand the modulus squared in Eq. (6.46) into three parts

$$\begin{aligned} I(t,\Delta_D) = &\quad \left|R_{\mathrm{Lorentz}}\theta(t)e^{-zt} + R_{\mathrm{SNXP}}(t,\Delta_D)\right|^2 \\ = &\quad |R_{\mathrm{Lorentz}}|^2\theta(t)e^{-2\,\mathrm{Re}\,(z)t} && (6.51)\\ &+ |R_{\mathrm{SNXP}}(t,\Delta_D)|^2 && (6.52)\\ &+ 2\,\mathrm{Re}\left(R^*_{\mathrm{Lorentz}}\theta(t)e^{-z^*t}R_{\mathrm{SNXP}}(t,\Delta_D)\right) && (6.53)\\ = &\quad I_1(t) + I_2(t,\Delta_D) + I_3(t,\Delta_D)\,, && (6.54) \end{aligned}$$

and calculate their corresponding Fourier transformations. The first expression can be computed straightforwardly as

$$I_1(\omega) = \frac{1}{\sqrt{2\pi}}\int_{-\infty}^{\infty} I_1(t)dt = \frac{|R_{\mathrm{Lorentz}}|^2}{\sqrt{2\pi}}\frac{1}{2\,\mathrm{Re}\,(z) - i\omega}\,. \tag{6.55}$$

In order to calculate the second Fourier integral we use the relations [250]

$$J_1\left(\sqrt{L\gamma t}\right)^2 = \sum_{n=1}^{\infty}\frac{2(-1)^{n+1}\Gamma(2n)}{\Gamma(n)^2\Gamma(n+1)\Gamma(n+2)}\left(\frac{L\gamma t}{4}\right)^n\,, \tag{6.56}$$

$$\int_0^\infty e^{-at}t^n dt = a^{-(n+1)}\Gamma(n+1)\,, \tag{6.57}$$

and obtain

$$\begin{aligned}
I_2(\omega,\Delta_D) &= \frac{1}{\sqrt{2\pi}}\int_{-\infty}^{\infty} 2\pi|R_{\text{Cavity}}(\Delta_D)|^2 e^{-\gamma(t-\tau)}\theta(t-\tau)\frac{L\gamma}{4(t-\tau)}J_1\left(\sqrt{L\gamma(t-\tau)}\right)^2 e^{i\omega t}dt \\
&= \sqrt{2\pi}|R_{\text{Cavity}}(\Delta_D)|^2 e^{i\omega\tau}\int_0^{\infty} e^{-\gamma t}\frac{L\gamma}{4t}J_1\left(\sqrt{L\gamma t}\right)^2 e^{i\omega t}dt \\
&= \sqrt{2\pi}|R_{\text{Cavity}}(\Delta_D)|^2 e^{i\omega\tau}\sum_{n=1}^{\infty}\frac{2(-1)^{n+1}\Gamma(2n)}{\Gamma(n)^2\Gamma(n+1)\Gamma(n+2)}\left(\frac{L\gamma}{4}\right)^{n+1}\int_0^{\infty} e^{-(\gamma-i\omega)t}t^{n-1}dt \\
&= \sqrt{2\pi}|R_{\text{Cavity}}(\Delta_D)|^2 e^{i\omega\tau}\sum_{n=1}^{\infty}\frac{2(-1)^{n+1}\Gamma(2n)}{\Gamma(n)^2\Gamma(n+1)\Gamma(n+2)}\left(\frac{L\gamma}{4}\right)^{n+1}\cdot\frac{\Gamma(n)}{(\gamma-i\omega)^n} \\
&= \sqrt{2\pi}|R_{\text{Cavity}}(\Delta_D)|^2 e^{i\omega\tau}\frac{L\gamma}{4}\left(1-e^{-\frac{L\gamma/2}{\gamma-i\omega}}\left(J_0\left(\frac{iL\gamma/2}{\gamma-i\omega}\right)-iJ_1\left(\frac{iL\gamma/2}{\gamma-i\omega}\right)\right)\right) .
\end{aligned} \tag{6.58}$$

Finally, we need to transform the interference term $I_3(t,\Delta_D) = 2\,\text{Re}[\tilde{I}_3(t,\Delta_D)]$ into frequency domain. Using basic Fourier transform properties, we rewrite

$$I_3(\omega,\Delta_D) = \tilde{I}_3(\omega,\Delta_D) + \tilde{I}_3(-\omega,\Delta_D)^* . \tag{6.59}$$

Hence, it is sufficient to calculate the Fourier transform of $\tilde{I}_3(t,\Delta_D)$ only. Assuming $\tau \geq 0$, such that $\theta(t)\theta(t-\tau) = \theta(t-\tau)$, this yields

$$\begin{aligned}
\tilde{I}_3(\omega,\Delta_D) &= \frac{1}{\sqrt{2\pi}}\int_{-\infty}^{\infty} R^*_{\text{Lorentz}}\theta(t)e^{-z^*t}R_{\text{SNXP}}(t,\Delta_D)dt \\
&= -R^*_{\text{Lorentz}}R_{\text{Cavity}}(\Delta_D)\int_{-\infty}^{\infty} e^{-(z^*+i\Delta_D)t}\,\theta(t-\tau)e^{-\frac{\gamma}{2}(t-\tau)}\sqrt{\frac{L\gamma}{4(t-\tau)}}J_1\left(\sqrt{L\gamma(t-\tau)}\right)dt \\
&= -R^*_{\text{Lorentz}}R_{\text{Cavity}}(\Delta_D)e^{-(z^*+i\Delta_D-i\omega)\tau}\int_0^{\infty} e^{-(z^*+i\Delta_D+\frac{\gamma}{2}-i\omega)t}\sqrt{\frac{L\gamma}{4t}}J_1\left(\sqrt{L\gamma t}\right)dt .
\end{aligned} \tag{6.60}$$

We use the series representation of the Bessel function to evaluate the integral

$$\begin{aligned}
&\int_0^{\infty} e^{-(z^*+i\Delta_D+\frac{\gamma}{2}-i\omega)t}\sqrt{\frac{L\gamma}{4t}}J_1\left(\sqrt{L\gamma t}\right)dt \\
&= \sum_{n=0}^{\infty}\frac{(-1)^n}{n!(n+1)!}\left(\frac{L\gamma}{4}\right)^{n+1}\int_0^{\infty} e^{-(z^*+i\Delta_D+\frac{\gamma}{2}-i\omega)t}t^n dt \\
&= \sum_{n=0}^{\infty}\frac{(-1)^n}{n!(n+1)!}\left(\frac{L\gamma}{4}\right)^{n+1}\frac{n!}{(z^*+i\Delta_D+\frac{\gamma}{2}-i\omega)^{n+1}} \\
&= 1-\exp\left(\frac{-iL\gamma/4}{\omega-\Delta_D+iz^*+i\frac{\gamma}{2}}\right) ,
\end{aligned} \tag{6.61}$$

and we finally obtain

$$\tilde{I}_3(\omega,\Delta_D) = -R^*_{\text{Lorentz}}R_{\text{Cavity}}(\Delta_D)e^{i(\omega-\Delta_D+iz^*)\tau}\left(1-\exp\left(\frac{-iL\gamma/4}{\omega-\Delta_D+iz^*+i\frac{\gamma}{2}}\right)\right) . \tag{6.62}$$

Now we have the Fourier transformations of all three parts in Eq. (6.54) at hand.

While the Fourier transformations here were carried out without approximations, it is important to remember that Eq. (6.47), which did enter the initial expression $I(t,\Delta_D)$, was obtained under the assumption that the cavity reflectance amplitude does not rapidly change, while the

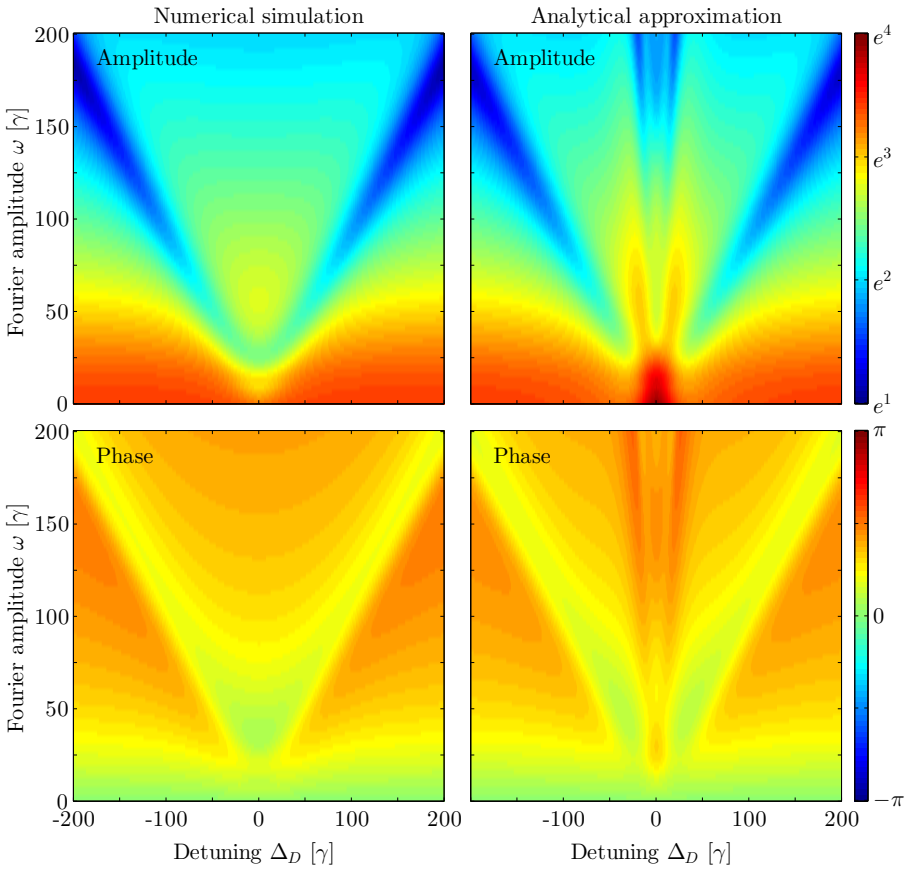

Figure 6.6: The numerical simulation and the analytic approximation of the time-resolved intensity in Fourier space is shown. The analytic calculation breaks down as expected in the range of small Δ_D. The additional features, in particular the diagonal structure and the overall scaling agree very well. Scaled parameters: $\kappa = 45$, $\kappa_R = 25$, $|g|\sqrt{N} = \sqrt{1400}$, $\Delta_C = 0$, $L = 78$.

phase was linearized, see Sec. 6.1.3. This leads to the time delayed signal of the Bessel-type response function and caused an unphysical discontinuity at $t = \tau$. Roughly, the erroneous area can be narrowed down to small times $0 \leq t \leq \tau$ and values of the Mössbauer drive detuning limited to $-50\gamma \lesssim \Delta_D \lesssim 50\gamma$, since a time delay τ occurs only close to the resonances of the nuclei in the cavity. From this we can expect, that the time-resolved intensity in Fourier space shows deviations from exact numerical results as well. In particular, the erroneous range is expected at large ω and small Δ_D. To test the validity of our analytical result, we compare it to an exact numerical solution. To this end, the response in time domain was computed numerically. In order to match the realistic scenario, the δ-like pulse was suppressed in the obtained data and finally, the modulus of the time resolved intensity was transformed back into frequency domain.

Both the numerical and the analytical results are shown in Fig. 6.6. Apart from the expected range already discussed above, the analytic model captures the essential parts of the structure from the numerical simulation extremely well. Probably the most dominant pattern is the V-type diagonal shape, visible both in the amplitude and the phase representation. Due to the agreement of the numerical data with the model we can identify its origin by examining the different parts of the theory. In fact, the diagonal structure originates from

$$\exp\left(\frac{-iL\gamma/4}{\pm\omega-\Delta_D+iz^*+i\frac{\gamma}{2}}\right) \tag{6.63}$$

in Eqs. (6.59) and (6.62). The exponential becomes minimal for $\pm\omega - \Delta_D + \mathrm{Im}(z) = 0$. From this we observe that the diagonal structure in Fig. 6.6 is actually shifted from the center by $\mathrm{Im}(z)$, which, according to Eq. (6.50), is the collective Lamb shift of the nuclei in the cavity. Thus, correctly identifying the diagonals offers an alternate method to extract the Lamb shift from the measurement data.

In principle, choosing a data section at large negative drive detuning Δ_D, then identifying its mirrored counterpart for positive detuning will allow us to reconstruct the Lamb shift $\Delta_{\mathrm{LS}} = \mathrm{Im}(z)$ from their center. However, this naive approach will generally fail. The reason is that in the cases where one would expect a non-zero Lamb shift, the Fourier spectra for large negative and large positive Mössbauer detunings Δ_D are not comparable, as their relative amplitude can strongly differ from each other. Hence, only the signature of the diagonals and not the structure of the circumjacent data may be used to obtain the Lamb shift in this fashion.

In order to apply this understanding to an experimental situation, we have to take into account that in a realistic scenario a time gating is usually applied during the measurement. While the theoretical considerations above only neglected the prompt δ-like pulse, in an experiment often the first several nanoseconds are suppressed. From numerical simulations, we observe that the time-resolved spectrum in Fourier space still contains the diagonals, but also oscillatory structures in the amplitude. For the phase, we find that the time gating causes the a linear rise along the ω-coordinate, which is superimposed with the structure shown in Fig. 6.6. This can easily be understood by noting that a shift in time domain corresponds to a linear slope of the phase in frequency domain. Indeed, we find from numerical simulations that the phase behavior is consistent with an additional global phase factor $\exp(i\omega t_{\mathrm{start}})$, where t_{start} denotes the beginning of the time gating window.

6.4.2 Lamb shift measurements revisited

Let us now see how the Lamb shift can be obtained in practice. We apply our analysis to the experimental data sets, which we also used in the analysis on Fano line shape control in Sec. 4.1.2. We choose the data sets of two different cavities measured at different incidence angles $\Delta\theta$, in which the diagonals in the Fourier spectra are well pronounced. In Fig. 6.7 we show their time resolved intensity as well as the amplitude in Fourier space.

As described above, we choose a suitable region around the diagonals and try to find its counterpart based on the diagonal structure only. This is illustrated in Figs. 6.8(a) and 6.8(b) for cavities 1 and 2, respectively. From the center of these two counterparts, the Lamb shift of the respective cavity setting is obtained. The accuracy of this procedure, however, is limited by the rather large pixel size along the Δ_D-axis. In Figs. 6.7, 6.8(a) and 6.8(b), the binning along the abscissa was chosen such that the frequency difference of two adjacent pixels corresponds to $\Delta_{\Delta_D} \approx 2.05\gamma$, such that the error in the Lamb shift is of the order of $\Delta_{\Delta_D}/2 \approx 1\gamma$. In principle, one could choose a smaller step size, however at the cost of less statistics for each bin. The Lamb shift from this analysis as well as the Lamb shift we obtained earlier from the fits performed in Sec. 4.1.2 are shown in the following table (in units of γ).

	Cavity 1 $\Delta\theta = 100\ \mu$rad	Cavity 2 $\Delta\theta = -46\ \mu$rad
Fourier space analysis	14.4 ± 1.0	-16.3 ± 1.0
Fano fit method (Sec. 4.1.2)	9.1 ± 1.6	-13.3 ± 1.3

Clearly, the Lamb shifts obtained with the two different methods are in the same range but do not agree very well. The reason for the discrepancy is most likely due to distortions in the recorded spectra which can strongly modify the Fano profile fits. We have already seen in Sec. 4.1.2 that the oscillatory structure in the spectra for large $\Delta\theta$ superimpose the narrow Fano spectra. As a consequence, the superradiantly broadened width of the nuclear resonances could

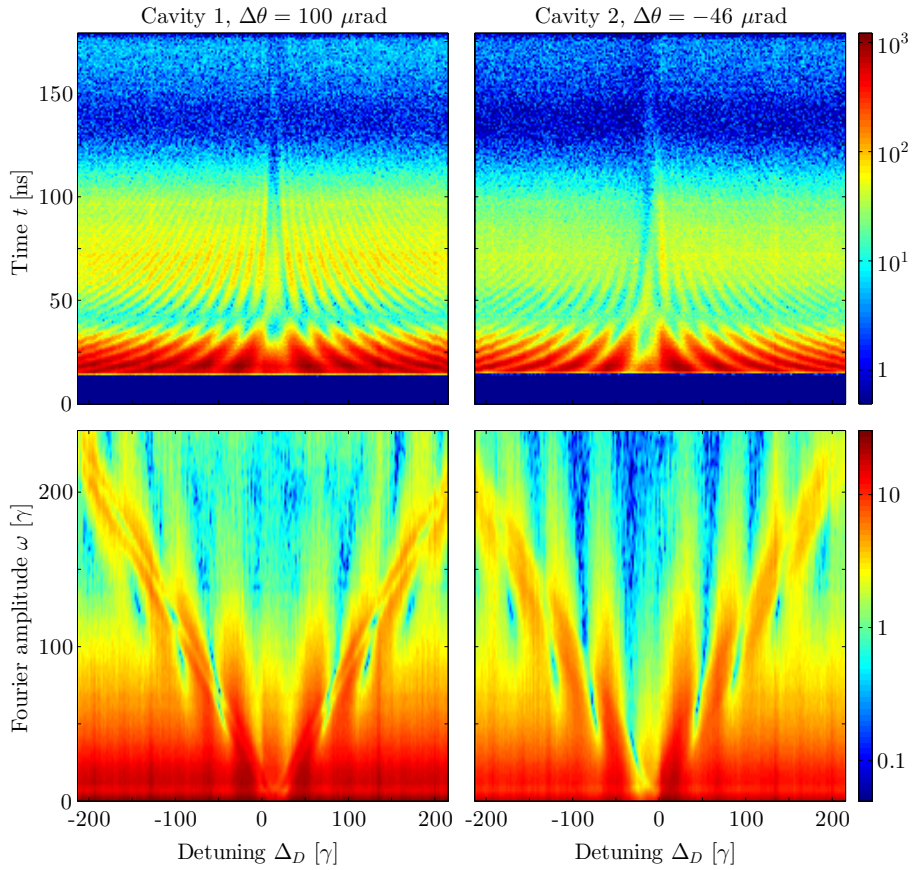

Figure 6.7: Experimentally measured time resolved spectrum (top row) and its Fourier representation (bottom) for two cavities at different incidence angles $\Delta\theta$ is shown. The diagonal structures in Fourier space are predicted by the theory and can be used to determine the Lamb shifts of the cavities.

not be detected properly. Thus, it is conceivable to assume that in the same parameter range also the exact position of the resonances, i.e. the Lamb shift, cannot be determined with high accuracy, since the measured data in the relevant frequency range is diffuse.

Based on this observation we can distinguish two complementary parameter ranges: For small $\Delta\theta$, the spectra obtained via the time gating technique are undistorted and Lamb shifts can be extracted by fitting a generic Fano curve to the data as performed in Sec. 4.1.2. The lack of characteristic oscillations in this parameter regime, however, limits the applicability of the Fourier space method described here. Conversely, in the range of large $\Delta\theta$, the situation is reversed. The pronounced oscillations in the data render an analysis via a Fano fit complicated, while in Fourier space the diagonal lines can in turn be identified with very high precision. Hence, these two fundamentally different methods to determine the Lamb shift from measured data complement one another as they are best applied in situations where the other method is expected to fail.

Finally, we want to emphasize that an analysis in Fourier space does not only reveal the Lamb shift of the nuclear resonances. For example, the diagonals mentioned before are true diagonals in the sense that their slope is unity, which can be seen from Eq. (6.63). Thus, their behavior in ω-Δ_D-space can serve as a crosscheck on the calibration of the time and frequency axis in the experiment. Apart from the features discussed here, it can be expected that more information is hidden in the Fourier space data. It could be promising to explore the general scaling of the amplitude in Fourier space, since Eq. (6.55) suggests that its behavior along the ω direction is

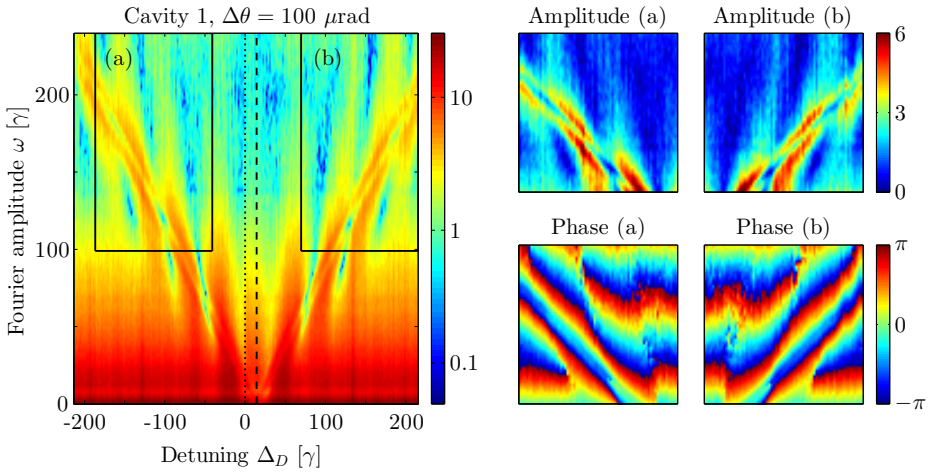

(a) Cavity 1 at $\Delta\theta = 100$ μrad

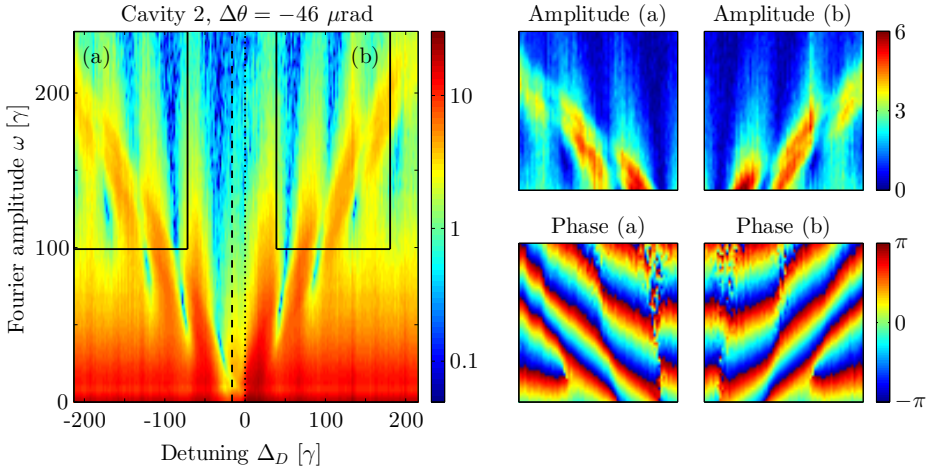

(b) Cavity 2 at $\Delta\theta = -46$ μrad

Figure 6.8: Time resolved intensity in Fourier space for two recorded data sets. The marked sections are mirrored counterparts. Their center is not located at $\Delta_D = 0$ (dotted line), but at the Lamb shift of the cavity (dashed line).

Lorentz-like with its width connected with the superradiant decay rate in the cavity. Another feature which could be worth investigating, is the underlying linear slope in the phase visible in Figs. 6.8(a) and 6.8(b). This might serve as a tool to determine the exact time gating window used in the experiment.

Chapter 7

Quantum Optical Model Extended

In the previous chapters we covered the description of cavities with a single layer of resonant ^{57}Fe nuclei. Already in this scenario a rich set of phenomena and effects, such as Fano line shape control or magnetically controllable reflection spectra modified by spontaneously generated coherences, could be observed. However, there is an additional cavity configuration which has sparked interest recently. In a setting with two particularly placed resonant layers in the cavity it was possible to observe a reflection spectrum with a deep interference minimum in the center due to the phenomenon of electromagnetically induced transparency (EIT) [56, 116, 117]. This is a remarkable result, since typically two coherent driving fields are required for this effect to emerge. In Ref. [56], however, the EIT experiment was established in a thin-film cavity with only a single excitation from a synchrotron beam, whereas the second field was intrinsically provided by intra-cavity couplings between the two ^{57}Fe layer. This experiment and the EIT interpretation was described in more detail in Sec. 2.1.4.

The quantum optical description we developed so far is not yet capable of describing this EIT experiment, or more generally spoken, it does not yet cover cavity settings with multiple resonant layers. But motivated by the expected significance of multilayer configurations, it would be highly desirable to also have a microscopic theory at hand, which allows for a deeper understanding, such as the nature of the intrinsic cavity-mediated coupling of the different resonant layers mentioned above. We note that other approaches based on scattering theory were employed to tackle this problem [251], however, so far they remained unsuccessful to provide a quantitative description of the EIT experiment.

In the following sections we will generalize our theory with the aim to describe the single photon EIT [56] and related settings. To this end, we will first extend the description to include multiple guided modes and later to multiple layers. As we will see, each of these extensions on its own will not give rise to fundamentally new effects in the nuclear reflection spectra. Only if both extensions are considered simultaneously, we can recover the new class of EIT-like spectra and this way provide a full quantum optical description for the EIT experiment in thin-film cavities [56].

7.1 Generalization to multiple modes

So far we included only one guided mode in the theoretical analysis of the cavity. This is typically justified, since guided modes are usually well separated from each other in terms of their respective resonant incidence angle. For example, from the reflection curve show in Fig. 2.2 it can be seen that the modes' resonance angles are separated by ≈ 1 mrad, which results in large cavity detunings Δ_C. Nevertheless, as we will show below, the additional modes can sometimes be of importance, since the nuclei can in principle scatter into them. Therefore, we will also include them into our theoretical description. In this part, we will discuss the influence of multiple modes on the reflectivity, while we still restrict ourselves to a single thin layer of resonant nuclei in the cavity.

We start by revisiting the input-output relation of the electromagnetic field. Compared to the initial analysis in Sec. 3.1.1, the input field does not only drive one mode a, but multiple modes $a^{[j]}$. At the same time, the output field is driven by these modes and, naturally, also

the resonant nuclei will interact with the different cavity field modes. This means, we also have to distinguish the coupling coefficients and decay rates for each cavity mode. In the following we will denote these rates by an upper index $[j]$ in squared brackets, which indicates that the respective quantity is related to the jth guided mode ("$a^{[j]}$") in the theory.

Generalizing Eq. (3.12) from the original theory, we write for the input-output relation

$$a_{\mathrm{out}} = -a_{\mathrm{in}}\left(\hat{\boldsymbol{a}}^*_{\mathrm{out}}\cdot\hat{\boldsymbol{a}}_{\mathrm{in}}\right) + \sum_j \sqrt{2\kappa_R^{[j]}}\left[a_1^{[j]}\left(\hat{\boldsymbol{a}}^*_{\mathrm{out}}\cdot\hat{\boldsymbol{a}}_1^{[j]}\right) + a_2^{[j]}\left(\hat{\boldsymbol{a}}^*_{\mathrm{out}}\cdot\hat{\boldsymbol{a}}_2^{[j]}\right)\right] \tag{7.1}$$

and for the Hamiltonian describing the dynamics of the modes

$$\begin{aligned} H_M = &\sum_j \Delta_C^{[j]}\left({a_1^{[j]}}^\dagger a_1^{[j]} + {a_2^{[j]}}^\dagger a_2^{[j]}\right) + i\sum_j\sqrt{2\kappa_R^{[j]}} \\ &\times\Big[\; a_{\mathrm{in}}{a_1^{[j]}}^\dagger\left(\hat{\boldsymbol{a}}_1^{[j]*}\cdot\hat{\boldsymbol{a}}_{\mathrm{in}}\right) - a^*_{\mathrm{in}}a_1^{[j]}\left(\hat{\boldsymbol{a}}^*_{\mathrm{in}}\cdot\hat{\boldsymbol{a}}_1^{[j]}\right) \\ &\quad + a_{\mathrm{in}}{a_2^{[j]}}^\dagger\left(\hat{\boldsymbol{a}}_2^{[j]*}\cdot\hat{\boldsymbol{a}}_{\mathrm{in}}\right) - a^*_{\mathrm{in}}a_2^{[j]}\left(\hat{\boldsymbol{a}}^*_{\mathrm{in}}\cdot\hat{\boldsymbol{a}}_2^{[j]}\right)\Big]\,. \end{aligned} \tag{7.2}$$

In a similar fashion, the couplings with nuclei are modified to include the sum over all modes j. The interaction with atom n or, more precisely, with its transitions μ, is given by

$$H_C = \sum_\mu\sum_j\left[\left(\hat{\boldsymbol{d}}^*_\mu\cdot\hat{\boldsymbol{a}}_1^{[j]}\right)g_\mu^{(n)[j]}S_{\mu+}^{(n)}a_1^{[j]} + \left(\hat{\boldsymbol{d}}^*_\mu\cdot\hat{\boldsymbol{a}}_2^{[j]}\right)g_\mu^{(n)[j]}S_{\mu+}^{(n)}a_2^{[j]}\right] + h.c.\,. \tag{7.3}$$

Here, we denoted the coupling coefficient between the mode j and the transition μ of an atom n by $g_\mu^{(n)[j]}$. This coupling constant can be decomposed into

$$g_\mu^{(n)[j]} = g^{[j]}c_\mu e^{i\phi^{(n)}}, \tag{7.4}$$

where c_μ is the Clebsch-Gordan coefficient of the transition μ, $\phi^{(n)}$ accounts for a potential phase imprinted on the nucleus by the field due to the atomic position, and $g^{[j]}$ denotes a global coupling constant between mode j and all nuclei and transitions. Note that this factorization is possible in this way only because we assumed a single thin layer of resonant nuclei in this analysis.

Next, we perform the adiabatic elimination as in the case with only one guided mode. The main difference is that we do not eliminate the two modes a_1 and a_2 for the two polarization directions only, but a total of $2j$ modes. Since the different modes are not mutually coupled, they can be eliminated independently and their contributions to the effective master equation sum up. In the same notation as in Sec. 3.2, we obtain the effective Hamiltonian contributions and the Lindblad terms

$$H_\Omega^{(n)} = \sum_\mu\left(\hat{\boldsymbol{d}}^*_\mu\cdot\mathbb{1}_\perp\cdot\hat{\boldsymbol{a}}_{\mathrm{in}}\right)\sum_j\left(\Omega^{[j]}g_\mu^{(n)[j]}\right)S_{\mu+}^{(n)} + h.c.\,, \tag{7.5}$$

$$H_{\mathrm{LS}}^{(n,m)} = \sum_{\mu,\nu}\left(\hat{\boldsymbol{d}}^*_\mu\cdot\mathbb{1}_\perp\cdot\hat{\boldsymbol{d}}_\nu\right)\sum_j\left(\delta_{\mathrm{LS}}^{[j]}g_\mu^{(n)[j]}g_\nu^{(m)[j]*}\right)S_{\mu+}^{(n)}S_{\nu-}^{(m)}\,, \tag{7.6}$$

$$\mathcal{L}_{\mathrm{cav}}[\rho] = \sum_{n,m}\sum_{\mu,\nu}\left(\hat{\boldsymbol{d}}^*_\mu\cdot\mathbb{1}_\perp\cdot\hat{\boldsymbol{d}}_\nu\right)\sum_j\left(-\zeta_S^{[j]}g_\mu^{(n)[j]}g_\nu^{(m)[j]*}\right)\mathcal{L}[\rho, S_{\mu+}^{(n)}, S_{\nu-}^{(m)}]\,. \tag{7.7}$$

Furthermore, we find that after the adiabatic elimination the reflection coefficient is given by

$$R = \left(-1 + \sum_j\frac{2\kappa_R^{[j]}}{\kappa^{[j]} + i\Delta_C^{[j]}}\right)\left(\hat{\boldsymbol{a}}^*_{\mathrm{out}}\cdot\hat{\boldsymbol{a}}_{\mathrm{in}}\right) - \frac{i}{a_{\mathrm{in}}}\sum_{n,\mu}\left(\sum_j\frac{\sqrt{2\kappa_R^{[j]}}g_\mu^{(n)[j]*}}{\kappa^{[j]} + i\Delta_C^{[j]}}\right)\left(\hat{\boldsymbol{a}}^*_{\mathrm{out}}\cdot\mathbb{1}_\perp\cdot\hat{\boldsymbol{d}}_\mu\right)\langle S_{\mu-}^{(n)}\rangle\,. \tag{7.8}$$

At this point it is useful to consider the nuclear contribution to the reflectance only. Comparing the effective master equation for one guided mode with the result above, we find that we can identify the corresponding expressions in each part

$$H_\Omega: \quad \Omega g_\mu^{(n)} \quad \to \sum_j \Omega^{[j]} g_\mu^{(n)[j]} \,, \tag{7.9}$$

$$H_{\mathrm{LS}}: \quad \delta_{\mathrm{LS}} g_\mu^{(n)} g_\nu^{(m)*} \to \sum_j \delta_{\mathrm{LS}}^{[j]} g_\mu^{(n)[j]} g_\nu^{(m)[j]*} \,, \tag{7.10}$$

$$\mathcal{L}_{\mathrm{cav}}: \quad \zeta_S g_\mu^{(n)} g_\nu^{(m)*} \to \sum_j \zeta_S^{[j]} g_\mu^{(n)[j]} g_\nu^{(m)[j]*} \,, \tag{7.11}$$

$$R: \quad \frac{\sqrt{2\kappa_R} g_\mu^{(n)*}}{\kappa + i\Delta_C} \to \sum_j \frac{\sqrt{2\kappa_R^{[j]}} g_\mu^{(n)[j]*}}{\kappa^{[j]} + i\Delta_C^{[j]}} \,. \tag{7.12}$$

Apart from these modifications no further changes are present in the newly derived effective master equation. The extensions above are only on the level of coefficients and, e.g., do not introduce additional operators. This is a consequence of the adiabatic elimination performed above. Therefore, we can use the upper set in Eq. (7.12) and simply replace the respective corresponding quantities in the results we already calculated from the single mode theory. Doing so for the linear reflectance without magnetic hyperfine splitting and neglecting the trivial polarization dependency ($\hat{\boldsymbol{a}}_{\mathrm{out}}^* \cdot \hat{\boldsymbol{a}}_{\mathrm{in}}$), this yields

$$R = -1 + \sum_j \frac{2\kappa_R^{[j]}}{\kappa^{[j]} + i\Delta_C^{[j]}} - i\frac{2N}{3} \frac{\sum_j \frac{\sqrt{2\kappa_R^{[j]}} g^{[j]}}{\kappa^{[j]} + i\Delta_C^{[j]}} \cdot \sum_j \frac{\sqrt{2\kappa_R^{[j]}} g^{[j]*}}{\kappa^{[j]} + i\Delta_C^{[j]}}}{\Delta + i\frac{\gamma}{2} + \frac{2N}{3}\left(\sum_j \left|g^{[j]}\right|^2 \left(i\zeta_S^{[j]} - \delta_{\mathrm{LS}}^{[j]}\right)\right)} \,. \tag{7.13}$$

We observe that the general structure of the nuclear part is unaffected by including multiple modes. It constitutes a Lorentzian line shape, shifted due to a collective Lamb shift and broadened due to superradiance. In comparison to the single mode result, it can be seen from the denominator that each mode induces its own Lamb shift and line broadening. But typically for any angle of incidence, all except (at most) one modes are driven far off-resonantly as mentioned above. Then, the according values for the cavity detuning Δ_C become large and their respective contributions to the Lamb shift and to the superradiance diminish. From the numerator of the nuclear part, we find that the strength of the nuclear signal is typically determined by one dominant mode with the smallest Δ_C. However, in general interferences between the different modes can arise. Nevertheless, the general Lorentzian structure of the line profile is unaffected by this and hence no qualitatively different features appear in the spectrum.

The main difference to the single mode result is found in the cavity contribution to the reflectance. Since we included multiple guided modes in the analysis above, it is clear that the resonances of these modes should become apparent in the reflection curve, i.e. when considering the cavity reflectance in dependence on the incidence angle θ. Indeed, the expression we derived in Eq. (7.13) highlights these resonances in its first sum. The resonance of a guided mode j is encountered at $\Delta_C^{[j]} = 0$, and the reflection curve will exhibit a local minimum in its vicinity.

At this point it is of interest, how well the actual reflection curve can be described by the cavity part of the reflectance. To this end, we compare the numerical results obtained with Parratt's formalism to the analytical expression of the multimode theory above. First, we note that in the numerical data an envelope of the reflection curve, formed by the total reflection range, appears. However, this is an effect of the bulk material properties and not related to the structure of the cavity, and hence it is not taken into account by the analytic expression found from our quantum optical theory. Therefore, we will heuristically combine the analytical formula, describing the guided modes, with the reflectivity of the cavity's mirror material, which approximately takes into account the total reflection envelope.

Furthermore, we have already seen in Sec. 4.1.3 that a dispersion phase is necessary to describe the asymmetry of the reflection curve around the minima of the guided modes. It can be included by simply generalizing the contribution which stems from the direct reflection on the cavity surface ("-1") with an additional phase factor $\exp(i\phi_C)$. Here, we want to handle the asymmetric behavior along a wider range of incidence angles. Also, to take into account possible effects of far off-resonant modes, which would give rise to a small constant contribution to the reflection coefficient, we allow for a complex variable r instead of the cavity surface amplitude -1 with $|r| \approx 1$.

With the heuristic modifications described above, the reflection curve reads

$$R(\theta) = R_{\text{Envelope}}(\theta) \left(r + \sum_j \frac{2\kappa_R^{[j]}}{\kappa^{[j]} + i\Delta_C^{[j]}(\theta)} \right) , \tag{7.14}$$

with the cavity detuning (c.f. Eq. (3.7))

$$\Delta_C^{[j]}(\theta) = \omega_0 \left[\sqrt{\cos(\theta)^2 + \sin\left(\theta_0^{[j]}\right)^2} - 1 \right] . \tag{7.15}$$

Let us now see how well this ansatz performs in practice. As we later aim to describe the EIT scenario from Ref. [56], which we mentioned in the introduction of this section, we specialize to this particular cavity. The cavity parameters are given in Tab. 7.1. Note that the two resonant iron layers cannot be described with the tools developed so far, however, for the description of the reflection curve, the nuclear resonances are omitted anyway. In the specified cavity platinum acts as cavity mirrors, therefore $R_{\text{Envelope}}(\theta)$ is the reflection coefficient of a single infinitely thick Pt layer. It can be calculated, e.g., using Parratt's formalism and the Fresnel formulas, see Sec. 2.2.1. We fitted Eq. (7.14) to the expected reflection curve for the cavity, which was obtained using Parratt's formalism. The result is shown in Fig. 7.1. Clearly, the quantum optical model together with the heuristic extensions, is well suited to describe the reflection curve. Interestingly, we find that also the phase behavior is reproduced very well. This is remarkable, because only absolute values were taken into account in the fit procedure. The analytic formula in Eq. (7.14) has only been corrected for a global phase to match the phase behavior predicted by the Parratt formalism.

From Fig. 7.1 we can see that for angles $\theta > 5$ mrad the two reflection curves do not agree anymore. This is expected, since we included only five guided modes in Eq. (7.14) and restricted ourselves to the range of the incidence angle $0 \leq \theta \leq 5$ mrad in the fit. Thus, guided modes beyond the angle $\theta = 5$ mrad are not taken into account. Considering the phases of the reflection curves, a clear deviation can be seen at the second guided mode at $\theta \approx 3$ mrad. In contrast to Parratt's formalism, the curve obtained with the quantum optical model features an apparent phase jump of 2π at the resonance. As we already discussed in Sec. 3.3.1, this is a sign that

Table 7.1: Cavity parameters for the two-layer cavity in node-anti-node configuration, which shows an EIT-like spectrum [56] (top to bottom).

Material	Thickness [nm]
Pt	3
C	10.5
^{57}Fe	3
C	6.5
^{57}Fe	3
C	21
Pt	10

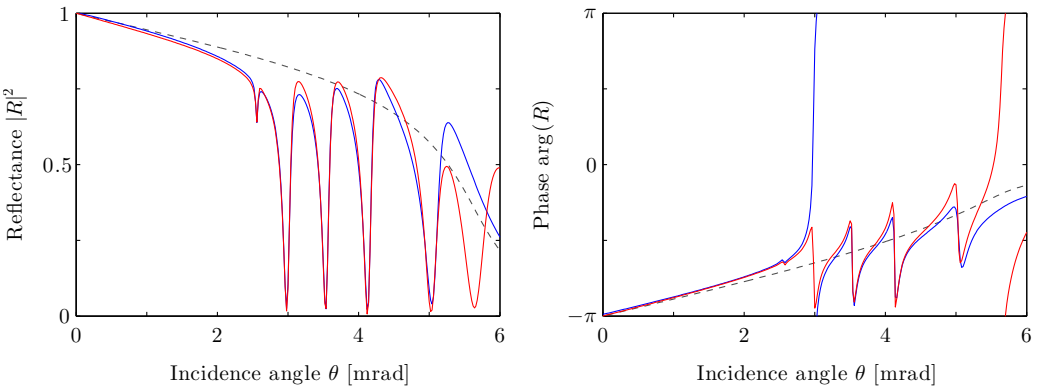

Figure 7.1: Cavity reflectance as a function of the incidence angle θ. The minima denote resonance angles at which guided modes are driven resonantly. Including a dispersion phase and the heuristic extension of an envelope given by the topmost layer (gray dashed line), the quantum optical theory (blue) can reproduce the exact result calculated with Parratt's formalism (red) very well. In the quantum optical model only the first five guided modes were taken into account. Although only the absolute value of the reflectance was fitted in the range $0 \leq \theta \leq 5$ mrad, the behavior of the phases calculated with the two descriptions are very similar.

the cavity mode is overcritically coupled, i.e. $2\kappa_R > \kappa$. Looking solely at the modulus, however, the overcritical case cannot be distinguished from the undercritical situation where $2\kappa_R < \kappa$ and no phase jump occurs. This is the reason why the quantum optical theory can predict a different phase behavior. Generally, it might be beneficial to not fit absolute values, but the complex values of the reflection curve directly. In this case also the over- and undercritically coupled resonances should be captured correctly by the quantum optical theory. However, since we are interested mainly at the third guided mode later on, which is the mode at which the EIT spectra have been measured in Ref. [56], we can use the parameters obtained in the fit discussed above for our further analysis. The cavity parameters we obtained from fitting the reflection curve are listed in Tab. 7.2. For the asymmetry parameter r in Eq. (7.14) we obtained $r \approx -0.981387 + 0.363327\,i \approx 1.046\,e^{i(\pi - 0.355)}$. We will use these parameters later when we look at the EIT scenario in more detail. Then, in addition to the discussion here, we will include the effect of the resonant nuclei in the two iron layers as well.

We conclude this section with a few remarks. First, we found that the energy spectrum of the nuclear reflection is not qualitatively affected by taking into account multiple modes in the theory. However, from Eq. (7.13) it becomes apparent that the relative phase and weight between the nuclear part and the cavity contribution to the reflectance can change from the relation we obtained in the single mode theory, see Sec. 4.1.1. This modification is expected to be small, because usually all but one modes are driven far off-resonantly and their contributions vanish. Nevertheless, a residual effect could distort the ideal Fano spectrum, which was discussed

Table 7.2: Cavity parameters of the EIT cavity (Tab. 7.1) for the quantum optical model.

Mode	θ_0 [mrad]	κ [γ]	κ_R [γ]
1	2.55947	143979	6063
2	2.99212	533490	311541
3	3.54938	614951	275657
4	4.14851	784506	373773
5	5.07939	1718304	767598

in Chap. 4 and potentially give a contribution to the Lamb shift measured for the Lorentzian spectrum, similar to the dispersion phase ϕ_C discussed in Sec. 4.1.3. But in any case, the extension to multiple cavity modes is not able to explain the asymmetry of the reflectance curves and the dispersion phase is still a necessary part to the theory. Finally, it should be mentioned that it is not meaningful to extend the quantum optical descriptions to very large incident angles θ. Reasons for this are the fact, that the theoretical description of the perpendicular polarization directions might break down, and that distinct non-grazing incidence effects are expected, since the cavity is no longer probed in (000) Bragg geometry. The angular cutoff should therefore be around the total reflection edge, which for typical cavity settings limits the number of guided modes to ≈ 5.

7.2 Multiple layers

In this part we will extend our theoretical description to additionally cover the cases where multiple layers of resonant nuclei are embedded in the cavity. So far, a thin resonant layer was assumed in the analysis and consequently the coupling factor g between the cavity mode and all resonant nuclei were identical up to a phase factor which, however, could be transformed away using collective states. As soon as we consider multiple layers, the assumption of uniform coupling strengths is clearly no longer justified. Roughly, an intensity profile with $\sin^2$ shape can be expected along the cavity for the guided modes. Different layers at different positions will thus experience different field strengths and the coupling coefficient g to the cavity mode cannot be considered as a constant anymore. Also, we want to emphasize that the same argument holds if a very thick layer of resonant nuclei is present in the cavity. Here, the nuclei close to the two layer boundaries might be exposed to strongly differing field strengths and the respective coupling coefficients become spatially dependent.

For simplicity, we will discuss the case, in which we include only one guided mode in the cavity. The general situation of multiple layers and multiple modes at the same time will be examined in the next section. In principle, the equations can be formulated by noting that every atom n couples to the cavity mode with a different coefficient $g^{(n)}$. However, we are not only interested in the microscopic description, but compact expressions for our observables of interest, such as the reflectance, are desirable. Therefore, we aim at repeating the analysis covering the linear regime, i.e. the case where at most one nucleus is excited. To this end, different kinds of basis transformations to introduce the collective states like in Chap. 3 have to be performed. Since the full procedure of the adiabatic elimination and the subsequent simplification to the linear regime is lengthy and does not provide new insights, the calculation is shortened and instead we start to generalize Eqs. (3.49)–(3.52) to include the multiple resonant layers in the cavity. In the following, we will mark an index related to a layer with curly brackets, whereas normal brackets denote an atomic index.

In the analysis with only one resonant layer, we introduced the collective states $|E_\mu^{(+)}\rangle$ which describe the state in which the whole ensemble of nuclei shares one excitation on transition μ. Here, we now generalize these states and denote a collectively excited state in layer l on transition μ by $|E_\mu^{\{l\}}\rangle$. This is possible, because each nucleus in a given layer couples to the field mode with the same strength and the basis transformations we performed in Sec. 3.2.2 can be performed for the subset of nuclei as well. However, by doing so, we have to take into account that Eqs. (3.49)–(3.52) include the number of nuclei N_{μ_g} which is the number of atoms initially in the ground state of the given transition μ. It has been already discussed that due to the small energy difference of the ground states, we can safely use $N_{\mu_g} = N/2$ for all practical purposes, where N is the total number of resonant nuclei in the cavity. Naturally, we have to write $N^{\{l\}}/2$ here instead, where $N^{\{l\}}$ is the number of nuclei in the particular layer l.

Exemplarily, we show how the driving part of the Hamiltonian in adiabatic elimination and linear response changes upon including multiple layers l. Instead of coupling the collective ground

state $|G\rangle$ to the excited state $|E_\mu^{(+)}\rangle$ with coupling coefficient g, each layer is now independently coupled with its respective coupling constant. This is visualized in the equation below as

$$\begin{aligned} H_\Omega &= \Omega\, g \sum_\mu \left(\hat{\boldsymbol{d}}_\mu^* \cdot \mathbb{1}_\perp \cdot \hat{\boldsymbol{a}}_{\text{in}}\right) c_\mu \sqrt{\tfrac{N}{2}} |E_\mu^{(+)}\rangle\langle G| + h.c. \\ &\rightarrow \quad \Omega \sum_l g^{\{l\}} \sum_\mu \left(\hat{\boldsymbol{d}}_\mu^* \cdot \mathbb{1}_\perp \cdot \hat{\boldsymbol{a}}_{\text{in}}\right) c_\mu \sqrt{\tfrac{N^{\{l\}}}{2}} |E_\mu^{\{l\}}\rangle\langle G| + h.c.\,. \end{aligned} \tag{7.16}$$

Other parts of the Hamiltonian and the incoherent part of the master equation are modified accordingly.

Now we want to analyze the case without magnetic hyperfine splitting in more detail. In this setting, the ground and excited states of the nuclei are degenerate, respectively, and we choose the quantization axis such that only the linear transitions $\mu = 2$ and $\mu = 5$ with Clebsch-Gordan coefficient $c_\mu = \sqrt{2/3}$ are driven, see Tab. 3.1. Further, we won't distinguish the two transitions and transform our equations such that only the state $|E^{\{l\}}\rangle = 1/\sqrt{2}\,(|E_2^{\{l\}}\rangle + |E_5^{\{l\}}\rangle)$, which consists of the symmetric combination of the two linearly polarized transitions, is used. In the relevant subspace, the Hamiltonian and the Lindblad operators then read

$$H_\Omega = \Omega \sqrt{\tfrac{2}{3}} \sum_l g^{\{l\}} \sqrt{N^{\{l\}}} |E^{\{l\}}\rangle\langle G| + h.c.\,, \tag{7.17}$$

$$H_{\text{LS}} = \delta_{\text{LS}} \tfrac{2}{3} \sum_{l,k} g^{\{l\}} {g^{\{k\}}}^* \sqrt{N^{\{l\}} N^{\{k\}}} |E^{\{l\}}\rangle\langle E^{\{k\}}|\,, \tag{7.18}$$

$$\mathcal{L}_{\text{cav}}[\rho] = -\zeta_S \tfrac{2}{3} \sum_{l,k} g^{\{l\}} {g^{\{k\}}}^* \sqrt{N^{\{l\}} N^{\{k\}}}\, \mathcal{L}[\rho, |E^{\{l\}}\rangle\langle G|, |G\rangle\langle E^{\{k\}}|]\,, \tag{7.19}$$

and for the reflection coefficient we find

$$R = \left[\left(\frac{2\kappa_R}{\kappa + i\Delta_C} - 1\right) - \frac{i}{a_{\text{in}}} \frac{\sqrt{2\kappa_R}}{\kappa + i\Delta_C} \sqrt{\tfrac{2}{3}} \sum_l g^{\{l\}*} \sqrt{N^{\{l\}}} \langle E^{\{l\}}|\rho|G\rangle\right] (\hat{\boldsymbol{a}}_{\text{out}}^* \cdot \hat{\boldsymbol{a}}_{\text{in}})\,. \tag{7.20}$$

In the next step we will further simplify this set of equations by introducing a new state which resembles a collective excitation which is distributed among the different layers. We define the collective layer state

$$|E^{\{+\}}\rangle = \frac{1}{\sqrt{A}} \sum_l g^{\{l\}} \sqrt{N^{\{l\}}} |E^{\{l\}}\rangle \tag{7.21}$$

with the normalization factor

$$A = \sum_l \left|g^{\{l\}}\right|^2 N^{\{l\}}\,. \tag{7.22}$$

With this new collective state we obtain

$$H_\Omega = \Omega \sqrt{\tfrac{2}{3}} \sqrt{A}\, |E^{\{+\}}\rangle\langle G| + h.c.\,, \tag{7.23}$$

$$H_{\text{LS}} = \delta_{\text{LS}} \tfrac{2}{3} A\, |E^{\{+\}}\rangle\langle E^{\{+\}}|\,, \tag{7.24}$$

$$\mathcal{L}_{\text{cav}}[\rho] = -\zeta_S \tfrac{2}{3} A\, \mathcal{L}[\rho, |E^{\{+\}}\rangle\langle G|, |G\rangle\langle E^{\{+\}}|]\,, \tag{7.25}$$

$$R = \left[\left(\frac{2\kappa_R}{\kappa + i\Delta_C} - 1\right) - \frac{i}{a_{\text{in}}} \frac{\sqrt{2\kappa_R}}{\kappa + i\Delta_C} \sqrt{\tfrac{2}{3}} \sqrt{A}\, \langle E^{\{+\}}|\rho|G\rangle\right] (\hat{\boldsymbol{a}}_{\text{out}}^* \cdot \hat{\boldsymbol{a}}_{\text{in}})\,. \tag{7.26}$$

From the last expression it can be seen that the nuclear part of the reflectance is determined by the coherence $\langle E^{\{+\}}|\rho|G\rangle$ only. Looking at the equations of motion in detail and keeping in

mind that we work in the linear regime where $\langle G|\rho|G\rangle \approx 1$, it can be readily seen that the time evolution of the coherence of interest is not coupled to any other density matrix elements and the coherence can be obtained straightforwardly as in Sec. 3.3. At the same time, due to the linearity of $\langle E^{\{+\}}|\rho|G\rangle$ and the detuning Δ in the upper expressions, it becomes clear that the form of the steady state of the coherence cannot go beyond a Lorentzian line shape. An explicit calculation shows that we obtain the reflection coefficient

$$R = \left[-1 + \frac{2\kappa_R}{\kappa + i\Delta_C} - i\frac{2\kappa_R}{(\kappa + i\Delta_C)^2}\frac{\frac{2}{3}A}{\Delta + i\frac{\gamma}{2} + \frac{2}{3}A(i\zeta_S - \delta_{\mathrm{LS}})}\right](\hat{\boldsymbol{a}}^*_{\mathrm{out}}\cdot\hat{\boldsymbol{a}}_{\mathrm{in}}) \ , \tag{7.27}$$

where the nuclear reflectance part indeed constitutes a Lorentz profile. Restricting ourselves to only one layer, the coefficient A reduces to $|g|^2N$ and we recover the result which we already derived in Sec. 3.3.

Even though we included multiple layers in our analysis, we see from Eq. (7.27) that it is not possible to explain an EIT-like spectrum as reported in Ref. [56]. Rather, it is the combined extension of multiple layers and multiple guided modes to the theory, which will be able to explain the EIT phenomenon. This will be shown in the following sections.

7.3 Multiple layers and multiple modes

In the last two sections we extended the theoretical description to include multiple modes and multiple resonant layers, respectively. In the results for the reflectance in linear response, i.e. Eqs. (7.13) and (7.27), we observed that both extensions give rise to additions in the nuclear amplitude and to the collective effects, while, however, leaving the general structure of a Lorentzian line shape unaffected.

A straightforward combination of the two results cannot be done. The reason for this is that both extensions require modifications in the coupling coefficient g. In the reflectance obtained from the two theories, different sums involving different combinations of the coupling constants appeared. Thus, the two modifications to the Lorentzian line shape cannot be added independently. Rather, it can be anticipated that the structure of the nuclear resonance will be more complicated and fundamentally different from a Lorentzian profile.

We will elaborate on this conjecture by setting up the Hamiltonian and the incoherent Lindblad term in the case of linear response and without magnetic hyperfine splitting in order to derive the reflection coefficient from first principles. We start with Eqs. (7.17)–(7.20), which we derived in the analysis of the multilayer extension. At this stage no basis transformation to introduce collective states was applied yet. Such a transformation could potentially interfere with the multimode extension, since for the definition of the collective layer state $|E^{\{+\}}\rangle$ in Eq. (7.21) we explicitly used the decisive coupling constant g. Hence, we first extend the multilayer equations given in Eqs. (7.17)–(7.20) and modify them according to the multimode replacement rules from Eqs. (7.9)–(7.12). Only after this step, a basis transformation can be applied. In the following analysis we again mark a layer index in curly brackets $\{l\}$ and indices of guided modes are denoted by squared brackets $[j]$. This yields

$$H_\Omega = \sum_j \Omega^{[j]}\sqrt{\tfrac{2}{3}}\sum_l g^{[j]\{l\}}\sqrt{N^{\{l\}}}|E^{\{l\}}\rangle\langle G| + h.c. \ , \tag{7.28}$$

$$H_{\mathrm{LS}} = \sum_j \delta^{[j]}_{\mathrm{LS}}\tfrac{2}{3}\sum_{l,k} g^{[j]\{l\}}{g^{[j]\{k\}}}^*\sqrt{N^{\{l\}}N^{\{k\}}}|E^{\{l\}}\rangle\langle E^{\{k\}}| \ , \tag{7.29}$$

$$\mathcal{L}_{\mathrm{cav}}[\rho] = -\sum_j \zeta^{[j]}_S\tfrac{2}{3}\sum_{l,k} g^{[j]\{l\}}{g^{[j]\{k\}}}^*\sqrt{N^{\{l\}}N^{\{k\}}}\mathcal{L}[\rho, |E^{\{l\}}\rangle\langle G|, |G\rangle\langle E^{\{k\}}|] \ , \tag{7.30}$$

$$R = \Big[-1 + \sum_j \frac{2\kappa^{[j]}_R}{\kappa^{[j]} + i\Delta^{[j]}_C}$$

$$- \frac{i}{a_{\text{in}}} \sum_j \frac{\sqrt{2\kappa_R^{[j]}}}{\kappa^{[j]} + i\Delta_C^{[j]}} \sqrt{\tfrac{2}{3}} \sum_l g^{[j]\{l\}^*} \sqrt{N^{\{l\}}} \langle E^{\{l\}}|\rho|G\rangle \Big] \, (\hat{\boldsymbol{a}}_{\text{out}}^* \cdot \hat{\boldsymbol{a}}_{\text{in}}) \ . \tag{7.31}$$

To simplify this set of equations, it would be desirable to perform a basis transformation which converts the different states $|E^{\{l\}}\rangle$ which describes an excitation in a single layer into a collective layer state, similar to the transformation we performed in Eq. (7.21). For that purpose, one would have to sum over the layers l, which then contains the coupling factor $g^{[j]\{l\}}$. But since this coupling coefficient now also depends on the guided mode index j, the basis transformation must also involve the sum over the modes $\sum_j$. However, it can be easily seen from the equations above that this sum would be different for every contribution to the equations of motion, since the prefactors depending on j are mutually different. Hence, it is not possible to transform the system into a form in which only one collectively excited state is needed. Rather, in a cavity configuration with l resonant layers the equations of motion need to be solved for the l coupled states $|E^{\{l\}}\rangle$. This implies that the response of the nuclear ensemble will generally not follow a Lorentzian line profile.

The different coupling coefficients $g^{[j]\{l\}}$ required for the extended theory need to be determined by fitting the analytical expressions to numerical data, obtained, e.g., from Parratt's formalism. To reduce the number of free parameters, however, it might be beneficial to derive them independently. In the future, this could be achieved by performing an eigenmode analysis for the given cavity geometry [72, 73, 252, 253].

7.3.1 Application to the EIT setting

Next, we will now consider a particular case, namely we will analyze a setting with two resonant layers in the cavity, which is the situation from Ref. [56]. In this work it was shown that the reflectance is an EIT spectrum. A detailed discussion on this cavity setting and the EIT interpretation was already given in Sec. 2.1.4.

Theoretical analysis

With our quantum optical theory and its extensions to multiple layers and multiple modes, we can now treat this scenario analytically as well. To this end, we restrict ourselves to two layers $l = 1, 2$, but we still allow for an arbitrary number of cavity modes j. As before, we consider the linear response case without magnetization and omit the trivial polarization dependence in the following. We rewrite the effective Hamiltonian from Eqs. (7.28) and (7.29) as well as the detuning part from Eq. (3.21) as

$$\begin{aligned} H = &\Big(\tilde{\Omega}^{\{1\}} |E^{\{1\}}\rangle\langle G| + h.c.\Big) + \Big(\tilde{\Omega}^{\{2\}} |E^{\{2\}}\rangle\langle G| + h.c.\Big) \\ &+ (\tilde{\delta}^{\{1\}} - \Delta) |E^{\{1\}}\rangle\langle E^{\{1\}}| + (\tilde{\delta}^{\{2\}} - \Delta) |E^{\{2\}}\rangle\langle E^{\{2\}}| \\ &+ \Big(\tilde{\delta}^{\{1,2\}} |E^{\{1\}}\rangle\langle E^{\{2\}}| + h.c.\Big) \ . \end{aligned} \tag{7.32}$$

Here, the first line covers the driving of the two layers, the second line accounts for the Lamb shifts and the detuning and the last line describes a coherent coupling between the two layers. Later, we will see that the last contribution can in parts be identified with the control field Ω_C from the EIT interpretation in Ref. [56]. The incoherent Lindblad terms in our description are given by

$$\begin{aligned} \mathcal{L} = &-\Big(\frac{\gamma}{2} + \tilde{\gamma}^{\{1\}}\Big) \mathcal{L}[\rho, |E^{\{1\}}\rangle\langle G|, |G\rangle\langle E^{\{1\}}|] - \Big(\frac{\gamma}{2} + \tilde{\gamma}^{\{2\}}\Big) \ \mathcal{L}[\rho, |E^{\{2\}}\rangle\langle G|, |G\rangle\langle E^{\{2\}}|] \\ &- \tilde{\gamma}^{\{1,2\}} \mathcal{L}[\rho, |E^{\{1\}}\rangle\langle G|, |G\rangle\langle E^{\{2\}}|] \qquad - \tilde{\gamma}^{\{1,2\}^*} \mathcal{L}[\rho, |E^{\{2\}}\rangle\langle G|, |G\rangle\langle E^{\{1\}}|] \ . \end{aligned} \tag{7.33}$$

Here, the first line accounts for spontaneous emission and superradiance. The other two terms describe an incoherent cross-damping term, which will contribute to the control field coupling in the EIT interpretation as well. The coefficients in Eqs. (7.32) and (7.33) are given by

$$\tilde{\Omega}^{\{l\}} = \sum_j \Omega^{[j]} \sqrt{\tfrac{2}{3}} g^{[j]\{l\}} \sqrt{N^{\{l\}}} \,, \tag{7.34}$$

$$\tilde{\delta}^{\{l\}} = \sum_j \delta_{\mathrm{LS}}^{[j]} \tfrac{2}{3} \left| g^{[j]\{l\}} \right|^2 N^{\{l\}} \,, \tag{7.35}$$

$$\tilde{\delta}^{\{1,2\}} = \sum_j \delta_{\mathrm{LS}}^{[j]} \tfrac{2}{3} g^{[j]\{1\}} g^{[j]\{2\}*} \sqrt{N^{\{1\}} N^{\{2\}}} \,, \tag{7.36}$$

$$\tilde{\gamma}^{\{l\}} = \sum_j \zeta_S^{[j]} \tfrac{2}{3} \left| g^{[j]\{l\}} \right|^2 N^{\{l\}} \,, \tag{7.37}$$

$$\tilde{\gamma}^{\{1,2\}} = \sum_j \zeta_S^{[j]} \tfrac{2}{3} g^{[j]\{1\}} g^{[j]\{2\}*} \sqrt{N^{\{1\}} N^{\{2\}}} \,. \tag{7.38}$$

Before we continue with our analysis, let us briefly look at the scaling of these coefficients. In the EIT setting, one of the layers does not couple to the driven guided mode. In our quantum optical language, we can represent this by setting the respective coupling constant to zero, for example $g^{[1]\{1\}} = 0$. At the same time, all other modes $j \neq 1$ are driven strongly off-resonantly, such that $\Delta_C^{[j]}$ becomes large for $j \neq 1$. In a simplified notation used to denote this scaling, we find

$$\begin{aligned} \tilde{\Omega}^{\{1\}} \,,\, \tilde{\delta}^{\{1\}} \,,\, \tilde{\delta}^{\{1,2\}} &\sim \frac{1}{\Delta_C} \,, \\ \tilde{\gamma}^{\{1\}} \,,\, \tilde{\gamma}^{\{1,2\}} &\sim \frac{1}{\Delta_C^2} \,, \end{aligned} \tag{7.39}$$

whereas $\tilde{\Omega}^{\{2\}}$, $\tilde{\delta}^{\{2\}}$ and $\tilde{\gamma}^{\{2\}}$ are not suppressed due to the mode detuning, as they still contain the non-zero coupling coefficient $g^{[1]\{2\}}$ for the resonantly driven mode. From these scalings we can already anticipate the EIT behavior in accordance with the interpretation discussed Sec. 2.1.4: Only the nuclei in the second layer decay superradiantly. The collective decay of atoms in the first layer and the cross-damping terms are suppressed quadratically in the detunings of the additional cavity modes and can be neglected in a naive picture. However, other contributions due to the presence of further cavity modes can have a substantial influence on the system, such as the coherent driving $\tilde{\delta}^{\{1,2\}}$ between the two layers, which can give rise to the coupling field required for EIT.

The effective level scheme of the system defined above is visualized in Fig. 7.2. The couplings between the collective ground and the two excited states are denoted by thick, solid and dashed lines and indicate the scaling behavior in terms of the cavity detunings Δ_C. Also from this, a close similarity with the EIT level scheme shown in Fig. 2.3 can be observed.

Hence, from only considering the cavity detuning scalings we can expect that the cavity behaves indeed like an EIT system. However, it is yet unclear how the additional driving terms and inter-layer coupling terms affect the spectrum. In order to answer this question in full detail, we will treat the problem more strictly by continuing with the solution of our theoretical description.

From Eqs. (7.32) and (7.33) we find that the equations of motion for the density matrix elements

$$\begin{aligned} \rho_{1G} &= \langle E^{\{1\}} | \rho | G \rangle \,, \\ \rho_{2G} &= \langle E^{\{2\}} | \rho | G \rangle \,, \\ \rho_{12} &= \langle E^{\{1\}} | \rho | E^{\{2\}} \rangle \,, \end{aligned} \tag{7.40}$$

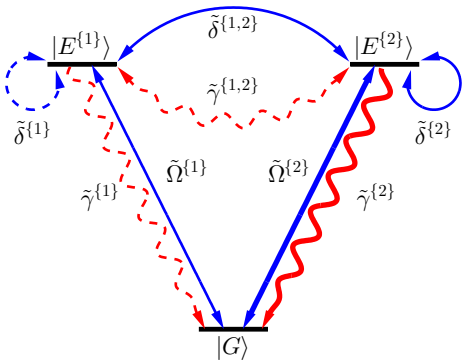

Figure 7.2: Level scheme in the EIT scenario. Two collective excited states are coupled to the ground state. Coherent couplings and Lamb shifts are marked in blue, superradiant spontaneous emission is denoted by red single headed arrows, cross-damping between the excited states by red double headed arrows. [Thick solid / solid / dashed] lines denote the cavity mode detuning scalings $\sim [1 \,/\, \Delta_C^{-1} \,/\, \Delta_C^{-2}]$ and mark the relative magnitude of the different couplings.

form a closed set of equations in the limit of linear response, i.e. where $\rho_{GG} \approx 1$ and $\rho_{11} = \rho_{22} \approx 0$. The equations of motion read

$$\frac{d}{dt}\rho_{1G} = \left[i(\Delta - \tilde{\delta}^{\{1\}}) - \tilde{\gamma}^{\{1\}} - \tfrac{\gamma}{2}\right]\rho_{1G} - i\tilde{\Omega}^{\{1\}} + i\tilde{\Omega}^{\{2\}}\rho_{12} - (i\tilde{\delta}^{\{1,2\}} + \tilde{\gamma}^{\{1,2\}})\rho_{2G}\,, \tag{7.41}$$

$$\frac{d}{dt}\rho_{2G} = \left[i(\Delta - \tilde{\delta}^{\{2\}}) - \tilde{\gamma}^{\{2\}} - \tfrac{\gamma}{2}\right]\rho_{2G} - i\tilde{\Omega}^{\{2\}} + i\tilde{\Omega}^{\{1\}}\rho_{12}^{*} - (i\tilde{\delta}^{\{1,2\}^*} + \tilde{\gamma}^{\{1,2\}^*})\rho_{1G}\,, \tag{7.42}$$

$$\frac{d}{dt}\rho_{12} = -\left[\gamma + \tilde{\gamma}^{\{1\}} + \tilde{\gamma}^{\{2\}} + i(\tilde{\delta}^{\{1\}} - \tilde{\delta}^{\{2\}})\right]\rho_{12} - i\tilde{\Omega}^{\{1\}}\rho_{2G}^{*} + i\tilde{\Omega}^{\{1\}^*}\rho_{1G}\,. \tag{7.43}$$

The limit of weak driving $\tilde{\Omega}^{\{l\}}$ additionally implies that no coherence between the excited states is built up. Hence, we can set $\rho_{12} = 0$ and find the steady state solutions

$$\rho_{1G} = \frac{\tilde{\Delta}^{\{2\}}\tilde{\Omega}^{\{1\}} - \left(-\tilde{\delta}^{\{1,2\}} + i\tilde{\gamma}^{\{1,2\}}\right)\tilde{\Omega}^{\{2\}}}{\tilde{\Delta}^{\{1\}}\tilde{\Delta}^{\{2\}} + \Omega_C^2}\,, \tag{7.44}$$

$$\rho_{2G} = \frac{\tilde{\Delta}^{\{1\}}\tilde{\Omega}^{\{2\}} - \left(-\tilde{\delta}^{\{1,2\}^*} + i\tilde{\gamma}^{\{1,2\}^*}\right)\tilde{\Omega}^{\{1\}}}{\tilde{\Delta}^{\{1\}}\tilde{\Delta}^{\{2\}} + \Omega_C^2}\,, \tag{7.45}$$

where

$$\tilde{\Delta}^{\{l\}} = \Delta - \tilde{\delta}^{\{l\}} + i\left(\tfrac{\gamma}{2} + \tilde{\gamma}^{\{l\}}\right), \tag{7.46}$$

$$\Omega_C^2 = \left(\tilde{\gamma}^{\{1,2\}} + i\tilde{\delta}^{\{1,2\}}\right)\left(\tilde{\gamma}^{\{1,2\}^*} + i\tilde{\delta}^{\{1,2\}^*}\right). \tag{7.47}$$

The same steady state solution is obtained if ρ_{12} is kept during the calculation and only the linear part in $\tilde{\Omega}^{\{1\}}$ and $\tilde{\Omega}^{\{2\}}$ is considered in the full solution.

With the solutions for the coherences at hand, we can now turn to our main observable, the complex reflection coefficient. According to Eq. (7.31), it is given by

$$R = -1 + \sum_j \frac{2\kappa_R^{[j]}}{\kappa^{[j]} + i\Delta_C^{[j]}} + R^{\{1\}}\rho_{1G} + R^{\{2\}}\rho_{2G}\,, \tag{7.48}$$

with

$$R^{\{l\}} = -\frac{i}{a_{\text{in}}}\sum_j \frac{\sqrt{2\kappa_R^{[j]}}}{\kappa^{[j]} + i\Delta_C^{[j]}}\sqrt{\tfrac{2}{3}}g^{[j]\{l\}^*}\sqrt{N^{\{l\}}}\,. \tag{7.49}$$

At this point it is instructive to discuss the scaling related to the cavity detuning Δ_C once again. As before, we assume that $g^{[1]\{1\}} = 0$, i.e. the first layer does not couple to the cavity mode $j = 1$ since it is located at an intensity node. In this case we find that $R^{\{1\}} \sim 1/\Delta_C$, while $R^{\{2\}}$ is not suppressed due to a cavity detuning, since the second layer can couple to the resonantly driven mode as $g^{[1]\{2\}} \neq 0$. Furthermore, from Eqs. (7.44) and (7.45) we find that $\rho_{1G} \sim 1/\Delta_C$, whereas the ρ_{2G} is not suppressed in this fashion. Therefore, for a qualitative understanding of the reflectance, it is well justified to drop the quadratically suppressed contribution $R^{\{1\}}\rho_{1G}$ and only consider the signal which originates from the second layer.

Keeping only terms up to linear order in $1/\Delta_C$ in the numerator of the reflectance and neglecting the tiny Lamb shift and superradiance of the nuclei in the first layer, we obtain

$$R = -1 + \sum_j \frac{2\kappa_R^{[j]}}{\kappa^{[j]} + i\Delta_C^{[j]}} + R^{\{2\}}\,\tilde{\Omega}_2\,\frac{\Delta + i\,\frac{\gamma}{2}}{\left(\Delta + i\,\frac{\gamma}{2}\right)\left(\Delta - \tilde{\delta}_2 + i\left(\frac{\gamma}{2} + \tilde{\gamma}_2\right)\right) + \Omega_C^2}\,. \tag{7.50}$$

The nuclear contribution to the reflectance is revealed in the second line. Its spectral shape is essentially that of a system featuring EIT. Hence, we recover the same result as in Ref. [56] which was described in Sec. 2.1.4: In a cavity with two resonant layers it is possible to realize the phenomenon of electromagnetically induced transparency.

Comparison to the semi-classical analysis

In Ref. [56], a semi-classical theory based on transfer matrix techniques was used to derive an expression for the nuclear reflectance and the result was given in Eq. (2.26). Comparing it with the quantum optical expression given in Eq. (7.50), we notice the agreement of the shapes of the two formulas. However, it is still to be verified if the scaling with the number of nuclei in the two layers agrees as well. In the semi-classical theory it was shown that the amplitude of the reflection coefficient and the superradiance of the nuclei in the second layer scale linear with the thickness of the second layer d_2, furthermore the control field Ω_C was shown to be proportional to $\sqrt{d_1 d_2}$. In our quantum optical theory we did not consider the thicknesses d_1, d_2 of the respective layers, but the total number of nuclei $N^{\{1\}}, N^{\{2\}}$. However, they differ only by a constant factor and thus it is sufficient to show that the scaling relations also hold for the number of nuclei. From Eqs. (7.34)–(7.38) and (7.49) it can indeed be seen that the relations are correctly reproduced by our theory.

This is an important result, since it is a strong hint that the two independently derived results do not coincide by chance, but also agree on a more fundamental level. Hence, the quantum description presented here can now be employed to shine light on the EIT scenario from a completely different perspective as in the semi-classical theory.

In the nuclear reflectance calculated in Eq. (7.50), the coupling Rabi frequency occurs as Ω_C^2 in the denominator, whereas in real EIT settings it appears as a positive real-valued variable $|\Omega_C|^2$. Taking a closer look at our definition of the coupling Rabi frequency in Eq. (7.47), we note that in our case Ω_C^2 can generally be complex. Also in the semi-classical theory the complex field amplitudes and transfer matrix elements allow for complex values. The results of Ref. [56], though, seem to imply that the imaginary component is very small and an EIT situation is well realized. However, from the theoretical analysis of the semi-classical models, this fact could not be understood and the influence of the imaginary component was unclear [107]. With our quantum theory, though, it is now possible to examine the complex nature of the coupling in more detail. From Eq. (7.47) we know that it is not only given by the coherent coupling $\tilde{\delta}^{\{1,2\}}$ between the two layers as written in the Hamiltonian in Eq. (7.32), but is also affected by the incoherent cross-damping term $\tilde{\gamma}^{\{1,2\}}$ between the two layers. In the discussion on the scalings we have already seen that in contrast to the coherent contribution, the incoherent term is suppressed

quadratically with the detuning of the cavity modes which are not driven resonantly. Thus, the incoherent part plays only a minor role and the real component of the coupling frequency Ω_C dominates. With this understanding, it might be possible in the future to specifically tailor systems in which a selected aspect, such as coherent versus incoherent couplings, dominates.

Furthermore, the microscopic ansatz of our quantum optical theory enables one to interpret the origin of the coupling between the layers. While in Ref. [56] it was shown that the EIT control field arises from radiative coupling between the two resonant layers, it can now be pinned down from Eqs. (7.36), (7.38) and (7.47) to

$$\Omega_C^2 = \left(\tfrac{2}{3}\right)^2 N^{\{1\}} N^{\{2\}} \left(\sum_j \frac{g^{[j]\{1\}} g^{[j]\{2\}*}}{\kappa^{[j]} + i\Delta_C^{[j]}} \right) \left(\sum_j \frac{g^{[j]\{1\}*} g^{[j]\{2\}}}{\kappa^{[j]} + i\Delta_C^{[j]}} \right) . \tag{7.51}$$

Since we assumed that the first layer does not couple to the first guided mode, i.e. $g^{[1]\{1\}} = 0$, we observe that the coupling field is only mediated via the remaining guided modes $j \neq 1$ in the cavity. This way, it becomes now also clear why the EIT phenomenon was not obtained in Sec. 7.2, where only one guided mode was included in the theoretical analysis. The fact that the additional cavity modes can be of importance is supported by the following experimental observation: If the cavity is driven at the resonance angle $\theta_0^{[j]}$ of one guided mode j, the reflected signal is not only observed at the emission angle $\pi - \theta_0^{[j]}$, but also small bumps seem to occur at the angles $\pi - \theta_0^{[k]}$, corresponding to the respective resonance angles of the other modes $k \neq j$ [254].

Numerical analysis

Let us now see how well our analytical expression for the reflectance derived above performs in practice. In particular, we aim to describe the spectrum of the EIT cavity defined in Tab. 7.1 with our quantum optical model. Moreover, we include a second cavity into the analysis: While the EIT cavity has its resonant layers in a node and anti-node of the field of the resonantly driven mode, respectively, we also consider a cavity in which the situation is reversed. Namely, the first resonant layer is located at a field anti-node and the second ensemble of nuclei at the field node. These two cavity layouts correspond to the cases discussed in Ref. [56], where it was shown that the first cavity exhibits the EIT phenomenon, while for the second system the control coupling Ω_C vanishes and only a Lorentz-like spectrum is measured. The layout parameters for this non-EIT cavity employed in this analysis are given in Tab. 7.3.

In order to determine the free parameters related to the cavities defined in Tabs. 7.1 and 7.3 for the quantum optical model in a consistent way, we employed the method discussed below. First, we restricted ourselves to the first five guided modes in the theory and did not take into account the resonant nuclei yet. For each of these modes the angles $\theta_0^{[j]}$, at which the modes are driven resonantly, and the decay and coupling rates $\kappa^{[j]}$ and $\kappa_R^{[j]}$ have to be determined.

Table 7.3: Cavity parameters for the two-layer cavity in anti-node-node configuration, which does not show an EIT-like spectrum [56] (top to bottom).

Material	Thickness [nm]
Pt	3
C	3.5
^{57}Fe	3
C	7.5
^{57}Fe	3
C	27
Pt	10

Table 7.4: Cavity parameters of the non-EIT cavity (Tab. 7.3) for the quantum optical model.

Mode j	$\theta_0^{[j]}$ [mrad]	$\kappa^{[j]}$ [γ]	$\kappa_R^{[j]}$ [γ]
1	2.44583	83492	2365
2	3.04302	326053	68417
3	3.53440	483792	286075
4	4.32412	1008149	464919
5	4.97965	2374218	967166

Table 7.5: Coupling parameters of the EIT cavity defined in Tab. 7.1 (left columns) and of the non-EIT cavity defined in Tab. 7.3 (right columns) for the quantum optical model.

Mode j	$g_{\text{EIT}}^{[j]\{1\}}\sqrt{N^{\{1\}}}$ [γ]	$g_{\text{EIT}}^{[j]\{2\}}\sqrt{N^{\{2\}}}$ [γ]	$g_{\text{non-EIT}}^{[j]\{1\}}\sqrt{N^{\{1\}}}$ [γ]	$g_{\text{non-EIT}}^{[j]\{2\}}\sqrt{N^{\{2\}}}$ [γ]
1	$1884 + 140\,i$	$-1391 + 2737\,i$	$833 + 490\,i$	$86 + 445\,i$
2	$3950 - 4516\,i$	$-304 + 2698\,i$	$302 + 4130\,i$	$-195 + 5213\,i$
3	$-1562 - 429\,i$	$4883 - 1840\,i$	$964 + 4919\,i$	$1326 + 324\,i$
4	$2061 + 2629\,i$	$221 + 2186\,i$	$1961 + 4465\,i$	$3580 - 2994\,i$
5	$-1376 + 5991\,i$	$599 - 5777\,i$	$5246 + 1545\,i$	$100 - 3733\,i$

The parameters can be found by fitting Eq. (7.14) to the angular dependent reflection curve as it was already done in Sec. 7.1. The cavity parameters for the EIT cavity were already given in Tab. 7.2, for the non-EIT cavity we found the values given in Tab. 7.4 and the asymmetry parameter $r \approx -0.969764 + 0.37942\,i \approx 1.041\,e^{i(\pi - 0.373)}$.

Having the cavity parameters at hand, the complex coupling coefficients $g^{[j]\{l\}}$ between the jth guided mode and the layer l of resonant nuclei have to be determined. Since we expect our theory to perform well in the case with only one resonant layer where only a Lorentzian line shape is expected for the nuclear contribution to the reflectance, we included the nuclear resonances of only one iron layer at a time. To account for the asymmetry and the envelope of the reflection curve, we extended the reflection coefficient given in Eq. (7.13) by the modifications from Eq. (7.14). From a subsequent fit to the numerical data calculated with Parratt's formalism, the coupling coefficients to the five guided modes could be determined for each resonant layer individually. In this procedure, the fit ranges have been restricted to $2 \leq \theta/\text{mrad} \leq 5$ and $-40 \leq \Delta/\gamma \leq 40$. This way, we obtained the coupling parameters for the EIT cavity as well as for the non-EIT cavity, given in Tab. 7.5. Note that the couplings between the layers in the node and the 3rd guided mode, characterized by the coefficients $g_{\text{EIT}}^{[3]\{1\}}$ and $g_{\text{non-EIT}}^{[3]\{2\}}$, do not completely vanish due to the finite thickness of the layers and a potential misplacement in the cavity. However, they are much smaller than the coupling coefficients of the respective layers in the cavity field anti-node.

Now we are able to benchmark our analytical result for the case of two resonant layers, which was calculated in Eqs. (7.44)–(7.49). A comparison with the frequency- and angular-dependent reflectance for the EIT and the non-EIT cavity is shown in Fig. 7.3(a) and Fig. 7.3(b), respectively. Clearly, the agreement between the two different models is very good. We stress that this is not an obvious result, since the parameters for the quantum optical model were determined independently and not obtained from a simultaneous fit to the numerical data.

The deviations at small incidence angles θ are probably caused by non-unique parameters in the fits. For instance, it cannot be distinguished if a mode is over- or undercritically coupled by considering the absolute value of the reflectance only, see Sec. 3.3.1. For the result with included resonant nuclei, though, this can give rise to differences. Another range in the figures where deviations can be found is the domain around $\Delta \approx 0$. Here, the exact numerical solution obtained from Parratt's formalism shows an additional structure. This can be understood from

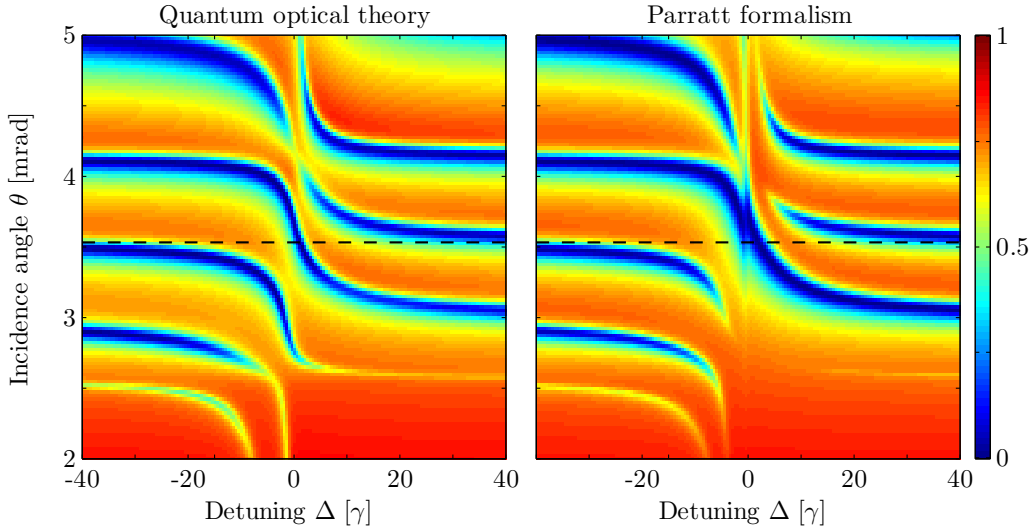

(a) EIT cavity

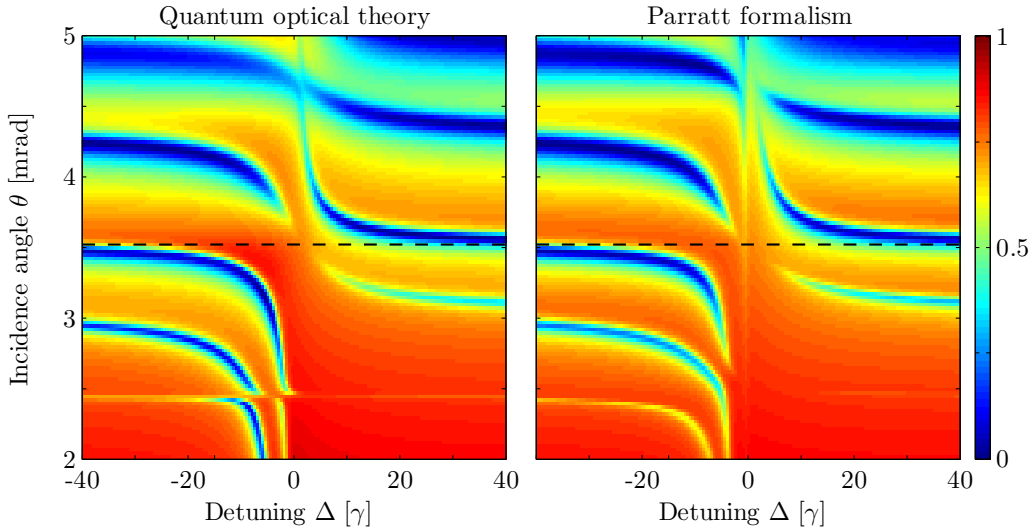

(b) Non-EIT cavity

Figure 7.3: The reflectance in the EIT scenario is shown as a function of the detuning Δ and the incidence angle θ. The results derived with the extended quantum optical model agree very well with the predictions from Parratt's formalism. The dashed line at $\theta \approx 3.5$ mrad marks the angle at which the 3rd cavity minimum is expected. A cut along this line corresponds to the spectrum measured in Ref. [56] and is shown in Fig. 7.4.

the following considerations. If the x-rays are not resonant to the transition in the ^{57}Fe nuclei, they will primarily be damped due to the electronic absorption in the cavity, before they can reach the lower resonant layer. If, however, their frequency is close to resonance, they will additionally be absorbed by the nuclei in the upper layer. Consequently, the field seen by the nuclei in the second layer is strongly modified compared to the off-resonant case, which would result in a smaller value for the coupling coefficient g, as its approximate $\sin^2$-shape is distorted. This effect, however, is not captured in our model description. Rather, it is assumed that the coupling coefficients are constants, whereas in reality they might depend on the frequency due to prior absorption of the radiation. An approach for future studies could thus be to comprise

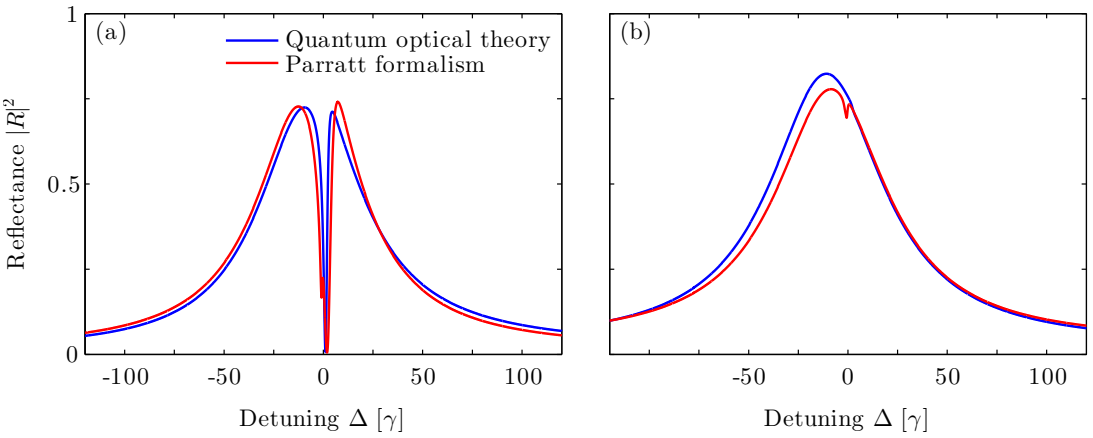

Figure 7.4: Spectra of the EIT (a) and the non-EIT (b) cavity at incidence angle $\theta \approx 3.5$ mrad, at which the third guided mode is excited. The quantum optical description is in accordance with the exact result derived with the Parratt formalism. In the case of the EIT cavity, the dip in the center of the spectrum is well reproduced.

this effect self-consistently into the quantum optical theory for an even better agreement with the numerical data.

Let us now turn to the most interesting part, which is the spectrum measured at the incidence angle corresponding to the third guided mode. This corresponds to the situation from Ref. [56]. The spectra for both the EIT and the non-EIT cavity defined in Tab. 7.1 and Tab. 7.3, respectively, are shown in Fig. 7.4. Again, we observe a very good agreement of our theory with the numerical data obtained with Parratt's formalism, which could already be anticipated from the accordance in Fig. 7.3. But in any case, the fact that the EIT as well as the non-EIT spectrum is well reproduced, supports the validity of our theoretical description. We note that the square of the coupling field Ω_C^2 does not vanish in the non-EIT case. Rather, its imaginary component dominates and it is the interplay with the other contributions to the reflection coefficient which results in the Lorentzian spectrum.

In summary, this shows that our quantum optical theory in the case of including both multiple layers and multiple guided modes is capable of describing the EIT experiment in Ref. [56]. Similar to the situations in the previous chapters, it could be used to provide a deeper understanding from a microscopic and quantum mechanical point of view. Most importantly, the question on the nature of the radiative coupling between the two resonant layers in the EIT cavity could be answered.

Finally, we emphasize that the extended theory description developed in this chapter is not restricted to a vanishing magnetization in the resonant layers. Rather, it is possible to include all Zeeman sublevels properly. This way, both the EIT phenomenon discussed above and the effect of spontaneously generated coherences discussed in Chap. 5 will emerge at the same time, giving rise to more elaborate reflection spectra. Also, from a theoretical point of view, the magnetization direction of the different layers do not necessarily have to agree. Therefore, it can be expected that a vast set of quantum optical level schemes with advanced features can be realized.

Chapter 8

Exploring The Non-Linear Regime

This chapter is devoted to the solution of the quantum optical model in cases where the external driving field is not necessarily weak. This is of particular interest if experiments are carried out at novel radiation sources. Current experiments on quantum optics in thin-film cavities, such as the ones reported in chapters 4, 5 and 6, are mostly performed at 3rd generation synchrotrons. Despite the high beam brilliance achieved with these light sources, the average photon number per pulse in the range of the nuclear resonance is well below one [7, 52, 106, 107]. This way, a maximum of only a single photon interacts with the combined system of cavity and nuclei at a time, thereby realizing the weak probe limit. This has been exploited in Chap. 3, where the quantum optical description could be significantly simplified for settings in the linear regime.

If, however, future experiments are performed using light sources with an even higher brilliance, the phenomena in the light-matter interaction are expected to go well beyond the linear regime. Examples of such intense sources are x-ray free-electron lasers [11], such as LCLS [12], SACLA [13], or the upcoming European XFEL [14]. With a possible self-seeding upgrade scheme [19], the latter could deliver several 10^3 photons per pulse in the tiny nuclear resonance bandwidth of ^{57}Fe [16]. About the same fluence could as well be generated by the proposed XFELO [15, 17, 18].

Hence, with these prospects in mind, it is worth to study the non-linear domain of the light-matter interaction. We emphasize, that the existing semi-classical theories discussed in Chap. 2 are not capable of describing this regime. The quantum theory developed in Chap. 3, however, provides a direct avenue to explore the non-linear effects, which emerge in the cavity. Additionally, other quantum approaches beyond the single-excitation regime could elucidate the non-linear setting from a different point of view [255].

In this chapter we will first review and generalize the definition of our main observable, the reflectance. Next, an approximation of our quantum optical description is mapped to a Dicke model, for which the stationary state can then be solved analytically for arbitrary field strengths and numbers of resonant nuclei in the cavity. Finally, we will numerically explore the more realistic scenario, in which a short, but intense x-ray pulse excites the system. As main results, we find that saturation effects of the nuclei excitation modify the reflectance and that the strength of incident pulse can be used to control the profile of the emission spectrum, reminiscent of the Fano line shape control observed in Chap. 4.

8.1 Generalization of the observables

The main observable, which is discussed in this work, is the reflectance $|R|^2$, since it is easily accessible in an experiment. In our theory from Chap. 3 it is calculated as follows: The internal cavity mode operator a is related to the external quantities a_{in} and a_{out}, describing the incident and the reflected field. The operators are connected via the input-output relation (c.f. Eq. (3.12)), which reads

$$a_{\mathrm{out}} = -a_{\mathrm{in}} + \sqrt{2\kappa_R}\, a \,. \tag{8.1}$$

In a next step, the reflection coefficient was calculated as $R = \langle a_{\mathrm{out}} \rangle / a_{\mathrm{in}}$, and the reflectance as its modulus squared

$$|R|^2 = \frac{|\langle a_{\mathrm{out}} \rangle|^2}{|a_{\mathrm{in}}|^2} \, . \tag{8.2}$$

However, this expression is implicitly based on the assumption of the weak driving regime, as we will show in the following.

In a real-world scenario, a detector measures "single clicks", created by the absorption of light quanta. As shown, e.g., in Ref. [145], the counting probability will be proportional to the expectation value $\langle a_{\mathrm{out}}^\dagger a_{\mathrm{out}} \rangle$. Properly normalized, we obtain the exact reflectance as

$$|R_{a^\dagger a}|^2 = \frac{\langle a_{\mathrm{out}}^\dagger a_{\mathrm{out}} \rangle}{|a_{\mathrm{in}}|^2} \, . \tag{8.3}$$

Clearly, this result differs from the reflectance in Eq. (8.2) we used so far. Hence, it is a vital task to discuss the validity and range of applicability of the definition which was used up to now.

In a first approach, we write the output operator

$$a_{\mathrm{out}} = \langle a_{\mathrm{out}} \rangle + \delta a_{\mathrm{out}} \tag{8.4}$$

as the sum of its expectation value and an fluctuation operator, for which $\langle \delta a_{\mathrm{out}} \rangle = 0$ by definition. Inserting this ansatz into Eqs. (8.2) and (8.3) yields

$$|R_{a^\dagger a}|^2 = |R|^2 \quad \Leftrightarrow \quad \langle \delta a_{\mathrm{out}}^\dagger \delta a_{\mathrm{out}} \rangle = 0 \, . \tag{8.5}$$

From this, we see that the two definitions of the reflectance coincide, if the fluctuation contribution vanishes. This condition is unhandily, though, as it is difficult relate it to the parameters which characterize the system. Thus, we will employ a second approach below.

We assume that the cavity modes can been adiabatically eliminated as shown in Sec. 3.2.1. We know that in this case a_{out} becomes the sum of a constant cavity contribution and a nuclear part, formed by the lowering operators S_-. For simplicity, we specialize to the case of a single nucleus and symbolically write for the cavity output operator

$$a_{\mathrm{out}} \sim \mathrm{const} + S_- \, . \tag{8.6}$$

From this, we find the condition

$$|R_{a^\dagger a}|^2 = |R|^2 \quad \Leftrightarrow \quad \langle S_+ S_- \rangle = \langle S_+ \rangle \langle S_- \rangle \, , \tag{8.7}$$

which allows to transfer the interpretation to statements on the nuclei. Assuming a state vector $|\Psi\rangle = c_g |g\rangle + c_e |e\rangle$ for the single nucleus system, one easily finds

$$\frac{\langle S_+ S_- \rangle}{\langle S_+ \rangle \langle S_- \rangle} = \frac{1}{1 - |c_e|^2} \, , \tag{8.8}$$

which approaches unity in the case where the nucleus is only weakly probed and hardly excited. As we have discussed before, this situation is fulfilled in current experiments and also allowed us to calculate the reflectance in linear response without the need to solve the complete N-body system formed by the nuclei in the cavity. As soon as a stronger probe intensity is employed, a significant amount of nuclei can be excited and the reflectance needs to be calculated with the expression given in Eq. (8.3) instead.

8.2 Steady state solution in the superradiant limit

The problem of N nuclei in the cavity is associated with a large Hilbert space. If, e.g., both ground states and all four excited states of the ^{57}Fe nucleus are considered, its dimension scales as 6^N. Thus, for a large number of atoms both a numerical and an analytical solution of the quantum optical model is rendered complicated. Here, we consider a simple, but important setting of the model. We will omit a possible magnetization in the ^{57}Fe layer, such that every nucleus can be described by a two-level system. Additionally, we will assume strong superradiance on the transitions, such that the single atom spontaneous emission rate γ can be neglected. In this case, the system can be mapped to a Dicke-type model, which then can be solved exactly on an analytical level. We emphasize that neglecting the spontaneous emission rate is a model assumption and its validity in a realistic setting is to be determined.

8.2.1 Mapping to the Dicke model

As mentioned above, we will restrict ourselves to the non-magnetized situation, i.e. each ^{57}Fe nucleus can be described by single ground state $|g\rangle$ and excited state $|e\rangle$. In the Chap. 3, we defined all parameters, such as coupling constants, for the nuclei with six hyperfine levels. Additionally, we considered two cavity modes to accommodate for the two perpendicular polarization directions. Here, we can simplify the calculation to only a single cavity mode a, as we can freely choose its polarization parallel to the incident beam. The second perpendicular mode is never coupled to the physical system of interest and can be omitted in the following analysis. Further, attention needs to be payed to the coupling constant between the cavity mode and the nuclear transition. We write the coupling Hamiltonian between the nuclei and the mode

$$H_C = \sum_{n=1}^{N} \tilde{g} \left(S_+^{(n)} a + a^\dagger S_-^{(n)} \right) , \tag{8.9}$$

with the nuclear raising [lowering] operator for the nth atom $S_+^{(n)}$ $[S_-^{(n)}]$ and $\tilde{g} = g\sqrt{\frac{2}{3}}$. This ensures that the Clebsch-Gordan coefficient of the linearly polarized transition in ^{57}Fe is properly taken into account.

With these modifications to the general theory in Chap. 3, the cavity mode can again be adiabatically eliminated, and with the same notation as in Sec. 3.2.1 we obtain the effective Hamiltonian and the incoherent Lindblad terms

$$H = -\Delta \sum_n S_+^{(n)} S_-^{(n)} + \Omega\tilde{g} \sum_n \left(S_+^{(n)} + S_-^{(n)} \right) + \delta_{\mathrm{LS}} \tilde{g}^2 \sum_{n,m} S_+^{(n)} S_-^{(m)} , \tag{8.10}$$

$$\mathcal{L}[\rho] = -\tfrac{\gamma}{2} \sum_n \mathcal{L}[\rho, S_+^{(n)}, S_-^{(n)}] - \zeta_S \tilde{g}^2 \sum_{n,m} \mathcal{L}[\rho, S_+^{(n)}, S_-^{(m)}] . \tag{8.11}$$

Specializing to the weak probe regime, we reobtain the reflection coefficient from the analysis of the general model. Hence, Eqs. (8.10) and (8.11) form the N-body model for two-level nuclei in consistent notation with the previous theory. Note that in this section we are interested in the steady state of the observables. Therefore, the adiabatic elimination on the level of operators will not affect the final results.

Next, we will map the upper equations to a Dicke model [256]. To this end we introduce the collective operators

$$J_+ = \sum_n S_+^{(n)} , \tag{8.12}$$

$$J_- = J_+^\dagger = \sum_n S_-^{(n)} , \tag{8.13}$$

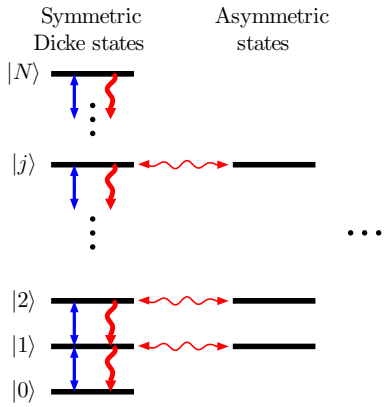

Figure 8.1: Level scheme of the system with N atoms in the Dicke basis. The symmetric states $|j\rangle$ on the left, resembling collective states with j excitations, are mutually coupled by the coherent driving in the Hamiltonian (blue arrows) and the superradiant decay (thick red arrows). The much weaker process of spontaneous emission (thin red arrows) can additionally couple the symmetric Dicke states to non-symmetric states. For the analytic solution in this chapter, this coupling is neglected such that all dynamics takes place only in the symmetric subspace.

$$J_x = \tfrac{1}{2}\left(J_+ + J_-\right) = \tfrac{1}{2}\sum_n \left(S_+^{(n)} + S_-^{(n)}\right) , \tag{8.14}$$

$$J_z = \tfrac{1}{2}[J_+, J_-] = \tfrac{1}{2}\sum_n \left(S_+^{(n)} S_-^{(n)} - S_-^{(n)} S_+^{(n)}\right) . \tag{8.15}$$

In order to rewrite the equations of motion in terms of these new operators, we first add a constant to the Hamiltonian. This corresponds to an energy offset only and hence does not affect any physical predictions. We change

$$H \to H + \tfrac{\Delta}{2}\mathbb{1} = H + \tfrac{\Delta}{2}\sum_n \left(S_+^{(n)} S_-^{(n)} + S_-^{(n)} S_+^{(n)}\right) , \tag{8.16}$$

and attribute the new component to the detuning part of the Hamiltonian, such that

$$\begin{aligned} H_\Delta &= -\Delta \sum_n S_+^{(n)} S_-^{(n)} + \tfrac{\Delta}{2}\sum_n \left(S_+^{(n)} S_-^{(n)} + S_-^{(n)} S_+^{(n)}\right) , \\ &= -\tfrac{\Delta}{2}\sum_n \left(S_+^{(n)} S_-^{(n)} - S_-^{(n)} S_+^{(n)}\right) = -\Delta J_z . \end{aligned} \tag{8.17}$$

The full Hamiltonian and the Lindblad terms from Eqs. (8.10) and (8.11) now become

$$H = -\Delta \cdot J_z + 2\Omega\tilde{g} \cdot J_x + \Delta_{\mathrm{LS}}/N \cdot J_+ J_- , \tag{8.18}$$

$$\mathcal{L}[\rho] = -\tfrac{\gamma}{2}\sum_n \mathcal{L}[\rho, S_+^{(n)}, S_-^{(n)}] - \tfrac{\gamma_S}{2N}\mathcal{L}[\rho, J_+, J_-] , \tag{8.19}$$

with the collective Lamb shift and the superradiant decay rate

$$\Delta_{\mathrm{LS}} = \delta_{\mathrm{LS}}\tilde{g}^2 N , \tag{8.20}$$

$$\gamma_S = 2\zeta_S \tilde{g}^2 N . \tag{8.21}$$

Now we will perform the key approximation of this section and omit the incoherent decay due to spontaneous emission by neglecting the first Lindblad term. In the linear regime we have seen that the system features a superradiantly enhanced decay rate, which is dominating

over the natural line width γ. In particular, this becomes visible in the measurements of the full transition width shown in Fig. 4.3. Dropping the spontaneous emission terms, Eqs. (8.18) and (8.19) can be written solely in terms of the collective operators introduced above. These operators are closely connected to the angular momentum operators and fulfill the canonical commutation relations [257]. The quantity

$$\langle J^2 \rangle = \langle J_+ J_- \rangle + \langle J_z^2 \rangle - \langle J_z \rangle \tag{8.22}$$

is conserved which can easily be seen by calculating $\mathrm{Tr}[\dot{\rho} J^2]$ and using the cyclicity of the trace, and equals $j(j+1)$ with $2j = N$ [258, 259]. Thus, the system obeys a symmetry. In particular, the symmetric excitation states, also known as Dicke states [256], form a closed set of equations, which is also visualized in Fig. 8.1. This can be exploited to solve the system with less effort, since the numbers of states in the Hilbert space can be reduced from 2^N to only $N+1$. But before we continue, we comment on a simplification we have implicitly made in our calculation so far. In Eq. (8.9), the local phase $\exp(i\phi^{(n)})$ for the nth nucleus was neglected, in contrast to the original model. However, this is not a problem since the phases can be absorbed in the definition of the collective operators $J_\pm$ [67, 136]. The commutation relations and therefore also the following arguments are unaffected by this.

Solution of the Dicke model

The general solution of the upper set of equations was calculated in Ref. [259]. The steady state density matrix reads

$$\rho^{(\mathrm{SS})} = \frac{1}{A} \sum_{n,m=0}^{N} a_{mn} J_-^m J_+^n \,, \tag{8.23}$$

$$a_{mn} = (-i\tilde{v})^{-m} \, (i\tilde{v}^*)^{-n} \, \frac{(1+i\tilde{\epsilon})_m \, (1-i\tilde{\epsilon}^*)_n}{m! n!} \,, \tag{8.24}$$

with the parameters

$$\tilde{v} = \frac{\sqrt{2\kappa_R}\, a_{\mathrm{in}}}{\tilde{g}} \,, \tag{8.25}$$

$$\tilde{\epsilon} = -\frac{\Delta\,(\kappa + i\Delta_C)}{\tilde{g}^2} = \frac{iN\Delta}{\Delta_{\mathrm{LS}} - i\frac{\gamma_S}{2}} \,, \tag{8.26}$$

the Pochhammer symbol $(a)_n = \Gamma(a+n)/\Gamma(a)$, and A being the proper normalization factor

$$A = \sum_{n=0}^{N} a_{nn} \, \mathrm{Tr}\left(J_-^n J_+^n\right) = \sum_{n=0}^{N} |\tilde{v}|^{-2n} |(1+i\tilde{\epsilon})_n|^2 (n!)^{-2} \, \mathrm{Tr}\left(J_-^n J_+^n\right) \,. \tag{8.27}$$

In Sec. 3.3, we found that in the linear regime the results are invariant under a rescaling of

$$\begin{aligned} \kappa &\to \kappa \cdot \xi \,, \\ \kappa_R &\to \kappa_R \cdot \xi \,, \\ \Delta_C &\to \Delta_C \cdot \xi \,, \\ \tilde{g} &\to \tilde{g} \cdot \sqrt{\xi} \,. \end{aligned} \tag{8.28}$$

It can be easily seen that the stationary density matrix above has the same property. Note that a_{in} does not take part in this rescaling and thus is a fixed parameter. The quantity $|a_{\mathrm{in}}|^2$ has the unit frequency and corresponds to the rate of photons impinging on the cavity.

Let us now introduce a set of basis states. As mentioned before, the equations of motion form a closed system within the symmetric states. We denote the collective ground state, in which no

nucleus is excited, by $|0\rangle$. The symmetric state $|j\rangle$ with j excitations can be created by j-times applying the operator J_+ to the ground state. From angular momentum algebra we find

$$J_+|j\rangle = \sqrt{(j+1)(N-j)}\,|j+1\rangle\,, \tag{8.29}$$

$$J_-|j\rangle = \sqrt{j(N-j+1)}\,|j-1\rangle\,, \tag{8.30}$$

$$J_+^n|j\rangle = \left(\prod_{k=j}^{j+n-1}\sqrt{(k+1)(N-k)}\right)|j+n\rangle\,, \tag{8.31}$$

$$J_-^n|j\rangle = \left(\prod_{k=j-n+1}^{j}\sqrt{k(N-k+1)}\right)|j-n\rangle\,, \tag{8.32}$$

and we obtain the following relations

$$\mathrm{Tr}\left(J_-^m J_+^n\right) = 0 \text{ for } n \neq m\,, \tag{8.33}$$

$$\begin{aligned}\mathrm{Tr}\left(J_-^n J_+^n\right) &= \sum_{j=0}^{N}\langle j|J_-^n J_+^n|j\rangle = \sum_{j=0}^{N}\|J_+^n|j\rangle\|^2 = \sum_{j=0}^{N}\prod_{k=j}^{j+n-1}(k+1)(N-k)\\ &= \mathrm{Tr}\left(J_+^n J_-^n\right) = \sum_{j=0}^{N}\prod_{k=j-n+1}^{j}k(N-k+1)\\ &= \frac{(n!)^2(1+n+N)!}{(1+2n)!(N-n)!} = (n!)^2\binom{N+n+1}{N-n}\,.\end{aligned} \tag{8.34}$$

8.2.2 Observables

With the solution for the stationary density matrix at hand, we are now able to turn to particular observables and calculate their expressions.

Reflectance

In Sec. 8.1 it was shown that going beyond the linear limit requires a different definition of the reflectance. Here, we consider both the linear reflectance $|R|^2$ as well as the general expression $|R_{a^\dagger a}|^2$. We begin by rewriting the observable from Eq. (3.29) in Sec. 3.2.1 in terms of the collective operators

$$\frac{a_{\mathrm{out}}}{a_{\mathrm{in}}} = \left(-1+\frac{2\kappa_R}{\kappa+i\Delta_C}\right)+\left(-i\frac{\sqrt{2\kappa_R}}{\kappa+i\Delta_C}\frac{\tilde{g}}{a_{\mathrm{in}}}\right)J_- =: R_C + B_N J_-\,, \tag{8.35}$$

$$\frac{a_{\mathrm{out}}^\dagger}{a_{\mathrm{in}}^*} = R_C^* + B_N^* J_+\,, \tag{8.36}$$

$$|R|^2 = \left|\frac{\langle a_{\mathrm{out}}\rangle}{a_{\mathrm{in}}}\right|^2 = \left|R_C + B_N\langle J_-\rangle\right|^2\,, \tag{8.37}$$

$$|R_{a^\dagger a}|^2 = \frac{\langle a_{\mathrm{out}}^\dagger a_{\mathrm{out}}\rangle}{|a_{\mathrm{in}}|^2} = |R_C|^2 + 2\,\mathrm{Re}\left(R_C^* B_N\langle J_-\rangle\right) + |B_N|^2\langle J_+J_-\rangle\,. \tag{8.38}$$

We find that the expectation values $\langle J_-\rangle$ and $\langle J_+J_-\rangle$ have to be evaluated. Using Eqs. (8.23)–(8.27) yields

$$\langle J_-\rangle = \mathrm{Tr}(J_-\rho^{(\mathrm{SS})}) = \frac{1}{A}\sum_{n=1}^{N}a_{n-1,n}\,\mathrm{Tr}(J_-^n J_+^n)\,, \tag{8.39}$$

$$\langle J_+ J_- \rangle = \mathrm{Tr}(J_- \rho^{(\mathrm{SS})} J_+) = \frac{1}{A} \sum_{n=1}^{N} a_{n-1,n-1} \,\mathrm{Tr}(J_-^n J_+^n) \,. \tag{8.40}$$

Nuclear excitation

A second observable of interest is the average number of excited nuclei in the cavity. This quantity might be experimentally accessible via measurements of the conversion electrons [191]. Here, it is of interest from a fundamental point of view as it can help to provide a proper understanding of the observed effects. The number of excited nuclei can be expressed in terms of the angular momentum operator J_z as

$$\hat{N}_e = \sum_{n=1}^{N} S_+^{(n)} S_-^{(n)} = \frac{N}{2} \mathbb{1} + J_z \,. \tag{8.41}$$

With the knowledge of the action of J_z on the system, the observable can in principle be evaluated employing Eqs. (8.23)–(8.27). However, we use a different method here. For this we use the basis states $|j\rangle$ introduced above. By definition, $\hat{N}_e|j\rangle = j|j\rangle$ as the state contains j (symmetrized) excited nuclei, and we find

$$\begin{aligned}
\langle \hat{N}_e \rangle &= \mathrm{Tr}(\rho^{(\mathrm{SS})} \hat{N}_e) = \frac{1}{A} \sum_{n=0}^{N} a_{nn} \,\mathrm{Tr}\left(J_-^n J_+^n \hat{N}_e \right) = \frac{1}{A} \sum_{n=0}^{N} a_{nn} \sum_{j=0}^{N} \langle j | J_-^n J_+^n \hat{N}_e | j \rangle \\
&= \frac{1}{A} \sum_{n=0}^{N} a_{nn} \sum_{j=0}^{N} j \| J_+^n |j\rangle \|^2 = \frac{1}{A} \sum_{n=0}^{N} a_{nn} \sum_{j=1}^{N} \frac{(j+n)!(N-j)!}{(j-1)!(N-j-n)!} \\
&= \frac{1}{A} \sum_{n=0}^{N} a_{nn} (n+1)! n! \binom{N+n+1}{N-n-1} = \frac{1}{A} \sum_{n=0}^{N} a_{nn} \,\mathrm{Tr}\left(J_-^n J_+^n \right) \frac{N-n}{2} \\
&= \frac{N}{2} - \frac{1}{2A} \sum_{n=0}^{N} a_{nn} n \,\mathrm{Tr}\left(J_-^n J_+^n \right) \,.
\end{aligned} \tag{8.42}$$

Here, the second part in the last equation corresponds to $\langle J_z \rangle$, which is identical to the result obtained in Ref. [259].

Photons in the cavity

Even though the photonic mode a in the cavity was adiabatically eliminated, it is possible to recover connected observables. From the elimination procedure, we know that (c.f. Eq. (3.28))

$$a = \frac{1}{\kappa + i\Delta_C} \left(\sqrt{2\kappa_R} \, a_{\mathrm{in}} - i\tilde{g} J_- \right) \,, \tag{8.43}$$

and thus the mean photon number in the cavity becomes

$$N_{\mathrm{Ph}} = \langle a^\dagger a \rangle = \frac{1}{\kappa^2 + \Delta_C^2} \left(2\kappa_R |a_{\mathrm{in}}|^2 - 2\,\mathrm{Re}\left(i\tilde{g} \sqrt{2\kappa_R} a_{\mathrm{in}}^* \langle J_- \rangle \right) + |\tilde{g}|^2 \langle J_+ J_- \rangle \right) \,. \tag{8.44}$$

Note that this observable changes upon a rescaling as defined in Eq. (8.28). It is therefore necessary to perform all calculations with the correct scaling factor ξ.

Photon correlation function

The input-output formalism yields operators a_{out} for the reflected light, even though if the incident field is purely classical. The reason for this is that the light interacts with a quantized

system and its quantum nature can be devolved to the reflected radiation. The operator formulation makes it possible to calculate advanced quantum mechanical observables, such as the photon correlation function $g^{(2)}$ given in Eq. (3.16). A value of unity for the correlation function corresponds to Poisson photon statistics, $g^{(2)} > 1$ or $g^{(2)} < 1$ to super- and sub-Poissonian statistics [1, 145]. The latter indicates a non-classical state of the electromagnetic field [146]. Note that the correlation function could be extended to the probability of two photons arriving with a certain time difference, characterizing bunching and antibunching of the photons.

In our equations, the external driving field is treated as a classical plane wave, which obeys Poissonian statistics. Thus, any deviation from $g^{(2)} = 1$ can be traced back to an interaction with the nuclei in the cavity.

Using Eq. (8.35), we find for the photon correlation function

$$\begin{aligned} g^{(2)} &= \frac{\langle (R_C^* + B_N^* J_+)(R_C^* + B_N^* J_+)(R_C + B_N J_-)(R_C + B_N J_-)\rangle}{\langle (R_C^* + B_N^* J_+)(R_C + B_N J_-)\rangle^2} \\ &= \frac{|R_C|^4 + |B_N|^4 \langle J_+^2 J_-^2\rangle + 4|R_C B_N|^2 \langle J_+ J_-\rangle}{|R_{a^\dagger a}|^4} \\ &\quad + \frac{2\,\mathrm{Re}\left({R_C^*}^2 B_N^2 \langle J_-^2\rangle + 2|R_C|^2 R_C^* B_N \langle J_-\rangle + 2|B_N|^2 R_C^* B_N \langle J_+ J_-^2\rangle\right)}{|R_{a^\dagger a}|^4} \,. \end{aligned} \tag{8.45}$$

Thus, the expectation values $\langle J_+^2 J_-^2\rangle$, $\langle J_+ J_-^2\rangle$, $\langle J_-^2\rangle$ are required in addition. Similar as the expectation values in Eqs. (8.39) and (8.40), the expressions can be calculated from the density matrix given in Eqs. (8.23)–(8.27).

8.2.3 Linear limit of observables

Before we turn to the observables in the case of a strong external driving field, we take a step back and consider the limit of a weak input pulse again. Up to the neglected spontaneous emission rate γ, the results from the non-linear solution should agree to the expressions obtained previously.

For a proper comparison, the scaling in the sums, e.g. in Eq. (8.39) and Eq. (8.40) need to be understood. For simplicity, let us consider the case $\Delta = 0$, i.e. $\tilde{\epsilon} = 0$. In this case, the coefficient a_{nn} reduces to $|\tilde{v}|^{-2n}$. Thus, a weak probe pulse, corresponding to $|\tilde{v}|^2 \ll 1$, will favor terms with a large summation index n. Additionally, the summands a_{nn} are weighted with $\mathrm{Tr}(J_-^m J_+^n)$. From Eq. (8.34) can be deduced, that this further increases the significance of terms with large n. Therefore, in the weak probe limit, the expectation values from Eqs. (8.39) and (8.40) can be reduced to

$$\langle J_-\rangle \approx \frac{a_{N-1,N}\,\mathrm{Tr}(J_-^N J_+^N)}{a_{N,N}\,\mathrm{Tr}(J_-^N J_+^N)} = \frac{a_{N-1,N}}{a_{N,N}} = \frac{-i\tilde{v}N}{N + i\tilde{\epsilon}} \,, \tag{8.46}$$

$$\langle J_+ J_-\rangle \approx \frac{a_{N-1,N-1}}{a_{N,N}} = \frac{N^2|\tilde{v}|^2}{|N + i\tilde{\epsilon}|^2} \,. \tag{8.47}$$

Indeed, if we use these expressions for the reflectance defined in Eqs. (8.37) and (8.38), we obtain identical results to the linear model. The only (expected) difference is the absence of the spontaneous emission rate γ. As the reflectance agrees with the previous result in the respective limit, this can be seen as a cross-check of the general non-linear solution.

With the knowledge of the scaling in the sums of Eqs. (8.39) and (8.40), we are now able to estimate when a deviation from the result obtained in the linear regime is expected. Taking the ratio of the two largest summands at $\Delta = \tilde{\epsilon} = 0$ yields

$$\frac{a_{N-1,N-1}\,\mathrm{Tr}(J_-^{N-1} J_+^{N-1})}{a_{N,N}\,\mathrm{Tr}(J_-^N J_+^N)} = |\tilde{v}|^2 \frac{2}{N} = \frac{4\kappa_R |a_{\mathrm{in}}|^2}{\tilde{g}^2 N} \,. \tag{8.48}$$

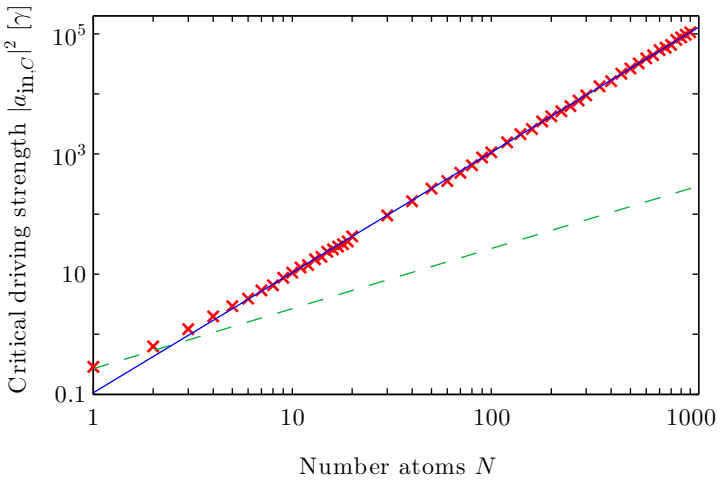

Figure 8.2: The critical driving strength required to observe non-linear effects is shown in dependency on the atom number N. The non-linear regime is defined via an excitation of $\geq 25\%$ of the nuclei. Red crosses are results from numerical simulations, dashed line is the lower limit condition from Eq. (8.48), solid line is the asymptotic behavior from Eq. (8.50). Parameters: $\kappa = 45\gamma, \kappa_R = 25\gamma, \Delta_C = 0, g^2 = 40\gamma^2$.

Thus, for non-linear effects to become important, this ratio must be at least of the order one, i.e. a large probing field intensity is required to overcome the $1/N$ scaling. Note, however, that at the same time this argument hold for the normalization factor A in Eqs. (8.39) and (8.40). Thus, the condition given above is only a lower bound for the probe field strength. The crossover to the non-linear regime will be discussed in more detail below.

Next, let us consider the linear limit of the second observable, the number of excited nuclei defined in Eq. (8.42). With the same argument as above, we need to consider only one term in the sum, which immediately yields

$$\langle \hat{N}_e \rangle \approx \frac{N}{2} - \frac{a_{NN} N \operatorname{Tr}(J_-^N J_+^N)}{2 a_{NN} \operatorname{Tr}(J_-^N J_+^N)} = 0 \,. \tag{8.49}$$

We see that also this observable takes the expected limit if a weak probe field is considered.

8.2.4 Results of the general model

Occurrence of non-linear effects

In the last section we already found a first condition which indicates when non-linear effects are expected, see Eq. (8.48). However, it forms only a lower boundary, since the argument is based on mathematical considerations and it is not clear if the observable of interest already exhibit non-linear phenomena.

Here, we tackle the question when non-linear effects occur by numerical means. For this, a quantity characterizing the non-linear crossover has to be defined. For weak probe beams the number of excited nuclei vanishes, while for a very strong driving it approaches $N/2$. Thus, we coarsely define the crossover to non-linearity as the point when the fraction of excited nuclei exceeds $1/4$.

We calculated the nuclear excitation with Eq. (8.42) for several sets of parameters in the detuning range $-100\gamma \leq \Delta \leq 100\gamma$. Thereby, we increased the driving field strength a_{in} until our criterion, i.e. $\langle \hat{N}_e \rangle \geq N/4$ was reached. We found that in the asymptotic limit of large N

the crossover to the non-linear regime can be approximated by the equation

$$|a_{\mathrm{in},C}|^2 \approx \frac{\tilde{g}^2}{10\kappa_R} \cdot N^2 \,. \tag{8.50}$$

This is illustrated in Fig. 8.2, where both the numerically obtained data and the asymptotic formula is plotted. The asymptotic behavior can be understood as follows. The cavity mode is driven with the rate $\sqrt{2\kappa_R}a_{\mathrm{in}}$, c.f. Eq. (3.8). As soon as this rate is comparable with the coupling coefficient g between the cavity mode and a nucleus, non-linear effects set in. In the case of N nuclei in the cavity, the cavity pump rate has to compete with $N \cdot g$. From this consideration, Eq. (8.50) is qualitatively obtained.

With the condition found above, this raises the question if non-linear effects can be observed at high-intensity x-ray light sources, such as free-electron lasers. Solving for the critical driving rate $|a_{\mathrm{in},C}|$ with the parameters of the toy-model cavity discussed in Sec. 3.3, we obtain the critical driving rate

$$|a_{\mathrm{in},C}|^2 \sim 4N \cdot 10^7 \text{ photons}/s \,. \tag{8.51}$$

Unfortunately, the exact number of nuclei taking part in the light-matter interaction is unknown, as only the product $|g|^2 N$ can be deduced from experimental data or from comparison with semi-classical theories. Thus, no value for the critical rate can be given this way. We emphasize, that the calculations in this section are based on the steady state analysis of the system, therefore implying a continuous driving field. X-ray free-electron laser sources, tough, provide extremely short laser pulses and a comparison of their performance to the continuously required photon rate is not meaningful. An analysis of such short pulse excitations will be performed in Sec. 8.3.

Finally, we want to mention that other criteria for the non-linear crossover could be defined. For example, in future studies the deviation of the linear and the non-linear spectrum, integrated along the detuning axis, could be employed instead of the nuclear excitation condition used above.

Observables in the non-linear regime

We now turn to the observables introduced above and their dependence on the driving field strength $|a_{\mathrm{in}}|^2$. Simulation results for $N = 1000$ atoms are shown in Fig. 8.3.

For the reflectance we observe that the spectrum becomes flatter as the driving field strength is increased. In the limit of very large $|a_{\mathrm{in}}|^2$, the reflectance approaches the empty-cavity limit. Mathematically, this can be understood as follows. For large a_{in}, the coefficients a_{nm} for the density matrix given in Eq. (8.23) converge to $a_{nm} = \delta_{n0}\delta_{m0}$, where δ denotes the Kronecker symbol. Hence, the expectation values $\langle J_- \rangle$ and $\langle J_+ J_- \rangle$ in this limit do not depend on the driving strength. On the other hand, the coefficient B_N in the reflectance (c.f. Eq. (8.35)) is suppressed due to its a_{in}^{-1} scaling. Thus, the nuclear contribution to the reflectance vanishes and only the empty-cavity response persists.

At this point it is instructive to calculate the exact single atom solution, and for simplicity, we consider the observable $|R|^2$. The solution for the nuclear part in the reflectance differs from the result $R = R_C + R_N$, which we obtained in the linear theory. Here, R_C denotes the cavity part and R_N the nuclear contribution to the reflectance as in Chap. 4, but with neglected spontaneous emission rate γ. The reason for the discrepancy is the normalization factor A for the density matrix defined in Eq. (8.27). Generally, it covers two summands $2 + a_{11}$ and restricting the analysis to the second term only, the linear result would be recovered exactly. For the full solution, however, we find

$$R\big|_{N=1} = R_C - i\,\frac{2\kappa_R}{\kappa}\,\frac{\kappa - i\Delta_C}{\kappa + i\Delta_C}\,\frac{\frac{\gamma_S}{2}\,(\Delta - \Delta_{\mathrm{LS}} - i\frac{\gamma_S}{2})}{(\frac{\gamma_S}{2})^2 + (\Delta - \Delta_{\mathrm{LS}})^2 + |a_{\mathrm{in}}|^2 \gamma_S \frac{2\kappa_R}{\kappa}} \,, \tag{8.52}$$

where Δ_{LS} is the collective Lamb shift and γ_S corresponds to the superradiant decay rate. From this expression it can be seen that an increasing field strength a_{in} gives rise to a smaller value

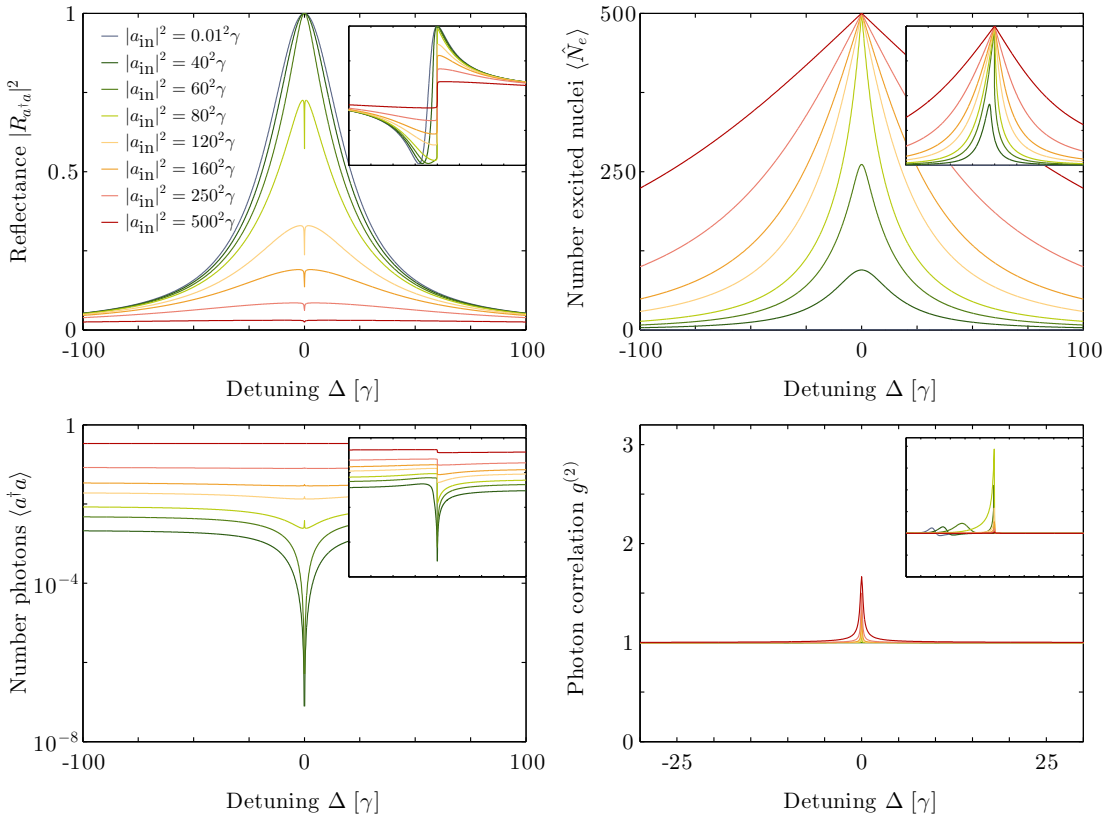

Figure 8.3: The observables are shown in dependence on the driving field strength $|a_{\rm in}|^2$. In the large panels a cavity detuning $\Delta_C = 0$ was used, the smaller insets show results for $\Delta_C = \kappa$ and cover the same range along the axes. Other parameters: $N = 1000, \kappa = 45\xi\gamma, \kappa_R = 25\xi\gamma, g^2N = 1400\xi\gamma^2, \xi = 18000$.

for the nuclear reflectance, since the denominator increases. Setting $a_{\rm in} = 0$ in Eq. (8.52), the linear result from Sec. 3.3 is reobtained. The effect observed here can be identified as power broadening [146]. The physical origin of the decreasing reflectance can be understood with the following intuitive picture. The nuclei can, in contrast to a cavity mode, only store a finite amount of excitations. As soon as the nuclei are saturated, their emission in the direction of the detector cannot keep up with the driving rate and the relative nuclear contribution to the reflectance decreases. As a consequence, the incident light is mainly reflected from the empty-cavity scattering channel.

The second observable shown in Fig. 8.3 is the number of excited nuclei. Not surprisingly, upon a stronger driving strength, it increases towards $N/2$, which corresponds to full saturation of the nuclear transitions. Also the number of photons in the cavity steadily increases, which is expected already from the first contribution in Eq. (8.44) that implies $N_{\rm Ph} \sim |a_{\rm in}|^2$.

Next, let us look at the photon correlation function $g^{(2)}$ and how it depends on the driving field strength. The result for different $|a_{\rm in}|^2$ is shown in the lower right panel of Fig. 8.3. Obviously, it does not differ much from Poissonian statistics. Only in a small frequency range a super-Poissonian behavior can be observed. However, we note that the result in the correlation function strongly depends on the number of atoms N. It turns out that a large N gives rise to a flat $g^{(2)}$. On the other hand, for a rather small number of atoms, ranges of both sub- and super-Poissonian statistics appear. This behavior is also related to saturation effects of the nuclei. For strong driving fields, the empty-cavity path is the dominant reflection channel and the Poissonian statistics of the incident light is directly transfered to the output field.

Finally, we want to focus on the observables in the case of a strong cavity detuning $\Delta_C = \kappa$, for which the simulation results can be seen in the insets of Fig. 8.3. Here, several sharp edges occur in the center. We find that this property is the stronger pronounced, the larger the number of atoms N is in the simulation. A sharp feature in the spectrum hints to a long time range, which is required until such a characteristic shape can be created. Here, the sharp edge can be seen since we consider the steady state of the observables, i.e. the state of the system after an infinite time.

8.2.5 Non-linear numerical solution in SGC setting

In this part we will analyze how an increased driving field strength will affect the system in the presence of a magnetic hyperfine splitting in the nuclei. Under the influence of a magnetic field, the ground and excited state of the ^{57}Fe nuclei split up into Zeeman sublevels. In Chap. 5 it was shown that the phenomenon of spontaneously generated coherences (SGC) arises in this setting, resulting in more complex reflectance spectra with, e.g., distinct interference minima. Here, for simplicity, we restrict the discussion to the π *geometry* defined in Sec. 5.1, in which only the two linearly polarized transitions in the nuclei are driven. This choice restricts the atomic subspace to four levels, i.e. two ground and two excited states, which are mutually coupled as described by the Hamiltonian in Eq. (3.30) and the Lindblad terms in Eq. (3.36). To our knowledge, no analytic solution for the stationary density matrix exists for this situation. Therefore, we will perform a numerical study in the following.

We include four nuclei in our simulation. As each nucleus consists of four internal states, this results in $4^{N\cdot 2} = 2^{16}$ coupled density matrix elements. To solve the system numerically, we employ the method `gsl_odeiv2_step_rkf45` from the GSL software package [260]. Initially, the four atoms are distributed equally over the two ground states and we propagate the system up to $t = 10/\gamma$, such that the steady state is reached. All observables shown in the following are evaluated at this time. As a crosscheck, we set the magnetization to zero and verified that the numerically obtained steady state observables agree with the analytical results discussed above.

The observables for the system with four atoms subjected to a magnetic splitting are shown in Fig. 8.4. Generally, the same trend as in the cases without a magnetization is observed. The spectrum of the reflectance decreases and approaches the empty-cavity limit. Interestingly, the central dip in the spectrum stemming from interference due to SGC remains visible even for strong driving fields $|a_{\text{in}}|^2$. At the same time, the number of excited nuclei and the number of photons in the cavity increase as we already observed for the non-magnetized case. Next, we focus on the photon correlation function $g^{(2)}$. It can be seen from Fig. 8.4 that ranges for both super- and sub-Poissonian statistics occur. However, this is most likely an artifact of the limited number of atoms. In calculations with the analytic solution for the non-magnetized case, we found that increasing the number of atoms leads to reduced features in $g^{(2)}$ and the overall result will eventually approach unity.

In summary, we have seen how the steady state of the observables is affected if a strong driving field is applied. However, this way of exploring the non-linear regime assumes a continuous monochromatic driving field on the time scale which is needed for the observables to converge. As mentioned above, this time range can be rather larger in the situation where the sharp edges are observed in the spectrum. From a theoretical point of view, these long times might interfere with the assumption that the single atom spontaneous emission rate γ was neglected in the analysis. Additionally, the requirements on the probing light are not met by current synchrotron radiation or upcoming x-ray free-electron laser sources. The required light can only be achieved with devices, which work in a much lower frequency regime. Therefore it is unlikely, that the cavity with embedded ^{57}Fe nuclei and their resonance at $\omega_0 = 14.4$ keV can be probed this way. However, it might be feasible to use other Mössbauer nuclei instead, which then offer a lower transition frequency.

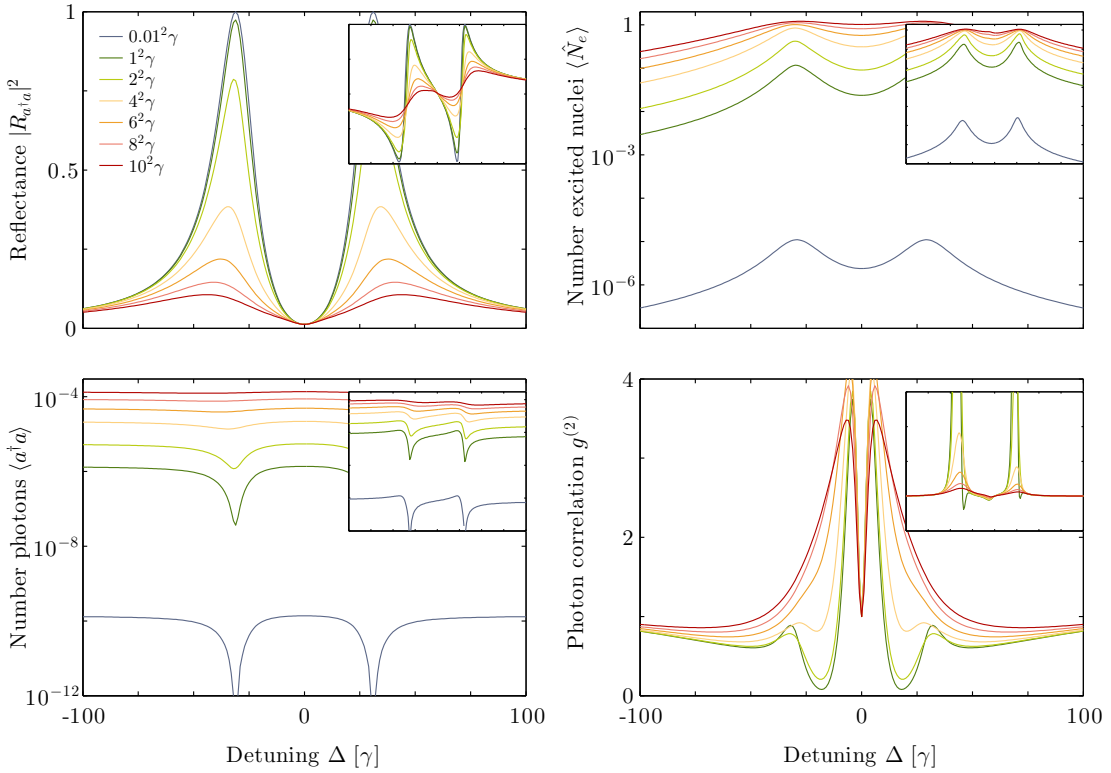

Figure 8.4: Numerical results for the setting of SGC atoms in the cavity. The observables for different field strengths $|a_{\text{in}}|^2$ are shown (Values are shown in the upper left panel). In the large panels a cavity detuning $\Delta_C = 0$ was used, the smaller insets show results for $\Delta_C = \kappa$ and cover the same range along the axes. Other parameters: $N = 4, \kappa = 45\xi\gamma, \kappa_R = 25\xi\gamma, g^2N = 1400\xi\gamma^2, \xi = 18000$. The photon correlation $g^{(2)}$ is not shown for the lowest a_{in} due to numerical instabilities during its evaluation.

8.3 Emission spectra after a δ-like pulse excitation

In this section we do not consider non-linear effects induced by a strong continuous driving field, but discuss the more realistic scenario of a short incidence pulse. This compares to the situation encountered in a realistic experimental setting. For example, a pulse delivered by an x-ray free-electron laser with short pulse durations in the pico- or even femtosecond range, together with a high photon number could be used to probe the thin-film cavity in the future. Clearly, this does not match the scenario discussed in the previous section, and therefore a thorough analysis for short incident pulses must be carried out. In this section, we restrict ourselves to the spectrum in the reflectance as the desired observable.

Theoretical considerations

In a first step, we review the definition of the spectrum, which can be observed in the reflected light. It was detailedly discussed in Sec. 3.4 and reads

$$|R_\delta|^2 = \frac{\langle a^\dagger_{\text{out}}(\omega) a_{\text{out}}(\omega) \rangle}{|a_{\text{in}}(\omega)|^2} \,, \tag{8.53}$$

where $a_{\text{out}}(\omega)$ denotes to Fourier transform of the output field operator $a_{\text{out}}(t)$. The denominator in Eq. (8.53) provides the proper normalization. For an input pulse $a_{\text{in}}(t) \sim \delta(t)$, the denominator is a constant, while in realistic scenarios the Fourier transform of the incident pulse needs to be

taken into account properly. Next, let us look at the numerator in Eq. (8.53) in more detail. It describes the emission spectrum and can be written as

$$\begin{aligned} S(\omega) = \langle a^\dagger_{\text{out}}(\omega) a_{\text{out}}(\omega)\rangle &= \frac{1}{2\pi}\int e^{-i\omega(t_1-t_2)}\langle a^\dagger_{\text{out}}(t_1) a_{\text{out}}(t_2)\rangle\, dt_1 dt_2 \\ &= \frac{1}{\pi}\,\text{Re}\left[\int_{-\infty}^{\infty} dt' \int_0^\infty d\tau e^{i\omega\tau}\langle a^\dagger_{\text{out}}(t'+\tau) a_{\text{out}}(t')\rangle\right] . \end{aligned} \tag{8.54}$$

Hence, solving the time dependence of the system provides access to the desired reflection spectrum.

In our quantum optical description of the cavity, which we developed in Chap. 3, we adiabatically eliminated the internal cavity modes. This elimination can again be applied here. The reason for this are the relevant time scales. The cavity mode equilibrates on the time scale $1/\kappa$, where κ is its decay rate. In Sec. 3.3, we found a typical value of $\kappa \approx 8 \cdot 10^5 \gamma$, which translates in a characteristic time scale of $1/\kappa \approx 175$ fs. In the following, we assume that the probing pulse has a longer duration, such that the adiabatic elimination of the cavity modes is justified.

Further, we will for simplicity consider an incident pulse with rectangular shape and with pulse duration t_0, given by the input field

$$a_{\text{in}}(t) = \tilde{a}_{\text{in}}\theta(t)\theta(t-t_0) . \tag{8.55}$$

Its Fourier transform is required for the normalization in the reflectance, which was defined in Eq. (8.53). We find

$$|a_{\text{in}}(\omega)|^2 = \frac{1-\cos(\omega t_0)}{\pi\omega^2}\theta(t_0) . \tag{8.56}$$

Next, we denote the sum of the transition lowering operators of the individual atoms as $J_- = J_+^\dagger = \sum_n S_i^{(n)}$, and similar as in the previous section, we can write for the output field operator (c.f. Eq. (8.35))

$$\begin{aligned} a_{\text{out}}(t) &= \left(-1 + \frac{2\kappa_R}{\kappa + i\Delta_C}\right) a_{\text{in}}(t) - i\frac{\sqrt{2\kappa_R}}{\kappa + i\Delta_C} g\sqrt{\tfrac{2}{3}}\, J_-(t) \\ &= R_C\, a_{\text{in}}(t) + b_N\, J_-(t) , \end{aligned} \tag{8.57}$$

where the output field is now distributed into a cavity component and a contribution from the embedded nuclei. For the expectation value in Eq. (8.54) we then obtain

$$\begin{aligned} \langle a^\dagger_{\text{out}}(t'+\tau) a_{\text{out}}(t')\rangle = {} & |R_C|^2 a_{\text{in}}(t') a_{\text{in}}(t'+\tau) \\ & + R_C^* a_{\text{in}}(t'+\tau) b_N \langle J^-(t')\rangle \\ & + b_N^* \langle J_+(t'+\tau)\,[R_C a_{\text{in}}(t') + b_N J_-(t')]\rangle . \end{aligned} \tag{8.58}$$

The first term in this sum is readily obtained from the definition of the incident pulse. The second part can be found by solving the equations of motion numerically. The last term, however, involves a two-time expectation value, for which the computation is more involved. In order to evaluate this expectation value, we employ the quantum regression theorem [158]. This theorem states, that the two-time average follows the same equations of motion as the one-time averages.

We illustrate this for the case of a single atom with ground state $|g\rangle$ and excited state $|e\rangle$. The operators and the density matrix elements characterizing this two-level system are

$$\vec{\sigma} = (|g\rangle\langle g|, |e\rangle\langle g|, |g\rangle\langle e|, |e\rangle\langle e|)^T , \tag{8.59}$$

$$\langle\vec{\sigma}\rangle = \vec{\rho} = (\rho_{gg}, \rho_{ge}, \rho_{eg}, \rho_{ee})^T . \tag{8.60}$$

We assume that the equations of motion can be written as

$$\frac{d}{dt}\vec{\rho}(t) = \frac{d}{dt}\langle\vec{\sigma}(t)\rangle = \boldsymbol{M}(t)\cdot\langle\vec{\sigma}(t)\rangle \;, \tag{8.61}$$

where $\boldsymbol{M}(t)$ is a matrix. According to the quantum regression theorem, the same equation holds for a two time expectation value

$$\frac{d}{d\tau}\langle\vec{\sigma}(t'+\tau)\sigma_i(t')\rangle = \boldsymbol{M}(t'+\tau)\cdot\langle\vec{\sigma}(t'+\tau)\sigma_i(t')\rangle \;, \tag{8.62}$$

where σ_i is any operator of the vector $\vec{\sigma}$. Now, in order to evaluate a two-time expectation value, one can use the upper equation, for which the initial state at $\tau = 0$ is known form the one-time solution and propagate the operator until the time τ is reached. Note that the second and the third component in Eq. (8.61) are their respective complex conjugates due to the hermiticity of the density matrix, and therefore the size of the problem can be reduced. However, this is no longer valid in Eq. (8.62) and therefore the complete matrix $M(t)$ is required.

Numerical implementation

In order to calculate the emission spectrum $S(\omega)$ defined in Eq. (8.54) numerically, we apply the following technique. First, the integral along dt' is discretized. Since the incident pulse is non-zero only for times $t \geq 0$, the lower boundary of the integral can be set to zero, since the contribution of the expectation value vanishes for smaller times. The upper boundary of the integral is determined by the time when the pulse ended and all excitations in the system have decayed.

Next, we numerically integrate the density matrix element of the system along t'. At each discretization step we integrate the two-time expectation values along τ such that $\langle a^\dagger_{\mathrm{out}}(t'+\tau)a_{\mathrm{out}}(t')\rangle$ is known for the current time t' and the relevant range in τ. Taking the Fourier transform of these values, the inner integral in Eq. (8.54) is obtained. The Fourier integrals for the different t' are finally added up and the real part is taken to obtain the desired emission spectrum $S(\omega)$.

We benchmarked our calculation technique in the linear regime, where we could compare the results with the exact analytic solution. This way, different choices of the discretization variables could be tested. Obviously, a high accuracy in the calculated spectrum comes with a trade-off of a fast numerical computation. As a reasonable compromise, we found the following numerical parameters. The integral over t' was discretized from 0 to $1/\gamma$ with a step size $10^{-4}/\gamma$. The same step size was used along τ. The grid size of the discretization along τ was chosen as 2^{16} corresponding to the range $|\tau| \lesssim 3.28/\gamma$, such that the Fourier transform can be computed quickly. The resulting spectrum is then obtained for steps $\approx 0.96\gamma$ along the frequency axis.

Using this technique, we explored the setting of a cavity without magnetization. In this case, the nuclei act as two-level systems and their dynamics is described by Eqs. (8.10) and (8.11). In contrast to the calculations in the last section, the spontaneous emission rate was not neglected in the simulations here. We performed numerical computations with the method described above for up to 4 nuclei in the cavity. Even though the size of the Hilbert space is moderate, the calculation of the two-time expectation values combined with the required small step sizes in t' and τ are time-consuming.

In the numerical simulations presented below, we used a pulse length $t_0 = 0.01/\gamma$ and the parameters $g = \sqrt{1400\xi/N}\gamma, \kappa = 45\gamma\xi, \kappa_R = 25\gamma\xi$ and $\xi = 18000$. This corresponds to the situation encountered in Sec. 3.3. For the cavity detuning $\Delta_C = 0$ and $\Delta_C = \kappa$ was used.

Contributions to the emission spectrum

Before we turn to the numerical results, let us first look at the two-time expectation value in more detail. By describing an operator $\mathcal{O}$ by its average value and a fluctuation operator $\langle\mathcal{O}\rangle + \delta\mathcal{O}$,

the expectation value in Eq. (8.54) can formally be rewritten as

$$\langle a^\dagger_{\rm out}(t'+\tau)a_{\rm out}(t')\rangle = \langle a^\dagger_{\rm out}(t'+\tau)\rangle\langle a_{\rm out}(t')\rangle + \langle \delta a^\dagger_{\rm out}(t'+\tau)\delta a_{\rm out}(t')\rangle \ . \tag{8.63}$$

In the study of resonance fluorescence, the contribution to the emitted radiation which stems from the first part in this sum is known as the coherent, while the second term is called the incoherent contribution. The reason for this is that for a continuous coherent driving field, the coherent part of the radiation is emitted with the same frequency as the driving laser. This is comparable with the picture of a classical dipole. In this sense, the incoherent part of the radiation accounts for non-classical effects beyond the classical dipole radiation. In the case of resonance fluorescence, this results in the celebrated Mollow triplet [261].

By omitting the fluctuation operators in Eq. (8.63), the two-time average reduces to one-time averages and the reflection spectrum of Eq. (8.54) becomes

$$S_{\rm coh} = \left| \frac{1}{\sqrt{2\pi}} \int_{-\infty}^{\infty} e^{i\omega t} \langle a_{\rm out}(t)\rangle dt \right|^2 \ , \tag{8.64}$$

and in turn we can define the coherent reflectance as

$$|R_{\delta,\rm coh}|^2 = \frac{S_{\rm coh}}{|a_{\rm in}(\omega)|^2} = \frac{|a_{\rm out}(\omega)|^2}{|a_{\rm in}(\omega)|^2} \ . \tag{8.65}$$

This expression also resembles an intuitive picture of the emitted spectrum often used in the context of spectroscopy: In the weak driving regime, the spectrum is given by the Fourier transform of the complete time-dependent response function, possibly including the initial δ-like pulse as in Refs. [172, 262, 263]. From the equations above, we observe that this intuitive interpretation can break down as soon as the incoherent contribution of the emitted radiation becomes important. In this case, the spectrum must be described with the complete expression given in Eq. (8.54).

Results

Both the full spectrum and its coherent part can be computed numerically, the incoherent contribution to the reflection spectrum can easily be obtained by subtraction. The coherent part, the incoherent part as well as the full reflection spectrum is shown in Fig. 8.5 for different driving strengths $a_{\rm in}$. In the left panel, the cavity is driven at the resonance angle of the first guided mode, such that $\Delta_C = 0$. With an increasing field strength, we observe the saturation effect already noticed in the previous section, where the steady state of the system was analyzed. Now, in addition we also recognize that the incoherent part, i.e. the non-classical contribution, has a huge impact on the reflection spectra. At $\tilde{a}_{\rm in} \approx 35\sqrt{\gamma}$, the emitted signal is nearly completely determined by the incoherent contribution to the spectrum. Interestingly, the shape of the incoherent contribution seems to be always given by a Lorentzian line profile and its width agrees with the expected superradiantly broadened decay rate $\Gamma = \gamma + \frac{4}{3}|g|^2 N\kappa/(\kappa^2 + \Delta_C^2)$ very well.

Also in the case where the incident angle of the pulse is changed, such that the cavity is driven off-resonantly with cavity detuning $\Delta_C = \kappa$, the incoherent part of the spectrum plays a crucial role. Again, we find that the shape of the incoherent spectra is roughly given by a Lorentzian, and its width is in accordance the superradiant width Γ. In contrast to the setting before where $\Delta_C = 0$, the line profiles are now shifted approximately by the collective Lamb shift $\Delta_{\rm LS} = -\frac{2}{3}|g|^2 N\Delta_C/(\kappa^2 + \Delta_C^2)$. This surprising result could be confirmed also for larger number of atoms and suggests that this effect is an universal property of our system. A possible explanation is that the incoherent part of the spectrum emitted by the nuclei has, by definition, no fixed phase relation with the driving field. Hence, no interference with the prompt part of the reflection occurs, and only the nuclear shape with superradiant broadening and the collective Lamb shift remains.

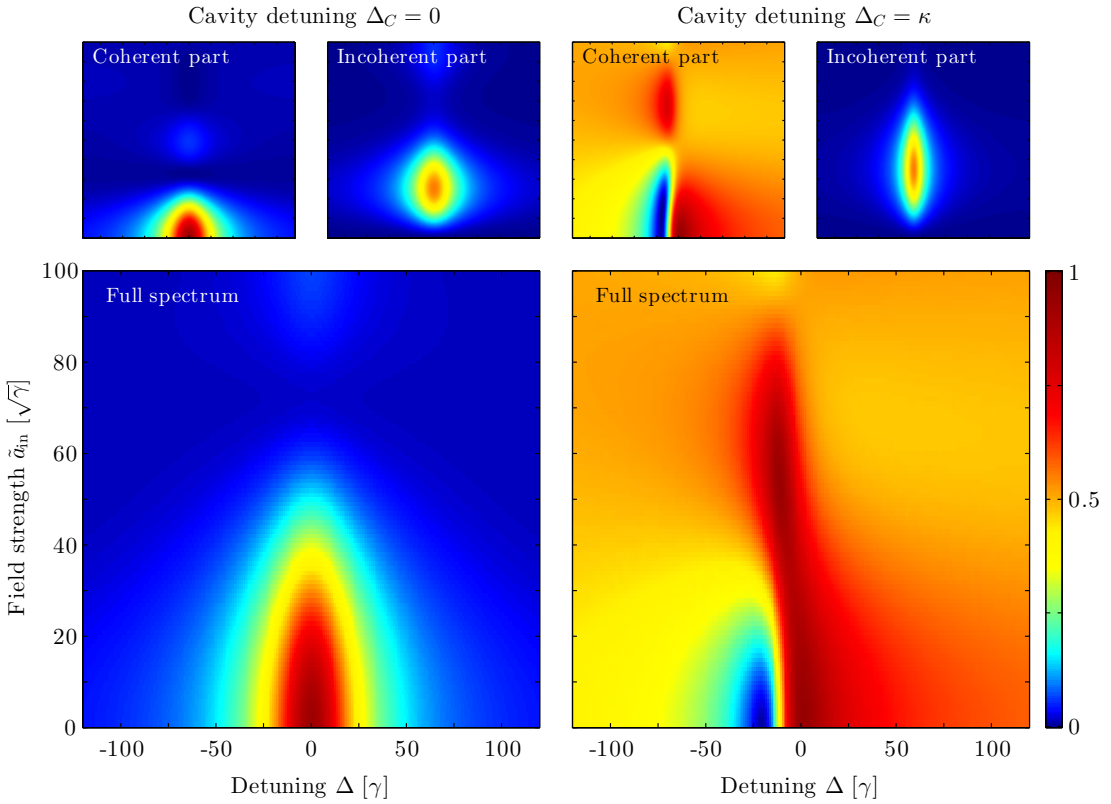

Figure 8.5: Reflection spectra after a δ-like pulse excitation with one resonant nucleus in the cavity are shown for different field strengths $\tilde{a}_{\rm in}$ and for two cavity detunings Δ_C. In the strong driving limit the spectrum becomes flat due to saturation effects in the nucleus. For increasing field strengths, the asymmetric Fano profile observed for $\Delta_C = \kappa$ changes its form significantly. The coherent and the incoherent parts of the spectra are shown in the upper panels in the same scale as the main figures. Parameters are given in the main text.

Line shape control

Next, we want to look into a particular feature which is observed in the full and the coherent spectrum in more detail. In Fig. 8.6, a small subset of the spectra from Fig. 8.5 with $\Delta_C = \kappa$ is shown. Both for the coherent and the full spectrum it can be seen that the line shape and its symmetry can be strongly affected by already a moderate change in the driving field strength $a_{\rm in}$. Since especially the coherent spectrum shows a distinct behavior, we focus on this part. We recall that it is given by the Fourier transform of the time resolved reflection signal. This time domain signal consists of a short δ-like cavity contribution and the delayed nuclear signal. In Chap. 4 it was shown that the interference of these to channels can give rise to Fano interference. The line shape was determined by the relative phase between the two amplitudes and could be controlled via the incidence angle. Here, however, the angle of incidence is kept constant. Therefore, it can be expected that a new mechanism causes a relative phase between the contributions to the reflectance, and consequently determines the spectral line profile. In fact, we find that the new control mechanism stems from nuclear excitation in the cavity. We emphasize that this is a non-linear feature, since any population of the nuclei could be safely neglected in the linear regime.

For the four different driving strengths shown in Fig. 8.6 we present the time resolved nuclear excitation in Fig. 8.7. Initially, the atoms reside in their ground state and during the pulse

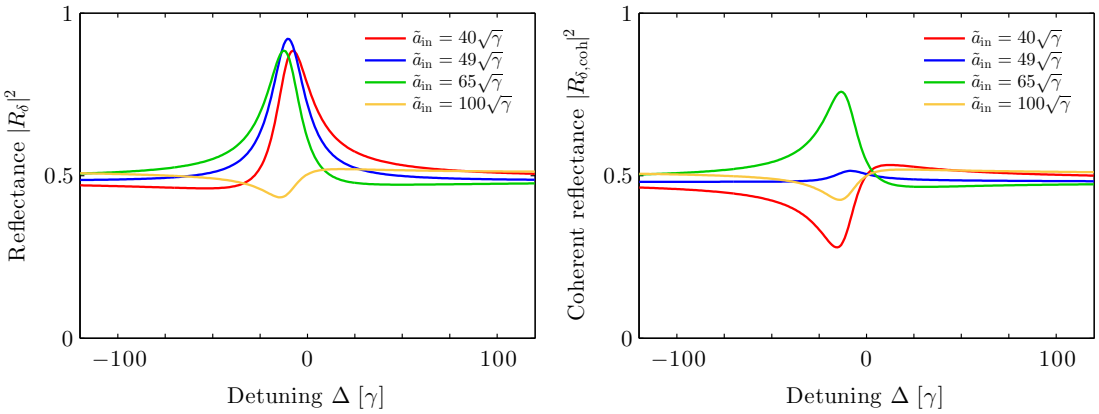

Figure 8.6: The full reflectance (left panel) and the coherent contribution (right panel) from Fig. 8.5 with $\Delta_C = \kappa$ is shown in more detail. Already moderate changes in the driving field strength can result in different spectral profiles.

duration they will be excited. During this time range, the large driving strength $\tilde{a}_{\mathrm{in}}$ dominates over the other coupling parameters, such that the atoms will undergo characteristic Rabi oscillations [1]. From our quantum optical theory, we know that each nucleus is driven with the Rabi frequency (c.f. Eq. (8.10))

$$\Omega_R = \frac{\sqrt{2\kappa_R}}{\kappa + i\Delta_C}\sqrt{\tfrac{2}{3}}\, g\, \tilde{a}_{\mathrm{in}} \,. \tag{8.66}$$

In a simplified picture we consider a single nucleus subjected to a driving with this frequency. Then, the equations correspond to the Rabi model and the solution reads [1]

$$H = \Omega_R |e\rangle\langle g| + \Omega_R^* |g\rangle\langle e| \,, \tag{8.67}$$
$$|\psi\rangle = c_g(t)|g\rangle + c_e(t)|e\rangle \,, \tag{8.68}$$
$$c_g(0) = 1 \,,\; c_e(0) = 0 \,, \tag{8.69}$$
$$c_g(t) = \cos\left(|\Omega_R| t\right) \,, \tag{8.70}$$
$$c_e(t) = -ie^{i\arg(\Omega_R)} \sin\left(|\Omega_R| t\right) . \tag{8.71}$$

The nuclear excitation obtained with this simple model is given by

$$N_{\mathrm{exc}}(t) = |c_e(t)|^2 = \sin\left(|\Omega_R| t\right)^2 \,, \tag{8.72}$$

and is shown as dashed curves in Fig. 8.7(a). Clearly, it matches the exact numerical simulation well, the differences are due to the neglected collective effects and the incoherent processes. From Fig. 8.7(a), we also see that after the pulse duration, marked as the shaded red area, the Rabi oscillations are differently advanced in time. This time progress effect also manifests in the phase of the nuclear contribution to the reflectance. In our simple Rabi model, the nuclear phase after the driving pulse is given by

$$\arg\left(J_-(t_0)\right) = \arg\left(-\tfrac{i}{2} e^{i\arg(\Omega_R)} \sin\left(2|\Omega_R| t_0\right)\right) . \tag{8.73}$$

From this expression, we see that the phase is particularly affected by the sinusoidal contribution. Its sign can flip if its argument exceeds a multiple of π, i.e. as soon as half a Rabi cycle is complete. This can be achieved by either increasing the pulse duration t_0 or the driving strength $\tilde{a}_{\mathrm{in}}$, as it is proportional to the Rabi frequency Ω_R. The nuclear phase as a function of $\tilde{a}_{\mathrm{in}}$ is visualized

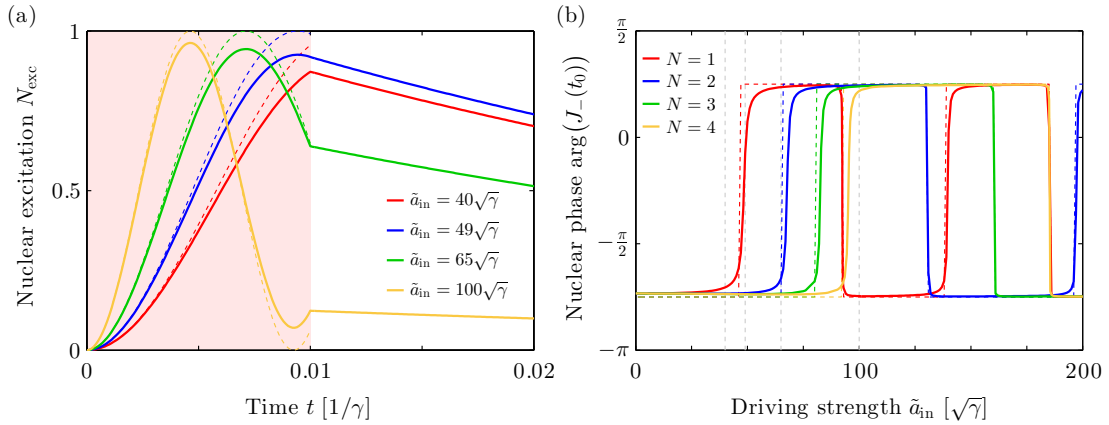

Figure 8.7: (a) The nuclear excitation in the cavity is shown. The shaded area denotes the time range in which the system is driven by the pulse. After $t_0 = 0.01/\gamma$ the population of the excited nuclei decays exponentially. Depending on the driving strength $\tilde{a}_{\mathrm{in}}$, the Rabi cycling of the population is differently advanced which influences the nuclear phase after the driving pulse. The solution of an ideal Rabi flopping without decay is given by the dashed lines. (b) The nuclear phase $\arg(J_-)$ at $t = t_0$ is shown for simulations with different number of atoms N. The dashed lines show the result of the simple Rabi model. Whenever half a Rabi cycle is complete, the nuclear phase changes by $\approx \pi$. The gray vertical lines denote the driving strength from (a) and Fig. 8.6. Parameters are as in Fig. 8.6.

in Fig. 8.7(b). Again, the simple Rabi model covers the essential behavior of the numerical simulations very well. We performed this analysis with up to four nuclei in our simulations while keeping $|g|^2 N$ constant, and always found a good agreement with our intuitive interpretation based on the Rabi model, see Fig. 8.7(b), despite the complicated interatomic couplings. Thus, the discussed effect can indeed rapidly change the phase of the nuclear contribution in general settings, which in turn gives rise to modified line shapes, c.f. Chap. 4 or Ref. [172].

Even though the analysis here was carried out for the coherent part of the spectrum, the signatures of the modified line shapes also remain visible for the full spectrum, which can be observed from Fig. 8.6. Therefore, the intensity-dependent line shape asymmetry constitutes a well-suited characteristic for an experimental study in the non-linear regime. Since the spectrum is very sensitive to the nuclear states in the cavities, it can also be understood as a signature for Rabi flopping. We emphasize that this line shape control mechanism is not restricted to the nuclear domain, but can be realized also in settings in different energy regimes, such as in the study of auto-ionizing helium systems with femtosecond pulses in the XUV range [172, 262, 263].

Finally, we note that a clear observation of the effect in the spectra poses a significant challenge to the light sources. While we performed our numerical simulations with a clean rectangular pulse, the situation encountered in (X)FEL experiments requires different models for the more noisy pulse shapes [40, 264]. With a possible self-seeding upgrade, though, the shape quality is expected to be enhanced significantly [16, 19]. Furthermore, we note that the analysis above was performed with adiabatically eliminated cavity modes, which is valid if the modes equilibrate fast on the time scale of the driving pulses. However, with ultrashort pulse durations in the 10 fs range provided by XFEL sources, this assumption might have to be revisited and the cavity dynamics might have to be taken into account. The influence of both the realistic pulses shapes as well as the explicit treatment of the cavity dynamics on the features in the spectrum could thus be analyzed in future works.

Chapter 9

Summary & Outlook

Summary

In this thesis a quantum optical framework for thin-film cavities, containing layers of resonant Mössbauer nuclei and probed by hard x-rays, was presented. This setting has recently been used in several experiments exploring the foundations of x-ray quantum optics. Compared to previously existing theoretical descriptions, the approach of this work allows for a quantum mechanical interpretation of all physical processes contributing to the observed signals on the basis of a full understanding of the involved states and their mutual couplings from a microscopic point of view. Additionally, a strong focus was put on a close relation to realistic implementations. In collaboration with experimental groups, several quantum optical phenomena could be successfully demonstrated.

The basic model was developed in chapter 3 by describing the x-ray light-matter interaction by quantum optical means. Special attention was given to the archetype Mössbauer isotope ^{57}Fe which is presently also in the focus of interest in experimental implementations. To overcome the difficulty of the large Hilbert space in the initial formulation of our theory, two well justified approximations were made. First, we adiabatically eliminated the cavity modes to obtain effective equations of motion for the nuclei. While there is no direct interaction among the nuclei initially, this procedure gives rise to mutual couplings in the equations. This way, an intuitive understanding of the relevant physical processes contributing to the coupling of the nuclei and thus to collective phenomena can be gained. In particular, it was found that the cavity leads to an enhanced decay rate and energy shifts due to cooperativity and the Purcell effect. The second approximation was to consider the system only in first order of the driving field, which is sufficient to describe current synchrotron-based experiments. This allowed for a description of the cavity and the collective behavior of the nuclei by one ground and up to only six collective excited states in the presence of a magnetic hyperfine splitting. In the respective limits, we found excellent agreement with previous semi-classical models as well as with numerical simulations throughout this thesis.

In chapter 4 the setting of a plain cavity without magnetic splitting of the resonant nuclei was studied. With the quantum optical theory we could show that tunable Fano resonances arise in the spectrum of the reflectance, which are externally controllable via the angle of incidence. This line shape control stems from the interference of two scattering channels, the empty-cavity reflection and scattering at the resonant nuclei, and was successfully demonstrated in an experiment. From the measured spectra we could extract spectroscopic signatures such as the cooperative Lamb shift or the superradiant decay rate with high precision, which opens up an avenue to metrology at x-ray energies with neV precision. During the data analysis we found that an additional phase depending on the cavity material is present in the system, which gives rise to asymmetric cavity mode resonances and a non-vanishing Lamb shift for the symmetric Lorentz spectrum. Including this phase shift in the theoretical description, a very good agreement to the experimental data was achieved. The line shape control mechanism with its two scattering channels can also be interpreted in terms of an x-ray interferometer setup. This way, phase-sensitive measurements of the nuclear resonance were demonstrated with good agreement to the theoretically expected phase of a Lorentz profile. The phase retrieval forms a first step

towards x-ray quantum state tomography.

A more involved scenario was studied in chapter 5 by introducing a magnetic hyperfine splitting in the ^{57}Fe nuclei. We observed that distinct minima in the spectral response are formed. However, their origin could not be understood by means of the semi-classical descriptions. Applying our quantum optical model, we showed that these modifications in the reflected signal are caused by interatomic interaction effects originating from the quantum nature of the vacuum. So-called spontaneously generated coherences (SGC) are formed, which is a hardly observed phenomenon in quantum optics since it requires stringent conditions naturally not met in atoms. In our x-ray setup, SGC occur due to the presence of cooperative effects and a magnetically controlled anisotropy of the cavity vacuum. SGC enable interference between different decay channels and allow to suppress the seemingly inevitable process of spontaneous emission. Therefore, SGC are a powerful resource in quantum engineering with numerous fascinating applications. We could demonstrate the effect of SGC experimentally and show that the cavity system can be operated essentially decoherence-free. On the theoretical side, we further found that a large set of level schemes can be engineered and controlled by suitable choices of the magnetization and polarization axes. This opens perspectives for the realization of advanced quantum optical level schemes with nuclei.

In chapter 6 the typical scheme employed in experiments on thin-film cavities was described in more detail and the time-dependent reflection intensity, which is experimentally accessible, was derived. In the process we found that the group velocity of the x-ray pulses can be controlled. We showed that large time delays can be engineered in cavities featuring SGC and with thin surface layers, and even super-luminal light propagation can be achieved with suitable cavity layouts. Since the concept of group velocity control requires spectrally narrow pulses, we proposed a scheme in which such narrowband pulses are created from broadband synchrotron radiation. Experimentally, we could observe x-ray pulse delays up to 35 ns employing this scheme. Since slow light is usually accompanied by huge optical non-linearities, our implementation motivates the study of related phenomena in the x-ray regime. Furthermore, a theory was formulated in order to analyze the time-resolved signal in Fourier space. This way, an alternative method to extract the Lamb shift from the measured data was introduced.

In chapter 7 the theoretical model was extended to cover multiple cavity modes as well as multiple resonant layers, such that a broader set of cavity layouts can be handled appropriately. Our analysis revealed that each of the two extensions individually does not yield new effects in the spectral line shapes beyond Lorentz and Fano profiles, but in combination qualitatively different reflection spectra emerge. This way, a recent experiment featuring electromagnetically induced transparency (EIT) in thin-film cavities [56] could be successfully modeled, the coupling coefficients in the scheme could be understood from a quantum optical point of view and their scaling laws could be reproduced.

In the main part of this thesis the quantum optical formalism was applied to situations studied in synchrotron experiments, where the linear response approximation is valid. The model, however, is not limited to the linear regime and can be applied to describe future experiments with much higher probe intensities, performed, e.g., at x-ray free-electron lasers. Non-linear effects emerging in this new parameter regime were investigated in chapter 8. In a first approach we approximated the system by neglecting the small spontaneous emission rate as it is dominated by the superradiant behavior and could find analytic solutions of the stationary observables for arbitrary x-ray driving strengths and atom numbers by mapping the equations of motion to a Dicke-type model. That way, saturation effects of the nuclear excitation could be observed. Second, a numerical study was performed in order to compute the emission spectrum after the excitation with a short, but intense x-ray pulse, which corresponds to the situation encountered in typical experimental scenarios. Here, a novel line shape control mechanism based on the dynamics of the nuclear phase was discovered. This effect might also serve as a signature for nuclear Rabi flopping.

In conclusion, our formalism allows to predict, observe and interpret a variety of quantum

optical phenomena and provides a promising platform for the further exploration of x-ray quantum optics with nuclei embedded in thin-film cavities. At the same time, this work supports the ongoing effort to establish a new domain of Mössbauer physics at the boundary of quantum optics and x-ray science.

Outlook

The results presented in this work invite for a broad range of promising research directions. Both on the theoretical and the experimental side, exciting physics can be expected in future studies on x-ray thin-film cavities.

A highly advantageous platform for further phenomena and applications of quantum optics can be formed by merging the two cavity layouts featuring EIT and SGC: The combination of multiple resonant layers in the cavity with suitably chosen magnetization to induce a hyperfine splitting in the nuclei would enable the engineering of a new class of quantum optical level schemes in the x-ray domain. Particularly desirable would be the formation of N-type level structures, which can be exploited to obtain huge Kerr non-linearities in the optical response [120]. Using other Mössbauer nuclei instead of the isotope ^{57}Fe, which was considered in most parts of this work, might provide an alternative road to access a broader collection of realizable level schemes. The quantum optical model developed here is suitable for any resonant nucleus with arbitrary hyperfine level structure and thus can be applied to such scenarios as well.

Next to the realization of novel level schemes, other extensions could encompass moving or vibrating cavities with the aim of controlling the waveform via sideband modulation, as it has been demonstrated in nuclear forward scattering setups [55, 57]. Also the spectral redistribution of the field intensity might be feasible in a related setting [172]. In a different application the interferometric nature of the x-ray cavity can provide access to fundamental questions of quantum mechanics. Currently, some effort is made to utilize the cavity setup to observe the violation of Bell-like inequalities [265].

Besides, a deepened analysis of several topics covered in this thesis offers great potential. Since the Fano spectra discussed in Chap. 4 were measured employing a time-resolved method, it could be possible to use our data to study the temporal build-up of Fano resonances [266] and compare it with results of different frequency regimes [267]. In Chap. 6 we introduced a method to extract the Lamb shift from these time dependent measurements via evaluation in Fourier space. The analysis of all available data sets as well as the identification of other spectroscopic parameters could be envisaged for the future. In particular, it would be interesting to investigate if the Fourier space analysis of the time-dependent Fano spectra allows for advanced characterization of the couplings as in Ref. [263]. It might be also beneficial to apply our technique of phase sensitive measurements based on Fano resonances to cases with more complex line shapes. A thorough study of the nuclear phases allows to specifically design cavities with distinct dispersion relations, which is of importance for the implementation of group velocity control as discussed in Chap. 6. Ultimately, this could lead to the realization of super-luminal x-ray pulses. A topic which was not yet extensively considered is the photon correlation function $g^{(2)}$. In contrast to previous models we used a quantized field description in our theoretical approach, which renders $g^{(2)}$ an accessible observable. Its features, however, have been only touched briefly in Chap. 8. A comprehensive analysis of the second-order correlations induced by the light-matter interaction of Mössbauer nuclei in thin-film cavities, possibly in combination with the properties of synchrotron radiation [268] or free-electron laser sources [269], constitutes a worthwhile subject for upcoming studies.

Even though the quantum optical model developed in this work has proven very successful in describing various realistic scenarios, some open questions in the foundations of the theory should be addressed in future works. An important point would be the self-consistent calculation of the coupling constants g between the different cavity modes and nuclear transitions. An independent approach via an eigenmode analysis could performed here. Since in the present work

only the product $g\sqrt{N}$ is known from comparison with experimental data or semi-classical models, this would allow to determine the absolute number of nuclei N taking part in the collective light-matter interaction. Due to the limited coherence of the x-rays beams in experiments the question arises if the coupling to the nuclei is homogeneous due to the formation of a uniform cavity mode, or if the nuclei are divided into smaller blocks with a certain coherence volume, which in turn determine the collective behavior [68]. Next to this question, also the emission characteristics require a deeper understanding. While the nuclear signal is coherently emitted in forward direction along the expected reflection channel, it has to be examined if this still holds true in the non-linear regime. There, the intermediately excited state in the nuclear ensemble strongly differs and the angular properties of the emission could be investigated by means of scattering theory or a radiative eigenstate analysis. Especially, it would be important to know if the coherent and incoherent part of the emission spectrum found in Chap. 8 exhibit different characteristics. This could facilitate the observation of the discovered line shape control mechanism in the coherent part of the emission spectrum.

The non-linear mechanism to control the line profiles further provides a signature for nuclear Rabi flopping as described in Chap. 8. Hence, its verification can be expected to fuel the field of nuclear quantum optics. An easier implementation of the same scheme could probably be achieved in lower frequency domains, such as in the study of helium with femtosecond pulses in the XUV range. Nevertheless, a more sophisticated theoretical study is required beforehand. Both the effects of the x-ray pulse shape and its partial coherence were not included in the analysis yet. Also, the adiabatic elimination of the cavity modes cannot be performed if pulses with a duration of less than $\approx$ 150 fs probe the system. Also the second non-linear scenario investigated in this work, the stationary case of a continuously driven cavity, opens up some challenges. On the theoretical side it could be analyzed if the approximations in the model are valid in the considered parameter ranges. In particular, it would be important to know if the non-symmetric Dicke states affect the system. Next, the question if the scheme is realizable is still to be answered. For this, the time scale of the system, determined by the decay rate of the Mössbauer nuclei, and the parameters of suitable future light sources need to be related.

Finally, we emphasize that the rapid development of new x-ray instrumentation increases the experimental possibilities and therefore allows to implement many more quantum optical phenomena in the next years, not necessarily restricted to settings in thin-film cavities. Examples of such novel equipment are diamond-based mirrors with near 100% reflectivity operating in normal incidence [270, 271] or Bragg beam splitters for hard x-rays [272]. Additionally, pulsed magnetic fields with controlled strengths up to 30 T [273] offer a tool to modify the hyperfine splitting of Mössbauer nuclei, such that the nuclear level schemes can be dynamically tuned. This way, innovative concepts of x-ray quantum optics can be expected to be realized in the future.

Bibliography

[1] M. Scully and S. Zubairy, *Quantum Optics* (Cambridge University Press, 1997).

[2] S. Haroche and J. Raimond, *Exploring the Quantum: Atoms, Cavities, and Photons*, Oxford Graduate Texts (Oxford University Press, 2006).

[3] G. Agarwal, *Quantum Optics* (Cambridge University Press, 2012).

[4] B. W. Adams, C. Buth, S. M. Cavaletto, J. Evers, Z. Harman, C. H. Keitel, A. Pálffy, A. Picón, R. Röhlsberger, Y. Rostovtsev, and K. Tamasaku, "X-ray quantum optics," Journal of Modern Optics **60**, 2–21 (2013).

[5] X. Huang, H. Yan, E. Nazaretski, R. Conley, N. Bouet, J. Zhou, K. Lauer, L. Li, D. Eom, D. Legnini, R. Harder, I. K. Robinson, and Y. S. Chu, "11 nm hard x-ray focus from a large-aperture multilayer Laue lens," Sci. Rep. **3** (2013).

[6] D. A. Shapiro, Y.-S. Yu, T. Tyliszczak, J. Cabana, R. Celestre, W. Chao, K. Kaznatcheev, KilcoyneA. L. David, F. Maia, S. Marchesini, Y. S. Meng, T. Warwick, L. L. Yang, and H. A. Padmore, "Chemical composition mapping with nanometre resolution by soft x-ray microscopy," Nature Photonics **8**, 765–769 (2014).

[7] G. Shenoy and R. Röhlsberger, "Scientific opportunities in nuclear resonance spectroscopy from source-driven revolution," Hyperfine Interactions **182**, 157–172 (2008).

[8] D. Sayre and H. N. Chapman, "X-ray microscopy," Acta Crystallographica Section A **51**, 237–252 (1995).

[9] K. Tamasaku, K. Sawada, E. Nishibori, and T. Ishikawa, "Visualizing the local optical response to extreme-ultraviolet radiation with a resolution of $\lambda/380$," Nature Physics **7**, 705–708 (2011).

[10] D. H. Bilderback, P. Elleaume, and E. Weckert, "Review of third and next generation synchrotron light sources," Journal of Physics B: Atomic, Molecular and Optical Physics **38**, S773 (2005).

[11] B. W. J. McNeil and N. R. Thompson, "X-ray free-electron lasers," Nature Photonics **4**, 814–821 (2010).

[12] P. Emma, R. Akre, J. Arthur, R. Bionta, C. Bostedt, J. Bozek, A. Brachmann, P. Bucksbaum, R. Coffee, F.-J. Decker, Y. Ding, D. Dowell, S. Edstrom, A. Fisher, J. Frisch, S. Gilevich, J. Hastings, G. Hays, P. Hering, Z. Huang, R. Iverson, H. Loos, M. Messerschmidt, A. Miahnahri, S. Moeller, H.-D. Nuhn, G. Pile, D. Ratner, J. Rzepiela, D. Schultz, T. Smith, P. Stefan, H. Tompkins, J. Turner, J. Welch, W. White, J. Wu, G. Yocky, and J. Galayda, "First lasing and operation of an angstrom-wavelength free-electron laser," Nature Photonics **4**, 641–647 (2010).

[13] T. Ishikawa, H. Aoyagi, T. Asaka, Y. Asano, N. Azumi, T. Bizen, H. Ego, K. Fukami, T. Fukui, Y. Furukawa, S. Goto, H. Hanaki, T. Hara, T. Hasegawa, T. Hatsui, A. Higashiya, T. Hirono, N. Hosoda, M. Ishii, T. Inagaki, Y. Inubushi, T. Itoga, Y. Joti, M. Kago, T. Kameshima, H. Kimura, Y. Kirihara, A. Kiyomichi, T. Kobayashi, C. Kondo, T. Kudo,

H. Maesaka, X. M. Maréchal, T. Masuda, S. Matsubara, T. Matsumoto, T. Matsushita, S. Matsui, M. Nagasono, N. Nariyama, H. Ohashi, T. Ohata, T. Ohshima, S. Ono, Y. Otake, C. Saji, T. Sakurai, T. Sato, K. Sawada, T. Seike, K. Shirasawa, T. Sugimoto, S. Suzuki, S. Takahashi, H. Takebe, K. Takeshita, K. Tamasaku, H. Tanaka, R. Tanaka, T. Tanaka, T. Togashi, K. Togawa, A. Tokuhisa, H. Tomizawa, K. Tono, S. Wu, M. Yabashi, M. Yamaga, A. Yamashita, K. Yanagida, C. Zhang, T. Shintake, H. Kitamura, and N. Kumagai, "A compact x-ray free-electron laser emitting in the sub-angstrom region," Nature Photonics **6**, 540–544 (2012).

[14] M. Altarelli, R. Brinkmann, M. Chergui, W. Decking, B. Dobson, S. Düsterer, G. Gerhard Grübel, W. Graeff, H. Graafsma, J. Hajdu, J. Marangos, J. Pflüger, H. Redlin, D. Riley, I. Robinson, J. Rossbach, A. Schwarz, K. Tiedtke, T. Tschentscher, I. Vartaniants, H. Wabnitz, H. Weise, R. Wichmann, K. Witte, A. Wolf, M. Wulff, and M. Yurkov, eds., *The European X-Ray Free-Electron Laser: Technical design report*, DESY No. 2006-097 (DESY XFEL Project Group, 2007).

[15] K.-J. Kim, Y. Shvyd'ko, and S. Reiche, "A proposal for an x-ray free-electron laser oscillator with an energy-recovery linac," Phys. Rev. Lett. **100**, 244802 (2008).

[16] G. Geloni, V. Kocharyan, and E. Saldin, "Extension of self-seeding to hard x-rays > 10 keV as a way to increase user access at the European XFEL," ArXiv e-prints (2011), arXiv:1111.5766 [physics.acc-ph] .

[17] R. R. Lindberg, K.-J. Kim, Y. Shvyd'ko, and W. M. Fawley, "Performance of the x-ray free-electron laser oscillator with crystal cavity," Phys. Rev. ST Accel. Beams **14**, 010701 (2011).

[18] G. Neil and W. Chou, eds., *Beam Dynamics Newsletter*, No. 60 (International Committee for Future Accelerators, 2013).

[19] J. Amann, W. Berg, V. Blank, F.-J. Decker, Y. Ding, P. Emma, Y. Feng, J. Frisch, D. Fritz, J. Hastings, Z. Huang, J. Krzywinski, R. Lindberg, H. Loos, A. Lutman, H.-D. Nuhn, D. Ratner, J. Rzepiela, D. Shu, Y. Shvyd'ko, S. Spampinati, S. Stoupin, S. Terentyev, E. Trakhtenberg, D. Walz, J. Welch, J. Wu, A. Zholents, and D. Zhu, "Demonstration of self-seeding in a hard-x-ray free-electron laser," Nature Photonics **6**, 693–698 (2012).

[20] T. Hara, Y. Inubushi, T. Katayama, T. Sato, H. Tanaka, T. Tanaka, T. Togashi, K. Togawa, K. Tono, M. Yabashi, and T. Ishikawa, "Two-colour hard x-ray free-electron laser with wide tunability," Nature Communications **4** (2013).

[21] H. N. Chapman, P. Fromme, A. Barty, T. A. White, R. A. Kirian, A. Aquila, M. S. Hunter, J. Schulz, D. P. DePonte, U. Weierstall, R. B. Doak, F. R. N. C. Maia, A. V. Martin, I. Schlichting, L. Lomb, N. Coppola, R. L. Shoeman, S. W. Epp, R. Hartmann, D. Rolles, A. Rudenko, L. Foucar, N. Kimmel, G. Weidenspointner, P. Holl, M. Liang, M. Barthelmess, C. Caleman, S. Boutet, M. J. Bogan, J. Krzywinski, C. Bostedt, S. Bajt, L. Gumprecht, B. Rudek, B. Erk, C. Schmidt, A. Hömke, C. Reich, D. Pietschner, L. Strüder, G. Hauser, H. Gorke, J. Ullrich, S. Herrmann, G. Schaller, F. Schopper, H. Soltau, K.-U. Kühnel, M. Messerschmidt, J. D. Bozek, S. P. Hau-Riege, M. Frank, C. Y. Hampton, R. G. Sierra, D. Starodub, G. J. Williams, J. Hajdu, N. Timneanu, M. M. Seibert, J. Andreasson, A. Rocker, O. Jönsson, M. Svenda, S. Stern, K. Nass, R. Andritschke, C.-D. Schröter, F. Krasniqi, M. Bott, K. E. Schmidt, X. Wang, I. Grotjohann, J. M. Holton, T. R. M. Barends, R. Neutze, S. Marchesini, R. Fromme, S. Schorb, D. Rupp, M. Adolph, T. Gorkhover, I. Andersson, H. Hirsemann, G. Potdevin, H. Graafsma, B. Nilsson, and J. C. H. Spence, "Femtosecond x-ray protein nanocrystallography," Nature **470**, 73–77 (2011).

[22] L. Redecke, K. Nass, D. P. DePonte, T. A. White, D. Rehders, A. Barty, F. Stellato, M. Liang, T. R. Barends, S. Boutet, G. J. Williams, M. Messerschmidt, M. M. Seibert, A. Aquila, D. Arnlund, S. Bajt, T. Barth, M. J. Bogan, C. Caleman, T.-C. Chao, R. B. Doak, H. Fleckenstein, M. Frank, R. Fromme, L. Galli, I. Grotjohann, M. S. Hunter, L. C. Johansson, S. Kassemeyer, G. Katona, R. A. Kirian, R. Koopmann, C. Kupitz, L. Lomb, A. V. Martin, S. Mogk, R. Neutze, R. L. Shoeman, J. Steinbrener, N. Timneanu, D. Wang, U. Weierstall, N. A. Zatsepin, J. C. H. Spence, P. Fromme, I. Schlichting, M. Duszenko, C. Betzel, and H. N. Chapman, "Natively inhibited *Trypanosoma brucei* cathepsin B structure determined by using an x-ray laser," Science **339**, 227–230 (2013).

[23] R. Neutze, R. Wouts, D. van der Spoel, E. Weckert, and J. Hajdu, "Potential for biomolecular imaging with femtosecond x-ray pulses," Nature **406**, 752–757 (2000).

[24] A. Barty, J. Küpper, and H. N. Chapman, "Molecular imaging using x-ray free-electron lasers," Annual Review of Physical Chemistry **64**, 415–435 (2013).

[25] J. Küpper, S. Stern, L. Holmegaard, F. Filsinger, A. Rouzée, A. Rudenko, P. Johnsson, A. V. Martin, M. Adolph, A. Aquila, S. Bajt, A. Barty, C. Bostedt, J. Bozek, C. Caleman, R. Coffee, N. Coppola, T. Delmas, S. Epp, B. Erk, L. Foucar, T. Gorkhover, L. Gumprecht, A. Hartmann, R. Hartmann, G. Hauser, P. Holl, A. Hömke, N. Kimmel, F. Krasniqi, K.-U. Kühnel, J. Maurer, M. Messerschmidt, R. Moshammer, C. Reich, B. Rudek, R. Santra, I. Schlichting, C. Schmidt, S. Schorb, J. Schulz, H. Soltau, J. C. H. Spence, D. Starodub, L. Strüder, J. Thøgersen, M. J. J. Vrakking, G. Weidenspointner, T. A. White, C. Wunderer, G. Meijer, J. Ullrich, H. Stapelfeldt, D. Rolles, and H. N. Chapman, "X-ray diffraction from isolated and strongly aligned gas-phase molecules with a free-electron laser," Phys. Rev. Lett. **112**, 083002 (2014).

[26] M. M. Seibert, T. Ekeberg, F. R. N. C. Maia, M. Svenda, J. Andreasson, O. Jönsson, D. Odić, B. Iwan, A. Rocker, D. Westphal, M. Hantke, D. P. DePonte, A. Barty, J. Schulz, L. Gumprecht, N. Coppola, A. Aquila, M. Liang, T. A. White, A. Martin, C. Caleman, S. Stern, C. Abergel, V. Seltzer, J.-M. Claverie, C. Bostedt, J. D. Bozek, S. Boutet, A. A. Miahnahri, M. Messerschmidt, J. Krzywinski, G. Williams, K. O. Hodgson, M. J. Bogan, C. Y. Hampton, R. G. Sierra, D. Starodub, I. Andersson, S. Bajt, M. Barthelmess, J. C. H. Spence, P. Fromme, U. Weierstall, R. Kirian, M. Hunter, R. B. Doak, S. Marchesini, S. P. Hau-Riege, M. Frank, R. L. Shoeman, L. Lomb, S. W. Epp, R. Hartmann, D. Rolles, A. Rudenko, C. Schmidt, L. Foucar, N. Kimmel, P. Holl, B. Rudek, B. Erk, A. Hömke, C. Reich, D. Pietschner, G. Weidenspointner, L. Strüder, G. Hauser, H. Gorke, J. Ullrich, I. Schlichting, S. Herrmann, G. Schaller, F. Schopper, H. Soltau, K.-U. Kühnel, R. Andritschke, C.-D. Schröter, F. Krasniqi, M. Bott, S. Schorb, D. Rupp, M. Adolph, T. Gorkhover, H. Hirsemann, G. Potdevin, H. Graafsma, B. Nilsson, H. N. Chapman, and J. Hajdu, "Single mimivirus particles intercepted and imaged with an x-ray laser," Nature **470**, 78–81 (2011).

[27] L. Young, E. P. Kanter, B. Krässig, Y. Li, A. M. March, S. T. Pratt, R. Santra, S. H. Southworth, N. Rohringer, L. F. DiMauro, G. Doumy, C. A. Roedig, N. Berrah, L. Fang, M. Hoener, P. H. Bucksbaum, J. P. Cryan, S. Ghimire, J. M. Glownia, D. A. Reis, J. D. Bozek, C. Bostedt, and M. Messerschmidt, "Femtosecond electronic response of atoms to ultra-intense x-rays," Nature **466**, 56–61 (2010).

[28] K. Tamasaku, E. Shigemasa, Y. Inubushi, T. Katayama, K. Sawada, H. Yumoto, H. Ohashi, H. Mimura, M. Yabashi, K. Yamauchi, and T. Ishikawa, "X-ray two-photon absorption competing against single and sequential multiphoton processes," Nature Photonics **8**, 313–316 (2014).

[29] P. Eisenberger and S. L. McCall, "X-ray parametric conversion," Phys. Rev. Lett. **26**, 684–688 (1971).

[30] Y. Yoda, T. Suzuki, X.-W. Zhang, K. Hirano, and S. Kikuta, "X-ray parametric scattering by a diamond crystal," Journal of Synchrotron Radiation **5**, 980–982 (1998).

[31] B. W. Adams, ed., *Nonlinear Optics, Quantum Optics, and Ultrafast Phenomena with X-Rays: Physics with X-Ray Free-Electron Lasers* (Springer, 2003).

[32] T. E. Glover, D. M. Fritz, M. Cammarata, T. K. Allison, S. Coh, J. M. Feldkamp, H. Lemke, D. Zhu, Y. Feng, R. N. Coffee, M. Fuchs, S. Ghimire, J. Chen, S. Shwartz, D. A. Reis, S. E. Harris, and J. B. Hastings, "X-ray and optical wave mixing," Nature **488**, 603–608 (2012).

[33] M. Beye, S. Schreck, F. Sorgenfrei, C. Trabant, N. Pontius, C. Schüßler-Langeheine, W. Wurth, and A. Föhlisch, "Stimulated x-ray emission for materials science," Nature **501**, 191–194 (2013).

[34] T. E. Glover, M. P. Hertlein, S. H. Southworth, T. K. Allison, J. van Tilborg, E. P. Kanter, B. Krässig, H. R. Varma, B. Rude, R. Santra, A. Belkacem, and L. Young, "Controlling x-rays with light," Nature Physics **6**, 69–74 (2010).

[35] N. Rohringer, D. Ryan, R. A. London, M. Purvis, F. Albert, J. Dunn, J. D. Bozek, C. Bostedt, A. Graf, R. Hill, S. P. Hau-Riege, and J. J. Rocca, "Atomic inner-shell x-ray laser at 1.46 nanometres pumped by an x-ray free-electron laser," Nature **481**, 488–491 (2012).

[36] S. M. Cavaletto, Z. Harman, C. Buth, and C. H. Keitel, "X-ray frequency combs from optically controlled resonance fluorescence," Phys. Rev. A **88**, 063402 (2013).

[37] Z. Liu, C. Ott, S. M. Cavaletto, Z. Harman, C. H. Keitel, and T. Pfeifer, "Generation of high-frequency combs locked to atomic resonances by quantum phase modulation," New Journal of Physics **16**, 093005 (2014).

[38] S. M. Cavaletto, Z. Harman, C. Ott, C. Buth, T. Pfeifer, and C. H. Keitel, "Broadband high-resolution x-ray frequency combs," Nature Photonics **8**, 520–523 (2014).

[39] C. Buth, R. Santra, and L. Young, "Electromagnetically induced transparency for x rays," Phys. Rev. Lett. **98**, 253001 (2007).

[40] T. Pfeifer, Y. Jiang, S. Düsterer, R. Moshammer, and J. Ullrich, "Partial-coherence method to model experimental free-electron laser pulse statistics," Opt. Lett. **35**, 3441–3443 (2010).

[41] T. J. Bürvenich, J. Evers, and C. H. Keitel, "Nuclear quantum optics with x-ray laser pulses," Phys. Rev. Lett. **96**, 142501 (2006).

[42] A. Pálffy, "A systematic study of nuclear photoexcitation with x-ray laser fields," Journal of Modern Optics **55**, 2603–2615 (2008).

[43] J. Gunst, Y. A. Litvinov, C. H. Keitel, and A. Pálffy, "Dominant secondary nuclear photoexcitation with the x-ray free-electron laser," Phys. Rev. Lett. **112**, 082501 (2014).

[44] G. Klingelhöfer, R. V. Morris, B. Bernhardt, C. Schröder, D. S. Rodionov, P. A. de Souza, A. Yen, R. Gellert, E. N. Evlanov, B. Zubkov, J. Foh, U. Bonnes, E. Kankeleit, P. Gütlich, D. W. Ming, F. Renz, T. Wdowiak, S. W. Squyres, and R. E. Arvidson, "Jarosite and hematite at meridiani planum from opportunity's Mössbauer spectrometer," Science **306**, 1740–1745 (2004).

[45] W. Demtröder, *Laserspektroskopie: Grundlagen und Techniken* (Springer, 2007).

[46] R. V. Pound and G. A. Rebka, "Gravitational red-shift in nuclear resonance," Phys. Rev. Lett. **3**, 439–441 (1959).

[47] R. V. Pound and G. A. Rebka, "Apparent weight of photons," Phys. Rev. Lett. **4**, 337–341 (1960).

[48] W.-T. Liao, S. Das, C. H. Keitel, and A. Pálffy, "Coherence-enhanced optical determination of the ^{229}Th isomeric transition," Phys. Rev. Lett. **109**, 262502 (2012).

[49] W. Sturhahn, "Nuclear resonant spectroscopy," Journal of Physics: Condensed Matter **16**, S497 (2004).

[50] K. P. Heeg, H.-C. Wille, K. Schlage, T. Guryeva, D. Schumacher, I. Uschmann, K. S. Schulze, B. Marx, T. Kämpfer, G. G. Paulus, R. Röhlsberger, and J. Evers, "Vacuum-assisted generation and control of atomic coherences at x-ray energies," Phys. Rev. Lett. **111**, 073601 (2013).

[51] J. Hannon and G. Trammell, "Coherent γ-ray optics," Hyperfine Interactions **123-124**, 127–274 (1999).

[52] R. Röhlsberger, K. Schlage, B. Sahoo, S. Couet, and R. Rüffer, "Collective Lamb shift in single-photon superradiance," Science **328**, 1248–1251 (2010).

[53] Y. V. Shvyd'ko, T. Hertrich, U. van Bürck, E. Gerdau, O. Leupold, J. Metge, H. D. Rüter, S. Schwendy, G. V. Smirnov, W. Potzel, and P. Schindelmann, "Storage of nuclear excitation energy through magnetic switching," Phys. Rev. Lett. **77**, 3232–3235 (1996).

[54] P. Helistö, I. Tittonen, M. Lippmaa, and T. Katila, "Gamma echo," Phys. Rev. Lett. **66**, 2037–2040 (1991).

[55] R. N. Shakhmuratov, F. Vagizov, and O. Kocharovskaya, "Radiation burst from a single γ-photon field," Phys. Rev. A **84**, 043820 (2011).

[56] R. Röhlsberger, H.-C. Wille, K. Schlage, and B. Sahoo, "Electromagnetically induced transparency with resonant nuclei in a cavity," Nature **482**, 199–203 (2012).

[57] F. Vagizov, V. Antonov, Y. V. Radeonychev, R. N. Shakhmuratov, and O. Kocharovskaya, "Coherent control of the waveforms of recoilless γ-ray photons," Nature **508**, 80–83 (2014).

[58] K. P. Heeg, C. Ott, D. Schumacher, H.-C. Wille, R. Röhlsberger, T. Pfeifer, and J. Evers, "Interferometric phase detection at x-ray energies via Fano resonance control," (2014), submitted.

[59] K. P. Heeg, J. Haber, D. Schumacher, L. Bocklage, H.-C. Wille, K. S. Schulze, R. Loetzsch, I. Uschmann, G. G. Paulus, R. Rüffer, R. Röhlsberger, and J. Evers, "Tunable sub-luminal propagation of narrowband x-ray pulses," ArXiv e-prints (2014), arXiv:1409.0365 [quant-ph] .

[60] A. Pálffy, C. H. Keitel, and J. Evers, "Single-photon entanglement in the keV regime via coherent control of nuclear forward scattering," Phys. Rev. Lett. **103**, 017401 (2009).

[61] W.-T. Liao and A. Pálffy, "Proposed entanglement of x-ray nuclear polaritons as a potential method for probing matter at the subatomic scale," Phys. Rev. Lett. **112**, 057401 (2014).

[62] W.-T. Liao, C. H. Keitel, and A. Pálffy, "Magnetic quantum-phase control between two entangled macroscopic nuclear ensembles," ArXiv e-prints (2014), arXiv:1407.3292 [quant-ph] .

[63] A. Pálffy, C. H. Keitel, and J. Evers, "Coherent control of the cooperative branching ratio for nuclear x-ray pumping," Phys. Rev. B **83**, 155103 (2011).

[64] W.-T. Liao, A. Pálffy, and C. H. Keitel, "Coherent storage and phase modulation of single hard-x-ray photons using nuclear excitons," Phys. Rev. Lett. **109**, 197403 (2012).

[65] X. Kong, W.-T. Liao, and A. Pálffy, "Field control of single x-ray photons in nuclear forward scattering," New Journal of Physics **16**, 013049 (2014).

[66] J. Odeurs, G. Hoy, Y. Rostovtsev, and R. Shakhmuratov, "Towards more relaxed conditions for a gamma-ray laser: Methods to realize induced transparency for nuclear resonant gamma radiation," Laser & Photonics Reviews **4**, 1–20 (2010).

[67] N. ten Brinke, R. Schützhold, and D. Habs, "Feasibility study of a nuclear exciton laser," Phys. Rev. A **87**, 053814 (2013).

[68] A. Reichegger and J. Evers, "Temporal dynamics of stimulated emission with applications in nuclear quantum optics," ArXiv e-prints (2014), arXiv:1406.7787 [quant-ph] .

[69] W.-T. Liao, A. Pálffy, and C. H. Keitel, "Nuclear coherent population transfer with x-ray laser pulses," Physics Letters B **705**, 134–138 (2011).

[70] W.-T. Liao, A. Pálffy, and C. H. Keitel, "Three-beam setup for coherently controlling nuclear-state population," Phys. Rev. C **87**, 054609 (2013).

[71] T. J. Bürvenich, J. Evers, and C. H. Keitel, "Dynamic nuclear stark shift in superintense laser fields," Phys. Rev. C **74**, 044601 (2006).

[72] T. Salditt, S. P. Krüger, C. Fuhse, and C. Bähtz, "High-transmission planar x-ray waveguides," Phys. Rev. Lett. **100**, 184801 (2008).

[73] F. Pfeiffer, C. David, M. Burghammer, C. Riekel, and T. Salditt, "Two-dimensional x-ray waveguides and point sources," Science **297**, 230–234 (2002).

[74] K. Okamoto, T. Noma, A. Komoto, W. Kubo, M. Takahashi, A. Iida, and H. Miyata, "X-ray waveguide mode in resonance with a periodic structure," Phys. Rev. Lett. **109**, 233907 (2012).

[75] L. G. Parratt, "Surface studies of solids by total reflection of x-rays," Phys. Rev. **95**, 359–369 (1954).

[76] R. Röhlsberger, "Theory of x-ray grazing incidence reflection in the presence of nuclear resonance excitation," Hyperfine Interactions **123-124**, 301–325 (1999).

[77] R. Röhlsberger, "Coherent elastic nuclear resonant scattering," in *Nuclear Condensed Matter Physics with Synchrotron Radiation*, Springer Tracts in Modern Physics, Vol. 208 (Springer, 2005) pp. 67–180.

[78] K. P. Heeg and J. Evers, "X-ray quantum optics with Mössbauer nuclei embedded in thin-film cavities," Phys. Rev. A **88**, 043828 (2013).

[79] W. Sturhahn and E. Gerdau, "Evaluation of time-differential measurements of nuclear-resonance scattering of x rays," Phys. Rev. B **49**, 9285–9294 (1994).

[80] W. Sturhahn, "CONUSS and PHOENIX: Evaluation of nuclear resonant scattering data," Hyperfine Interactions **125**, 149–172 (2000).

[81] J. P. Hannon, G. T. Trammell, M. Mueller, E. Gerdau, H. Winkler, and R. Rüffer, "Impedance-matched grazing-incidence films: Pure nuclear reflections, resonant filtering of synchrotron radiation, and x-ray interferometry," Phys. Rev. Lett. **43**, 636–639 (1979).

[82] J. P. Hannon, N. V. Hung, G. T. Trammell, E. Gerdau, M. Mueller, R. Rüffer, and H. Winkler, "Grazing-incidence antireflection films. I. Basic theory," Phys. Rev. B **32**, 5068–5080 (1985).

[83] J. P. Hannon, G. T. Trammell, M. Mueller, E. Gerdau, R. Rüffer, and H. Winkler, "Grazing-incidence antireflection films. III. General theory for pure nuclear reflections," Phys. Rev. B **32**, 6363–6373 (1985).

[84] E. Gerdau, M. Grote, and R. Röhlsberger, "Computer simulations of GIAR-film spectra," Hyperfine Interactions **58**, 2433–2438 (1990).

[85] R. Röhlsberger, E. Gerdau, E. Lüken, H. D. Rüter, J. Metge, and O. Leupold, "Nuclear diffraction experiments with grazing incidence antireflection films," Zeitschrift für Physik B Condensed Matter **92**, 489–499 (1993).

[86] R. L. Mössbauer, "Kernresonanzfluoreszenz von Gammastrahlung in Ir^{191}," Zeitschrift für Physik **151**, 124–143 (1958).

[87] R. L. Mössbauer, "Recoilless nuclear resonance absorption of gamma radiation: A new principle yields gamma lines of extreme narrowness for measurements of unprecedented accuracy," Science **137**, 731–738 (1962).

[88] P. Gütlich, "Physikalische Methoden in der Chemie: Mößbauer-Spektroskopie I," Chemie in unserer Zeit **4**, 133–144 (1970).

[89] R. Coussement, Y. Rostovtsev, J. Odeurs, G. Neyens, H. Muramatsu, S. Gheysen, R. Callens, K. Vyvey, G. Kozyreff, P. Mandel, R. Shakhmuratov, and O. Kocharovskaya, "Controlling absorption of gamma radiation via nuclear level anticrossing," Phys. Rev. Lett. **89**, 107601 (2002).

[90] R. N. Shakhmuratov, F. Vagizov, J. Odeurs, and O. Kocharovskaya, "Slow γ photon with a doublet structure: Time delay via a transition from destructive to constructive interference of collectively scattered radiation with the incoming photon," Phys. Rev. A **80**, 063805 (2009).

[91] S. L. Ruby, "Mössbauer experiments without conventional sources," J. Phys. Colloques **35**, 209–211 (1974).

[92] E. Alp, T. Mooney, T. Toellner, and W. Sturhahn, "Nuclear resonant scattering beamline at the Advanced Photon Source," Hyperfine Interactions **90**, 323–334 (1994).

[93] R. Rüffer and A. I. Chumakov, "Nuclear resonance beamline at ESRF," Hyperfine Interactions **97-98**, 589–604 (1996).

[94] Y. Yoda, M. Yabashi, K. Izumi, X. Zhang, S. Kishimoto, S. Kitao, M. Seto, T. Mitsui, T. Harami, Y. Imai, and S. Kikuta, "Nuclear resonant scattering beamline at SPring-8," Nuclear Instruments and Methods in Physics Research Section A: Accelerators, Spectrometers, Detectors and Associated Equipment **467–468**, 715–718 (2001), 7th Int.Conf. on Synchrotron Radiation Instrumentation.

[95] H.-C. Wille, H. Franz, R. Röhlsberger, W. A. Caliebe, and F.-U. Dill, "Nuclear resonant scattering at PETRA III: Brillant opportunities for nano – and extreme condition science," Journal of Physics: Conference Series **217**, 012008 (2010).

[96] E. Gerdau, R. Rüffer, H. Winkler, W. Tolksdorf, C. P. Klages, and J. P. Hannon, "Nuclear Bragg diffraction of synchrotron radiation in yttrium iron garnet," Phys. Rev. Lett. **54**, 835–838 (1985).

[97] G. V. Smirnov, U. van Bürck, A. I. Chumakov, A. Q. R. Baron, and R. Rüffer, "Synchrotron Mössbauer source," Phys. Rev. B **55**, 5811–5815 (1997).

[98] T. Mitsui, M. Seto, R. Masuda, K. Kiriyama, and Y. Kobayashi, "Synchrotron radiation Mössbauer spectroscopy using Doppler-shifted 14.4 keV single-line ^{57}Fe-Mössbauer radiation," Japanese Journal of Applied Physics **46**, L703 (2007).

[99] M. Seto, R. Masuda, S. Higashitaniguchi, S. Kitao, Y. Kobayashi, C. Inaba, T. Mitsui, and Y. Yoda, "Synchrotron-radiation-based Mössbauer spectroscopy," Phys. Rev. Lett. **102**, 217602 (2009).

[100] M. Seto, R. Masuda, S. Higashitaniguchi, S. Kitao, Y. Kobayashi, C. Inaba, T. Mitsui, and Y. Yoda, "Mössbauer spectroscopy in the energy domain using synchrotron radiation," Journal of Physics: Conference Series **217**, 012002 (2010).

[101] V. Potapkin, A. I. Chumakov, G. V. Smirnov, J.-P. Celse, R. Rüffer, C. McCammon, and L. Dubrovinsky, "The ^{57}Fe synchrotron Mössbauer source at the ESRF," Journal of Synchrotron Radiation **19**, 559–569 (2012).

[102] J. B. Hastings, D. P. Siddons, U. van Bürck, R. Hollatz, and U. Bergmann, "Mössbauer spectroscopy using synchrotron radiation," Phys. Rev. Lett. **66**, 770–773 (1991).

[103] R. Röhlsberger, T. S. Toellner, W. Sturhahn, K. W. Quast, E. E. Alp, A. Bernhard, E. Burkel, O. Leupold, and E. Gerdau, "Coherent resonant x-ray scattering from a rotating medium," Phys. Rev. Lett. **84**, 1007–1010 (2000).

[104] R. Röhlsberger, "Resonant x-ray scattering from a rotating medium: The nuclear lighthouse effect," Hyperfine Interactions **126**, 425–429 (2000).

[105] R. Röhlsberger, T. Toellner, K. Quast, W. Sturhahn, E. Alp, and E. Burkel, "The nuclear lighthouse effect: a new tool for high-resolution x-ray spectroscopy," Nuclear Instruments and Methods in Physics Research Section A: Accelerators, Spectrometers, Detectors and Associated Equipment **467–468**, 1473–1476 (2001), proceedings of the 7th Int. Conf. on Synchrotron Radiation Instrumentation.

[106] R. Röhlsberger, "The collective Lamb shift in nuclear γ-ray superradiance," Hyperfine Interactions **204**, 89–96 (2012).

[107] R. Röhlsberger, "Cooperative emission from nuclei: The collective Lamb shift and electromagnetically induced transparency," Fortschritte der Physik **61**, 360–376 (2013).

[108] G. T. Trammell and J. P. Hannon, "Quantum beats from nuclei excited by synchrotron pulses," Phys. Rev. B **18**, 165–172 (1978).

[109] D. Zaretskii and V. Lomonosov, "Spontaneous emission of gamma quanta from crystals," Soviet Journal of Experimental and Theoretical Physics **21**, 243 (1965).

[110] M. O. Scully, "Collective Lamb shift in single photon Dicke superradiance," Phys. Rev. Lett. **102**, 143601 (2009).

[111] Y. Li, J. Evers, H. Zheng, and S.-Y. Zhu, "Collective spontaneous emission beyond the rotating-wave approximation," Phys. Rev. A **85**, 053830 (2012).

[112] Y. Li, J. Evers, W. Feng, and S.-Y. Zhu, "Spectrum of collective spontaneous emission beyond the rotating-wave approximation," Phys. Rev. A **87**, 053837 (2013).

[113] W. Feng, Y. Li, and S.-Y. Zhu, "Effect of atomic distribution on cooperative spontaneous emission," Phys. Rev. A **89**, 013816 (2014).

[114] E. Purcell, "Spontaneous emission probabilities at radio frequencies," Physical Review **69**, 681 (1946).

[115] J. Keaveney, A. Sargsyan, U. Krohn, I. G. Hughes, D. Sarkisyan, and C. S. Adams, "Cooperative Lamb shift in an atomic vapor layer of nanometer thickness," Phys. Rev. Lett. **108**, 173601 (2012).

[116] M. Fleischhauer, A. Imamoğlu, and J. P. Marangos, "Electromagnetically induced transparency: Optics in coherent media," Rev. Mod. Phys. **77**, 633–673 (2005).

[117] S. E. Harris, "Electromagnetically induced transparency," Physics Today **50**, 36 (1997).

[118] S. E. Harris, J. E. Field, and A. Kasapi, "Dispersive properties of electromagnetically induced transparency," Phys. Rev. A **46**, R29–R32 (1992).

[119] A. Kocharovskaya and Y. I. Khanin, "Population trapping and coherent bleaching of a three-level medium by a periodic train of ultrashort pulses," Soviet Journal of Experimental and Theoretical Physics **63**, 945 (1986).

[120] H. Schmidt and A. Imamoğlu, "Giant Kerr nonlinearities obtained by electromagnetically induced transparency," Opt. Lett. **21**, 1936–1938 (1996).

[121] S. E. Harris and L. V. Hau, "Nonlinear optics at low light levels," Phys. Rev. Lett. **82**, 4611–4614 (1999).

[122] M. D. Lukin and A. Imamoğlu, "Nonlinear optics and quantum entanglement of ultraslow single photons," Phys. Rev. Lett. **84**, 1419–1422 (2000).

[123] D. K. G. de Boer, "Glancing-incidence x-ray fluorescence of layered materials," Phys. Rev. B **44**, 498–511 (1991).

[124] H. Kramers and W. Heisenberg, "Über die Streuung von Strahlung durch Atome," Zeitschrift für Physik A Hadrons and Nuclei **31**, 681–708 (1925).

[125] V. Weisskopf, "Die Streuung des Lichts an angeregten Atomen," Zeitschrift für Physik A Hadrons and Nuclei **85**, 451–481 (1933).

[126] W. Demtröder, *Experimentalphysik 3: Atome, Moleküle und Festkörper*, Springer-Lehrbuch (Springer, 2005).

[127] T. Schoonjans, A. Brunetti, B. Golosio, M. S. del Rio, V. A. Solé, C. Ferrero, and L. Vincze, "The XRAYLIB library for x-ray–matter interactions. recent developments," Spectrochimica Acta Part B: Atomic Spectroscopy **66**, 776–784 (2011).

[128] R. Röhlsberger, H. Thomas, K. Schlage, E. Burkel, O. Leupold, and R. Rüffer, "Imaging the magnetic spin structure of exchange-coupled thin films," Phys. Rev. Lett. **89**, 237201 (2002).

[129] R. Röhlsberger, J. Bansmann, V. Senz, K. L. Jonas, A. Bettac, K. H. Meiwes-Broer, and O. Leupold, "Nanoscale magnetism probed by nuclear resonant scattering of synchrotron radiation," Phys. Rev. B **67**, 245412 (2003).

[130] K. Schlage and R. Röhlsberger, "Nuclear resonant scattering of synchrotron radiation: Applications in magnetism of layered structures," Journal of Electron Spectroscopy and Related Phenomena **189**, 187–195 (2013).

[131] R. Röhlsberger, T. Klein, K. Schlage, O. Leupold, and R. Rüffer, "Coherent x-ray scattering from ultrathin probe layers," Phys. Rev. B **69**, 235412 (2004).

[132] J. Kane and H. Osterberg, "Optical characteristics of planar guided modes," J. Opt. Soc. Am. **54**, 347–352 (1964).

[133] R. E. De Wames and S. K. Sinha, "Possibility of guided-neutron-wave propagation in thin films," Phys. Rev. B **7**, 917–921 (1973).

[134] R. Bullough, "Photon, quantum and collective, effects from Rydberg atoms in cavities," Hyperfine Interactions **37**, 71–108 (1987).

[135] P. Rice and H. J. Carmichael, "Single-atom cavity-enhanced absorption. I. Photon statistics in the bad-cavity limit," IEEE Journal of Quantum Electronics **24**, 1351–1366 (1988).

[136] R. J. Brecha, P. R. Rice, and M. Xiao, "N two-level atoms in a driven optical cavity: Quantum dynamics of forward photon scattering for weak incident fields," Phys. Rev. A **59**, 2392–2417 (1999).

[137] S. I. Schmid, K. Xia, and J. Evers, "Pathway interference in a loop array of three coupled microresonators," Phys. Rev. A **84**, 013808 (2011).

[138] S. I. Schmid, *Quantum optics with whispering gallery resonators coupled to atoms and fibers*, Ph.D. thesis, Ruprecht-Karls-Universität Heidelberg (2011).

[139] H. Breuer and F. Petruccione, *The Theory of Open Quantum Systems* (Oxford University Press, 2002).

[140] M. Kiffner, M. Macovei, J. Evers, and C. H. Keitel, "Vacuum-induced processes in multilevel atoms," in *Progress in Optics*, Vol. 55 (Elsevier Science, 2010) pp. 85–197.

[141] B. Dayan, A. S. Parkins, T. Aoki, E. P. Ostby, K. J. Vahala, and H. J. Kimble, "A photon turnstile dynamically regulated by one atom," Science **319**, 1062–1065 (2008).

[142] C. Gardiner and P. Zoller, *Quantum Noise: A Handbook of Markovian and Non-Markovian Quantum Stochastic Methods with Applications to Quantum Optics*, Springer Series in Synergetics (Springer, 2004).

[143] D. Walls and G. Milburn, *Quantum Optics* (Springer, 2008).

[144] R. J. Glauber, "The quantum theory of optical coherence," Phys. Rev. **130**, 2529–2539 (1963).

[145] R. J. Glauber, "Nobel lecture: One hundred years of light quanta," Rev. Mod. Phys. **78**, 1267–1278 (2006).

[146] P. Meystre and M. Sargent, *Elements of quantum optics*, 4th ed. (Springer, 2007).

[147] Z. Ficek and S. Swain, *Quantum Interference and Coherence: Theory and Experiments*, Springer Series in Optical Sciences (Springer, 2005).

[148] G. Agarwal, *Quantum Optics: Quantum Statistical Theories of Spontaneous Emission and Their Relation to Other Approaches*, Springer tracts in modern physics (Springer, 1974).

[149] A. K. Patnaik and G. S. Agarwal, "Cavity-induced coherence effects in spontaneous emissions from preselection of polarization," Phys. Rev. A **59**, 3015–3020 (1999).

[150] G. S. Agarwal, "Anisotropic vacuum-induced interference in decay channels," Phys. Rev. Lett. **84**, 5500–5503 (2000).

[151] F. Schwabl, *Quantenmechanik (QM I): Eine Einführung*, 7th ed., Springer-Lehrbuch (Springer, 2004).

[152] M. O. Scully, E. S. Fry, C. H. R. Ooi, and K. Wódkiewicz, "Directed spontaneous emission from an extended ensemble of n atoms: Timing is everything," Phys. Rev. Lett. **96**, 010501 (2006).

[153] R. J. Thompson, G. Rempe, and H. J. Kimble, "Observation of normal-mode splitting for an atom in an optical cavity," Phys. Rev. Lett. **68**, 1132–1135 (1992).

[154] P. F. Herskind, A. Dantan, J. P. Marler, M. Albert, and M. Drewsen, "Realization of collective strong coupling with ion coulomb crystals in an optical cavity," Nature Physics **5**, 494–498 (2009).

[155] A. Wickenbrock, P. Phoonthong, and F. Renzoni, "Collective strong coupling in a lossy optical cavity," Journal of Modern Optics **58**, 1310–1316 (2011).

[156] J. Cresser, "Theory of the spectrum of the quantised light field," Physics Reports **94**, 47–110 (1983).

[157] R. Puri, *Mathematical Methods of Quantum Optics*, Springer Series in Optical Sciences (Springer, 2001).

[158] M. Lax, "Formal theory of quantum fluctuations from a driven state," Phys. Rev. **129**, 2342–2348 (1963).

[159] F. Dimer, B. Estienne, A. S. Parkins, and H. J. Carmichael, "Proposed realization of the Dicke-model quantum phase transition in an optical cavity QED system," Phys. Rev. A **75**, 013804 (2007).

[160] U. Fano, "Effects of configuration interaction on intensities and phase shifts," Phys. Rev. **124**, 1866–1878 (1961).

[161] U. Fano, "Sullo spettro di assorbimento dei gas nobili presso il limite dello spettro d'arco," Il Nuovo Cimento **12**, 154–161 (1935).

[162] R. P. Madden and K. Codling, "New autoionizing atomic energy levels in He, Ne, and Ar," Phys. Rev. Lett. **10**, 516–518 (1963).

[163] U. Fano and J. W. Cooper, "Spectral distribution of atomic oscillator strengths," Rev. Mod. Phys. **40**, 441–507 (1968).

[164] J. M. Rost, K. Schulz, M. Domke, and G. Kaindl, "Resonance parameters of photo doubly excited helium," Journal of Physics B: Atomic, Molecular and Optical Physics **30**, 4663 (1997).

[165] G. Tanner, K. Richter, and J.-M. Rost, "The theory of two-electron atoms: between ground state and complete fragmentation," Rev. Mod. Phys. **72**, 497–544 (2000).

[166] J. A. Fan, C. Wu, K. Bao, J. Bao, R. Bardhan, N. J. Halas, V. N. Manoharan, P. Nordlander, G. Shvets, and F. Capasso, "Self-assembled plasmonic nanoparticle clusters," Science **328**, 1135–1138 (2010).

[167] A. R. Schmidt, M. H. Hamidian, P. Wahl, F. Meier, A. V. Balatsky, J. D. Garrett, T. J. Williams, G. M. Luke, and J. C. Davis, "Imaging the Fano lattice to 'hidden order' transition in URu_2Si_2," Nature **465**, 570–576 (2010).

[168] M. Kroner, A. O. Govorov, S. Remi, B. Biedermann, S. Seidl, A. Badolato, P. M. Petroff, W. Zhang, R. Barbour, B. D. Gerardot, R. J. Warburton, and K. Karrai, "The nonlinear Fano effect," Nature **451**, 311–314 (2008).

[169] A. E. Miroshnichenko, S. Flach, and Y. S. Kivshar, "Fano resonances in nanoscale structures," Rev. Mod. Phys. **82**, 2257–2298 (2010).

[170] B. Luk'yanchuk, N. I. Zheludev, S. A. Maier, N. J. Halas, P. Nordlander, H. Giessen, and C. T. Chong, "The Fano resonance in plasmonic nanostructures and metamaterials," Nature Materials **9**, 707–715 (2010).

[171] N. Michel, W. Nazarewicz, M. Płoszajczak, and K. Bennaceur, "Gamow shell model description of neutron-rich nuclei," Phys. Rev. Lett. **89**, 042502 (2002).

[172] C. Ott, A. Kaldun, P. Raith, K. Meyer, M. Laux, J. Evers, C. H. Keitel, C. H. Greene, and T. Pfeifer, "Lorentz meets Fano in spectral line shapes: A universal phase and its laser control," Science **340**, 716–720 (2013).

[173] S. Fan, "Sharp asymmetric line shapes in side-coupled waveguide-cavity systems," Applied Physics Letters **80**, 908–910 (2002).

[174] P. J. Black and P. B. Moon, "Resonant scattering of the 14-keV iron-57 γ-ray, and its interference with Rayleigh scattering," Nature **188**, 481–482 (1960).

[175] S. Bernstein and E. C. Campbell, "Nuclear anomalous dispersion in Fe^{57} by the method of total reflection," Phys. Rev. **132**, 1625–1633 (1963).

[176] F. Parak, R. L. Mössbauer, U. Biebl, H. Formanek, and W. Hoppe, "Experimental test of a new method for phase determination using gamma resonance spectroscopy," Zeitschrift für Physik **244**, 456–467 (1971).

[177] G. Smirnov, "Coherent effects in resonant diffraction: experiment," Hyperfine Interactions **27**, 203–218 (1986).

[178] G. V. Smirnov, "Coherent nuclear resonance fluorescence," in *The Rudolf Mössbauer Story: His Scientific Work and Its Impact on Science and History*, edited by G. Kalvius and P. Kienle (Springer, 2012).

[179] Y. V. Shvyd'ko and G. V. Smirnov, "Experimental study of time and frequency properties of collective nuclear excitations in a single crystal (gamma-ray resonance)," Journal of Physics: Condensed Matter **1**, 10563 (1989).

[180] K. Kobayashi, H. Aikawa, S. Katsumoto, and Y. Iye, "Tuning of the Fano effect through a quantum dot in an Aharonov-Bohm interferometer," Phys. Rev. Lett. **88**, 256806 (2002).

[181] A. Bärnthaler, S. Rotter, F. Libisch, J. Burgdörfer, S. Gehler, U. Kuhl, and H.-J. Stöckmann, "Probing decoherence through Fano resonances," Phys. Rev. Lett. **105**, 056801 (2010).

[182] F. Goos and H. Hänchen, "Ein neuer und fundamentaler Versuch zur Totalreflexion," Annalen der Physik **436**, 333–346 (1947).

[183] A. Zavatta and M. Bellini, "Quantum optics: The quantum picture of a detector," Nature Photonics **6**, 350–351 (2012).

[184] G. Taylor, "The phase problem," Acta Crystallographica Section D **59**, 1881–1890 (2003).

[185] S. Marchesini, "Invited article: A unified evaluation of iterative projection algorithms for phase retrieval," Review of Scientific Instruments **78**, 011301 (2007).

[186] G. L. Taylor, "Introduction to phasing," Acta Crystallographica Section D **66**, 325–338 (2010).

[187] P. Hariharan, *Basics of Interferometry* (Elsevier Science, 1992).

[188] K. Vogel and H. Risken, "Determination of quasiprobability distributions in terms of probability distributions for the rotated quadrature phase," Phys. Rev. A **40**, 2847–2849 (1989).

[189] G. M. D'Ariano, M. G. Paris, and M. F. Sacchi, "Quantum tomography," (Elsevier, 2003) pp. 205–308.

[190] D. T. Smithey, M. Beck, M. G. Raymer, and A. Faridani, "Measurement of the Wigner distribution and the density matrix of a light mode using optical homodyne tomography: Application to squeezed states and the vacuum," Phys. Rev. Lett. **70**, 1244–1247 (1993).

[191] W. Sturhahn, K. W. Quast, T. S. Toellner, E. E. Alp, J. Metge, and E. Gerdau, "Electron emission from ^{57}Fe nuclei excited with synchrotron radiation," Phys. Rev. B **53**, 171–175 (1996).

[192] T. S. Toellner, E. E. Alp, W. Sturhahn, T. M. Mooney, X. Zhang, M. Ando, Y. Yoda, and S. Kikuta, "Polarizer/analyzer filter for nuclear resonant scattering of synchrotron radiation," Applied Physics Letters **67**, 1993–1995 (1995).

[193] E. Alp, W. Sturhahn, and T. Toellner, "Polarizer–analyzer optics," Hyperfine Interactions **125**, 45–68 (2000).

[194] B. Marx, I. Uschmann, S. Höfer, R. Lötzsch, O. Wehrhan, E. Förster, M. Kaluza, T. Stöhlker, H. Gies, C. Detlefs, T. Roth, J. Härtwig, and G. Paulus, "Determination of high-purity polarization state of x-rays," Optics Communications **284**, 915–918 (2011).

[195] D. A. Lidar, I. L. Chuang, and K. B. Whaley, "Decoherence-free subspaces for quantum computation," Phys. Rev. Lett. **81**, 2594–2597 (1998).

[196] P. G. Kwiat, A. J. Berglund, J. B. Altepeter, and A. G. White, "Experimental verification of decoherence-free subspaces," Science **290**, 498–501 (2000).

[197] O. A. Kocharovskaya and Y. I. Khanin, "Coherent amplification of an ultrashort pulse in a three-level medium without a population inversion," Soviet Journal of Experimental and Theoretical Physics Letters **48**, 630 (1988).

[198] S. E. Harris, "Lasers without inversion: Interference of lifetime-broadened resonances," Phys. Rev. Lett. **62**, 1033–1036 (1989).

[199] M. Fleischhauer, C. Keitel, L. Narducci, M. Scully, S.-Y. Zhu, and M. Zubairy, "Lasing without inversion: interference of radiatively broadened resonances in dressed atomic systems," Optics Communications **94**, 599–608 (1992).

[200] D. A. Cardimona, M. G. Raymer, and C. R. Stroud Jr., "Steady-state quantum interference in resonance fluorescence," Journal of Physics B: Atomic and Molecular Physics **15**, 55 (1982).

[201] S.-Y. Zhu, R. C. F. Chan, and C. P. Lee, "Spontaneous emission from a three-level atom," Phys. Rev. A **52**, 710–716 (1995).

[202] Y. Niu and S. Gong, "Enhancing Kerr nonlinearity via spontaneously generated coherence," Phys. Rev. A **73**, 053811 (2006).

[203] P. Zhou and S. Swain, "Quantum interference in probe absorption: Narrow resonances, transparency, and gain without population inversion," Phys. Rev. Lett. **78**, 832–835 (1997).

[204] D. Bortman-Arbiv, A. D. Wilson-Gordon, and H. Friedmann, "Phase control of group velocity: From subluminal to superluminal light propagation," Phys. Rev. A **63**, 043818 (2001).

[205] H. Schmidt, K. L. Campman, A. C. Gossard, and A. Imamoğlu, "Tunneling induced transparency: Fano interference in intersubband transitions," Applied Physics Letters **70**, 3455–3457 (1997).

[206] J. Faist, F. Capasso, C. Sirtori, K. W. West, and L. N. Pfeiffer, "Controlling the sign of quantum interference by tunnelling from quantum wells," Nature **390**, 589–591 (1997).

[207] Z.-H. Tang, G.-X. Li, and Z. Ficek, "Entanglement created by spontaneously generated coherence," Phys. Rev. A **82**, 063837 (2010).

[208] D. Kielpinski, V. Meyer, M. A. Rowe, C. A. Sackett, W. M. Itano, C. Monroe, and D. J. Wineland, "A decoherence-free quantum memory using trapped ions," Science **291**, 1013–1015 (2001).

[209] F. Verstraete, M. M. Wolf, and J. Ignacio Cirac, "Quantum computation and quantum-state engineering driven by dissipation," Nature Physics **5**, 633–636 (2009).

[210] M. O. Scully, "Quantum photocell: Using quantum coherence to reduce radiative recombination and increase efficiency," Phys. Rev. Lett. **104**, 207701 (2010).

[211] M. O. Scully, K. R. Chapin, K. E. Dorfman, M. B. Kim, and A. Svidzinsky, "Quantum heat engine power can be increased by noise-induced coherence," Proceedings of the National Academy of Sciences **108**, 15097–15100 (2011).

[212] P. Zhou and S. Swain, "Cavity engineering of quantum interference," Optics Communications **179**, 267–274 (2000).

[213] M. Fleischhauer, C. H. Keitel, M. O. Scully, C. Su, B. T. Ulrich, and S.-Y. Zhu, "Resonantly enhanced refractive index without absorption via atomic coherence," Phys. Rev. A **46**, 1468–1487 (1992).

[214] G. A. Wilson, K. K. Meduri, P. B. Sellin, and T. W. Mossberg, "Inversionless gain in driven three-level ssV-type atoms: A comparison of broadband and monochromatic excitation," Phys. Rev. A **50**, 3394–3400 (1994).

[215] Z. Ficek and S. Swain, "Simulating quantum interference in a three-level system with perpendicular transition dipole moments," Phys. Rev. A **69**, 023401 (2004).

[216] H.-R. Xia, C.-Y. Ye, and S.-Y. Zhu, "Experimental observation of spontaneous emission cancellation," Phys. Rev. Lett. **77**, 1032–1034 (1996).

[217] L. Li, X. Wang, J. Yang, G. Lazarov, J. Qi, and A. M. Lyyra, "Comment on "experimental observation of spontaneous emission cancellation"," Phys. Rev. Lett. **84**, 4016–4016 (2000).

[218] S. E. Economou, R.-B. Liu, L. J. Sham, and D. G. Steel, "Unified theory of consequences of spontaneous emission in a Λ system," Phys. Rev. B **71**, 195327 (2005).

[219] A. Aspect, E. Arimondo, R. Kaiser, N. Vansteenkiste, and C. Cohen-Tannoudji, "Laser cooling below the one-photon recoil energy by velocity-selective coherent population trapping: theoretical analysis," J. Opt. Soc. Am. B **6**, 2112–2124 (1989).

[220] M. Schubert, I. Siemers, R. Blatt, W. Neuhauser, and P. E. Toschek, "Transient internal dynamics of a multilevel ion," Phys. Rev. A **52**, 2994–3006 (1995).

[221] B. Weber, H. P. Specht, T. Müller, J. Bochmann, M. Mücke, D. L. Moehring, and G. Rempe, "Photon-photon entanglement with a single trapped atom," Phys. Rev. Lett. **102**, 030501 (2009).

[222] D. G. Norris, L. A. Orozco, P. Barberis-Blostein, and H. J. Carmichael, "Observation of ground-state quantum beats in atomic spontaneous emission," Phys. Rev. Lett. **105**, 123602 (2010).

[223] D. G. Norris, A. D. Cimmarusti, L. A. Orozco, P. Barberis-Blostein, and H. J. Carmichael, "Spontaneous creation and persistence of ground-state coherence in a resonantly driven intracavity atomic ensemble," Phys. Rev. A **86**, 053816 (2012).

[224] M. V. G. Dutt, J. Cheng, B. Li, X. Xu, X. Li, P. R. Berman, D. G. Steel, A. S. Bracker, D. Gammon, S. E. Economou, R.-B. Liu, and L. J. Sham, "Stimulated and spontaneous optical generation of electron spin coherence in charged GaAs quantum dots," Phys. Rev. Lett. **94**, 227403 (2005).

[225] P. R. Berman, "Analysis of dynamical suppression of spontaneous emission," Phys. Rev. A **58**, 4886–4891 (1998).

[226] G. S. Agarwal and A. K. Patnaik, "Vacuum-induced coherences in radiatively coupled multilevel systems," Phys. Rev. A **63**, 043805 (2001).

[227] J. I. Cirac and P. Zoller, "Goals and opportunities in quantum simulation," Nature Physics **8**, 264–266 (2012).

[228] T. F. Krauss, "Why do we need slow light?" Nature Photonics **2**, 448–450 (2008).

[229] L. V. Hau, S. E. Harris, Z. Dutton, and C. H. Behroozi, "Light speed reduction to 17 metres per second in an ultracold atomic gas," Nature **397**, 594–598 (1999).

[230] M. M. Kash, V. A. Sautenkov, A. S. Zibrov, L. Hollberg, G. R. Welch, M. D. Lukin, Y. Rostovtsev, E. S. Fry, and M. O. Scully, "Ultraslow group velocity and enhanced nonlinear optical effects in a coherently driven hot atomic gas," Phys. Rev. Lett. **82**, 5229–5232 (1999).

[231] D. Budker, D. F. Kimball, S. M. Rochester, and V. V. Yashchuk, "Nonlinear magneto-optics and reduced group velocity of light in atomic vapor with slow ground state relaxation," Phys. Rev. Lett. **83**, 1767–1770 (1999).

[232] T. Baba, "Slow light in photonic crystals," Nature Photonics **2**, 465–473 (2008).

[233] L. Thévenaz, "Slow and fast light in optical fibres," Nature Photonics **2**, 474–481 (2008).

[234] M. Mücke, E. Figueroa, J. Bochmann, C. Hahn, K. Murr, S. Ritter, C. J. Villas-Boas, and G. Rempe, "Electromagnetically induced transparency with single atoms in a cavity," Nature **465**, 755–758 (2010).

[235] M. Albert, A. Dantan, and M. Drewsen, "Cavity electromagnetically induced transparency and all-optical switching using ion coulomb crystals," Nature Photonics **5**, 633–636 (2011).

[236] F. J. Lynch, R. E. Holland, and M. Hamermesh, "Time dependence of resonantly filtered gamma rays from Fe^{57}," Phys. Rev. **120**, 513–520 (1960).

[237] Y. Kagan, A. Afanas'ev, and V. Kohn, "Time delay in the resonance scattering of synchrotron radiation by nuclei in a crystal," Physics Letters A **68**, 339–341 (1978).

[238] Y. Kagan, A. M. Afanas'ev, and V. G. Kohn, "On excitation of isomeric nuclear states in a crystal by synchrotron radiation," Journal of Physics C: Solid State Physics **12**, 615 (1979).

[239] Y. V. Shvyd'ko, "Coherent nuclear resonant scattering of x-rays: Time and space picture," Hyperfine Interactions **123-124**, 275–299 (1999).

[240] R. Callens, R. Coussement, T. Kawakami, J. Ladrière, S. Nasu, T. Ono, I. Serdons, K. Vyvey, T. Yamada, Y. Yoda, and J. Odeurs, "Principles of stroboscopic detection of nuclear forward-scattered synchrotron radiation," Phys. Rev. B **67**, 104423 (2003).

[241] W.-T. Liao, *Coherent Control of Nuclei and X-Rays*, Ph.D. thesis, Ruprecht-Karls-Universität Heidelberg (2013).

[242] A. Oppenheim and J. Lim, "The importance of phase in signals," Proceedings of the IEEE **69**, 529–541 (1981).

[243] H. Chang, D. D. Smith, K. A. Fuller, J. O. Dimmock, D. A. Gregory, and D. O. Frazier, "Slow and fast light in coupled microresonators," in *Proc. SPIE*, Vol. 5735 (2005) pp. 40–51.

[244] S. Longhi, M. Marano, P. Laporta, M. Belmonte, and P. Crespi, "Experimental observation of superluminal pulse reflection in a double-Lorentzian photonic band gap," Phys. Rev. E **65**, 045602 (2002).

[245] J. E. Heebner and R. W. Boyd, "'Slow' and 'fast' light in resonator-coupled waveguides," Journal of Modern Optics **49**, 2629–2636 (2002).

[246] S. Chu and S. Wong, "Linear pulse propagation in an absorbing medium," Phys. Rev. Lett. **48**, 738–741 (1982).

[247] T. S. Toellner, E. E. Alp, T. Graber, R. W. Henning, S. D. Shastri, G. Shenoy, and W. Sturhahn, "Synchrotron Mössbauer spectroscopy using high-speed shutters," Journal of Synchrotron Radiation **18**, 183–188 (2011).

[248] Y. V. Shvyd'ko, U. van Bürck, W. Potzel, P. Schindelmann, E. Gerdau, O. Leupold, J. Metge, H. D. Rüter, and G. V. Smirnov, "Hybrid beat in nuclear forward scattering of synchrotron radiation," Phys. Rev. B **57**, 3552–3561 (1998).

[249] U. van Bürck, "Coherent pulse propagation through resonant media," Hyperfine Interactions **123-124**, 483–509 (1999).

[250] I. S. Gradshteyn and I. M. Ryzhik, *Table of Integrals, Series, and Products*, 7th ed., edited by A. Jeffrey and D. Zwillinger (Academic Press, 2007).

[251] D. Z. Xu, Y. Li, C. P. Sun, and P. Zhang, "Collective effects of multiscattering on the coherent propagation of photons in a two-dimensional network," Phys. Rev. A **88**, 013832 (2013).

[252] J. Hu and C. R. Menyuk, "Understanding leaky modes: slab waveguide revisited," Adv. Opt. Photon. **1**, 58–106 (2009).

[253] K. J. Tsanaktsidis, D. M. Paganin, and D. Pelliccia, "Analytical description of partially coherent propagation and absorption losses in x-ray planar waveguides," Opt. Lett. **38**, 1808–1810 (2013).

[254] J. Haber, private communication (2014).

[255] P. Longo and J. Evers, "Probing few-excitation eigenstates of interacting atoms on a lattice by observing their collective light emission in the far field," ArXiv e-prints (2014), arXiv:1408.2961 [quant-ph] .

[256] R. H. Dicke, "Coherence in spontaneous radiation processes," Phys. Rev. **93**, 99–110 (1954).

[257] R. Puri, S. Lawande, and S. Hassan, "Dispersion in the driven Dicke model," Optics Communications **35**, 179–184 (1980).

[258] S. Kilin, "Collective effects in resonant fluorescence," Soviet Journal of Experimental and Theoretical Physics **51**, 1081 (1980).

[259] S. Kilin, "Critical phenomena in cooperative resonant fluorescence of a system of interacting atoms," Soviet Journal of Experimental and Theoretical Physics **55**, 38 (1982).

[260] M. Galassi, J. Davies, J. Theiler, B. Gough, G. Jungman, M. Booth, and F. Rossi, *GNU Scientific Library Reference Manual* (Network Theory Ltd., 2009).

[261] B. R. Mollow, "Power spectrum of light scattered by two-level systems," Phys. Rev. **188**, 1969–1975 (1969).

[262] A. Kaldun, C. Ott, A. Blättermann, M. Laux, K. Meyer, T. Ding, A. Fischer, and T. Pfeifer, "Extracting phase and amplitude modifications of laser-coupled Fano resonances," Phys. Rev. Lett. **112**, 103001 (2014).

[263] A. Blättermann, C. Ott, A. Kaldun, T. Ding, and T. Pfeifer, "Two-dimensional spectral interpretation of time-dependent absorption near laser-coupled resonances," Journal of Physics B: Atomic, Molecular and Optical Physics **47**, 124008 (2014).

[264] S. M. Cavaletto, C. Buth, Z. Harman, E. P. Kanter, S. H. Southworth, L. Young, and C. H. Keitel, "Resonance fluorescence in ultrafast and intense x-ray free-electron-laser pulses," Phys. Rev. A **86**, 033402 (2012).

[265] L. Zhang, private communication (2014).

[266] M. Wickenhauser, J. Burgdörfer, F. Krausz, and M. Drescher, "Time resolved Fano resonances," Phys. Rev. Lett. **94**, 023002 (2005).

[267] A. Bärnthaler, *Beutler-Fano resonances with time-dependence and decoherence: A theoretical and experimental study*, Master's thesis, Technische Universität Wien (2009).

[268] A. Singer, U. Lorenz, A. Marras, A. Klyuev, J. Becker, K. Schlage, P. Skopintsev, O. Gorobtsov, A. Shabalin, H.-C. Wille, H. Franz, H. Graafsma, and I. A. Vartanyants, "Intensity interferometry of single x-ray pulses from a synchrotron storage ring," Phys. Rev. Lett. **113**, 064801 (2014).

[269] A. Singer, U. Lorenz, F. Sorgenfrei, N. Gerasimova, J. Gulden, O. M. Yefanov, R. P. Kurta, A. Shabalin, R. Dronyak, R. Treusch, V. Kocharyan, E. Weckert, W. Wurth, and I. A. Vartanyants, "Hanbury Brown–Twiss interferometry at a free-electron laser," Phys. Rev. Lett. **111**, 034802 (2013).

[270] Y. V. Shvyd'ko, S. Stoupin, A. Cunsolo, A. H. Said, and X. Huang, "High-reflectivity high-resolution x-ray crystal optics with diamonds," Nature Physics **6**, 196–199 (2010).

[271] Y. Shvyd'ko, S. Stoupin, V. Blank, and S. Terentyev, "Near-100% Bragg reflectivity of x-rays," Nature Photonics **5**, 539–542 (2011).

[272] T. Osaka, M. Yabashi, Y. Sano, K. Tono, Y. Inubushi, T. Sato, S. Matsuyama, T. Ishikawa, and K. Yamauchi, "A Bragg beam splitter for hard x-ray free-electron lasers," Opt. Express **21**, 2823–2831 (2013).

[273] C. Strohm, P. Van der Linden, and R. Rüffer, "Nuclear forward scattering of synchrotron radiation in pulsed high magnetic fields," Phys. Rev. Lett. **104**, 087601 (2010).

Acknowledgments

Mein ganz besonderer Dank geht an Jörg Evers, unter dessen Betreuung diese Arbeit entstanden ist. Deine Anregungen und die vielen gemeinsamen Diskussionen in angenehmer Atmosphäre waren mir eine unschätzbare Hilfe. Ein Dankeschön auch für das Vertrauen, das du mir entgegengebracht hast, sowie für die große Freiheit, mit der ich meine eigenen Ideen verfolgen konnte. Das hat nicht nur diese Arbeit, sondern auch mich selbst entscheidend beeinflusst.

Des Weiteren gebührt mein herzlicher Dank Prof. Keitel, in dessen Abteilung ich die letzten Jahre verbringen durfte und der mir die Teilnahme an zahlreichen Konferenzen sowie mehrere Fahrten zu den Synchrotronquellen in Hamburg und Grenoble ermöglicht hat.

Eine ungemeine Unterstützung habe ich auch durch Ralf Röhlsberger erfahren. Unsere Diskussionen haben enorm zu meinem Verständnis der Mößbauerphysik beigetragen und die gemeinsamen Projekte haben nicht nur meine Motivation gefördert, sondern auch zahlreiche Impulse für diese Arbeit geliefert. Dafür möchte ich mich herzlich bedanken.

Ein herzliches Dankeschön geht an Prof. Jäckel für die freundliche Übernahme des Zweitgutachtens dieser Promotion.

An dieser Stelle möchte ich mich ebenfalls bei den weiteren Personen bedanken, die unsere gemeinsamen Experimente an PETRA-III und an der ESRF ermöglicht und mir einen ganz neuen Einblick in die Physik erlaubt haben: Hans-Christian Wille, Kai Schlage, Lars Bocklage, Daniel Schumacher, Johann Haber, Tatyana Guryeva, Rudolf Rüffer, Kai S. Schulze, Tino Kämpfer, Robert Loetzsch, Ingo Uschmann, Gerhard G. Paulus, Christian Ott und Thomas Pfeifer.

Bei der Studienstiftung des deutschen Volkes möchte ich mich ganz herzlich für die finanzielle und ideelle Förderung bedanken. Den Graduiertenschulen HGSFP und IMPRS-QD danke ich außerdem für die ideelle Unterstützung während meiner Promotionszeit.

Eine große Freude war es mir, meine Zeit im Büro in so angenehmer Atmosphäre zu verbringen. Dafür danke ich meinen jetzigen und ehemaligen Kollegen Martin Gärttner, Lida Zhang, Sandra Schmid, Andreas Reichegger und Patrick Reiser.

Auch bei den Personen, die mich beim Korrekturlesen dieser Arbeit unterstützt haben, Martin Gärttner, Paolo Longo, Jonas Gunst und Wen-Te Liao, möchte ich mich an dieser Stelle für ihre Hinweise bedanken.

Ganz besonders bedanke ich mich bei meiner Familie, die mich während meines gesamten Studiums und der Doktorarbeit unterstützt hat. Danke Mama, Papa, Max und Flo! Ebenso danke ich Simone Werner für die wunderbare Zeit, ihr liebevolles Verständnis und ihre Geduld mit mir.